Wireless and Conventional Electrochemiluminescence for Analytical Applications

Author

Samantha Douman (MSc)

A thesis submitted at Dublin City University for the degree of
Doctor of Philosophy

School of Chemical Sciences

Supervisors:
Prof. Robert J. Forster
Prof. Emmanuel I. Iwuoha (UWC)

September 2018

DECLARATION

I hereby certify that this material, which I now submit for assessment on the programme of study leading to the award of doctor of philosophy is entirely my own work, that I have exercised reasonable care to ensure that the work is original, and does not to the best of my knowledge breach any law of copyright, and has not been taken from the work of others save and to the extent that such work has been cited and acknowledged within the text of my work.

Signed:………………

ID no.:……………….

Date:…………………

DEDICATION

Dedicated to My Dear Parents

"Education is the most powerful weapon

which you can use to change the world"

-Nelson Rolihlahla Mandela

ACKNOWLEDGEMENTS

I would like to take this opportunity and platform to express my deep sense of appreciation to everyone who contributed towards this challenging venture. Without your help and counsel, which were given without a hassle and with so much support, the completion of this work would have been immensely more challenging. So with a joyful heart and a bursting genuine gratitude, I thank you all!

First and foremost, I would like to thank my Father in heaven for giving me the strength, patience and wisdom to be able to accomplish yet another goal in life.

To my supervisors, Professor Robert Forster and Professor Emmanuel Iwuoha, I owe you a huge depth of appreciation for providing me with invaluable advice, encouragements, enthusiastic discussion and most of all life-changing opportunities. I am forever grateful for your continuous support and honoured to be taught by you.

I would like to extend my appreciation to all my colleagues in our research group, both past and present. Eadaoin, Colm, Kellie, Elaine, Jamie, Hazel, Andrea, Bincy, Mohammad, Eoin, Dave, Loanda, Sara and Ausra. And of course my colleagues over in X246, Ciaran, Chris, Aisling, Darragh, Sean, Siva, Vinnie, Abdel, Aurélien and Guilherme. Thank you all for providing a very friendly and pleasant working environment. Thank you for making my stay memorable, especially the coffee mornings and cake afternoons. The surprise birthday celebrations, Halloween dress-up, and my all-time favourite, Christmas celebrations. I have never seen any country celebrate Christmas like the Irish do- totally magical!

To my short lived excited state Post doc (inside joke), Kerileng aka Miss K, you were truly amazing even if it was only for a short time. Thank you for helping me to transition smoothly into the Irish culture. Thank you for sharing of knowledge. Your support and friendship over the past few years has been nothing short of amazing.

My sincere thanks goes to the School of Chemistry secretary, Julie Mcarthur, and the technical staff of the School of Chemistry, especially those who I have dealt with personally, Veronica Dobbyn, Vincent "Vinny" Hooper and Ambrose May. Thank you for always assisting me and always going the extra mile when I needed a helping hand.

My thanks also go to the technical staff of NRF, especially Josephine Ozoani, Maurice Burke, Una Prendergast and Barry O’Connel. Thank you for assisting with consumables, training and advice. I am truly grateful for your support!

A special thanks goes to some of my good friends here in Ireland. Izabel, Alice, Eline, Billy and David. Thank you all for your friendship, pep talks and advice. Thank you for the long nights of laughter and just being there to listen to me ranting about things or people. Daria, Veronica, Marco and

Nico aka "the moving squad" thank you for your compassion and support during this challenging time from moving apartments to providing accommodation. You guys are truly incredible and I couldn’t have done it without you all! I have definitely made some "real" life-long friends!!

On a more personal note, I would like to thank my family. Mammie, deddie and boeta! I honestly do not have words to describe how thankful I am. I am who I am today much to your love, guidance and motivation. All the success that I have achieved is undoubtedly due to all your sacrifices and support each day. So this is for you!

TABLE OF CONTENTS

LIST OF ABBREVIATIONS

Acronyms	Explanation
AM :	Additive manufacturing
AMI :	Acute Myocardial Infarction
BE :	Backscattered electrons
Bpy :	2,2'-bipyridyl
BPE :	Bipolar electrochemistry
BP_{elec} :	Bipolar electrode
BSA :	Bovine Serum Albumin
cTnI :	Cardia Troponin-I
CVD :	Cardiovascular disease
CCD :	Charge coupled device
CL :	Chemiluminescence
CV :	Cyclic voltammetry
DC :	Direct current
DMF :	Dimethyl formamide
DMSO :	Dimethylsulfoxide
DPA :	9,10-Diphenylanthracene

ECL :	Electrochemiluminescence
EDC :	1-Ethyl-3-(3-dimethylaminopropyl)carbodiimide
EDX :	Energy dispersive x-ray spectroscopy
FE-SEM :	Field emission-scanning electron microscopy
FWHM :	Full width at half maximum
ISC :	Inter-system crossing
ITO :	Indium Tin Oxide
Mab :	Monoclonal antibody
MeCN :	Acetonitrile
MLCT :	Metal to ligand charge transfer
^{1}MLCT :	Singlet metal to ligand charge transfer
^{3}MLCT :	Triplet metal to ligand charge transfer
^{3}MC :	Triplet metal centred
NHS :	N-Hydroxysuccinimide
PANI :	Polyaniline
PAH :	Polyaromatic hydrocarbon
PBS :	Phosphate buffer solution
PET :	Polyethylene terephthalate
PMT :	Photo multiplier tube

RF :	Roughness factor
RUB :	Rubrene
SAM :	Self-assembled monolayers
SE :	Secondary electrons
SLM :	Selective laser melting
TMPD :	Tetramethyl-*p*-phenylenediamine
TPA :	Tripropylamine
UV-Vis :	Ultraviolet Visible
3D :	Three-dimensional
2D :	Two-dimensional
16-MHDA :	16-Mercaptohexadecanoic acid
16-PHDA :	16-Phosphonohexadecanoic acid

LIST OF SYMBOLS

Symbols	Explanation	Units
ΔG :	Gibbs energy	kJ mol^{-1}
E_{final} :	Final potential	V
$E_{initial}$:	Initial potential	V
E^{o} :	Formal potential	V
E_p :	Peak potential	V
$E_{p,a}$:	Anodic peak potential	V
$E_{p,c}$:	Cathodic peak potential	V
ΔE_p :	Separation peak potential	V
F :	Faraday constant	C mol^{-1}
A :	Surface area	cm^2
n :	Number of electrons	–
R :	Gas constant	J mol^{-1} K^{-1}
$I_{p,c}$:	Cathodic current	A
$I_{p,a}$:	Anodic current	A
I_p :	Peak current	A
Q :	Charge	C

ν :	Scan rate	$mV\ s^{-1}$
Γ :	Surface concentration	$mol\ cm^{-2}$
ΔE :	Difference in potential	V
E_{appl} :	Applied potential	V
k^o :	standard heterogeneous electron transfer rate constant	$cm\ s^{-1}$
α_a :	Anodic transfer coefficient	_
α_c :	Cathodic transfer coefficient	_
V_0 :	Electric field	$V\ m^{-1}$
σ :	Conductivity	$S\ m^{-1}$
φ_c :	Percolation threshold	_
t :	Critical exponent	_
ϕf :	Fluorescence quantum yield	_

LIST OF FIGURES

LIST OF SCHEMES

LIST OF TABLES

RESEARCH OUTPUTS

PUBLISHED PAPERS

1. Samantha Douman, Eoin Brennan, Emmanuel I. Iwuoha, and Robert J. Forster, *Analytical Chemistry*, **2017**, 89 (21), pp 11614-11619.
2. Samantha Douman, Stephen Beirne, Gordon G. Wallace, Zhilian Yue, Robert J. Forster and Emmanuel I. Iwuoha, Electron Transfer and Electrochemiluminescence Properties of 3D Titanium Electrodes. *Submitted*.
3. Samantha Douman, Kellie Adamson, Hui Ma, Richard, O'Kennedy, Robert J. Forster and Emmanuel I. Iwuoha, Sandwich-type ECL Sensing Platform for Ultrasensitive Detection of Cardiac Troponin I, a Biomarker for Cardiovascular Disease. *Manuscript*.

POSTER PRESENTATIONS

XXIV International Symposium on Bioelectrochemistry and Bioenergetics (3-7 July 2017)

Samantha F. Douman, Kellie Adamson, Seán Fitzgerald, Emmanuel I. Iwuoha, Richard, O'Kennedy and Robert J. Forster, Highly Sensitive Electrochemiluminescence Signaling of Cardiac Troponin I based on Bipolar Electrochemistry.

ABSTRACT

Samantha Douman

Wireless and Conventional Electrochemiluminescence Platforms for Analytical Applications

Electrochemiluminescence (ECL) or alternatively electrogenerated chemiluminescence is a light-emitting process brought about by electron-transfer reactions. ECL can occur via two pathways namely, ion annihilation and coreactant pathway. Coreactant ECL generation predominates over annihilation pathway due to the ease of ECL generation in aqueous solution. The discovery of ECL emission in aqueous media has led to major applications in analytical chemistry, especially in the field of biosensing, that is, immunoassays and DNA-probe assays. Thus, the scope of this work was to develop a simple, sensitive ECL immunosensor for cardiac injury and to study and present newly fabricated platforms for analytical applications by using conventional and bipolar ECL as detection mechanism.

Herein, two types of electrodes were investigated, that is, thin film electrodes made up of carbon micro-particles and three-dimensional (3D) printed electrodes made up of titanium alloy (Ti-6Al-4V) powder. The generation of ECL at these electrodes was based on two approaches, that is, ECL generated by conventional electrochemistry and ECL generation based on bipolar or wireless electrochemistry. Firstly, the conductivity of the thin film electrodes as well as their ability to generate ECL was investigated. The obtained results revealed that the films exhibited very low conductivity ($<6 \times 10^3$ S m^{-1}) for low carbon particle loadings, but once the percolation threshold was reached (volume percentage of 71 ± 8% carbon particles), the conductivity increased dramatically and a maximum conductivity of $2.0 \pm 0.1 \times 10^7$ S m^{-1} was achieved. The electrochemical properties of the thin film electrodes, including heterogeneous electron transfer rates, were probed using cyclic voltammetry. While the structural and topographical analysis was achieved by Raman and scanning electron microscopy, respectively. Significantly, bipolar ECL can be generated with films that contain >65% (by volume) carbon particles using $[Ru(bpy)_3]^{2+}$ as the luminophore and tripropylamine as the coreactant, at an electric field of 14 V cm^{-1}. A simple additive 3D printing technique based on selective laser melting (SLM) technology was used to fabricate 1 cm^2 footprint 3D-printed titanium electrodes. The 3D-printed structures were characterised topographically and electrochemically by scanning electron microscopy and cyclic voltammetry, respectively. An electrochemical surface modification method was used to functionalise the surface of the 3D titanium electrodes with a thin gold layer which significantly enhanced the dynamics of heterogeneous electron transfer. Despite the slow rate of heterogeneous electron transfer at the bare 3D titanium electrodes, significant ECL was generated and the intensity increased with increasing scan rate. The obtained results suggest that it's possible to fabricate customisable electrodes with control over the morphology, size, and performance, thus opens up exciting new possibilities for specific functions and studies like chemical sensing and biology, respectively.

Secondly, the thesis focused on the synthesis, characterisation and application of an interesting ECL luminophore, ruthenium (II) (bis-2,2-bipyridyl)-2(4-carboxylphenyl) imidazo[4,5-f][1,10]phenanthroline $[Ru(bpy)_2(picCOOH)]^{2+}$. The luminophore was found to exhibit impressive electrochemical and photophysical properties, and for this reason, was covalently coupled to a secondary antibody via NHS/EDC for employment as ECL emitters in the fabrication of a sandwich-type immunosensor for the detection of cardiac troponin I, an important biomarker for cardiac injury. The ECL immunosensor was fabricated by the assembly of a new custom-made primary antibody with a carboxylic acid-terminated alkanethiol modified gold electrode. The primary antibody modified gold electrode was first treated with 1% bovine serum albumin and thereafter it was reacted with various concentrations of human cardiac troponin-I, followed by the introduction of the secondary antibody dye-conjugate. In the presence of the tripropylamine coreactant, an increase in ECL signal was observed. The ECL intensity versus the concentration of cardiac troponin I was linear in the range from 0.001 pg mL^{-1} to 0.50 pg mL^{-1} with an extremely low detection limit of 0.03 pg mL^{-1} (SD, n=3). Furthermore, this immunoassay was extended to a bipolar electrochemical system so that wireless detection of cTnI could be realised. Comparison studies were also carried out to study the difference in ECL intensity between conventional and bipolar ECL approach.

1 Chapter 1:

Survey of Literature

1.1 INTRODUCTION

The work presented in this thesis focused on ways to improve the sensitivity and performance of ECL detection systems by fabricating interesting transduction platforms that ranged from carbon particles- to bulk- metallic three-dimensional designs (Figure 1.1). Coupled with bipolar electrochemistry, these platforms were utilised in a proof-of-concept approach to investigate their performance for possible use in bioanalytical applications.

Electrochemiluminescence (ECL) or electrogenerated chemiluminescence is a phenomenon in which light emission is produced via an electrochemical reduction–oxidation reaction. The excitation processes of ECL fundamentally depend on the energy of the excited state, thus ECL complexes can be distinguished by not only their wavelengths of emission, but also the voltages required for their excitation.[1] For this reason, ECL has been extensively used to study new compounds, complexes and clusters which displays novel photochemical and electrochemical properties. The discovery of ECL emission in aqueous media has led to major applications in bioanalytical chemistry, especially ECL based on the extensively studied $[Ru(bpy)_3]^{2+}$/tripropylamine system. For example, ECL-generating species have been used extensively as labels on biological molecules, allowing many clinically relevant analytes to be determined at subpicomolar concentrations via conventional antibody or nucleic acid assay approaches.[2] In such systems, the efficiency and stability of the ECL signal does not only depend on the ECL generating species, but also on the type of electrode needed to facilitate an electrochemical reaction.

For example, ECL generation at planar gold, glassy carbon, and indium tin oxide electrodes are quite different from one another due to their stability, possibilities to interact with ECL reagents, and differences in their conductivity.[3] Especially, when dealing in aqueous media ECL can be limited by the electrode's narrow electrochemical window, high capacitive and adsorption currents and unstable behaviour during electrolysis.[4] Furthermore, because these electrodes have a two-dimensional design, the versatility and the sensitivity of the ECL process can be limited.[5] However, this limitation can be addressed by changing the geometry of the electrode. Meaning, if the electrode has a three-dimensional (3D) design, the ECL light can be generated in a 3D format. This type of ECL generation can pave the way to some interesting possibilities for example, the integration of ECL in miniaturised components. Three-dimensional platforms have the ability to outperform two-dimensional platforms, because a key consideration for miniaturisation lies in the footprint area/surface area of the substrate.[6]

Moreover, the utilisation of 3D structures in traditional three-electrode setups, require direct electrical connection for read-out. This can be quite difficult to implement on miniaturised point-of-care devices. However, this issue can be addressed by bipolar electrochemistry (BPE), a process which is based on a piece of conducting material (known as the bipolar electrode) that can be polarised without the need of directly connecting it to a power source.[7] The downsizing of the components of the ECL generation/detection system combined with the wireless capabilities of BPE can allow for favourable features such as portability, short analysis time, low consumption of reactants, multiplex detection, and integration of separation and detection on the same device.[8,9] BPE/ECL system will not only grow as a powerful detection strategy, but will help to understand the electric field distribution within any given structure or material, and give insight into how the properties of these materials can be altered to get increased ECL signal output which will result in higher sensitivities.

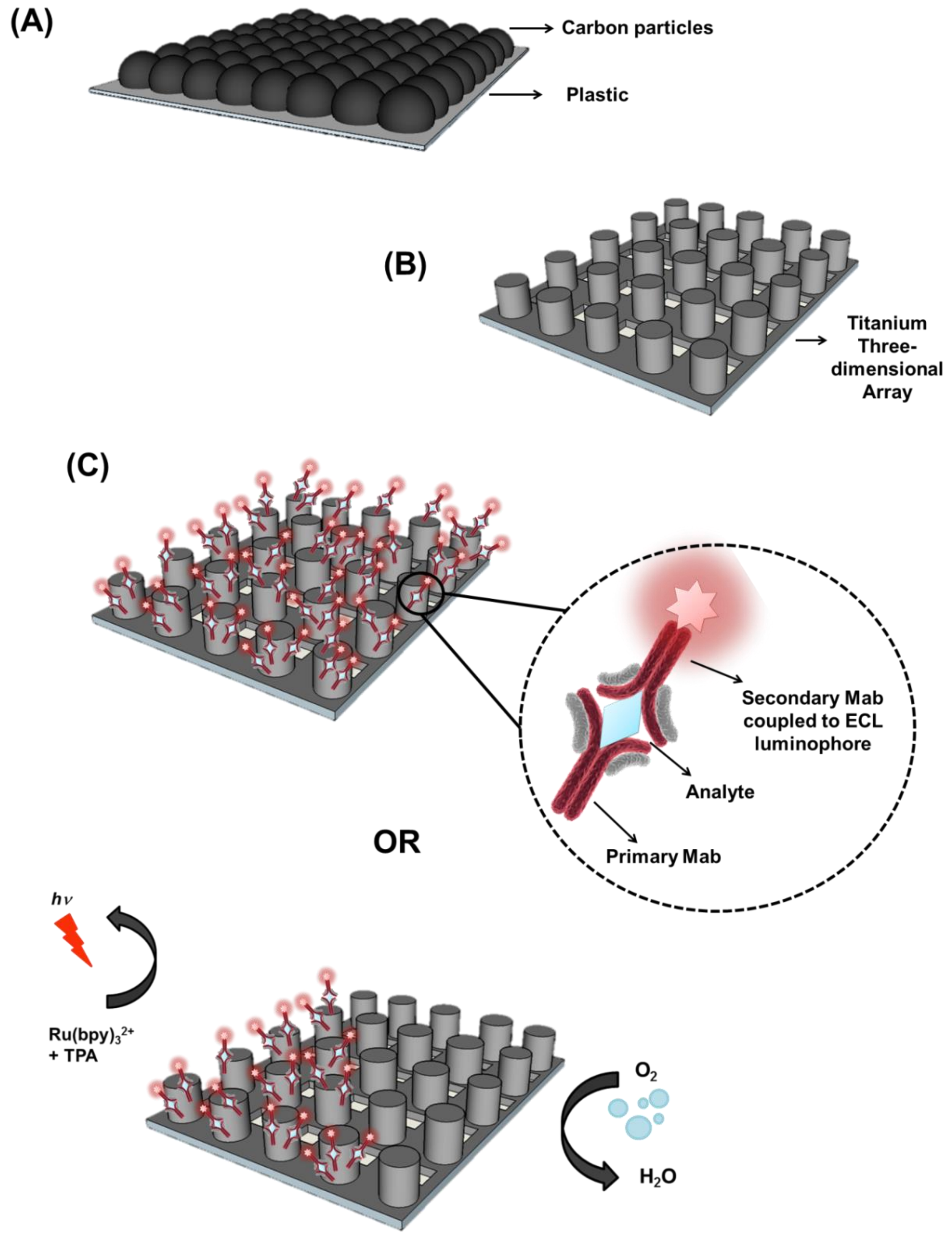

Figure 1.1: Illustrates new ECL sensing platforms reported in this thesis (A) carbon particles spin coated on non-conducting plastic, (B) three-dimensional titanium electrode fabricated by selective laser melting technique, and (C) possible utilisation of an immunoassay on the three-dimensional electrode using either conventional or bipolar electrochemiluminescence as detection and readout mechanism.

1.2 ELECTROCHEMILUMINESCENCE

1.2.1 Introduction

Electrochemiluminescence (ECL) is a process in which reactive species undergo electron transfer reactions in the presence of ECL active precursors, to produce photons, in the form of light.[10–12] In simple terms, ECL is a combination of electrochemistry and chemiluminescence (CL).[13] CL is a type of luminescence whereby the light produced, stems from energetic electron transfer reactions. However, the manner in which the emission of light is controlled is what differentiates ECL from CL. In CL, luminescence is initiated by carefully mixing reagents in reaction vessel and manipulating fluid flow, whereas in ECL luminescence is governed and controlled by altering the electrode potential.[11] ECL is an analytical technique that not only holds the advantages of sensitivity, selectivity and wide dynamic range inherent to conventional CL,[12] but exhibits additional advantages such as it allows greater control over the time of ECL reactions, thus improves reproducibility and simplifies operation.[14] In ECL, there is better control over the spatial location of the light emitting reactions; therefore it can be used for multi-analyte detection. Furthermore, ECL emitters can be regenerated after the light emission process, thus making it possible to take part in the reaction once again.[15]

Hercules[16] and co-workers were among the first to study the chemiluminescence of the ECL emitter $[Ru(bpy)_3]^{2+}$ in aqueous solution, while Bard[17] and co-workers were the first to show ECL of $[Ru(bpy)_3]^{2+}$ in both aqueous and non-aqueous solutions. However, reports on light emitted during electrolysis date back to the 1920s.[18,19] Since then, ECL attracted interest as a method to study new compounds and complexes that exhibited novel photochemical and electrochemical properties.[14] Several reviews ranging from fundamental theory to ECL applications have been published and include diverse ECL luminophores such as polyaromatic hydrocarbons (PAHs) and transition metal complexes (ruthenium, osmium, platinum and palladium)[20–23]. Emerging as a powerful analytical technique, ECL has been successfully applied across different research fields such as in the area of testing,[24,25] sensing[26] and imaging.[27] ECL is progressively more used as a diagnostic tool and has become quite a useful technique in flow injection analysis (FIA), high-performance liquid chromatography (HPLC), capillary electrophoresis (CE) and micro total analysis (μTAS) systems. The ability of ECL to couple to these systems can be ascribed to its simplicity, low cost, high sensitivity and selectivity. The combination of ECL with other techniques allows researchers to design and develop detection strategies required for specific experimental analysis.

1.2.2 Principles of Electrochemiluminescence

There are two main methods for ECL generation. Annihilation ECL and co-reactant ECL, the latter will be used throughout this thesis. For this reason, applications pertaining to co-reactant ECL will be discussed in greater detail.

1.2.2.1 Annihilation Pathway

Annihilation involves the electrochemical production of a stable radical cation $R^{\bullet+}$ and anion $R^{\bullet-}$.[28] The formed radical intermediates interact to generate excited states that emit light. The following mechanism shows the reaction sequence for the production of light using the annihilation pathway.

$R + e^- \rightarrow R^{\bullet-}$ *Cathodic Reduction* **[1.1]**

$R - e^- \rightarrow R^{\bullet+}$ *Anodic Oxidation* **[1.2]**

$R^{\bullet-} + R^{\bullet+} \rightarrow R^* + R$ *e^- transfer* **[1.3]**

(Excited State Formation)

followed by,

$R^* \rightarrow R + h\nu$ *Chemiluminescence* **[1.4]**

(Light Emission)

where R^* represents the excited molecule that emits light, and $h\nu$ is a photon of light. These processes are regarded as energy-sufficient because the free energy of the chemical reaction between the electrogenerated radicals is greater than or equal to the energy of the emissive state.[29] Energy-sufficient systems are said to follow the singlet route (S-route) because a singlet excited state is produced. The free Gibbs energy ΔG can be defined through the following equation:

$$\Delta G = nF(E^{\circ}_{Donor} - E^{\circ}_{Acceptor})$$ **[1.5]**

where, E°_{donor} and $E^{\circ}_{acceptor}$ represent the formal potentials of the ground-state reduction and oxidation processes, respectively. ECL systems based on aromatic compounds such as Rubrene (RUB), Tris(2, 2'-bipyridyl)ruthenium (II) $[Ru(bpy)_3]^{2+}$ and 9,10-diphenylanthracene (DPA) systems, generally follow the S-route.[30] The mechanism below demonstrates the S-route for the DPA system.

S-route: DPA System

$$DPA + e^- \rightarrow DPA^{\bullet -}$$ **[1.6]**

$$DPA - e^- \rightarrow DPA^{\bullet +}$$ **[1.7]**

$$DPA^{\bullet -} + DPA^{\bullet +} \rightarrow {}^1DPA^* + DPA$$ *Singlet Annihilation* **[1.8]**

(Energy-Sufficient System)

$${}^1DPA^* \rightarrow DPA + h\nu$$ **[1.9]**

In contrast to the energy-sufficient systems, energy-deficient systems also exist. The energy-deficient systems follow the triplet-triplet route (T-route). In some instances, energy-sufficient systems may also follow the T-route. The T-route is followed when two triplets of the same species react with each other to form one singlet excited state. Many ECL reactions with different precursors follow this route.[14] A typical example is the ECL of the 9,10-diphenylanthracene (DPA) and *N,N,N',N'*-tetramethyl-*p*-

phenylenediamine (TMPD) systems. The reaction between $DPA^{\bullet-}$ and $TMPD^{\bullet+}$ does not create enough energy to generate the ultimate emissive state; therefore it is regarded as an energy-deficient system. In addition, ECL annihilation pathway can also operate in the E-route, ensuring the formation of excimers (excited dimers) and exciplexes (excited state complexes). The following mechanism demonstrates the T-route for the DPA-TMPD system.

T-route: DPA-TMPD System

$\mathrm{DPA} + \mathrm{e}^- \rightarrow \mathrm{DPA}^{\bullet-}$ **[1.10]**

$\mathrm{TMPD} - \mathrm{e}^- \rightarrow \mathrm{TMPD}^{\bullet+}$ **[1.11]**

$\mathrm{DPA}^{\bullet-} + \mathrm{TMPD}^{\bullet+} \rightarrow {}^3\mathrm{DPA}^* + \mathrm{TMPD}$ **[1.12]**

${}^3\mathrm{DPA}^* + {}^3\mathrm{DPA}^* \rightarrow {}^1\mathrm{DPA}^* + \mathrm{DPA}$ *Triplet-Triplet Annihilation* **[1.13]**

(Energy-Deficient System)

${}^1\mathrm{DPA}^* \rightarrow \mathrm{DPA} + \mathrm{h}\nu$ **[1.14]**

In the annihilation pathway the presence of an electrochemiluminescent species is sufficient to generate light, thus no additional catalyst or reagent is required to assist with signal amplification reactions. Aprotic solvents such as acetonitrile (MeCN), dimethylformamide (DMF) and dimethyl sulfoxide (DMSO) are the most commonly used because of their ability to dissolve organic compounds. These solvents have wide potential windows, which allow for both oxidation and reduction of the electrochemiluminescent species. However, the radicals produced may be highly unstable in aprotic solvents and these solvents might quench the ECL light due to the presence of either water or dissolved oxygen in the solvent/supporting electrolyte solution. Therefore, researchers have investigated and explored other forms of emitters, specifically water-soluble emitters. This approach requires water-soluble species, a second reactive component known as the co-reactant that could generate the reductant upon oxidation to allow for stable and reproducible aqueous ECL generation. The following section deals with co-reactants for ECL generation.

1.2.2.2 Co-reactant Pathway

The second method for ECL generation is the co-reactant pathway that is the primary focus of this thesis. This method involves the electrochemical production of a radical intermediate (a strong reducing or oxidizing agent) that reacts with the ECL emitter to produce an excited state. Compared with annihilation ECL, the use of a co-reactant can enhance the ECL efficiency of a system.[12] Co-reactants have the ability to generate a strong oxidising agent upon electrochemical reduction and are referred to as reductive-oxidation ECL, while those that involve generation of strong reducing agents by electrochemical oxidation are referred to as oxidative-reduction ECL.[11,13] One key example of an oxidative-reduction ECL system is the ruthenium(II) polypyridyl ($[Ru(bpy)_3]^{2+}$) emitter with the co-reactant , oxalate ion ($C_2O_4^{2-}$). The oxalate can produce a strong reducing agent ($CO_2^{\bullet-}$) upon oxidation in aqueous solution.[11] The sequence of reactions is shown below.

Ruthenium-Oxalate System

$$[\mathrm{Ru(bpy)_3}]^{2+} - \mathrm{e}^- \rightarrow [\mathrm{Ru(bpy)_3}]^{3+} \qquad \textbf{[1.15]}$$

$$[\mathrm{Ru(bpy)_3}]^{3+} + \mathrm{C_2O_4}^{2-} \rightarrow [\mathrm{Ru(bpy)_3}]^{2+} + \mathrm{C_2O_4}^{\bullet-} \qquad \textbf{[1.16]}$$

$$\mathrm{C_2O_4}^{\bullet-} \rightarrow \mathrm{CO_2}^{\bullet-} + \mathrm{CO_2} \qquad \textbf{[1.17]}$$

$$[\mathrm{Ru(bpy)_3}]^{3+} + \mathrm{CO_2}^{\bullet-} \rightarrow [\mathrm{Ru(bpy)_3}]^{2+*} + \mathrm{CO_2} \qquad \textbf{[1.18]}$$

$$[\mathrm{Ru(bpy)_3}]^{2+} + \mathrm{CO_2}^{\bullet-} \rightarrow [\mathrm{Ru(bpy)_3}]^{+} + \mathrm{CO_2} \qquad \textbf{[1.19]}$$

$$[\mathrm{Ru(bpy)_3}]^{3+} + [\mathrm{Ru(bpy)_3}]^{+} \rightarrow$$

$$[\mathrm{Ru(bpy)_3}]^{2+} + [\mathrm{Ru(bpy)_3}]^{2+*} \qquad \textbf{[1.20]}$$

$$[\mathrm{Ru(bpy)_3}]^{2+*} \rightarrow [\mathrm{Ru(bpy)_3}]^{2+} + \mathrm{h\nu} \qquad \textbf{[1.21]}$$

In this system, the electrode oxidises both $C_2O_4^{2-}$ and $[Ru(bpy)_3]^{2+}$; to produce the $[Ru(bpy)_3]^{3+}$ cation and $C_2O_4^{\bullet-}$ anion. The anion breaks down to form a highly reducing radical anion $CO_2^{\bullet-}$ and carbon dioxide (CO_2). The $CO_2^{\bullet-}$ then either reduces the $[Ru(bpy)_3]^{3+}$ complex back to the parent complex in an excited state $[Ru(bpy)_3]^{2+*}$, or it reduces $[Ru(bpy)_3]^{2+}$ to form $[Ru(bpy)_3]^{+}$, which reacts with $[Ru(bpy)_3]^{3+}$ to generate the excited state $[Ru(bpy)_3]^{2+*}$ that emits photons in the form of light. Another example of an oxidative-reduction system is the $[Ru(bpy)_3]^{2+}$ emitter with tripropylamine (TPA) co-reactant. This is the most widely used ECL system and its practical application in clinical settings has been thoroughly studied.[31–33] The $[Ru(bpy)_3]^{2+}$/TPA system can be easily influenced by environmental factors such solution pH, viscosity, temperature, surfactant and ion strength. However, TPA gives an intense ECL and is often the preferred emitter/co-reactant system.[23,34,35] The mechanism of the $[Ru(bpy)_3]^{2+}$/TPA system has been extensively studied and four possible reaction routes between $[Ru(bpy)_3]^{2+}$ and TPA have been proposed.[11,28,36,37] The ECL emission of the $[Ru(bpy)_3]^{2+}$/TPA system arise when the deprotonated TPA radical ($TPA^{\bullet}$) formed from the reduction of $[Ru(bpy)_3]^{3+}$ or via direct electrode oxidation, reacts with either $[Ru(bpy)_3]^{2+}$ or $[Ru(bpy)_3]^{3+}$ to produce the excited state $[Ru(bpy)_3]^{2+*}$, and upon decay to the ground state, emits photons in the form of light. A simplified ECL reaction mechanism of the $[Ru(bpy)_3]^{2+}$/TPA system is shown below.

Ruthenium-Tripropylamine system

$$[\mathrm{Ru(bpy)_3}]^{2+} - \mathrm{e}^- \rightarrow [\mathrm{Ru(bpy)_3}]^{3+} \qquad \textbf{[1.22]}$$

$$\mathrm{TPA} - \mathrm{e}^- \rightarrow \mathrm{TPA}^{\bullet +} \rightarrow \mathrm{TPA}^{\bullet} + \mathrm{H}^+ \qquad \textbf{[1.23]}$$

$$[\mathrm{Ru(bpy)_3}]^{3+} + \mathrm{TPA}^{\bullet} \rightarrow [\mathrm{Ru(bpy)_3}]^{2+*} + \mathrm{products} \qquad \textbf{[1.24]}$$

$$[\mathrm{Ru(bpy)_3}]^{2+*} \rightarrow [\mathrm{Ru(bpy)_3}]^{2+} + h\nu \qquad \textbf{[1.25]}$$

Other common co-reactants combined with $[Ru(bpy)_3]^{2+}$ for ECL generation have been persulfate ion ($S_2O_8^{2-}$)[38,39] and hydrogen peroxide (H_2O_2),[40,41] both of which operates in the reductive-oxidation mode. The generation of ECL based on co-reactant pathway has become a sensitive detection method in a variety of analytical applications and its popularity can be attributed to its ability to generate ECL in both aqueous and non-aqueous solvents. The design and selection of co-reactants are important in improving the sensitivity and reproducibility of ECL systems. Thus, when choosing a co-reactant different factors should be considered such as solubility, stability, electrochemical properties, kinetics, quenching effect and ECL background.

There are a variety of transition metal based inorganic complexes, organic molecules and semiconductor nanomaterials that exhibit ECL but, $[Ru(bpy)_3]^{2+}$ remains the standard model and reference complex. The vast majority of publications are concerned with employing $[Ru(bpy)_3]^{2+}$ as the ECL emitter because of its excellent chemical, electrochemical and photochemical properties.[42] The following section focuses on the ruthenium(II)polypyridyl complex, outlining its photo-physical/chemical properties and its application in analytical processes.

1.2.3 Electrochemiluminescence Emitter

1.2.3.1 Ruthenium(II) polypyridyl complex

The $[Ru(bpy)_3]^{2+}$ compound has been the first to demonstrate ECL[43] and has showed to be the most valuable in both fundamental studies and commercial applications (Figure 1.2).[11,30,44] It has been widely used for determination of a variety of co-reactants such as oxalate,[45] peroxydisulfate[37] and TPA,[35] including alkylamines,[34,46] amino acids,[47] ascorbic acid[48] and many pharmaceutical compounds.[49,50] Furthermore, numerous studies utilising $[Ru(bpy)_3]^{2+}$ as an ECL emitter have followed, and much of this work has been reviewed.[23,36,51]

The ECL efficiency of the overall system is an important parameter that is normally determined by comparing the ECL efficiencies of the analyte of interest to a known standard, in this case, $[Ru(bpy)_3]^{2+}$. The ECL efficiency of the $[Ru(bpy)_3]^{2+}$ complex has previously been determined to be 5%, which is relatively high compared to other systems that exhibit ECL. The overall ECL efficiency (ϕ_{ECL}) is a product of the photoluminescence quantum yield and the efficiency of production of the excited state.[52] The values of ECL efficiency can be obtained using Equation 1.26.

$$\phi_{\mathrm{ECL}} = \phi^0{}_{\mathrm{ECL}} \frac{\mathrm{I}}{\mathrm{Q}} \frac{\mathrm{Q}^0}{\mathrm{I}^0} \qquad \textbf{[1.26]}$$

where $\phi^0{}_{ECL}$ is the ECL efficiency of the $[Ru(bpy)_3]^{2+}$ standard; I and I^0 are the ECL emission intensities of the target emitter and the $[Ru(bpy)_3]^{2+}$ standard, respectively; Q and Q^0 represents the charge passed in coulombs for the target emitter and the $[Ru(bpy)_3]^{2+}$ standard, respectively.

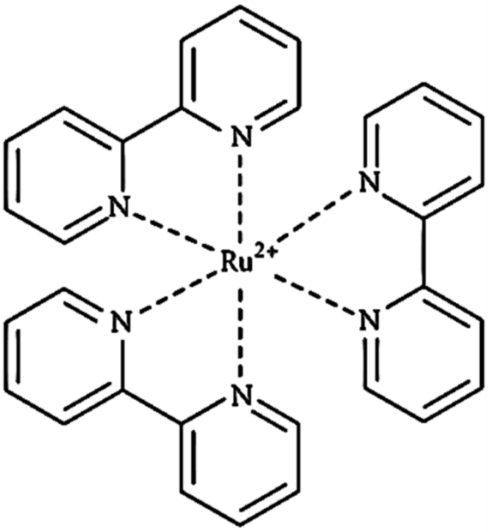

Figure 1.2: Tris(2,2’-bipyridyl)ruthenium (II)

The photophysical and photochemical properties of $[Ru(bpy)_3]^{2+}$ are generally well understood and it has been determined that their photoreactivity arises from both the triplet metal to ligand charge transfer state (^{3}MLCT) and the triplet metal centred state (^{3}MC). The metal to ligand charge transfer (MLCT) orbital character entails the promotion of an electron from the metal (d orbitals) to the ligand (π* orbitals). The photochemistry that arises from the ^{3}MLCT excited state is of most interest because it is this level which will determine the emissive and inter-component energy/electron transfer properties of $[Ru(bpy)_3]^{2+}$. The generation of ECL signal is a result of the transition from the ^{3}MLCT to the ground state (GS).[44] The ^{3}MLCT state is obtained with unit efficiency regardless of the excitation wavelength, thus, it’s responsible for exhibiting long lifetime and intense luminescence emission. While ^{3}MC excited state results in ligand dissociation. ^{3}MLCT lies below the ^{3}MC and the singlet metal to ligand charge transfer state (^{1}MLCT) (Scheme 1.1).[45]

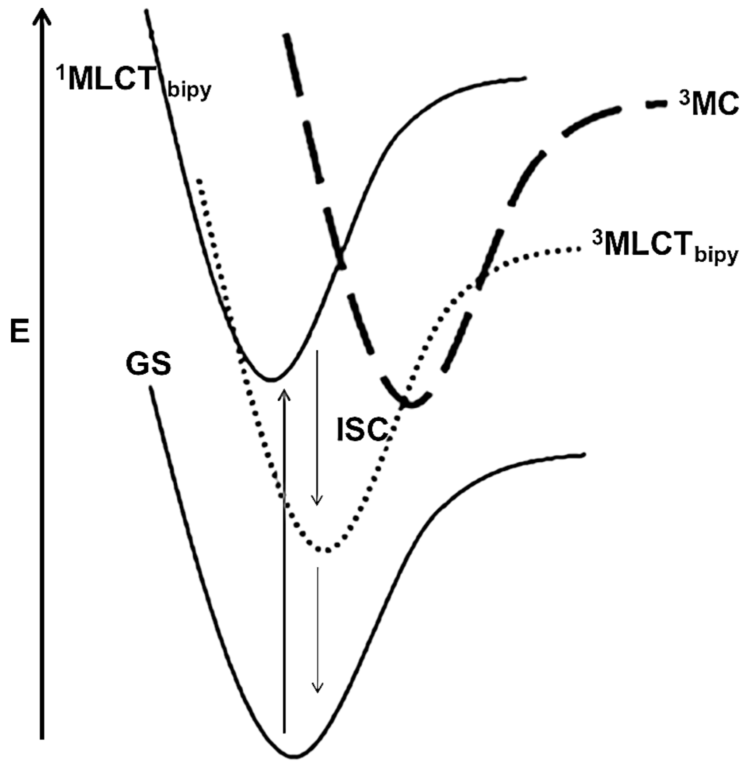

Scheme 1.1: Basic electronic state manifolds of $[Ru(bpy)_3]^{2+}$. Reproduced from Browne, W. R.; O'Boyle, N. M.; McGarvey, J. J.; Vos, J. G. *Chem. Soc. Rev.* 2005, *34* (8), 641.

The ruthenium(II)polypyridyl compounds also exhibit a rich redox behaviour with reversible processes for both the metal and ligand. The electrochemical properties of these complexes are controlled by the ligand's σ-donor and π-acceptor properties. If the ligands of the ruthenium(II) compound are good σ-donors it will result in an increase in the electron density of the metal centre, and hence greater crystal field splitting of ruthenium(II). In contrast, ligands with increased π-acceptor properties will have a decrease in the electron density of the metal centre, and hence a reduction in the crystal field splitting of the complex. So, in terms of the 2,2′-bipyridine ligands of the $[Ru(bpy)_3]^{2+}$ complex they demonstrate to be stronger σ-donors.

There are a number of metal polypyridyl ECL systems other than the ruthenium(II) systems, these include iridium, osmium and aluminium. Osmium(II) complexes share similarities with ruthenium(II) complexes and have been studied as ECL emitters.[55,56] The first report of ECL on osmium complexes was with $[Os(phen)_3]^{2+}$ in DMF and MeCN in the presence of persulfate ion to generate the excited state.[57] The ECL efficiency of these $[Os(phen)_3]^{2+}$ complexes are smaller compared to their ruthenium(II) counterparts, most likely due to their lower emission quantum yields in accordance with the energy gap law.[58] However, much higher ECL intensities were observed for osmium(II) complexes with supplementary bidentate phosphine or arsine ligands like 1,2-bis(diphenylphosphino) ethane or 1,2-bis(diphenylarsino)ethane.[59,60] These complexes show very intense photoluminescence with efficiencies 2-3 orders of magnitude higher than that of $[Os(phen)_3]^{2+}$. Iridium based complexes have also shown much higher efficiencies in a wide range of emission wavelengths.[61,62] Iridium(III) neutral complexes have also been studied in aqueous and non-aqueous media.[63,64] However, they tend to be insoluble in water and are susceptible to oxygen quenching.[44,65,66] Quenching of the ECL of iridium complexes in aqueous solutions can be attributed to their structural design, which can either expose or shield their excited states from oxygen. Ionic iridium complexes have favourable solubility in aqueous solutions and show comparable chemiluminescent intensity to that of ruthenium(II) complexes.[14] The examining and coupling of more efficient ECL labels with established co-reactants may have profound impact on the sensitivity of ECL for a variety of applications.[29]

1.2.4 Applications of Electrochemiluminescence

ECL setups can be either solution- or solid- based. Most ECL processes are performed in solution-based approaches and requires that the ECL reagent must be continuously supplied to the reaction zone. However, an ECL emitter like $[Ru(bpy)_3]^{2+}$ can also be immobilised as solid formats (mono- or multilayer films). These solid formats provide several advantages over solution-based ECL systems; including, simpler experimental design, enhanced ECL signal, low consumption of expensive ECL reagent and reusable sensing applications based on $[Ru(bpy)_3]^{2+}$ recycled at the electrode surface.[67] The $[Ru(bpy)_3]^{2+}$ films can be developed by methods like Langmuir-blodgett,[68] self-assembly (SA)[69] and layer-by-layer (LBL) techniques.[70] The efficiency and stability of ECL at these films depends on the ECL dyes (e.g., $[Ru(bpy)_3]^{2+}$) and the co-reactants (e.g., TPA) used to generate light and on the type of electrode needed to facilitate an electrochemical reaction.[71–73] The electrode's geometry and size are also important factors determining the kinetics and the mass transfer of the overall ECL reaction. Furthermore, surface effects like surface oxidation, adsorption and electrode hydrophobicity can influence the electrode performance and hinder the electrochemistry of the $[Ru(bpy)_3]^{2+}$/TPA ECL output;[45] however, these effects can be limited or eliminated by modifying the electrode surface with conducting polymers[74] and/or nanomaterials.[75]

In conjunction with co-reactants, ECL has been employed in a wide range of analytical applications, especially in clinical diagnostics, with focus being placed on developing bio-assays in DNA sensing, enzymatic detection, and immunoassays.[76–78] These assays can involve either direct labelling of antibody/DNA with the ECL emitter or indirect labelling with the emitter that catalyse an ECL reaction. Blackburn and co-workers were the first to report the use of $[Ru(bpy)_3]^{2+}$ ECL detection for the development of immuno- and DNA probe assays.[10] Since then, a great number of publications on these assays using ECL as detection mechanism have been reported; particularly, in the areas of forensic chemistry, environmental investigations, pharmaceutical studies and biological warfare agent detections.[14] Figure 1.3 illustrates a general principle of DNA probe assays based on ECL technique using ECL labels. Here, the complementary single-stranded DNA labelled with $[Ru(bpy)_3]^{2+}$ hybridises with the single-stranded DNA immobilized on the surface of a thiol modified electrode. The electrode assembly is placed in a solution or flow cell containing a co-reactant, followed by direct ECL analysis.[76] Other methods of DNA detection include nanoparticle-based ECL.[79] By employing nanomaterials in sensing systems, alternative and more powerful strategies for highly sensitive ECL detection systems can be created.

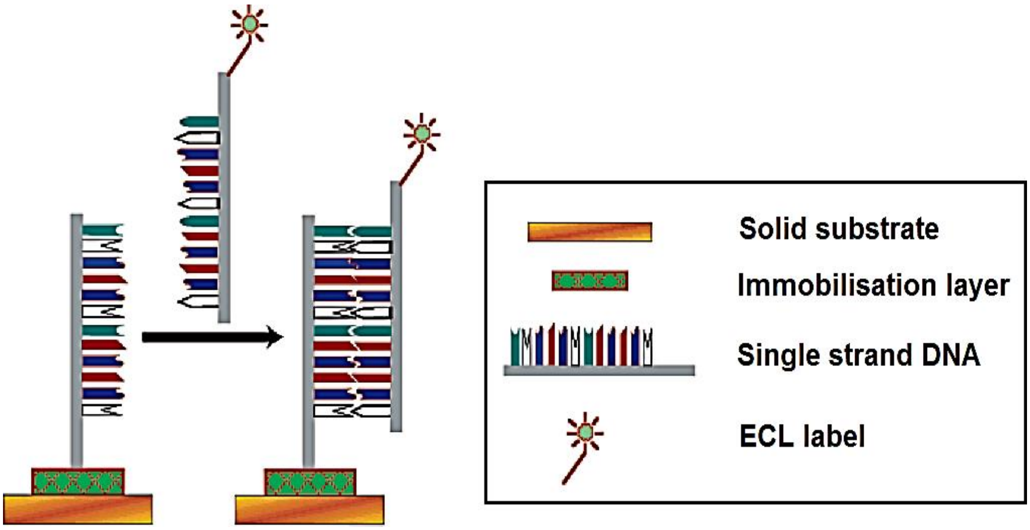

Figure 1.3: Schematic diagram of a solid-phase ECL detection system monitoring DNA hybridisation. Adapted from Miao, W.; Bard, A. J. *Anal. Chem.* 2003, 75 (21), 5825–5834.

Figure 1.4 shows another example of ECL detection that is based on immunoassay fabrication. Here, an ECL immunosensor for prostate specific antigen (PSA) was illustrated.[80] This detection strategy is of particular relevance to this thesis as one of the key objectives of the thesis is to develop an ECL immunosensor for troponin detection. As seen from Figure 1.4, $[Ru(bpy)_3]^{2+}$ doped silica nanoparticles were employed as ECL tags and carbon nanotubes (CNT) forests as efficient electrical communication pathways. Here, the captured antibodies Ab_1 was chemically attached to the CNT forests immobilised on pyrolytic graphite disks. This Ab_1/CNT modified pyrolytic graphite disk was then incubated in PSA. After washing with non-specific binding blockers, the RuBPY-silica-Ab_2 nanoparticle bio-conjugate was added and ECL successfully measured.

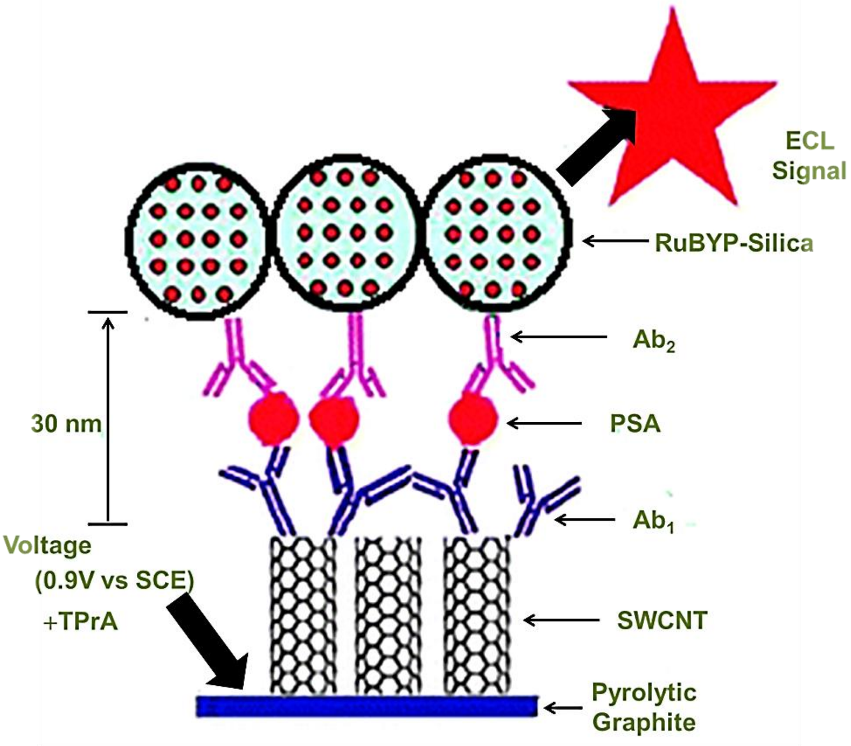

Figure 1.4: Representation of ECL-based SWCNT immunosensors after addition of PSA and the RuBPY–silica–Ab2 nanoparticles. Adapted from Sardesai, N.; Pan, S.; Rusling, J. *Chem. Commun.* 2009, 33, 4968–4970.

Besides clinical assays, co-reactant ECL has found many applications in other fields of research, such as light-emitting devices, imaging technology, and scanning microscopy.[81]

It is evident from literature that the most important commercial application to date for ECL is their use in diagnostic assays, and it is believed that >50 of the assays including those for thyroid diseases, tumour and cardiac markers, fertility therapies, and analytes relevant to infection diseases, are commercially available.[11] The use of coreactant ECL has a promising future in analytical science because it can be used in both biological and non-biological assays. Although impressive analytical performance has been achieved, there is still room for improvement and further work is required so that the inherent sensitivity of the technique can be fully exploited. For instance, the use of ECL as a detection system for miniaturised analytical systems, especially three-dimensional (3D) micromechanical/miniaturised systems.

Recently, the on-chip generation of $[Ru(bpy)_3]^{2+}$ ECL has been discussed in literature, examples include, the use of interdigitated Au micro-electrodes mounted above a photodiode in a 5×6 mm silicon chip, demonstrated by Faiccabrino and co-workers.[82] Furthermore, Dhanuka and co-workers described a high-throughput ECL-based fluidic platform for chemical toxicity screening, followed by rapid detection of DNA damage,[52] while Ge and co-workers described a wax-patterned 3D paper-based ECL device for the detection of tumour markers (AFP, CA125, CA199 and CEA) in serum samples using the tris-(bipyridine)-ruthenium (II) ($Ru(bpy)_3^{2+}$) - tri-*n*-propylamine (TPA) ECL system.[83]

1.2.5 Electrochemiluminescence Instrumentation and Fundamentals

A typical ECL instrument makes use of a three-electrode setup embedded in an electrochemical cell containing an electrolyte solution and a photodetector (photomultiplier tube or charge-coupled device) to measure light. The setup is contained within a light tight casing to ensure that no background signals interfere with detection of the ECL. In contrast to a charge-coupled device camera, the photomultiplier tube is the most sensitive means of detecting light, and are capable of detecting single photons.[84] The ECL photodetector can be coupled to spectroscopic and microscopic methods. The coupling of ECL to the above mentioned techniques, allows independent information to be obtained, like, topographical, spatial, and temporal resolutions of current and luminescence data.[44] In addition, the coupling of the ECL photodetector to electrochemical methods gives more complete analysis about the state of the electrode and the nature of the species produced on the electrode surface (Scheme 1.2). Most of the electrochemical methods to which ECL can be coupled are based on conventional electrochemistry. However, coupling of ECL can also be demonstrated by an interesting phenomenon, known as bipolar electrochemistry. In contrast to conventional electrochemistry, bipolar electrochemistry is a wireless type technique where the electrode polarization is controlled externally and indirectly via the electric field gradient in the solution potential. Subsequent sections will discuss this phenomenon to give an understanding on the basics when coupled to the ECL technique and demonstrate their joined use in material and sensing strategies.

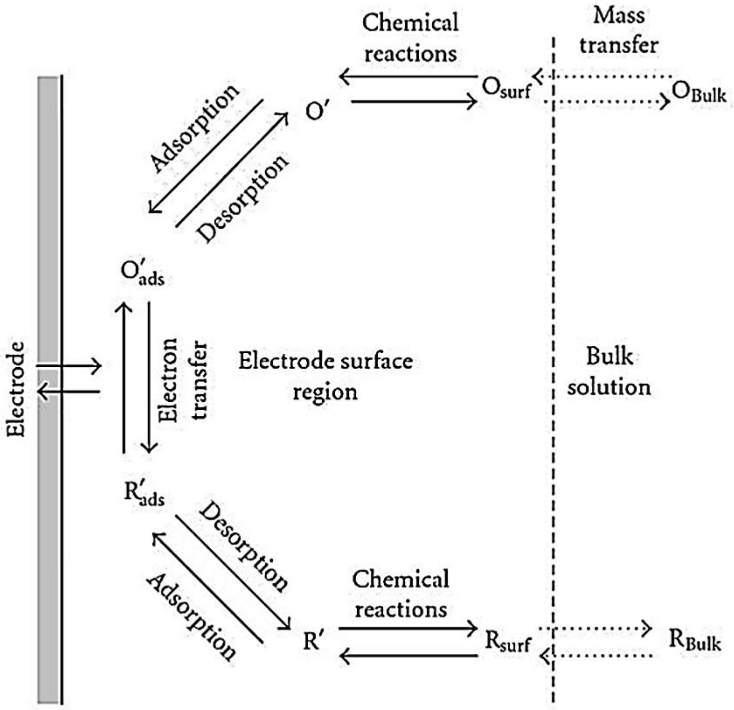

Scheme 1.2: Pathway of a general electrode reaction. Reprinted from Bard, A. J.; Faulkner, L. R. *Electrochemical methods: fundamentals and applications*, 2nd ed.; Wiley: New York, 2001.

1.3 BIPOLAR ELECTROCHEMISTRY

1.3.1 Introduction

In simple terms the word “bipolar” is normally defined as something that exhibits two opposite extremes. In bipolar electrochemistry (BPE) it implies that that an object acts simultaneously as an anode and a cathode when an electric field is established across the object.[85,86] In this context, the object is referred to as a bipolar electrode (BP_{elec}). The BP_{elec} does not differ from the working electrode of a conventional two or three-electrode system because in either case, it is the interfacial potential difference that drives electrochemical reactions.[7] However, the difference lies in the fact that we need to consider which side of the interface are being controlled, the solution or the electrode.[87] For a conventional electrochemical cell, the potential of the working electrode is controlled against a reference electrode and the counter electrode act as the current source (Scheme 1.3A). Here the potential of the solution is at a floating value in the absence of an externally applied electric field.[85] By driving the working electrode to more negative potentials, electrons will flow from the electrode to the solution, resulting in a reduction current (Scheme 1.3B).[51] Likewise, when the potentials are scanned to more positive values, electrons transfer from redox active species in the solution to the electrode and results in oxidation reactions (Scheme 1.3B). The interfacial potential difference is generally considered to be uniform, however, all this will depend on how the cell is designed, the placement of the three electrodes relative to one another, and the concentration of the electrolyte solution.[87]

Thus, in conventional electrochemistry the driving force of the redox reactions is directly controlled by tuning the potential of the working electrode that is connected to a power source (potentiostat).

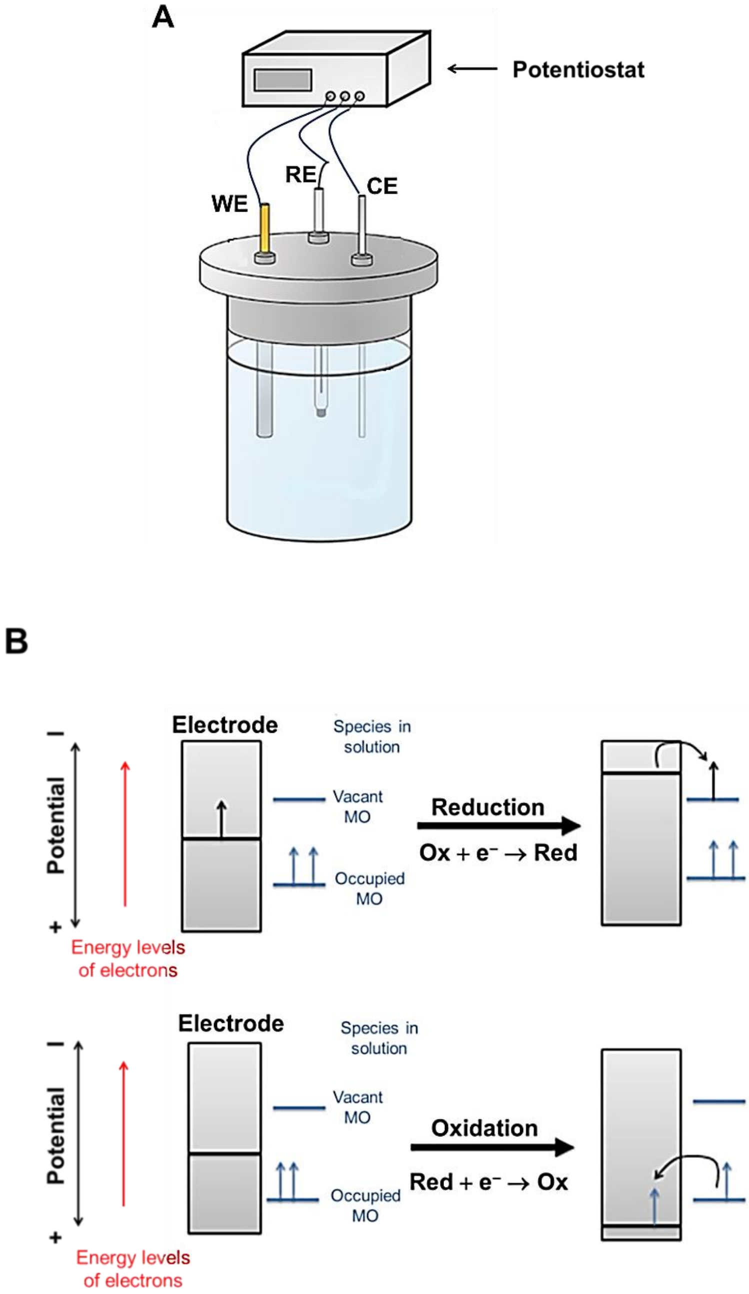

Scheme 1.3: (A) Illustrates a three-electrode setup, where all electrodes are in electrical contact to the power source. The three-electrode setup

consist of: a working electrode (WE) which is the electrode of interest, a counter electrode through which current from the WE flows and a reference electrode (RE) against which the potential of the WE is controlled. (B) Schematic illustration of reduction and oxidation reactions as a result of changes in the electrode potential.

In bipolar electrochemistry the BP_{elec} has no direct electrical contact with the power source (Scheme 1.4A). Its polarisation is controlled externally and indirectly via the electric field gradient in the solution, generated by the feeder electrodes (driving electrodes). In simple terms the solution potential will be controlled and hence the electrode potential will be floating. Thus, as a result, charge transfer reactions will occur simultaneously at both ends (anodic and cathodic poles) of the BP_{elec} (Scheme 1.4B).

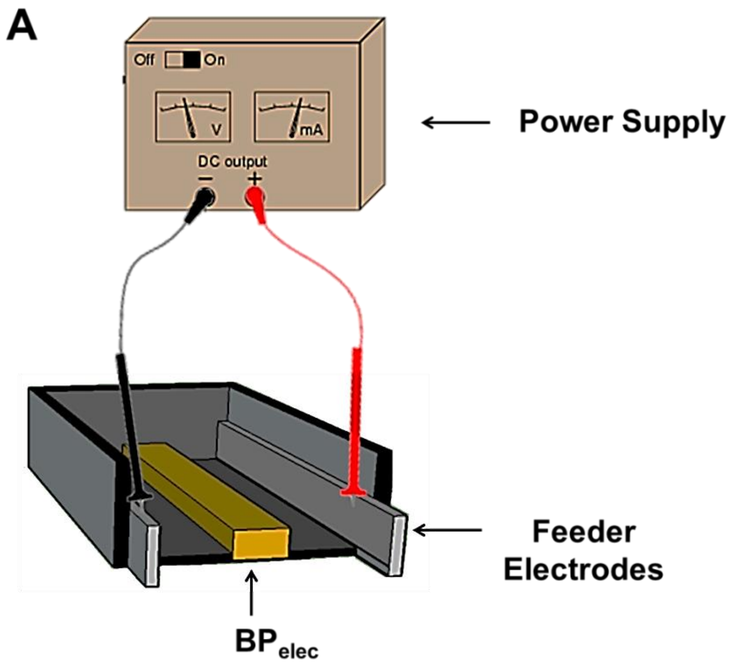

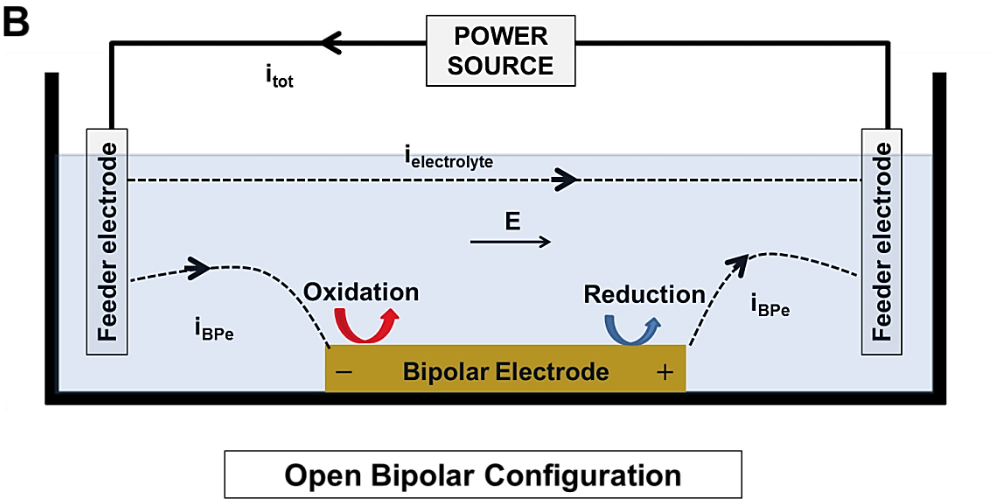

Scheme 1.4: (A) Bipolar electrochemical setup where the BP_{elec} is positioned between two feeder electrodes. (B) Schematic illustration of the bipolar system where the BP_{elec} is free in solution with the total cell current (i_{tot}) passing through the BP_{elec} and the remaining current passing through the electrolyte solution ($i_{electrolyte}$). The current paths are illustrated by the dashed lines. E indicates the direction of the applied external electric field.

1.3.2 Principles of Bipolar Electrochemistry

There are a few number of parameters that control bipolar electrochemical processes.[86] One crucial parameter is the potential difference (ΔE) generated across the BP_{elec}. The ΔE can be formulated by evaluating the following variables where (i) E_a and E_c represent the potential of the anode and cathode, respectively, (ii) E_{appl}, is the voltage applied between the feeder electrodes, (iii) $l_{channel}$, the length of the channel (or the distance separating the feeder electrodes) and (iv) l_{elec}, the length of the BP_{elec} (Scheme 1.5).[7,88]

$$\Delta E = E_c - E_a = \frac{E_{appl}}{l_{channel}} l_{elec} \qquad \textbf{[1.27]}$$

According to Equation 1.27, the potential drop depends on both the applied voltage and the length of the BP_{elec}. The minimum value of ΔE needs to be at least equal to the difference between the theoretical standard potentials of the two half reactions of the electroactive species before simultaneous redox reactions can be realised. The oxidation reactions occur on the anodic side which is near to the negative feeder electrode and the reduction reactions occur on the cathodic side which is near to the positive feeder electrode.[89] The coupled redox reactions ensure that electroneutrality is maintained within the BP_{elec} because the BP_{elec} itself do not accumulate any net charge. The “point” on the BP_{elec} that divides the BP_{elec} into its anodic and cathodic pole is known as x_0, the point where the net faradaic current is zero.[90] The location of x_0 is assumed to be in the centre (Scheme 1.5B).[91] However, depending on the position of the BP_{elec} in the electric field or the nature of the faradaic reactions (one process may limit the other) the position of x_0 might shift.

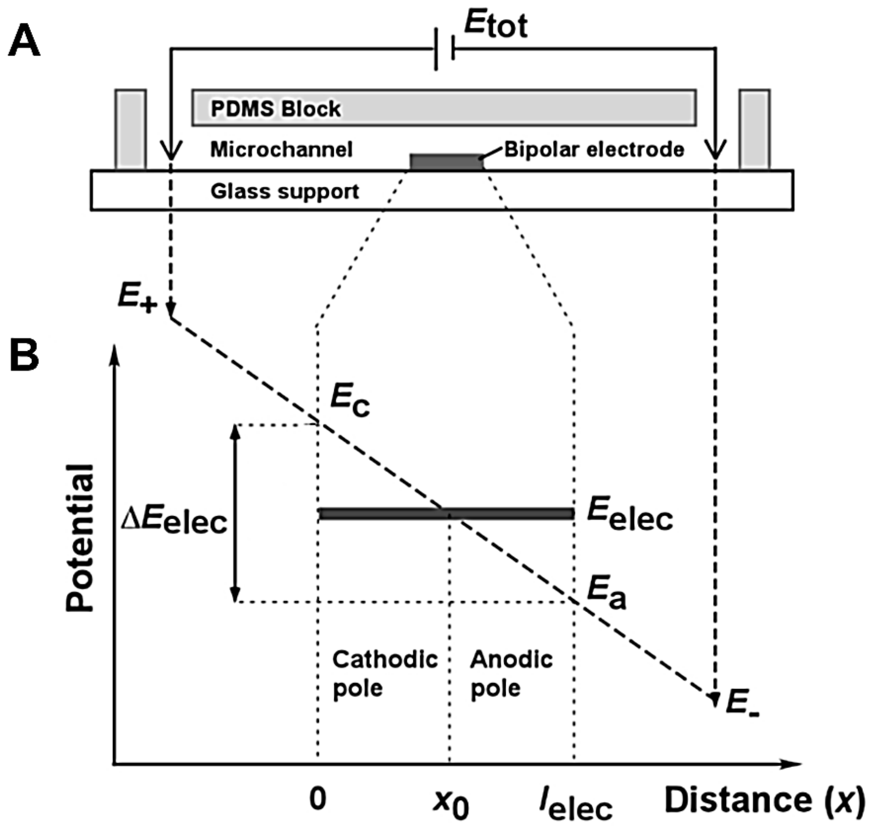

Scheme 1.5: (A) A simple PDMS microfluidic channel, with one bipolar electrode fixed in the middle of the cell, and two feeder electrodes connected to a power source. (B) Schematic illustration of potential distribution within the bipolar electrochemical cell. Adapted from Mavré, F.; Chow, K.-F.; Sheridan, E.; Chang, B.-Y.; Crooks, J. A.; Crooks, R. M. *Anal. Chem.* 2009, *81* (15), 6218–6225.

1.3.2.1 Open Configuration

Most of the studies are based on “open” bipolar cell configurations. A typical open bipolar cell consists of a single sample compartment; one such example is a microfluidic channel (Scheme 1.5A). Some of the applied total potential can be lost at the feeder electrodes of a microfluidic channel, however, assuming the potential drop at the feeder electrode/solution interface is negligible, E_{appl} will drop linearly across the solution (Scheme 1.5B). Therefore, the resulting electric field (V_0) in the solution can be expressed as,

$$V_0 = \frac{E_{appl}}{l_{elec}} \qquad \textbf{[1.28]}$$

If E_{appl} is sufficiently high and if the length of the bipolar electrode is quite long, successful faradaic electrochemical reactions can be established at low electric field strengths. However, if smaller length objects were to be employed, the magnitude of the electric field strengths needed to drive redox reactions would increase up to kV cm^{-1}.[92] It has been proved that the nature of the electric field not only depends on the cell design, but it also depends on the composition of the electrolyte solution.[91] The lower the solution resistance the more current will flow through it. However, since the flow of current in this instance will be entirely ionic it will impact the electric field distribution and in turn hinder faradaic reactions. This is because there is no additional path for current in the form of electrons (electronic current) to pass through the BP_{elec}.[87]

Crooks and others have described the onset of bipolar electrochemistry at an open bipolar cell configuration.[93–96] They provide theoretical and experimental models that simplify the understanding of these parameters and the effect they have on the bipolar system.[91,97,98] Despite the fact that the open bipolar electrochemistry approach can be generalised to different types of objects and used in the deposition of various materials with different characteristics, its application might still be limited when subjected to diagnostics or sensing. With this in mind, closed bipolar configurations might be suitable for these types of systems.

1.3.2.2 Closed Configuration

A closed bipolar configuration consists of a BP_{elec} whose poles are stretched across two separate solution compartments (Scheme 1.6). In simple terms, there is no direct contact or ion exchange between the solutions in which the BP_{elec} anode and cathode are embedded. The only electrical connection between the two feeder electrodes is the BP_{elec} itself.[99]

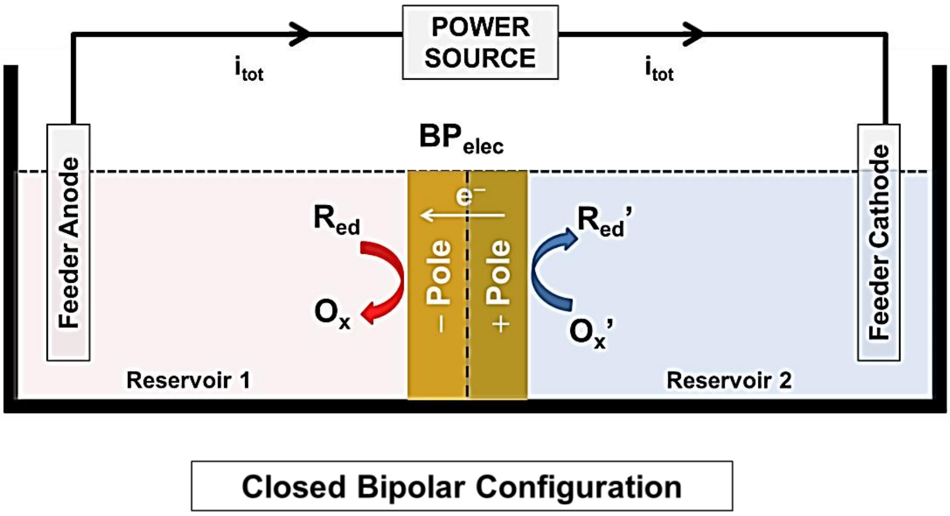

Scheme 1.6: Schematic illustration of a closed bipolar electrochemical cell where the BP_{elec} is the only current path between the two separate reservoirs.

In this setup the current that passes through the BP_{elec} can be directly measured due to the absence of the ionic current path, thus, providing information on the rates of the faradaic processes.[100] Since the BP_{elec} is the only current path, none of the total potential is lost at the non-polarisable feeder electrode/solution interface, thus the potential difference generated across the BP_{elec} is equal to the total applied potential via the feeder electrodes.[101]

1.3.3 Application of Bipolar Electrochemistry

As there is such a broad range of bipolar electrodes utilised in different applications, it is beyond the scope of this chapter to discuss them all. Thus, focus will only be placed on the topics relevant to this thesis which is the use of bipolar electrodes in sensing and screening applications.

The key advantage of using the bipolar system lies in the fact that no physical contact is necessary between the electrode and the power source, thus making it simpler to apply to objects of different shape or sizes that otherwise might have been difficult to connect to a circuit. The BP_{elec} can be any kind of material such as carbon, metals, semiconductors or coated insulators.[94,102–104] Fleischman and co-workers were the first to demonstrate bipolar electrochemistry on fluidised bed electrodes.[105] Their bipolar setup comprised of a large number of micro-particles embedded between two feeder electrodes in both conducting and non-conducting media, respectively. Under the influence of a sufficient voltage electrochemical reactions occurred at the surface of the particles. Bipolar fluidised bed electrodes have been utilised in industrial processes for many decades. Applications include electro-organic synthesis,[106–108] trace metal recovery,[109] and photoelectrochemical cells.[110,111] Aside from the large scale industrial applications, bipolar electrochemistry creates a multitude of promising research opportunities. Early studies based on the fluidised bed electrodes have opened up the doors to many exciting experiments which allowed bipolar electrochemistry to become quite established. Today, bipolar electrochemistry has been applied in a variety of fields ranging from materials to analysis. Examples of these include polymer synthesis,[112,113] materials enrichment and separation,[114,115] and sensors.[89,116,117]

In a typical bipolar setup there is no means of directly measuring the current passing through the BP_{elec}, thus, their use in electroanalytical applications can be quite challenging. However, the combination of this technique with other signal transduction methods has since been implemented and reported in literature.

One of the applications targeted in this thesis is to explore and develop the bipolar electrode as a tool for screening and sensing strategies by implementing an optical transduction method as signal readout. In a bipolar sensing and screening setup, the sensing reaction correlates to an electrochemical reduction taking place at the cathodic pole, while a coupled oxidative reporting reaction occurs at the anodic pole of the bipolar electrode. In this thesis electrochemiluminescence will be used as the reporting/measuring signal for processes occurring at the bipolar electrode.

1.3.3.1 Bipolar Electrochemistry based on ECL

Manz and co-workers were the first to demonstrate ECL as a reporting readout signal at the BP_{elec}.[89] Their bipolar setup made use of a floating platinum BP_{elec} placed across a capillary electrophoresis separation channel. The BP_{elec} was micro-fabricated into a U-shaped structure and each of the two legs of the U-shaped electrode functioned as an anode and cathode, respectively. When a sufficient electric field was established across the U-shaped BP_{elec}, ECL was observed at the anodic leg and resulted from the interaction between ruthenium and the amino acids, while simultaneous water reduction occurred at the cathodic leg. In addition, they showed the indirect detection of label free amino acids employed as co-reactants for the $[Ru(bpy)_3]^{2+}$ ECL emitter. In their approach, both detection and readout signals were collected at the anodic pole of the BP_{elec}. This means that the detection of analytes is limited to species that either participate or compete with the ECL-producing reaction. Crooks and co-workers advanced the Manz approach by taking advantage of both the anodic and cathodic poles of the BP_{elec}; thereby, eliminating the previous requirement that analytes be capable of direct participation in the ECL reaction.[117] They showed that the detection of various electroactive analytes is possible. In this new development the sensing and reporting poles were decoupled, but their electrochemical relationship was preserved via conservation of charge.[117] This means that the reduction of an analyte at the cathodic pole (sensing pole) can be reported by the emission of light due to the oxidation of $[Ru(bpy)_3]^{2+}$/TPA system at the anodic pole (Figure 1.5). Their study focused on the detection of benzyl viologen (BV^{2+}) at the BP_{elec} cathode and its presence were reported by luminescence of $[Ru(bpy)_3]^{2+}$ at the anode. They also showed that by changing the position and dimensions of the BP_{elec} within the electric field the ECL signal output could be enhanced. Mavré and co-workers later undertook similar studies and reported on the theoretical and experimental framework related to ECL emission at BP_{elec}.[91] They showed that the intensity of ECL emission is directly related to the amount of current flowing through the BP_{elec}. Some of these findings were discussed previously in Section 1.3.2.

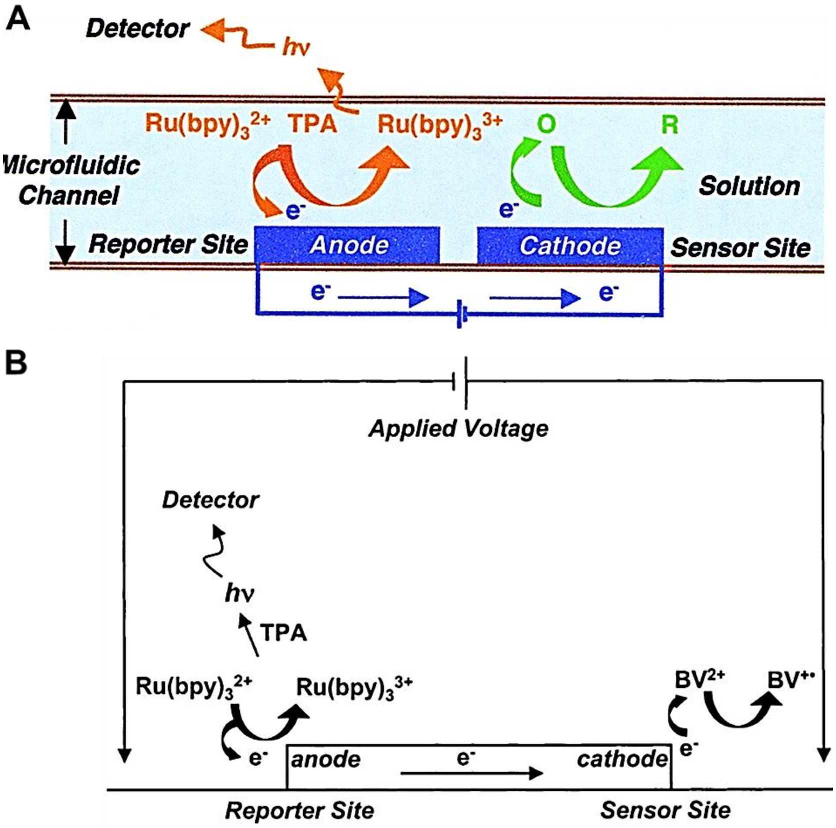

Figure 1.5: (A) Operating principles of the dual sensing/reporting bipolar system. (B) Experimental illustration of benzyl viologen (BV^{2+}) detection

using an ECL emitter, $[Ru(bpy)_3]^{2+}$, as reporting signal. Adapted from Zhan, W.; Alvarez, J.; Crooks, R. M. *J. Am. Chem. Soc.* 2002, *124* (44), 13265–13270.

Based on the successful operating conditions of the BPE-ECL, this approach was further extended to biological molecules. Chow and co-workers described the detection of DNA using an electrochemical microarray sensor.[116] Their bipolar setup made use of a micro-fabricated Au BP_{elec} placed between two platinum feeder electrodes. In their study, the cathodic pole of the BP_{elec} was modified with the capture DNA hybridised to its complementary target DNA labelled with platinum nanoparticles (Figure 1.6). In the presence of the $[Ru(bpy)_3]^{2+}$/TPA system, ECL light was generated at the anodic pole upon electro-catalytic reduction of oxygen at the cathodic pole. In this sensing experiment, the oxygen reduction reaction (ORR) was catalysed by the presence of the target DNA modified with the platinum nanoparticles. No ECL light could be observed in the absence of the hybridisation event.

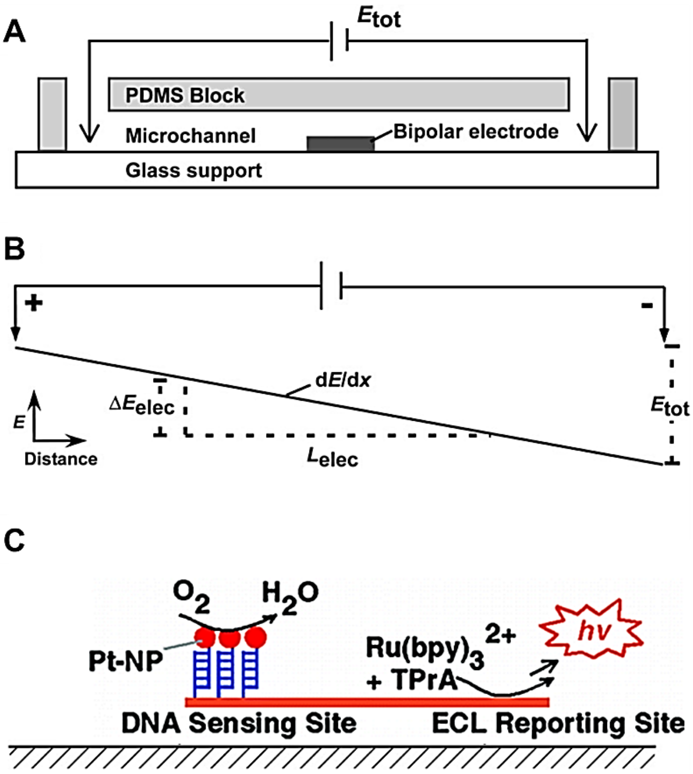

Figure 1.6: (A) BP_{elec} fixed in the middle of a microfluidic channel. (B) Schematic illustration of potential distribution across the BP_{elec}. (C) Experimental illustration of the bipolar configuration for DNA detection. Adapted from Chow, K.-F.; Mavré, F.; Crooks, R. M. *J. Am. Chem. Soc.* 2008, *130* (24), 7544–7545.

Furthermore, Chow and co-workers took advantage of the BPE-ECL system to realise simultaneous light emission at a 1000 individual bipolar electrodes (Figure 1.7).[118] In their approach, an electric field generated across the microarray of bipolar electrodes resulted in the luminescence of $[Ru(bpy)_3]^{2+}$/TPA at the anodic end and simultaneous reduction of oxygen at the cathodic end. The size, shape and separation of each BP_{elec} relative to one another were kept constant, thus, the potential difference generated across all the electrodes was identical and ECL light output the same.

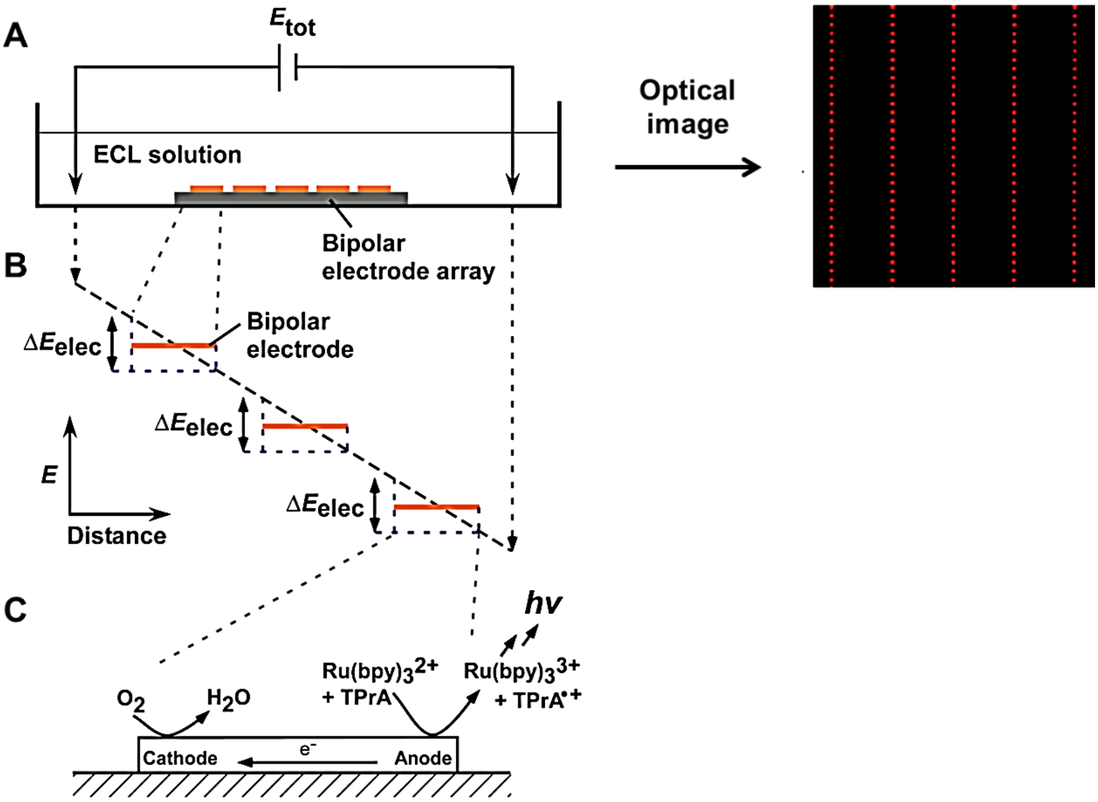

Figure 1.7: (A) A microarray of bipolar electrodes placed between two feeder electrodes. (B) Schematic illustration of potential distribution across each BP$_{elec}$. (C) Experimental illustration of detection and readout signals using the [Ru(bpy)$_3$]$^{2+}$/TPA system. Adapted from Chow, K.-F.; Mavré, F.; Crooks, J. A.; Chang, B.-Y.; Crooks, R. M. *J. Am. Chem. Soc.* 2009, *131* (24), 8364–8365.

All previously discussed applications are based on an open BPE-ECL system, where ECL producing reagents are in the same reaction medium as target analytes. This type of setup might not be ideal in some applications because the presence of the ECL reagents might chemically interfere with the target analyte in solution. Chang and co-workers addressed this difficulty by developing a two-channel microfluidic system or in other words, a "closed" bipolar configuration, for BPE-ECL sensing.[119] In their setup, the anodic and cathodic poles of the BP_{elec} are housed in separate microfluidic channels (Figure 1.8). The cathodic pole is located in the sensing channel filled with $Fe(CN)_6^{3-}$, while the anodic pole is located in the reporting channel containing the ECL mixture. In this study, the ECL signal output increased with increasing concentration of $Fe(CN)_6^{3-}$. They also showed the indirect detection of glycated haemoglobin upon coupled reduction of $Fe(CN)_6{}^{3-}$ at the cathodic pole.

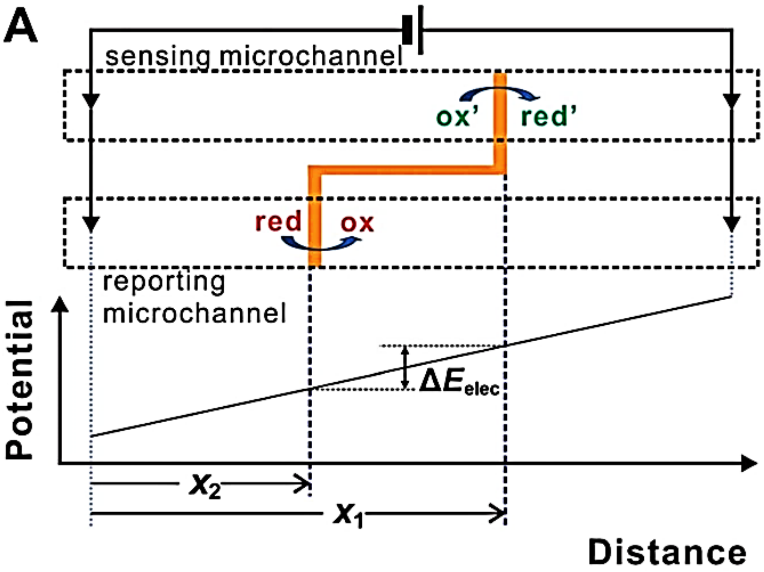

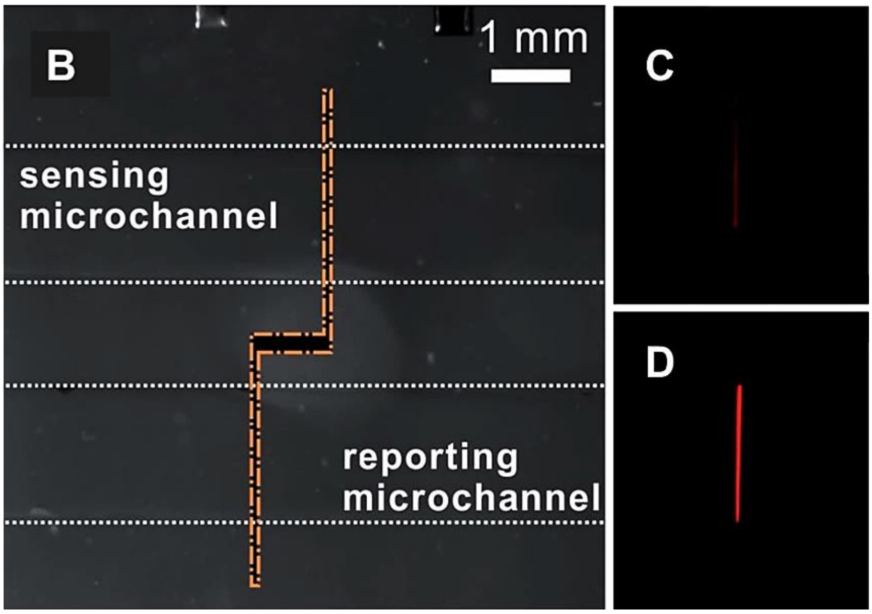

Figure 1.8: (A) Illustrates the operating principle of a closed bipolar configuration. (B) Micrograph of an interchannel BP_{elec} spanning parallel sensing and reporting microchannels. The individual poles of the BP_{elec} are 50.0 mm wide. The sensing microchannel was filled with the target molecule ($Fe(CN)_6^{3-}$) and the reporting microchannel was filled with the ECL cocktail $[Ru(bpy)_3]^{2+}$/TPA. Luminescence micro-graphs obtained with (C) 0.10 mM and (D) 5.0 mM $Fe(CN)_6^{3-}$ present in the reporting channel. Adapted from Chang, B.-Y.; Chow, K.-F.; Crooks, J. A.; Mavré, F.; Crooks, R. M. *The Analyst* 2012, *137* (12), 2827.

It's evident that the BPE-ECL phenomenon has gained a lot of attention and it is considered as a simple, efficient, and suitable system for both detection and multiplexed screening.[120,121] The BPE-ECL approach has been employed in various analytical applications ranging from micrometre- to large-sized systems.[86,122] It has been proven that the coupling of ECL to BPE is advantageous because the time scale for other electrochemical methods is slow compared to this optical driven process; especially, when dealing with large arrays of bipolar electrodes.[118] In addition, the BPE-ECL approach does not require a light source and is free from the effects of scattered light in samples compared with fluorescence.[99] Since ECL readout mechanism is based on the light emission from the ECL process, signal collection in BPE-ECL systems can be accomplished by either a photomultiplier tube (PMT), which is great for increased sensitivity; or by a charge-coupled-device (CCD) used for visual detection. By employing ECL as a reporting mechanism for BPE, it opens up the possibility of developing new tools for screening of materials, medical sensing strategies as well as fabrication of smart electronics.

1.4 CHARACTERISATION TECHNIQUES

1.4.1 Electrochemical Methods

1.4.1.1 Cyclic Voltammetry

Cyclic Voltammetry (CV) is one of the more commonly used electrochemical techniques for acquiring qualitative information about fairly complicated electrode reactions.[123] It provides considerable information about the thermodynamics of a redox process, kinetics of heterogeneous electron-transfer reactions and analysis of coupled electrochemical reactions or adsorption processes.[51] A single cyclic voltammogram is useful for determining whether a species is electroactive or not.[124] Assuming the reaction is reversible (i.e., follows the Nernst equation); the number of electrons transferred during the oxidation/reduction reaction can be calculated. A typical cyclic voltammogram for a reversible single electron transfer reaction can be obtained by scanning the potential between two values (initial potential (E_{intial}) to final potential (E_{final})), at a fixed rate.[125] When the potential is scanned from $E_{initial}$ to E_{final}, the scan is reversed and the potential is swept back to $E_{initial}$. Depending on the information sought, either single or multiple cycles can be performed. During the potential sweep, a potentiostat (source of potential) measures the current resulting from the applied potential and a typical current (i) vs potential (E) curve is obtained.[126] Figure 1.9 illustrates an example of a voltammogram with its characteristic reversible redox peaks. Prior to the start of the cathodic peak potential corresponding to the reduction, the current starts to increase, At this point the diffusion layer is relatively small.

The current reaches a maximum and starts to decrease (mass transport control) as the diffusion layer extends further away from the surface (diffusion layer thickness increase). Thus, at this point the voltammogram is under diffusion control whereas at the start it was the electrode kinetics which controlled the response. The direction of the voltammetric scan is reversed. At this point, oxidation of the reduced species begins, resulting in an increase in the anodic peak current and a depletion of the oxidised species.

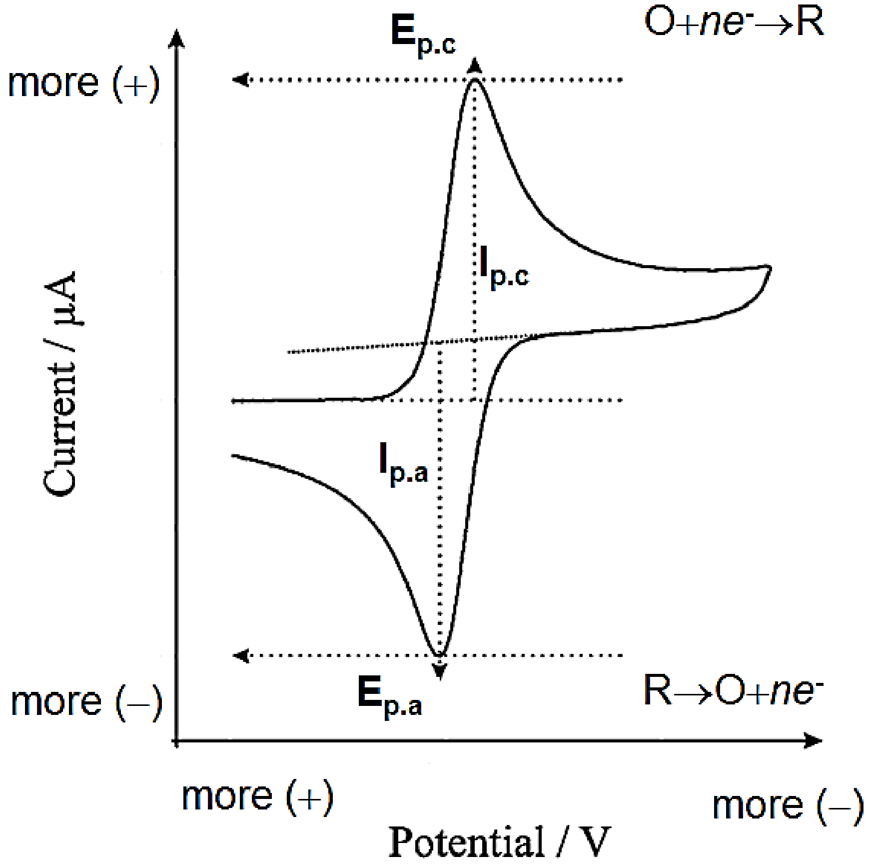

Figure 1.9: Typical cyclic voltammogram depicting a fully reversible redox couple showing the important parameters: (i) peak potentials (E_P); (ii) peak currents (I_P).

The criteria required for a reversible voltammogram depends on two important parameters namely, the peak height (anodic and cathodic peak currents) and the potential at which the peak occurs. The peak current (i_p) for a reversible system at 25°C, can be expressed by the Randles Sevcik equation,[127]

$$i_p = (2.69 \times 10^5) n^{3/2} A C D^{1/2} \upsilon^{1/2} \qquad \textbf{[1.29]}$$

Here, n is the number or electrons, A is the electrode area in (cm^2), C is the concentration in ($mol\ cm^{-3}$), D is the diffusion coefficient in ($cm^2\ s^{-1}$), and ν is the scan rate in ($V\ s^{-1}$). The current is directly proportional to the concentration and increases with the square root of the scan rate. For a reversible system, the peak current for the return potential scan ($i_{p,r}$) should be equal to that for the forward potential scan ($i_{p,f}$).

$$\frac{i_{p,r}}{i_{p,f}} = 1 \qquad \textbf{[1.30]}$$

These peak currents are commonly measured by extrapolating the preceding baseline current. The position of the peaks on the potential axis is related to the formal potential (E^o) of the redox process which is given by:

$$E^{\circ} = \frac{E_{p,a} + E_{p,c}}{2} \qquad \textbf{[1.31]}$$

With respect to the above, the potential separations between the peak potentials (ΔEp) can be given by,

$$\Delta E_p = \frac{59}{n} mV \qquad \textbf{[1.32]}$$

The value obtained is independent of the scan rate and it can be used to determine the number of electrons transferred. At certain scan rates the Nernstian equilibrium cannot be maintained at the electrode surface. One reason might be due to electron transfer process that takes more time to respond to the applied potential. Thus, voltammograms with characteristics of quasi-reversible or irreversible behaviour are brought about.[128]

1.4.1.1.1 Study of adsorption Processes

Electroactive materials can also be employed as adsorbed species on the electrode surface. Voltammograms of adsorbed species are quite different from voltammograms of solution phase species (Figure 1.10).[129] This is because fixed species on the electrode surface do not have to diffuse to/or from the electrode surface, and thus cannot be influenced by mass transport. Both the reactants and products of fixed species can be involved in adsorption-desorption processes.[130] These processes may occur for organic compounds or metal complexes during characterization analyses.

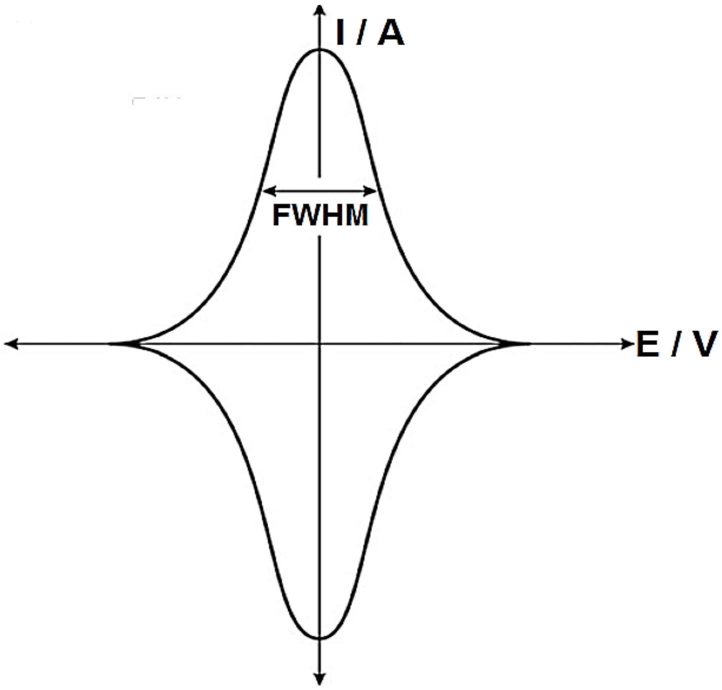

Figure 1.10: Cyclic voltammetric response for the reversible reaction of an adsorbed species. Reprinted from Brownson, D. A. C.; Banks, C. E. In *The Handbook of Graphene Electrochemistry*; Springer London: London, 2014; pp 23–77.

The separation between the peak potentials is zero unlike that observed for solution-phase processes. This is revealed by the symmetrical cyclic voltammetric peaks,[131] where $\Delta E_p = 0$ and by the full width at half height (FWHM) of the anodic and cathodic peak, which is given by,

$$\mathrm{FWHM} = \frac{90.6}{\mathrm{n}}\,\mathrm{mV} \qquad \textbf{[1.33]}$$

The peak current can be related directly to the surface coverage (Γ) and the potential scan rate for a reversible process, as illustrated below.[132]

$$i_p = \frac{n^2F^2\Gamma A\nu}{4RT} \qquad \textbf{[1.34]}$$

Where n is the no of electrons, F is the Faraday constant in (C mol^{-1}), A is the electrode area in (cm^2), ν is the scan rate in (V s^{-1}), R is the gas constant in (J K^{-1} mol^{-1}) and T is the absolute temperature in (K). By Integrating the charge (Q) under the peaks shown in Figure 1.10 it is possible to determine the surface coverage according to Equation 1.35.

$$Q = nFA\Gamma \qquad \textbf{[1.35]}$$

Once the microscopic electrode area is known, it is possible to determine the area occupied by the adsorbed material and perhaps the orientation of the molecules on the electrode surface. Voltammetry can detect very small number of molecules (low concentrations) on the electrode surface and it is quite sensitive without any special effort or experimental precautions.[133] However, for non-surface confined electroactive materials, the concentration of the analyte must be at least 10 µM for the attainment of reliable mechanistic information.

The characteristics of a CV depend on several factors. These include electrode surface pre-treatment, the rate of the electron transfer reactions, the thermodynamic properties of chemical and biological species present, the concentration of electroactive species and their rates of diffusion and the scan rate.[134] It should also be noted that the material of the electrode typically has an influence on the reversibility of a system. This is due to the surface coverage of the adsorbate, roughness and function groups present on the electrode surface.[134]

1.4.1.2 Chronoamperometry

In chronoamperometry, the potential is stepped from the open circuit or a potential, where the target analyte does not undergo any electrochemical reactions to a potential beyond that required for the target analyte to be electrochemically oxidised or reduced.[135] In solution phase experiments, chronoamperometry can be used to measure current–time dependence for the diffusion controlled process occurring at the electrode surface.[136] The faradaic current under diffusion controlled conditions is related directly to the concentration gradient.[51] This means that as the slope of the concentration profile at the electrode surface declines with time, so will the current (Figure 1.11). The characteristic shape of the resulting chronoamperogram can be represented by the Cottrell equation below.

$$i_t = \frac{nFAC_0D_0^{1/2}}{\pi^{1/2}t^{1/2}} \qquad \textbf{[1.36]}$$

Where, n is the moles of electrons involved in the reaction, F is the Faraday constant, A is the area of the electrode (cm^2), C_0 the concentration of the analyte in the bulk solution (mol dm^{-3}), D_0 is the diffusion coefficient (cm^2 s^{-1}), and t is time (s). Consequently, i will be proportional to t$^{-1/2}$.

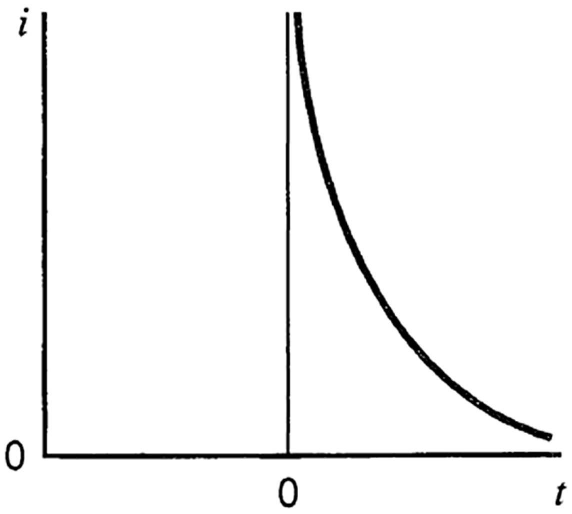

Figure 1.11: Current-time curves. Reprinted from Bard, A. J.; Faulkner, L. R. *Electrochemical Methods: Fundamentals and Applications*, 2nd ed.; Wiley: New York, 2001.

Chronoamperometry experiments are most commonly either *single potential step*, in which only the current resulting from the forward step as described above is recorded, or *double potential step*, in which the potential is returned to a final potential value following a time period. Due to its relative simplicity, chronoamperometry is one of the most commonly employed techniques for studying electrodeposition and electrochemical nucleation.[137]

1.4.1.3 Impedance

Electrochemical impedance spectroscopy (EIS) has become quite popular in recent years due to being a powerful non-destructive method for studying interfacial behaviour in electrochemical systems.[138] EIS is based on the application of an AC voltage or current to the system under study and the response of the current or voltage is measured over a broad range of frequencies.[139] The frequencies may span from 10^5 KHz down to 10^{-3} Hz. The EIS data can be conveniently presented in two ways namely, the Nyquist plot, which involves plotting of Imaginary numbers Z'' against real numbers Z', and the Bode plot, in which absolute values of impedance or phase angle are plotted against the frequency.[140,141]

There are two fundamental equations (Equation 1.37 and Equation 1.38) that can describe the real and imaginary impedances of the most common representation of an EIS experiment.[142] That is,

$$Z' = R_s + \frac{R_{ct}}{1+\omega^2 R_{ct}^2 C_{dl}^2} \tag{1.37}$$

$$Z'' = R_s + \frac{R_{ct}^2 C_{dl}\omega}{1+\omega^2 R_{ct}^2 C_{dl}^2} \tag{1.38}$$

Where Z' and Z'' are the observed impedance due to the real and imaginary parts, respectively, R_s is the solution resistance, R_{ct} is the charge transfer resistance, ω is the angular frequency and C_{dl} is the double layer capacitance. Extraction of the system characteristics requires interpreting the Nyquist plots. The Nyquist plots can be interpreted by equivalent circuit models. EIS circuits can give insight into different components contributing to the overall impedance.

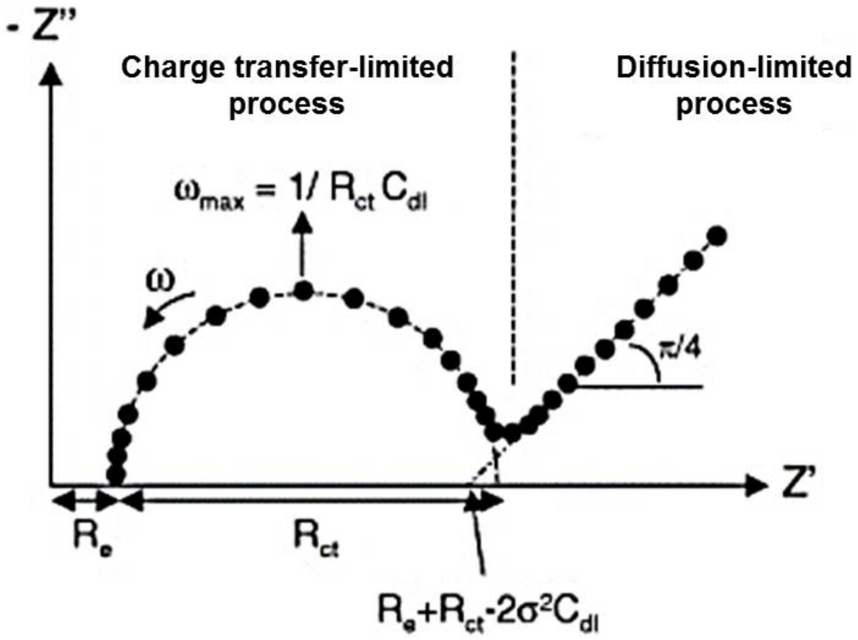

Figure 1.12: A Nyquist plot that describe impedance behaviour of a simple electrochemical cell involving a single Faradaic process. Each dot of the Nyquist Plot represents the impedance at a given frequency. Adapted from Fernández-Sánchez, C.; McNeil, C. J.; Rawson, K. Electrochemical Impedance Spectroscopy Studies of Polymer Degradation: Application to Biosensor Development. *TrAC Trends Anal. Chem.* 2005, *24* (1), 37–48.

A typical Nyquist plot can be seen in Figure 1.12 for an electroactive species in solution. The right hand side of Figure 1.12 illustrates the diffusional controlled region of a Nyquist plot. This is represented by the Warburg Element in an EIS circuit model (Figure 1.13). There is also a region on the Nyquist plot that is kinetically controlled (presented by R_{ct}) and is related to the heterogeneous electron transfer rate constant, k^0.[142] The Nyquist plots can give information about interfacial charging, charge transfer processes and mass transfer effects.[138] However, one short coming of the Nyquist plots is that it is unable to show at what frequency the specific impedance point is recorded. For this reason, Bode plots might be useful because the frequency information is given. Figure 1.14 shows the Bode plots for the Randles circuit. From Bode plots it is possible to find capacitive or inductive effects of electrochemical systems.[143]

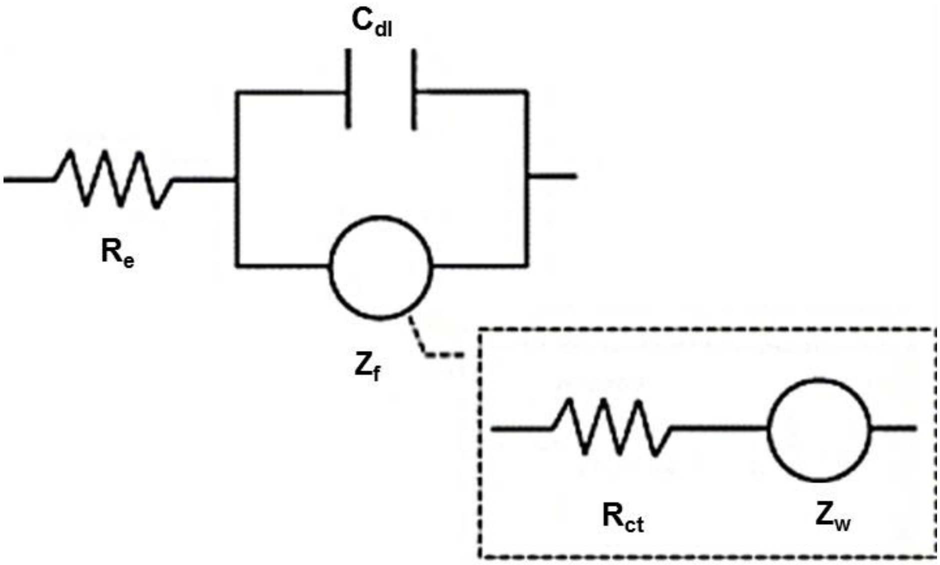

Figure 1.13: Simple Randles equivalent circuit for an electrochemical cell with a solution phase species. Adapted from Fernández-Sánchez, C.; McNeil, C. J.; Rawson, K. Electrochemical Impedance Spectroscopy Studies of Polymer Degradation: Application to Biosensor Development. *TrAC Trends Anal. Chem.* 2005, *24* (1), 37–48.

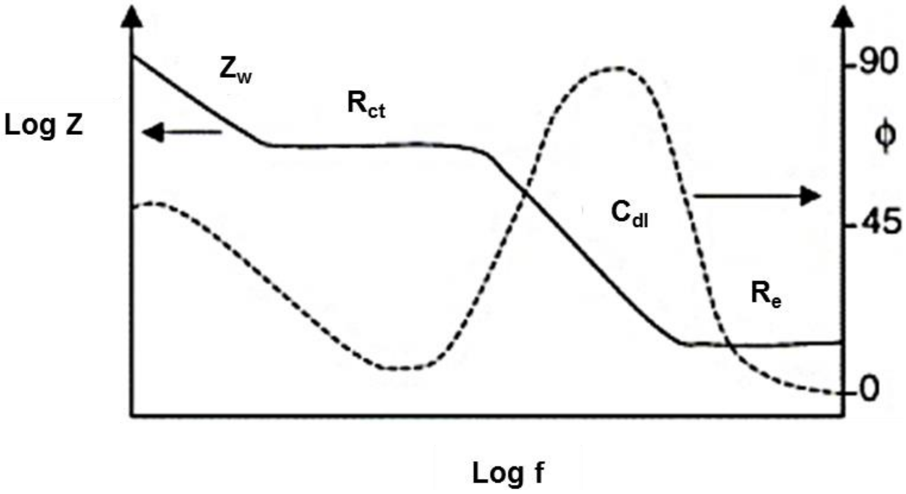

Figure 1.14: Bode plot, where the impedance and phase angle is plotted against frequency. Adapted from Fernández-Sánchez, C.; McNeil, C. J.; Rawson, K. Electrochemical Impedance Spectroscopy Studies of Polymer Degradation: Application to Biosensor Development. *TrAC Trends Anal. Chem.* 2005, *24* (1), 37–48.

1.4.1.4 Four-point probe

Various models and methods have been suggested to measure the electrical conductivity of a conducting sample. Factors affecting the suitability of various methods and precision attainable include contact resistance and shape of the sample i.e. whether is it in the form of single crystal, thin film, powder pellet or small crystallite.[144] Generally, four-point probe characterisation is a standard method for studying the electrical properties of solids and thin films in material science and semiconductor industries.[145] The set-up consists of four-point collinear probes, where a constant current is applied in the two outer probes and the voltage drop is measured in the two inner probes. Here, current passes through the outer contacts which are close to the edges of the sample. The four probes can be arranged in a variety of geometries, but they are often placed in a straight line with some known spacing between them (Figure 1.15).

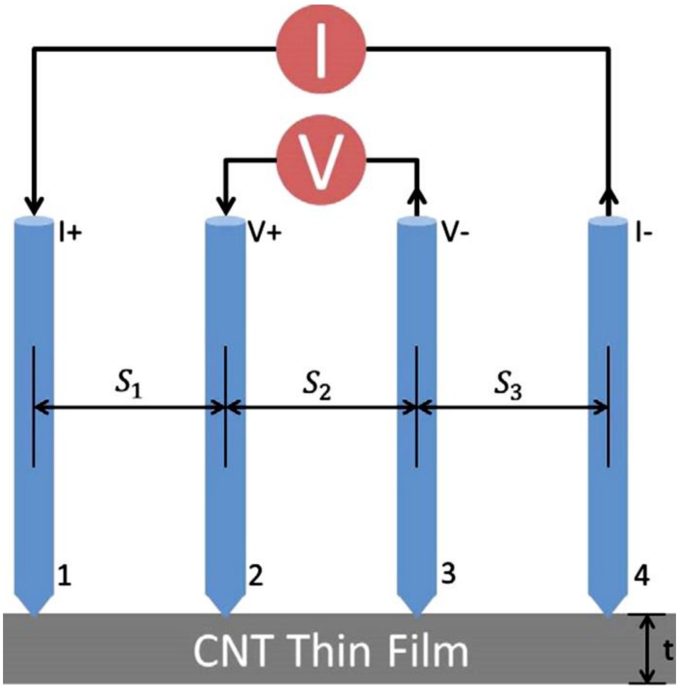

Figure 1.15: An illustration of typical four-point probe arrangement. Reprinted from Li, M.-Y.; Yang, M.; Vargas, E.; Neff, K.; Vanli, A.; Liang, R. *Meas. Sci. Technol.* 2016, *27* (9), 095004.

This method is particularly useful for measuring very small samples because the dimensions of the sample and the spacing of the contacts are insignificant.[146] However, contact resistance is particularly likely to occur in small or thin film materials, where the material volume through which charge can move is small. The four-point probe technique circumvents this issue by separating the current-applying and voltage-measuring probes and eliminating contact resistance, thus it is most suitable for accurate resistance measurements.[147]

1.4.2 Spectroscopic Methods

1.4.2.1 Absorbance

Ultraviolet-visible (UV-Vis) absorption is a simple, versatile, fast, and accurate technique that studies the sample’s reaction to light.[148–150] It measures the absorption of radiation by a material, as a function of the wavelength. Although it provides a limited amount of qualitative information it is almost entirely used for quantitative analysis. For qualitative analysis this technique can provide information on the identity of certain compounds and the wavelength of the key electronic transitions that will correlate with formal potentials. However, for quantitative analysis this technique is able to estimate the amount of a compound known to be present in the sample. The sample under analysis is usually examined in solution. UV-Vis is mainly used for multicomponent analysis, thus minimising the cumbersome task of separating interference and allowing the determination of an increasing number of analytes, consequently reducing analysis time and cost.[151] The Lambert's (or Bouguer's) Law states that each layer of equal thickness of an absorbing medium absorbs an equal fraction of the radiant energy that traverses it.[152] For instance, when a beam of light passes through a substance or a solution, some of the light may be absorbed and the remainder transmitted through the sample. The ratio of the intensity of the light entering the sample (I_0) to that exiting the sample (I) at a particular wavelength is defined as the transmittance (T) given by,

$$T = \frac{I}{I_0} \qquad \textbf{[1.39]}$$

The absorbance (A) is directly proportional to the concentration (c, g.L^{-1}) of the absorbing species and to the path length (b, cm) of the absorbing medium. Therefore, the above equation can be transformed into a linear expression by taking the logarithm and is expressed by:

$$A = -logT = -log\frac{I}{I_0} = log\frac{I_0}{I} = \varepsilon bc \qquad \textbf{[1.40]}$$

where ε is the molar extinction coefficient (ε, L.mol^{-1}cm^{-1}). The expression above is known as the Lambert-Beer's law and it states that there is a linear relationship between absorbance and path length at a fixed concentration.[153] However, the linearity of the Beer-Lambert law is limited by chemical and instrumental factors. UV-vis absorption occupies only a very narrow frequency or wavenumber region within the overall range of electromagnetic radiation, that is, from 190 nm to 900 nm. However, this range is of great importance, since the energy differences correspond to those of the electronic states of atoms and molecules. For this reason, UV-Vis spectroscopy can be used to characterize the absorption, transmission, and reflectivity of a variety of technologically important materials, such as pigments, coatings, windows, and filters.[154]

1.4.2.2 Fluorescence

Fluorescence is a powerful tool for investigating the structure and dynamics of matter or living systems at a molecular or supramolecular level.[155] Fluorescence occurs subsequent to absorption of ultraviolet or visible light of a fluorescent molecule or substructure, called a fluorophore.[156] The processes that occur between the absorption and emission of light are generally illustrated by the Jablonski diagram (Scheme 1.7). Here absorption of photons in the UV-vis range causes the electronic transition from the lowest vibrational energy level ν_0, of the ground electronic singlet state S_0, to an excited singlet state S_1. Molecules in condensed phases rapidly undergo vibrational relaxation to the lowest vibrational energy level of the excited state from which it may be de-excited by one of several competitive pathways, some occurring either with non-radiative processes or by the emission of photons (fluorescence).[157] According to the Jablonski diagram, the energy of the emission of photons is lower (shifted to longer wavelengths) than that of excitation (shifted to shorter wavelengths) for fluorophores. The difference between the excitation and emission wavelengths of fluorophores is known as the Stokes shift, which is a result of rapid decay to the lowest vibrational energy level of S_1. Fluorophores can display further Stokes shifts due to solvent effects, excited-state reactions, complex formation, and/or energy transfer.[158]

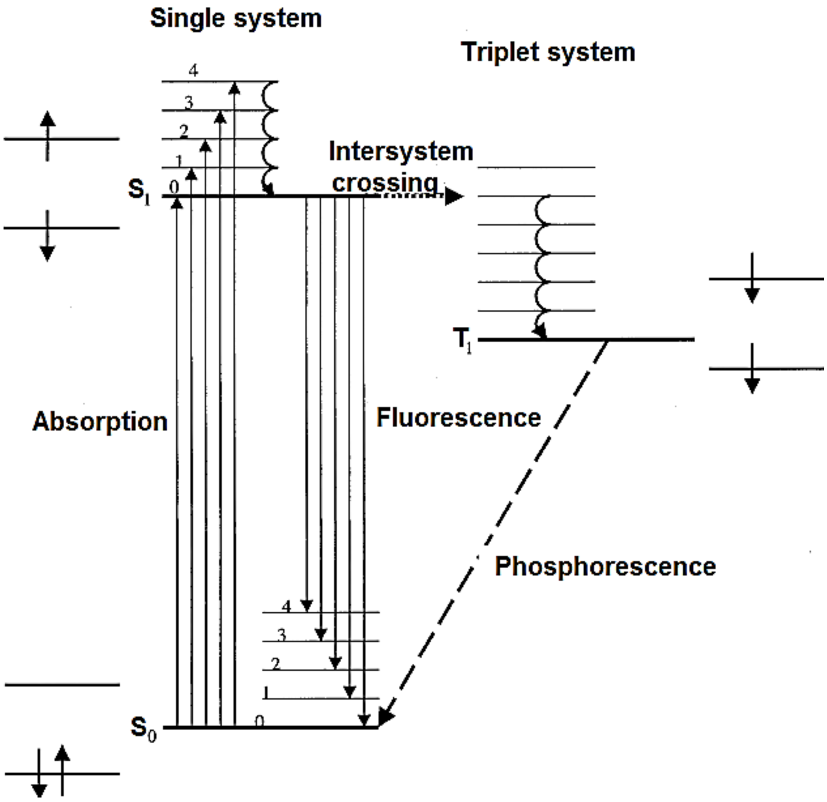

Scheme 1.7: Representation of energy levels and molecular orbitals during the absorption and emission of radiation. Reprinted from Bard, A. J. *Electrogenerated Chemiluminescence*; CRC Press, 2004.

In a fluorescence spectrum the intensity of the emission band is measured as a function of wavelength. The totally intensity of the emission at all wavelengths is related to the fluorescence quantum yield. The quantum yield is the ratio of photons emitted to photons absorbed and it reflects probabilities of various photochemical and photophysical processes leading to radiation or radiationless deactivation of the excited state.[159] It is also known that molecules in the excited state can be quenched by another molecule to produce the ground state. The quenching effect can occur by either energy or electron transfer. A very well-known collisional quencher is oxygen.[156] Oxygen, present in solution at a concentration of 10^{-3} M, normally reduces the fluorescence of a typical compound by 20%.[160] Organic molecules in solution are readily quenched by solution species like oxygen before emission. The kinetics of quenching reaction is governed by the Stern-Volmer equation below,

$$\frac{\phi^0}{\phi-1} = \frac{R^0}{R-1} = \kappa_Q \tau_0 [Q] \qquad \textbf{[1.41]}$$

Where ϕ^0 and ϕ are the fluorescence efficiencies and R^0 and R are the fluorescence responses in the absence and presence of a quencher at concentration [Q], respectively, κ_Q is the rate constant for quenching, and τ_0 is the lifetime of the excited state in the absence of a quencher.[44]

1.4.2.3 Raman

Spectroscopy is the study of how light (electromagnetic radiation) interacts with matter. Spectroscopic methods can be based on phenomena like emission, absorption, fluorescence or scattering.[161] Raman Spectroscopy is a spectroscopic technique based on scattered light obtained from a laser source following interaction with the sample. Raman spectroscopy utilises scattered light to gain knowledge about molecular vibrations which can provide information regarding the structure, symmetry, electronic environment and bonding of a molecule.[162] Different molecules give different Raman spectra thus; Raman spectroscopy can be employed to study various molecular samples such as solids, liquids, gels, slurries, powders and films. In a Raman spectrum the relative intensity of the Raman peaks or bands is related to the nature of the material and the type and concentration of the atoms undergoing vibrations.[163] As a result, Raman can be used for both qualitative and quantitative purposes. A typical Raman spectrum is acquired by scattered light that results from the interaction between the incoming incident radiation (laser light) and the molecules of the sample.[164] When monochromatic radiation strikes the sample, it scatters in all directions. Much of this scattered radiation has a frequency which is equal to frequency of the laser light and constitutes elastic scattering (Rayleigh scattering). Only a small fraction of scattered radiation has a frequency different from frequency of the laser light and is known as inelastic scattering (Raman scattering). Inelastic scattering is the shift in photon frequency due to excitation or deactivation of molecular vibrations in which either the photon may lose some amount of energy or gain energy.[162] When this happens two types of phenomena can occur namely, anti-Stokes and Stokes Raman scattering. In an anti-Stokes Raman shift, when the light interacts with the molecule, the light photon can gain energy from the molecule and thus result in a higher frequency of scattered light compared to the incident light. While in Stokes Raman shift, if the interaction causes the molecule to gain energy from the light photon then the frequency of the scattered light will be lower than that of the incident light. The energy increase or decrease from the excitation is related to the vibrational energy spacing in the ground electronic state of the molecule, and therefore, the wavenumber of the Stokes and anti-Stokes lines are a direct measure of the vibrational energies of the molecule (Figure 1.16).

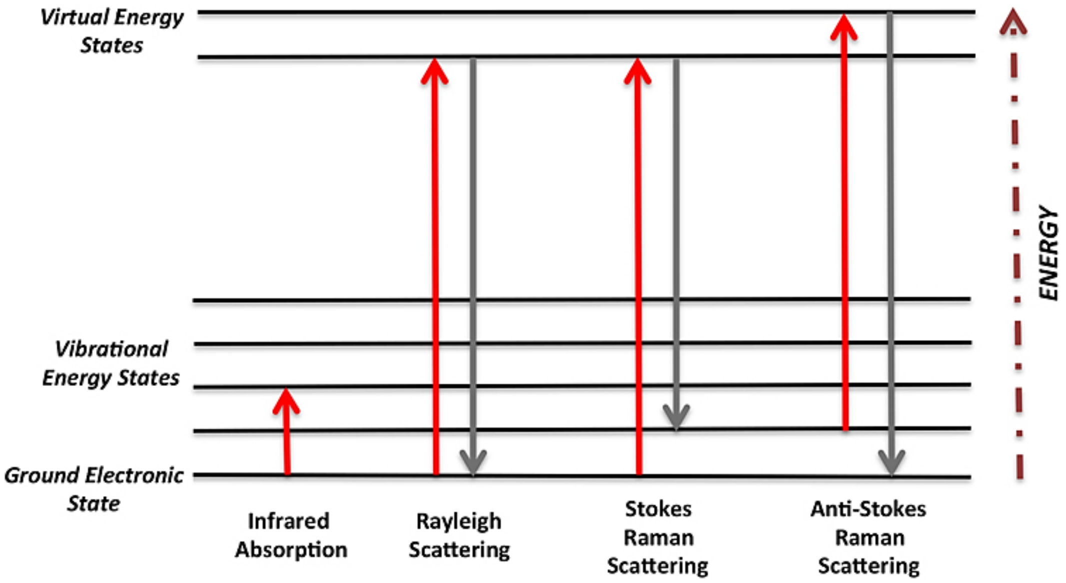

Figure 1.16: An energy level diagram illustrating the transitions occurring during Rayleigh scattering and Stokes and anti-Stokes Raman scattering.

In contrast to other vibrational techniques, Raman's operational wavelength range is usually independent of the vibrational modes being studied. Furthermore, Raman spectroscopy is considered to be a non-destructive technique because it does not require any special sample preparation.[165] When dealing with samples that consist of single layered materials (monolayers), analysis using conventional Raman can become quite challenging. A greater sensitivity for detecting films can be achieved by employing Resonance Raman Spectroscopy (RRS).[166] This type of Raman is very powerful for analysing very dark or coloured samples and has the ability to enhance signal output because the frequency of the laser overlaps within the electronic transition of the sample.

1.4.3 Microscopic Methods

1.4.3.1 Scanning Electron Microscopy

Microscopy is the study of specialised optical instruments designed to observe small objects in fine detail. There are three well-known branches of microscopy namely, optical, electron, and scanning probe microscopy. This thesis reports electron microscopy which involves the diffraction, reflection, or refraction of electron beams interacting with the sample to produce an image.

Scanning electron microscopy (SEM), in particular, is a very important imaging approach because it is capable of providing in-depth information on the external morphology or surface topography of a sample.[167] In SEM, a fine probe of electrons with energies typically up to 40 keV are focused on the surface of material, and scanned along a pattern of parallel lines.[168] The interaction of the electron beam with the material surface produce various signals such as secondary electrons, backscattered electrons, characteristic X-rays, and light (cathodoluminescence).[169] The two most common signals responsible for the formation of SEM images are secondary and backscattered electrons (Figure 1.16). Secondary electrons results from inelastic collision and possess energies of less than 50 eV.[170] They have the ability to provide high spatial resolution images of ~10 nm or better.[171] Backscattered electrons results from the sample by elastic scattering and have much higher energies in comparison to secondary electrons.[167] They produce lower spatial resolution images because they originate from deeper within the sample. Backscattered electron images provide information about the distribution of different elements within the sample. This can be attributed to the fact that the signals generated by backscattered electrons are proportional to the mean atomic number of the sample.[167] This means that heavier elements (high atomic number) will backscatter electrons more strongly (give higher signal) than light elements (low atomic number), and thus give rise to a brighter appearance (Figure 1.16(b)).[172,173]

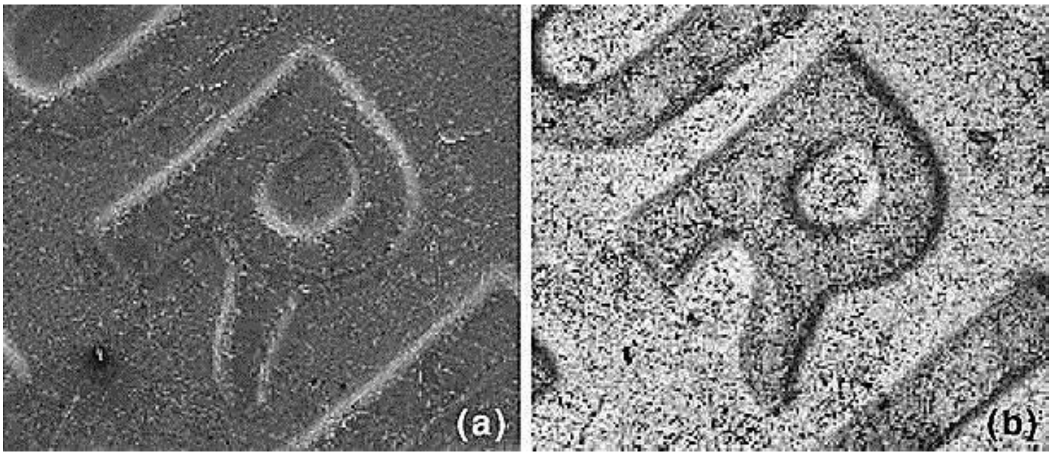

Figure 1.17: SEM images acquired of a US penny with (a) secondary electron detector and (b) back-scattered electron detector. Reprinted from

Sutton, M. A.; Li, N.; Joy, D. C.; Reynolds, A. P.; Li, X. Scanning Electron Microscopy for Quantitative Small and Large Deformation Measurements Part I: SEM Imaging at Magnifications from 200 to 10,000. *Exp. Mech.* 2007, *47* (6), 775–787.

Furthermore, characteristics x-rays also work in synchronisation with the secondary and backscattered signals in order to provide highly detailed spatial and compositional information of microscopic features of the sample. The x-ray signal is a result of recombination interactions between free electrons and positive electron holes that are generated within the material. Characteristic x-rays are detected by either an energy dispersive or a wavelength dispersive spectrometer.[167] Energy dispersive x-ray spectroscopy (EDS or EDX) is the more common attachment to scanning electron micrographs as it provides rapid qualitative analysis of the material.

Secondary and backscattered electrons has distinct advantages over other high-resolution imaging techniques because it is surface-sensitive, and it can provide quantitative information in two or even three dimensions, about the microstructure, the chemistry, the crystallography and the electronic properties of the material.[169] Because SEM is based on surface interaction, all kinds of samples conducting and non-conducting (stain coating needed) can be investigated.[174]

1.5 CONCLUSION

In conclusion, this chapter introduced some important ECL literature with focused placed on different ECL generation pathways. It discussed $[Ru(bpy)_3]^{2+}$ a standard luminophore for ECL generation. Emphasis was placed on ECL applications, which involved both solution and solid phase formats. A brief review on bipolar electrochemistry was also provided. Here, the difference between conventional and bipolar electrochemistry were discussed. Emphasis was placed on the co-joint use of BPE/ECL, especially for analytical applications. Furthermore, this chapter described some techniques used either for characterisation and/or application purposes. These include electrochemical methods, spectroscopic methods and microscopic methods.

From the reported literature, it can be concluded that ECL has been applied in various analytical applications, especially in bio-systems commercialised for clinical diagnostics. However, as the present trends in chemistry are miniaturised, ECL generation at miniaturised biological devices is still under studied, and thus warrants further investigation. The miniaturisation of ECL platforms provides the opportunity to investigate some interesting dynamics of ECL and heterogeneities existing at their interfaces. Furthermore, existing ECL platforms designed for biomedical diagnostics lacks sensitivity and are not capable for use as point-of-care devices. For this reason, this thesis focuses on the development of new sensing platforms (ranging from particles to bulk metallic three-dimensional designs) and demonstrates their use in a proof of concept approach by using BPE/ECL as detection mechanism.

2 Chapter 2:

Experimental Section

2.1 REAGENTS AND CHEMICALS

Glassy carbon spherical powder 2-12 μm, tris(2,2′-bipyridyl)dichlororuthenium(II) hexahydrate $[Ru(bpy)_3]Cl_2{\cdot}6H_2O$), potassium ferro/ferricyanide ($Fe(CN)_6^{3-/4-}$), N-hydroxysuccinimide (NHS), N-(3-dimethylaminopropyl)-N-ethyl carbodiimidehydro-chloride (EDC), 16-mercaptohexadecanoic acid (MHDA) (($HS(CH_2)_{15}CO_2H$, ≥ 90%), bovine serum albumin (BSA), nafion® 117 solution, tripropylamine (TPA), aniline, sulfuric acid (H_2SO_4), ethanol, Chloride-free phosphate buffer solution (0.1 M PBS, pH 7.4) and Dulbecco's phosphate buffered saline (DPBS, pH 7.4, 0.1 M) were purchased from Sigma Aldrich. All other chemicals were of reagent grade and used as received.

Alumina polishing slurries (in the range of 1, 0.3 and 0.05 μm) and micro polishing pads were purchased from Buehler. Aqueous gold plating solution containing gold sulphite was purchased from Technic Inc. Highly purified human cardiac troponin-I antigen (cTnI) and mouse anti-cardiac troponin-I secondary monoclonal antibody (Mab), 19C7, were obtained from HyTest Ltd. Primary 20B3 Mab anti-cardiac troponin-I was supplied by Prof. Richard O'Kennedy group, School of Biotechnology, DCU. Ruthenium (II) (bis-2,2-bipyridyl)-2(4-carboxylphenyl) imidazo[4,5-f][1,10]phenanthroline $[Ru(bpy)_2(picCOOH)]^{2+}$ was synthesized by Dr. Kellie Adamson, School of Chemistry, DCU, according to a procedure previously described by Pellegrin and co-workers.[175] Ultra-pure water was prepared by a Millipore Milli-Q system (resistivity = 18 MΩ cm) and used to prepare all working solutions.

2.2 MATERIALS AND INSTRUMENTATION

2.2.1 Electrochemical Methods

All electrochemical experiments were performed with a conventional single-compartment three-electrode cell unless otherwise stated. Indium tin oxide coated polyethylene terephthalate plastic from Sigma Aldrich, indium tin oxide coated glass from Delta Technologies, gold coated silica wafer from Amsbio, planar gold- and glassy carbon disc electrodes from CH Instruments, independently addressable microband gold electrodes from ABTECH Scientific, a custom-made carbon film (supporting film is Zeonor 1020R plastic from Zeon Chemicals), and a three-dimensional printed titanium structure (supplied by Prof. Gordon G. Wallace group, Intelligent Polymer Research Institute, ARC Centre of Excellence for Electromaterials Science, UOW) were all employed as working electrodes throughout the thesis. The counter electrode was a large area platinum (Pt) wire from Sigma Aldrich while a silver/silver chloride (Ag/AgCl in 3 M KCl) from BAS was used as the reference electrode.

Conventional and bipolar electrochemical cells were fabricated using materials like Teflon and Polymethyl methacrylate (PMMA) purchased from Radionics. Pressure sensitive adhesive (PSA) was supplied by Adhesives Research.

2.2.1.1 Cyclic Voltammetry, Electrochemiluminescence and Electrochemical Impedance Spectroscopy

Cyclic voltammetry (CV) and Electrochemiluminescence (ECL) measurements were carried out using a CH Instrument, Model 760B Potentiostat. ECL were performed with an Oriel 70680 Photomultiplier Tube (PMT) biased at -850V using a high-voltage power supply (Oriel, Model 70705) and an amplifier/recorder (Oriel, Model 70701). During the ECL experiments, the three-electrode cell was kept in a light-tight box in a specially designed holder where the working electrode was positioned directly opposite to the fibre optic bundle; with the other end coupled to the PMT.

AC impedance was performed using a CH Instrument, Model 760E electrochemical workstation. Impedance measurements were carried out at open potential, in 1mM PBS in the frequency range of 1 MHz to 1 Hz, with a 25 mV ac amplitude using a conventional three-electrode cell placed inside a Faraday cage.

A direct current (DC) power supply (Bang & Olufsen SN16) was used to generate the electric field required for the bipolar electrochemistry experiments.

All electrochemical experiments were carried out at room temperature (22±2 ^{o}C).

2.2.2 Spectroscopic Methods

2.2.2.1 Raman

Raman measurements were acquired by a Veeco/Horiba Nano-Raman/Atomic Force Microscope set at a power of 2 mW. The x-axis was calibrated versus the Rayleigh line at 0 nm and the photon mode from a silicon wafer at 520 cm^{-1}. The samples were excited at a certain wavelength (wavelengths depends on the type of material under study) from a water-cooled argon-ion laser. The laser was focused onto the samples using specific objectives. The spectral data was acquired and analysed using LabSpec software.

2.2.2.2 Absorbance

Ultraviolet-visible spectra were recorded on a Jasco V-670 UV/Vis/NIR Spectrophotometer and the measurements were conducted at room temperature in a Hellma quartz cuvette of 1 cm optical path length. The UV/Vis data were background-corrected using a blank

2.2.2.3 Fluorescence

Fluorescence emission experiments were performed with a Varian Cary Eclipse Fluorescence Spectrophotometer with an excitation slit width of 5 nm and an emission slit width of 5 nm. All experiments were conducted at room temperature in 1 cm path length quartz cuvette and the background was corrected using a blank before each fluorescence measurements.

The fluorescence response of the immuno/sandwich ELISA (enzyme-linked immunosorbent assay) was determined using a Tecan Safire 2 monochromator- based microplate reader.

2.2.3 Microscopic Methods

2.2.3.1 Scanning Electron Microscopy

Scanning electron microscopy (SEM) micrographs were acquired from both a Hitachi S5500 field emission-, Hitachi S3400N VP- and a Jeol JSM-IT 100 InTouchScope- scanning electron microscope, each operating with an accelerating voltage of either 5 kV or 10 kV, respectively, with a probe current of 35 mA.

Energy dispersive X-ray graphs was acquired by a Hitachi S5500 field emission-scanning electron microscope.

2.2.3.1.1 Sample Preparation

Each sample was mounted on a mounting stub with double-sided carbon tape.

2.2.3.2 Light Microscopy

Optical micrographs were acquired from a Keyence 3D digital microscope VHX-5000 series by employing a high-performance low-magnification zoom lens (VH-Z00R/VH-Z00W/VH-Z00T 0x to 50x) and a high-resolution zoom lens (VH-Z500R/VH-Z500W/VH-Z500T 500x to 5000x).

2.2.4 Photographic Methods

2.2.4.1 Digital Camera

BPE/ECL images were captured using a commercial Sony Alpha 7S digital camera equipped with a Sony E-mount lens.

2.3 PROCEDURES

2.3.1 Wireless Electrochemiluminescence at Nafion-Carbon Microparticle Composite Films

2.3.1.1 Fabrication of Spin Coater

In order to form very thin uniform coating of solutions a cheap and simple spin coater was developed by using a computer fan. The spin coater consists of a sample mounting stage (small petri dish) fixed on top of the fan (the sample stage was centred to avoid wobbling and shaking once the ideal rotation rates were reached). The fan was placed in a large exterior enclosure with a transparent lid to avoid material from reaching the bench top. A small hole was cut into the lid so that the pipette tip expels the solution on the rotating sample stage which is fixed within the enclosure.

2.3.1.2 Fabrication of Carbon Film Electrodes

All working electrodes (for both conventional- and bipolar-electrochemistry experiments) were fabricated using the above mentioned custom built spin coater capable of generating rotation rates from 0 to 2500 rpm. Carbon particles were placed in 1.25% v/v nafion/ethanol mixture and ultrasonicated for 2 hours at room temperature (21°C) to give a homogeneous suspension. The viscosity of the suspensions did not depend significantly on the carbon particle loading. The carbon suspension was then vortexed at 1000 rpm and further serial dilutions were made from a stock concentration of 98.41% carbon/ 1.58% nafion v/v using 1.25% v/v nafion/ethanol mixture. Zeonor plastic (5 cm long × 3 cm wide) was mounted on the spin coater stage. After the fan has reached the desired rotational speed of 1875 rpm, 100 μL of the carbon suspension was deposited on plastic and spun until fully dry to give an adherent, uniform nafion-carbon particle composite coating. The carbon/plastic substrate was then cut to give 1 cm long × 0.5 cm wide samples.

2.3.1.3 Electrical Conductivity Measurements of Carbon Film Electrodes

For highly resistive samples (σ values less than 10^{-2} – 10^{-4} Sm^{-1}), the DC conductivity were measured using a Guildline Programmable Digital Tera-ohmmeter 6500A. To reduce the complications arising from electrode-specimen contact resistance, the four-electrode method was used.[176]

2.3.1.4 Polymerization of Aniline at Carbon Film Electrodes

Aniline was polymerised under *potentiodynamic* conditions in acidic media using the 98% carbon v/v film electrode. For electro-synthesis of PANI, a solution containing 0.2 M aniline and 0.5 M H_2SO_4 was cycled between -0.2 V to +0.8 V, at a potential scan rate of 0.2 V s^{-1}. The electropolymerisation of PANI was stopped after 30 voltammetric cycles. The carbon/PANI modified electrode was removed from the polymerisation solution, and rinsed with deionised water to remove excess monomer.

2.3.1.5 Bipolar Electrochemical Setup

The experiments were carried out in a two-electrode PMMA electrochemical bipolar cell (Figure 2.1). Two gold coated silica driving/feeder electrodes (3 cm long × 0.5 cm wide) were cleaned by sonicating in ethanol and then water for 15 minutes, followed by drying under nitrogen gas. The feeder electrodes were placed 0.73 cm apart in the cell walls. The carbon based bipolar electrode was placed symmetrically in a slot between the feeder electrodes and the cell was filled with a solution containing 5.0 mM $[Ru(bpy)_3]^{2+}$ and 25.0 mM TPA in ultra-pure water. Experiments were conducted in both ultra-pure water and a low electrolyte solution, but the former was preferred to minimise the loss of electric field (potential) close to the surface of the feeder electrodes. The feeder electrodes were connected to a DC power supply and the required potential was applied.

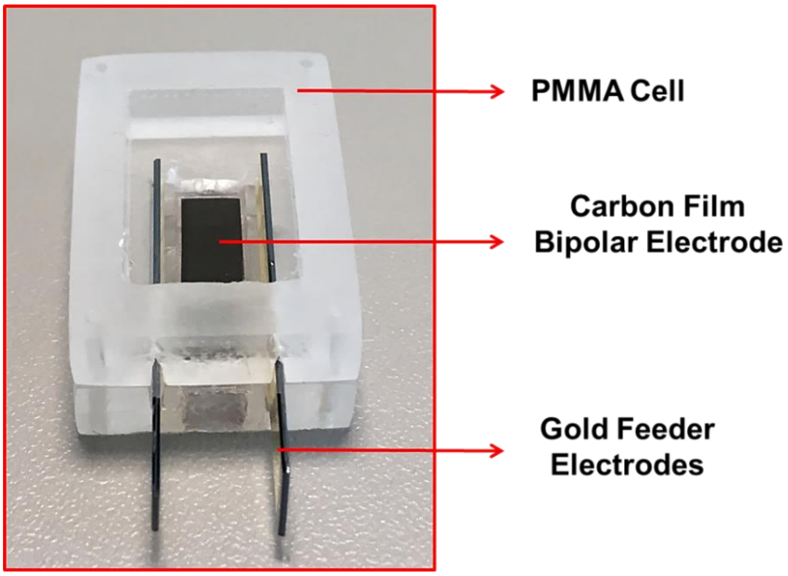

Figure 2.1: “Open” bipolar electrochemical cell.

2.3.1.6 BPE/ECL Imaging and Analysis

ECL images were captured in a dark room using a commercial digital camera positioned on top of the BPE cell. Each image was captured 10 s after the application of the driving voltage. The images were analysed according to a method described by Chang and co-workers.[119] The ECL intensity was determined by selecting the light-emitting zone and converting the brightness of each pixel in this region to photon counts. Because a camera was used to detect real-time BPE/ECL at the carbon film electrode any background from the feeder electrodes can be conveniently removed.

2.3.2 Electron Transfer and Electrochemiluminescence at 3D-Printed Titanium Electrodes

2.3.2.1 Fabrication of 3D-Printed Electrodes

3D-printed titanium (Ti) electrodes were fabricated according to a procedure previously reported by Zhao et al.[177] In brief, the electrode design was drawn using SolidWorks modelling software. Metal 3D printing was carried out with a Realizer SLM50 metal printer (Realizer, Germany) using selective laser melting (SLM) technique. A focused, high-energy laser beam fused and linked Ti alloy (Ti-6Al-4V) powder (ranged from 45 to 100 µm) on a printing stage in a layer by layer fashion to create an array of 25 vertical round posts spaced evenly on a 0.48x0.48 cm square base that contained 0.75x0.75 mm holes (Figure 2.2).

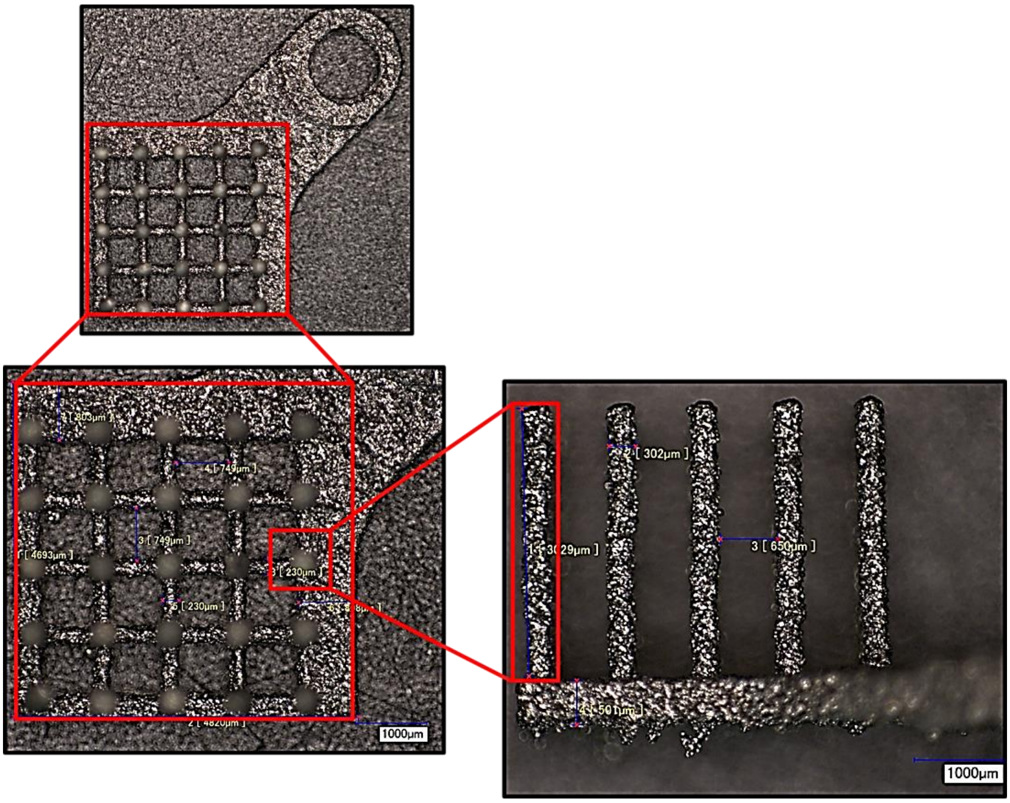

Figure 2.2: Top-view and cross-sectional optical micrographs of the 3D-printed Ti electrode.

2.3.2.2 Surface Modification

The fabricated 3D-printed electrodes were cleaned by sonication in a 50:50 v/v milli-Q water/ethanol solution before use. The electrodes were then dried under a stream of nitrogen. The Au plating solution was first deoxygenated with nitrogen for 30 min prior to deposition. The 3D-printed electrodes were then immersed into the aqueous Au plating solution in the presence of a Ag/AgCl reference electrode and a platinum counter electrode. Gold was potentiostatically deposited at -0.9 V while measuring the charge passed. The deposition time used was 1000 sec. Following electrodeposition, the 3D-printed electrodes were electrochemically cleaned by cycling in an aqueous solution containing 0.1 M H_2SO_4 as supporting electrolyte. The 3D-printed electrodes were then rinsed thoroughly with deionised water before use.

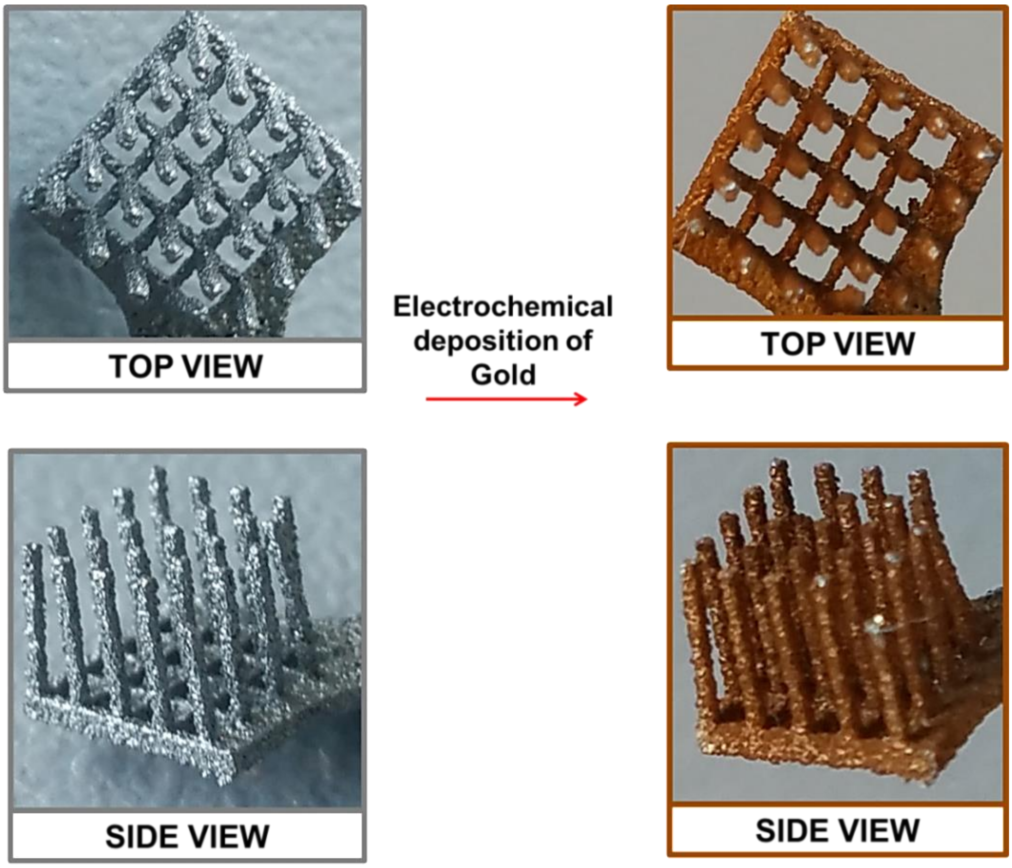

Figure 2.3: 3D-printed Ti electrode undergoing Au electrodeposition using a constant voltage of -9V with a run time of 1000 seconds.

2.3.2.3 BPE/ECL at 3D-Printed Electrodes

The bipolar electrochemical cell consists of a solution compartment with a pocket t into which the 3D-printed bipolar electrode array can fit. This was done to keep the 3D-printed bipolar electrode array in the same position and at a constant distance (2.5 mm from the anodic and cathodic feeder electrodes) between the two Au feeder electrodes that are located 10 mm apart in the cell walls. The 3D-printed electrode array was designed with a handle for the attachment of an electrical contact (Figure 2.4 (A)). However, for bipolar experiments the handle was covered with Teflon tape (Figure 2.4 (B)). The solution compartment was filled with 5.0 mM $[Ru(bpy)_3]^{2+}$ and 25.0 mM TPA in ultra-pure water up to a level that covered the 3D-printed bipolar electrode array in the vertical dimension. The electric fields required for the BPE/ECL process was established by controlling the potential difference between the two feeder electrodes on either side of the bipolar electrode.

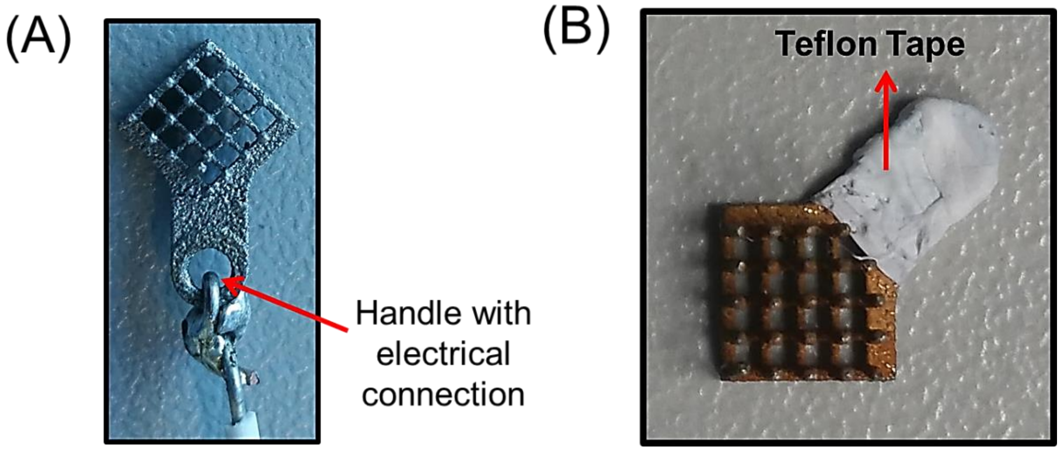

Figure 2.4: (A) 3D-printed Ti electrode connected to an insulating silver wire for electrical connection to alligator clips, and (B) handle of the 3D-printed Au coated Ti electrode insulated by Teflon tape.

2.3.3 Sandwich-type ECL Sensing Platform for Ultrasensitive Detection of Cardiac Troponin I, a Biomarker for Cardiovascular Disease

2.3.3.1 Electrode Cleaning

All working electrodes were cleaned and prepared before sensor fabrication. Au disc electrodes were first cleaned by successive polishing using 1, 0.3 and 0.05 µm alumina polishing slurries on micro polishing pads and rinsed with deionised water, followed by sonication in ethanol and water to remove any traces of bound alumina on the surface. The electrodes was then thoroughly rinsed with deionised water and dried under nitrogen. ITO and Au coated silica wafer electrodes were cleaned by sonicating in deionised water, followed by sonication in acetone and ethanol, respectively. The electrodes were then dried under a stream of nitrogen.

2.3.3.2 Surface Roughness

The Au disc electrodes were also electrochemically cleaned and cycled between 0 V and +1.5 V, at 0.1 V s^{-1}, in 0.1 M H_2SO_4 to determine the surface roughness and optimise the surface accordingly using the surface roughness factor (RF) given by Equation 2.1, below.

$$Rf = \frac{A_P}{(390\times10^{-6}\ C\ cm^{-2})\times A_G} \qquad \textbf{[2.1]}$$

where, A_p is the charge passed under the area of the reduction peak for each Au disc electrode (typically at 0.8 V) and A_g is the geometrical surface area (2 mm Au disc electrode= 0.0314 cm^2).

2.3.3.3 Preparation of Antibody-Dye Conjugates

The $[Ru(bpy)_2(picCOOH)]^{2+}$complex (0.015M) was dissolved in a mixture of DMSO-H_2O (1:9, v/v) and incubated with NHS/EDC (3:1 ratio) for 30 minutes at room temperature. Following this, the activated Ru complex (30 µL) was added directly to a 1 mL DPBS solution (pH 7.4) containing 100 µg/mL of the anti-cTnI secondary Mab. This mixture was allowed to react for 4 hours in the dark, at room temperature, under gentle stirring on a rotor shaker. The antibody-dye conjugate reaction mixture was purified using an Amicon ultra-centrifugal filter tube with a molecular weight cut-off (MWCO) of 30K. The mixture was centrifuged at 4000 rpm with 3×DPBS buffer (7 minutes each wash) to remove unbound dye. After the washing step the mixture was redispersed in DPBS and stored either long term at -20°C or short-term at 4 °C until required. The conjugation process of the dye and the antibody can be seen in Figure 2.5.

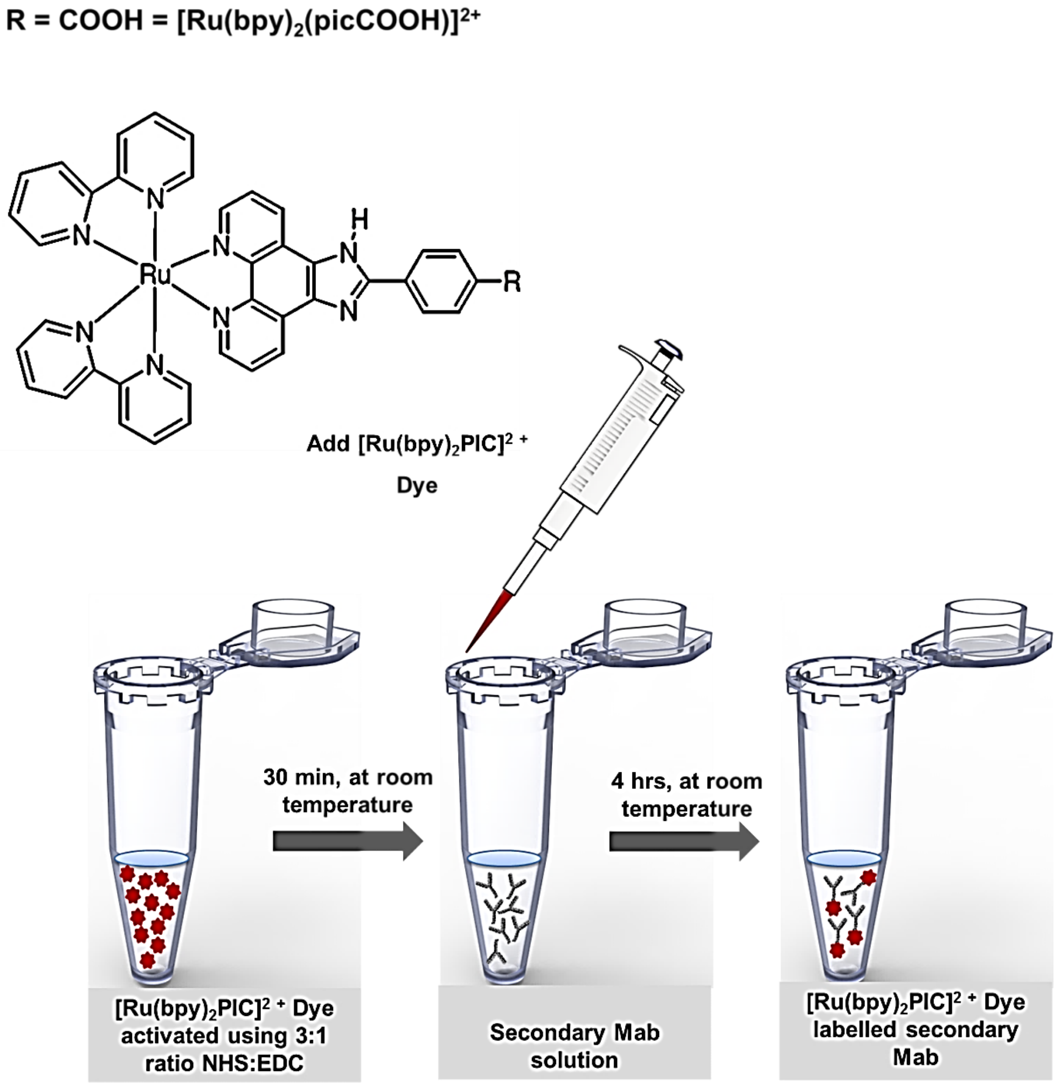

Figure 2.5: Schematic illustration of the antibody-Ru dye conjugate formation through a two-step covalent crosslinking process.

2.3.3.4 Fluorescent Sandwich ELISA of Mouse Anti-cTnI Secondary Mab Labelled with $[Ru(bpy)_2PIC]^{2+}$ Dye

A black 96 well fluorescence plate (Greiner®) was coated with 100 µL of 100 µg/mL mouse anti-cTnI primary Mab (known as 20B3 Mab) and left to incubate at 37°C for 1 hour. The solution was removed and each of the wells were washed with 200 µL washing buffer (DPBS containing 0.05% (v/v) Tween-20) for 3 x 5 minutes. The coated wells were then blocked with 300 µL of 1% (w/v) BSA-PBS solution for 1 hour, at 37°C, followed with a wash using the washing buffer. 100 µL of 1 µg/mL cTnI antigen was added to each of the coated/blocked wells and incubated at 37°C for 1 hour. Thereafter, the wells were washed using the washing buffer for 3 x 5 minutes to remove any unbound cTnI antigen. To determine the optimal coating concentration of the anti-cTnI secondary Mab labelled dye, different concentrations (5, 10, 50, 100 µg/mL) of mouse anti-cTnI secondary Mab (known as 19C7 Mab) was incubated with fixed concentrations of anti-cTnI primary Mab (100 µg/mL) and cTnI antigen (1 µg/mL) for 1 hour, at 37°C. Following incubation, the plates were washed using the washing buffer for 3 x 5 minutes to remove any unbound labelled secondary Mab. For performance of negative control experiments, some of the wells were incubated with only the anti-cTnI primary Mab and the anti-cTnI secondary Mab using the same ELISA procedure as described above. The absorbance was then read on a Safire 2 plate reader (Tecan).

It should be noted that typical working concentrations for coating and detection antibodies is normally in the range of 2-4 µg/mL for fluorescence ELISA; however, in this study the concentrations were increased due to the fact that a black 96 well plate was used instead of a white 96 well plate. The primary difference between white and black plates is their reflective properties. White plates reflect light and will maximise light output signal, whereas black plates absorb light but reduce background.

2.3.3.5 Fabrication of Sandwiched ECL Immunosensor

Clean Au disc electrodes were immersed in 1 mM 16-MHDA–ethanol solution, for 12 hours, at room temperature. The self-assembled monolayer (SAM) modified electrodes was then washed with deionised water and dried under nitrogen. The surface of the electrodes were activated by incubating it in NHS:EDC (3:1 ratio) solution mixture for 30 minutes. The electrodes were rinsed gently and 20 µL of the mouse anti-cTnI primary 20B3 Mab were immobilised on the surface and was allowed to incubate for 1 hour, at 37 °C. Thereafter, the electrodes were incubated in 1% BSA blocking buffer solution for 30 minutes. The coated/blocked electrodes were then coated with 20 µL of various concentrations of human cTnI antigen, respectively, for 1 hour, at 37°C. After the anti-cTnI primary Mab-cTnI antigen interaction the cTnI/BSA/20B3 Mab/16-MHDA modified Au electrodes were finally coated with the mouse anti-cTnI secondary 19C7 Mab labelled Ru dye and allowed to react for 1 hour, at 37 °C. After each modification step the electrodes were gently rinsed with a washing buffer that contained 0.01 M DPBS and 0.05% Tween 20 (pH 7.4). Accordingly, the 19C7 Mab-Ru dye/cTnI/BSA/20B3 Mab/16-MHDA modified Au electrodes, *i.e.* immunosensor, was constructed successfully and was ready for analysis. The process for the fabrication of the immunosensor is schematically illustrated in Figure 2.6.

For optimisation and comparison studies, Au coated silicon wafer electrodes and ITO glass/plastic electrodes were also used to fabricate the immunosensor. The same fabrication protocol was followed; however, 16-PHDA SAM was used on the ITO electrodes.

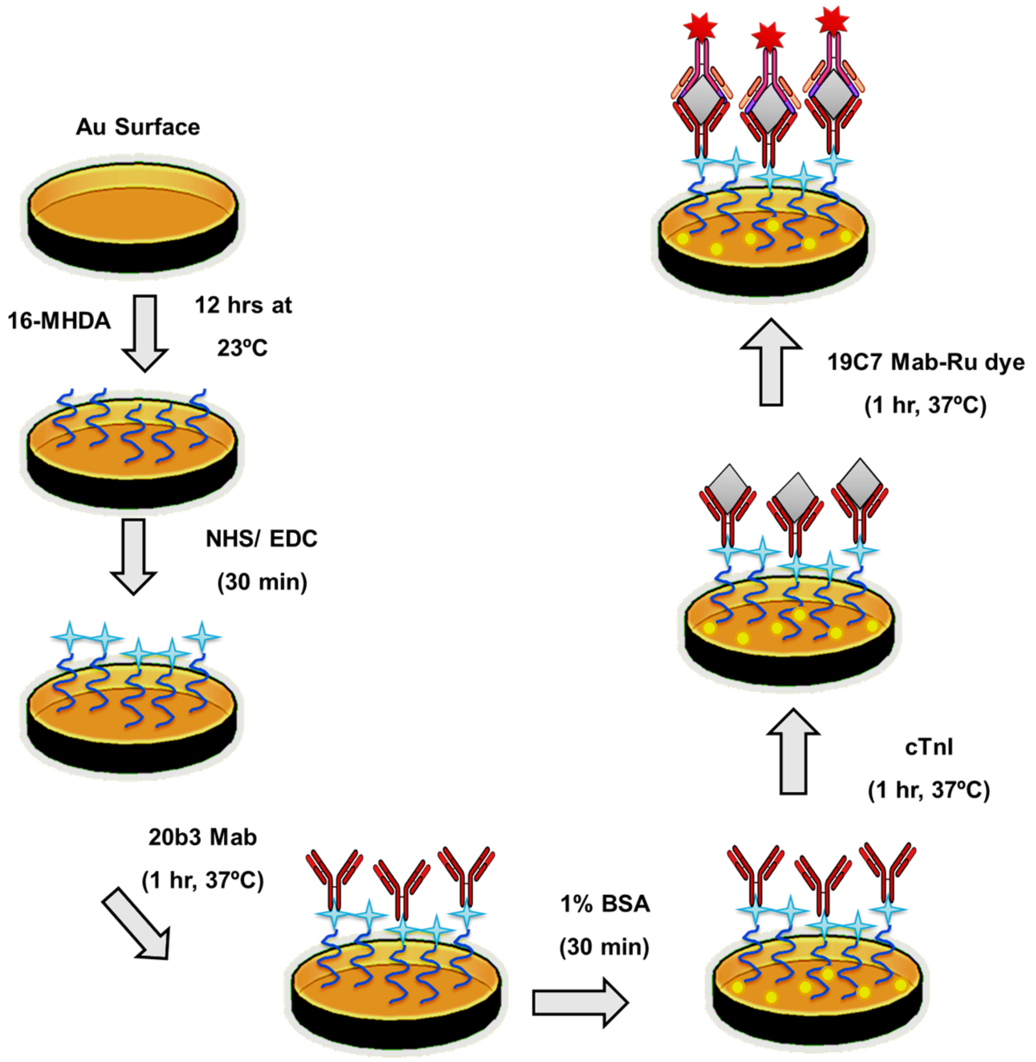

Figure 2.6: Schematic diagram illustrating the fabrication process of the sandwich-type ECL immunosensor on a gold disc electrode.

2.3.3.6 Bipolar Cell Fabrication and Description

2.3.3.6.1 Teflon Cell

Several cells made from different materials and with different dimensions were employed in bipolar experiments throughout this thesis. In particular, a Teflon based bipolar cell was developed for wireless detection of troponin (Figure 2.7). The Teflon bipolar cell was designed by computeraided-design (CAD) software. The cell itself was formed from a piece of Teflon block and cut to the desired dimensions. The driving electrode holders, bipolar electrode holder and the solution channel were milled out according to the dimensions shown in Figure 2.8. The driving electrodes used were either platinum disc electrodes or Tin wires. ITO was employed as the bipolar electrode.

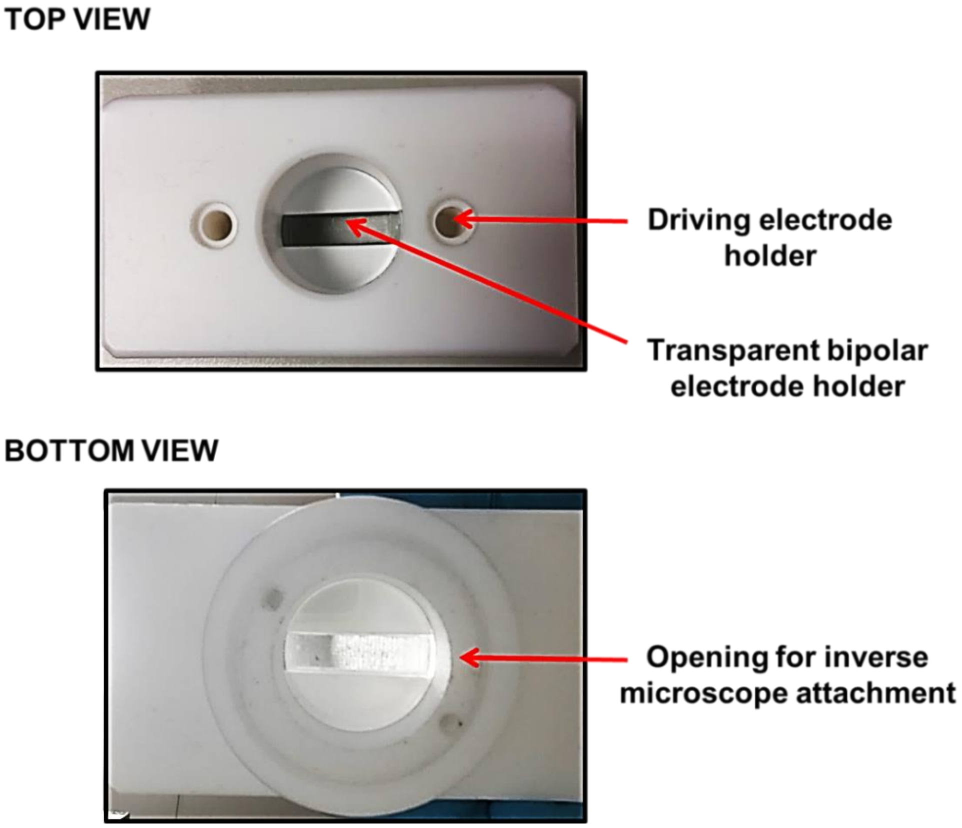

Figure 2.7: Photographs of the Teflon bipolar electrochemical cell showing the basic components of the cell.

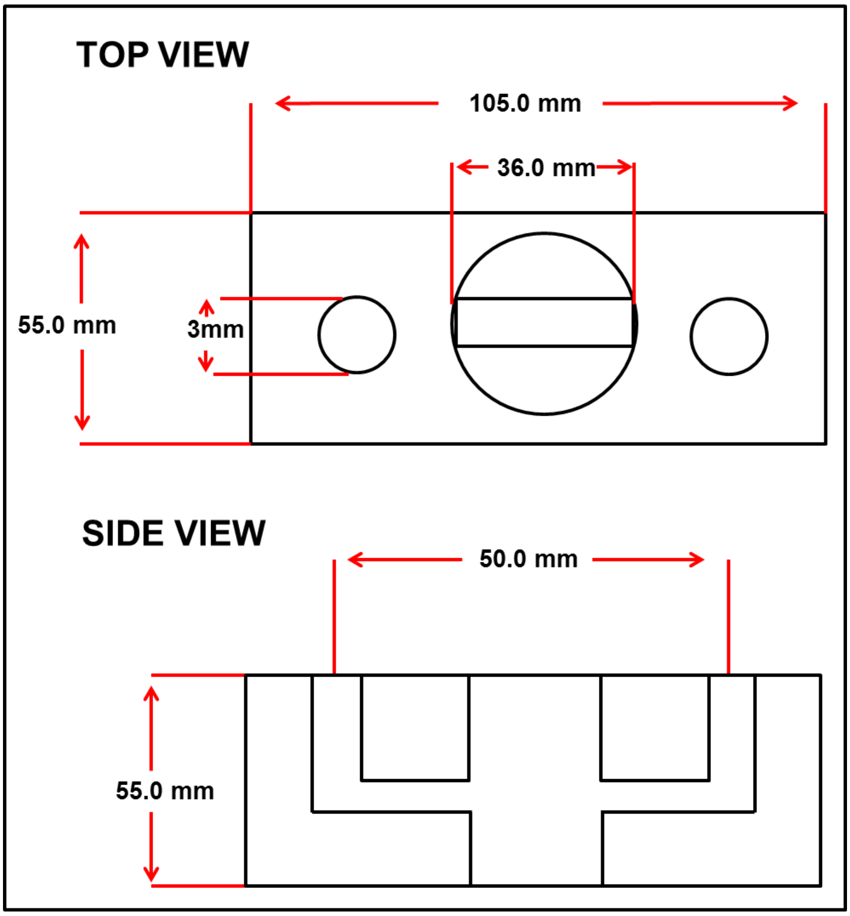

Figure 2.8: A 2D geometrical model with dimensions of the Teflon bipolar electrochemical cell.

2.4 CONCLUSION

In this chapter, the chemicals, materials and instrumentation used throughout this thesis are described. This chapter specifically focused on the parameters used for each instrument whether it is based on electrochemistry, spectroscopy and/or microscopy. Furthermore, this chapter gives a detailed outlay of the experimental procedures followed for each working chapter. Emphasis was placed on the design and fabrication of newly developed electrodes that were employed in both conventional and bipolar electrochemistry experiments. In addition, the design and function of newly developed bipolar electrochemical cells were discussed.

3 Chapter 3:

Wireless ECL at Nafion-Carbon Microparticle Composite Films

3.1 INTRODUCTION

Bipolar, or “wireless” electrochemistry (BPE) opens up new possibilities for driving redox reactions without the need for a direct electrical connection to the electrode.[85] As discussed in Section 1.3.2, when an electrical conductor is placed within the electric field generated by two external feeder electrodes, it assumes a potential whose value depends on the electric field strength and the size of the electrode.[87] In this way, redox reactions, including those that lead to the emission of light via electrochemiluminescence, can be driven wirelessly.[89] One useful strategy is to use the bipolar approach to drive redox processes at conducting particles. However, *single* microparticles require an intense electric field, e.g., 10^4 V cm^{-1} to generate a 1 V potential difference on a 1 µm diameter particle, which is not possible for some applications, e.g., *in vivo*. The field strength depends directly on the size of the electrode so assemblies of particles can dramatically reduce the electric field strength required. For example, Sentic and co-workers were able to demonstrate bulk 3D ECL using BPE.[5] In their approach, they used microbeads dispersed in a capillary containing PBS solution (pH 7.4), 2.5 mM tris(2,20-bipyridyl) dichlororuthenium(II) hexahydrate, 1.4% of agarose and 20 mM 2-(dibutylamino)ethanol. They were able to generate wireless ECL from each individual microbead leading to a bulk signal output. However, their system required very high electric fields (kV cm^{-1}).

The goal of this work is to use preformed particles as building blocks with defined composition, size, shape and surface chemistry, to assemble 2- and 3-dimensional structures at an interface that can act either as a conventional or bipolar electrode. Particles are particularly attractive building blocks since structures with significant complexity and with properties optimised for specific applications can be created. One significant challenge is to understand the effect of inter-particle separation, or loading of the particles, on the overall conductivity/bipolar properties of the electrode.

The loading of the particles leads to films ranging from isolated particles to the formation of a continuous network of particles making the film electrically conducting. This phenomenon is directly tied to the percolation theory, a process which is based on the onset of conductivity across an insulating region once conducting links have been added at a density exceeding some critical value, known as the percolation threshold (Scheme 3.1).[178] As more links are added, new conducting paths are formed which results in a higher conductivity. In conventional four point conductivity measurements, an abrupt increase in the conductivity of the film would be expected at the percolation threshold.[179] It is known that the physicochemical properties of the material as well as the processing methods and conditions can influence the apparent percolation threshold.[180,181]

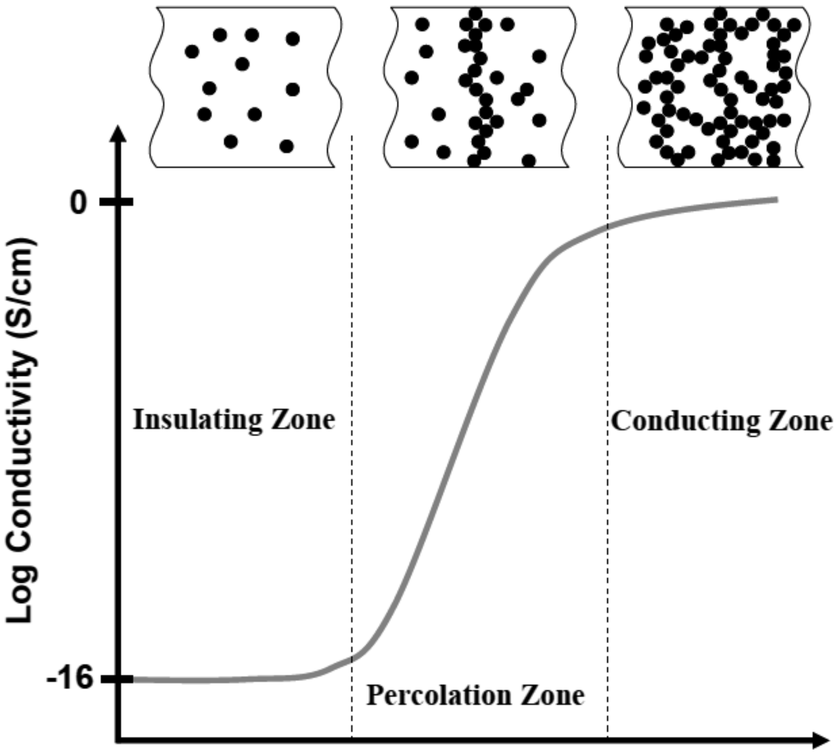

Scheme 3.1: Schematic diagram of electrical conductivity as a function of particle concentration.

In this thesis, films that contain different particle loadings have been used as conventional and bipolar electrodes to measure the conventional and wireless electrochemiluminescence intensity, respectively. These experiments were carried out in a solution containing ruthenium tris bipyridyl and tripropylamine (TPA). When a sufficiently intense electric field is present (depends on the size of the “electrode” that can range from single isolated particles (low carbon particle loadings) to the entire film (loading above the percolation threshold)), this induces potentials that can simultaneously drive reduction and oxidation reactions wirelessly on either sides of the bipolar electrode, as illustrated in Figure 3.1.[182] Furthermore, surface modification of the carbon containing films with polyaniline is considered. Small conducting particles assembled on a non-conducting substrate opens up the possibility of self-assembling the bipolar electrode *in situ* allowing low electric field strengths to be employed to drive redox and light emitting reactions.

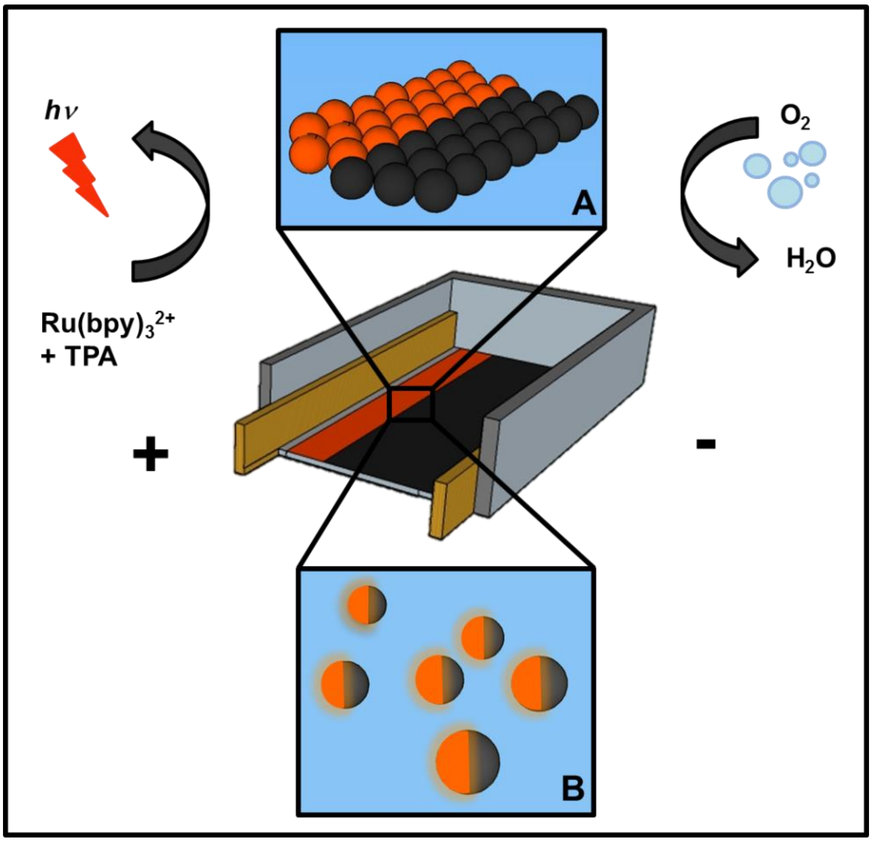

Figure 3.1: Schematic diagram showing the principle of bipolar electrochemiluminescence using a particulate carbon film. (A) Carbon particle loading is above the percolation threshold and the entire film becomes conducting and ECL can be generated at low electric field strengths. (B) Particles are electrically isolated from one another and ECL can only be generated at individual particles using intense electric fields.

3.2 RESULTS AND DISCUSSION

3.2.1 Structural Characterisation

3.2.1.1 Raman Analysis

Charge transport through assemblies of particles depends not only on their loading but also on their shape and chemical composition.[183] Raman spectroscopy is a promising tool to characterise the nature of the carbon particles and the degree of graphitisation within these films. Figure 3.2 shows the Raman spectra for carbon films acquired by using a 532 nm laser in the range 1000-3100 cm^{-1}. In this spectrum, two main Raman bands named "G" and "D" are observed. These bands are present in almost all carbon-based materials and are associated with sp^2 hybridisation.[184] The G peak at 1585 cm^{-1} is associated with the graphitic vibration mode and the D peak at 1340 cm^{-1} arises from structural defects and partially disordered structures.[185] In addition, two smaller peaks at 2670 cm^{-1} and 2920 cm^{-1}, named 2D and (D+G), can also be observed. The (D+G) peak is induced by the disorder in the film structure and the 2D peak originates from second order Raman scattering process and can be used to determine the number of layers of carbon particle in the film.[186] The narrowness of the 2D features suggests that this film most likely consists of a single microparticle layer. It should be noted that the Raman spectrum of the carbon films resembles that of commercial graphite.[187]

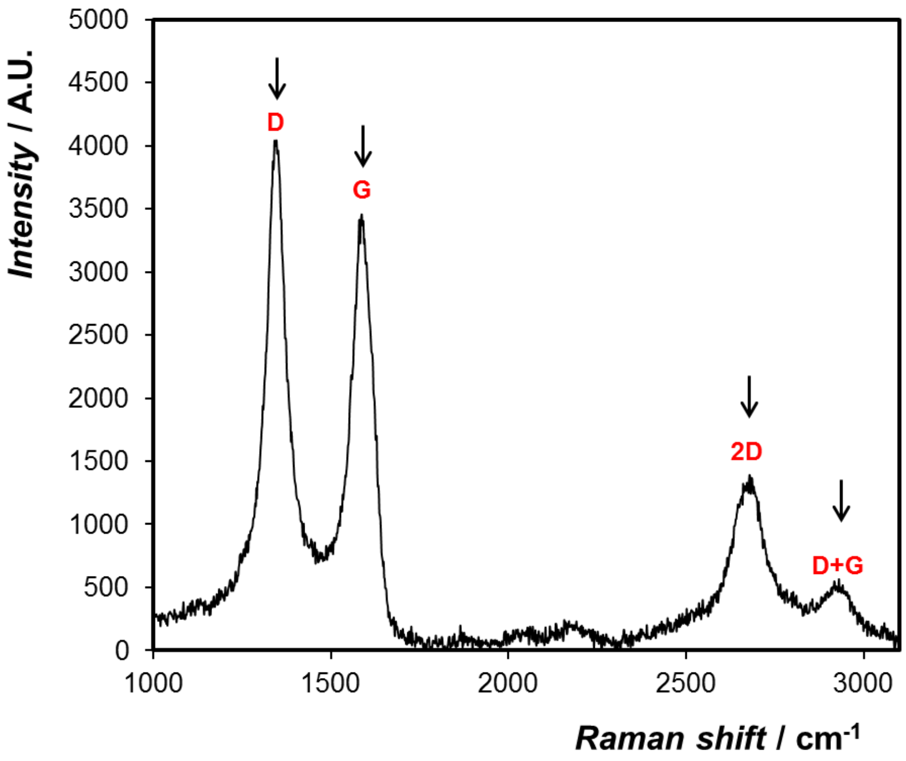

Figure 3.2: Raman spectra of carbon particle:nafion composite film where the particle loading is 98% carbon v/v. The excitation wavelength is 532 nm. The characteristic bands associated with graphite-type structures are highlighted.

3.2.1.2 SEM Analysis

Figure 3.3 shows SEM images of the carbon films and reveals that the particles are approximately spherical and that some agglomeration of the particles occurs within the films.[188] At low carbon particle loadings, charging is observed which is consistent with a relatively low film conductivity.[189] Overall, the films consist of a random array of particles in which the average separation between adjacent particles depends on the particle loading.

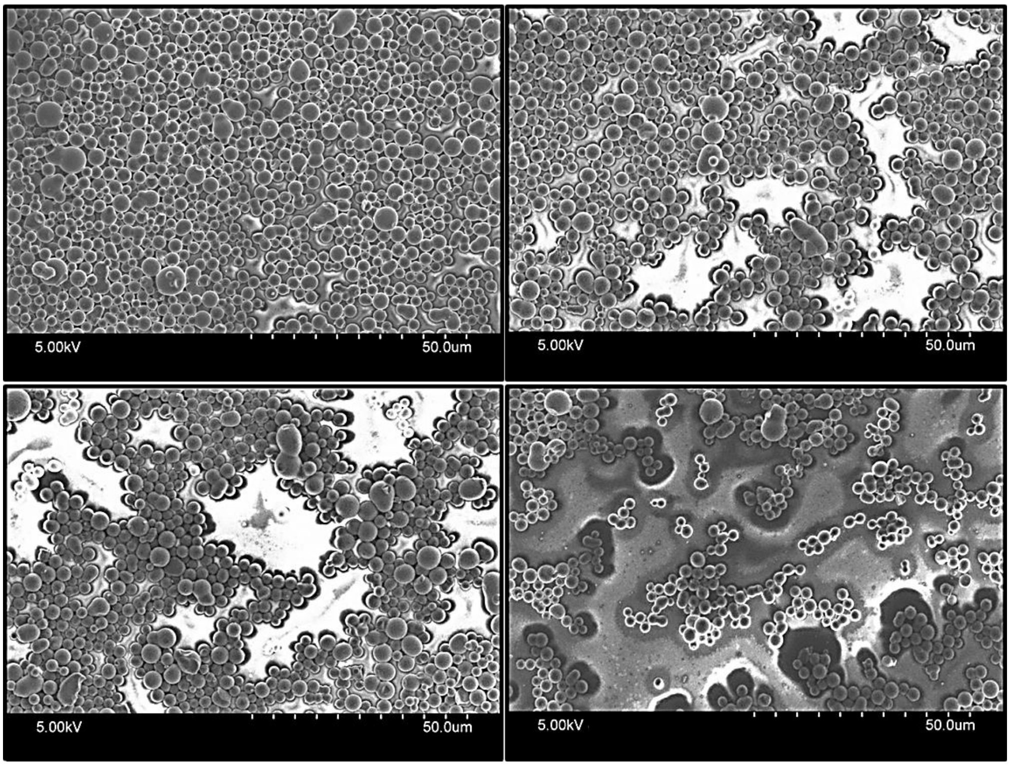

Figure 3.3: SEM images of the carbon particle-nafion composite films where, from top right to bottom left, the % carbon v/v is 88%, 69%, 64%, and 48%, respectively.

3.2.2 Electrochemical Performance

3.2.2.1 Voltammetry Studies

Cyclic voltammetry was used to determine the available potential window as well as the rate of heterogeneous electron transfer to the ECL dye, $[Ru(bpy)_3]^{2+}$. Figure 3.4 shows cyclic voltammograms for both glassy carbon and carbon film electrodes in 0.1 M H_2SO_4 as supporting electrolyte. The potential windows for the two electrodes are indistinguishable.[190,191] However, the capacitance for the carbon particle composite electrode is approximately 3.5 times lower than observed for the glassy carbon electrode. The reason for this behaviour might be that at high scan rates (in this case its 0.1 V s^{-1}) the electrolyte ions do not have enough time to diffuse completely inside the particulate carbon electrode to make use of its larger surface area, hence the capacitance is lower. Redox responses associated with surface oxygen groups that undergo proton coupled electron transfer reactions are evident in both electrodes at approximately 0.3 V.[192] The inset of Figure 3.4 illustrates the background corrected response in this region and reveals well defined oxidation and reduction processes[193] with peak-to-peak separations, ΔE_P, of approximately 170 mV and 150 mV for the glassy carbon and carbon film electrodes, respectively. The charge passed indicates that the surface coverage, Γ, of the oxygen functionalities is approximately $1.8 \pm 0.3\times10^{-11}$ mol cm^{-2} for the carbon particle film. This coverage is less than 10% of that expected for full monolayer coverage and is likely to be a significant over estimate since it is based on the geometric area of the electrode rather than the true microscopic area of the carbon particle electrode. These low coverages of oxygen functionalities are not expected to significantly influence the voltammetric properties.

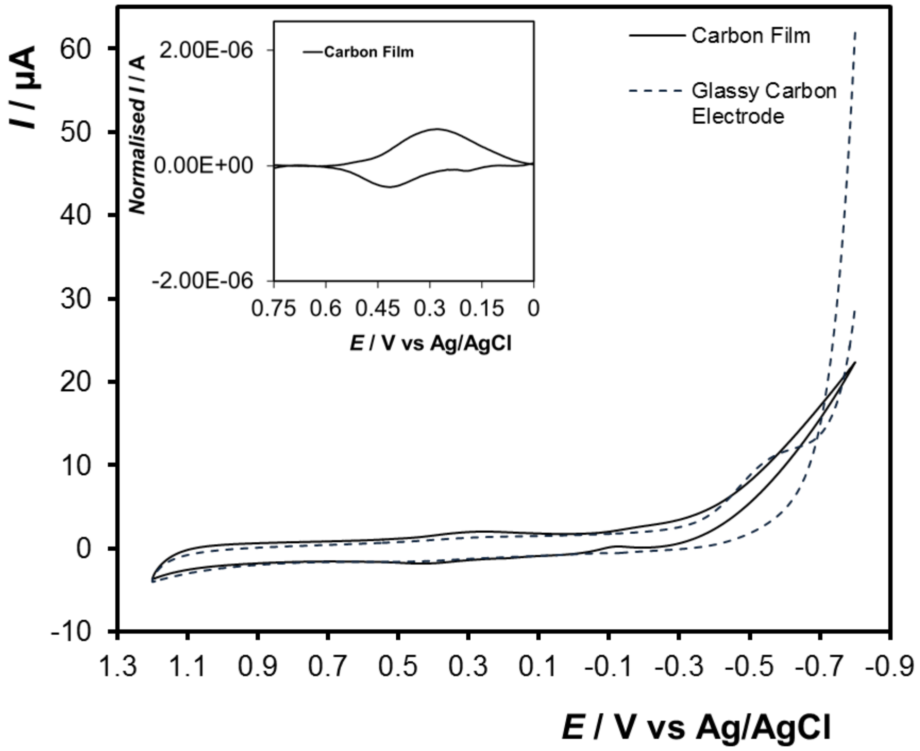

Figure 3.4: Cyclic voltammograms of a carbon:nafion composite film deposited on plastic where the carbon loading is 98% v/v (solid line) with active area of 0.25 cm^2 and a glassy carbon electrode (dashed line) with area of 0.071 cm^2 in 0.1 M H_2SO_4 at a scan rate of 0.1 V s^{-1}.

Figure 3.5 shows the voltammograms obtained for a 98% v/v loading carbon film in a 0.1 M PBS solution of 100 µM $[Ru(bpy)_3]^{2+}$. The film electrode shows well defined oxidation and reduction processes corresponding to oxidation of the $Ru^{2+/3+}$ centres at approximately +1.25 V (Figure 3.5A). The peak-to-peak separation, ΔE_P, is approximately 340 mV which could arise from either ohmic drop or slow heterogeneous electron transfer. Significantly, the solution resistance is approximately 250 Ω, which, in conjunction with the observed peak current, should give an ohmic drop of approximately 1 mV, that is, ohmic drop cannot explain the large ΔE_P observed. Figure 3.5B illustrates the theoretical voltammogram obtained under semi-infinite linear diffusion conditions. The best fit is obtained using a standard heterogeneous electron transfer rate constant, k^o, of $5x10^{-4}$ cm s^{-1} and an anodic transfer coefficient, α_a of 0.6. The best fit k^o is significantly lower than that reported previously for this complex at a glassy carbon electrode,[36] $1x10^{-2}$ cm s^{-1}, perhaps suggesting that heterogeneous electron transfer is slow at these particulate electrodes. However, while the model satisfactorily reproduces the peak potentials and currents, the general quality of the fit is not good with the theoretical response showing a significant diffusional tail not observed experimentally. The carbon particle composite is formed using nafion which is capable of entrapping cationic and anionic species and the particulate nature of the film could also cause the response to exhibit a finite diffusion type behaviour. Figure 3.5C shows the best fit voltammogram obtained under finite diffusion conditions where k^o is $8x10^{-2}$ cm s^{-1} and α_a is 0.6. This model satisfactorily reproduces the peak potentials and currents and the general overall shape of the experimental response. While the quality of the fit using the finite diffusion model is superior to the semi-infinite linear diffusion model, it appears that the experimental response shows mixed finite and semi-infinite linear diffusion control.

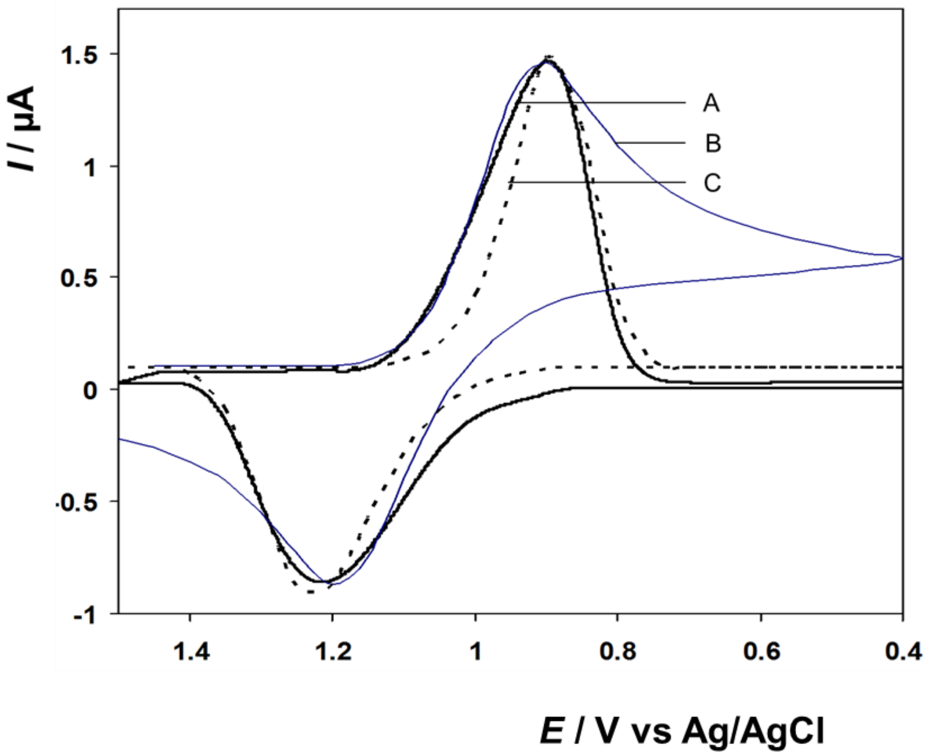

Figure 3.5: Solid black line, background corrected voltammogram of a 100 μM solution of $[Ru(bpy)_3]^{2+}$ dissolved in 0.1 M PBS at a 0.25 cm^2 carbon particle/nafion film electrode where the carbon loading is 98% v/v ((A) solid thick line). Best fit voltammograms modelled under semi-infinite linear diffusion ((B) solid thin line, $k^o = 5\times10^{-4}$ cm s^{-1}, $\alpha_c = 0.4$, $\alpha_a = 0.6$) and finite diffusion conditions ((C) dashed line, $k^o = 8\times10^{-2}$ cm s^{-1}, $\alpha_c = 0.4$, $\alpha_a = 0.6$). The scan rate is 0.1 V s^{-1}.

3.2.2.2 Electrochemiluminescence Studies

Conventional ECL was generated at the 98% v/v carbon film electrode by scanning the potential linearly from 0.2 V to 1.5 V in a solution containing 100 μM $[Ru(bpy)_3]^{2+}$ and 5.0 mM TPA dissolved in PBS. Figure 3.6 shows that ECL of $[Ru(bpy)_3]^{2+}$ is observed at potentials more positive than approximately +1.2 V with maximum intensity being observed at ≈+1.4 V, depending on the scan rate. The inset in Figure 3.6 shows that the ECL intensity decreases significantly with increasing scan rate before becoming less sensitive for the highest scan rates investigated. This observation suggests that the rate of production of $[Ru(bpy)_3]^{3+}$ by heterogeneous electron transfer significantly influences the overall light generating process especially at the higher scan rates. However, it is important to note that the pH within the nafion-carbon films is expected to be lower than the contacting pH of the electrolyte solution. This may have an effect on the TPA reactions. The radical intermediate $TPA^{\bullet}$ which is responsible for the generation of the excited state luminophore ($[Ru(bpy_3)]^{2+*}$) is a strong reducing agent, but due to the low pH within the nafion-carbon films the concentration of this deprotonated radical intermediate will be low and thus a decrease in ECL is possible. The protonated radical ($TPA^{\bullet+}$) does not have efficient energy to create the excited state.

Figure 3.6 also shows the best fit results (open squares) obtained by fitting the ECL response obtained at 0.05 V s^{-1} to the following model:

$$[\mathrm{Ru(bpy)_3}]^{2+} - \mathrm{e}^- \rightarrow [\mathrm{Ru(bpy)_3}]^{3+} \qquad \textbf{[3.1]}$$

$$\mathrm{TPA} - \mathrm{e}^- \rightarrow \mathrm{TPA}^{\bullet+} \rightarrow \mathrm{TPA}^{\bullet} + \mathrm{H}^+ \qquad \textbf{[3.2]}$$

$$[\mathrm{Ru(bpy)_3}]^{3+} + \mathrm{TPA}^{\bullet} \rightarrow$$

$$[\mathrm{Ru(bpy)_3}]^{2+*} + [(\mathrm{C_3H_7})_2\mathrm{N} = \mathrm{CHC_2H_5})]^+ \qquad \textbf{[3.3]}$$

$$[\mathrm{Ru(bpy)_3}]^{2+*} \rightarrow [\mathrm{Ru(bpy)_3}]^{2+} + h\nu \qquad \textbf{[3.4]}$$

The best fit parameters for the standard heterogeneous electron transfer rate constants, k°, for steps 1 and 2 are 5×10^{-4} cm s^{-1} and 1×10^{-6} cm s^{-1}, respectively, and the rate of step 3 is 1×10^{5} M^{-1} s^{-1}. For the scan rates investigated, the modelled response is insensitive to the rate of the homogeneous reaction provided it is greater than 10^{5} M^{-1} s^{-1}, that is, the rate of this highly exergonic reaction is not rate limiting. Significantly, the value of k^{o} obtained for the Ru^{2+}/Ru^{3+} couple from fitting the voltammetry (Figure 3.5) and ECL data (Figure 3.6) are indistinguishable. The values of k° were optimised for the 0.05 V s^{-1} and the 0.01 V s^{-1} responses; model data is generated using no freely adjustable parameters. The response predicted for a scan rate of 0.01 V s^{-1} with no freely adjustable parameters is acceptable, but the ECL onset potential is approximately 100 mV more positive than that observed experimentally. This behaviour most likely arises from a distribution of heterogeneous rate constants, perhaps at discrete particles or regions of individual particles, which make a relatively larger contribution to the observed response at the higher scan rate. Overall, in conventional ECL experiments these carbon films exhibit excellent electrochemical behaviour and have properties that could be interesting for application as bipolar electrodes.

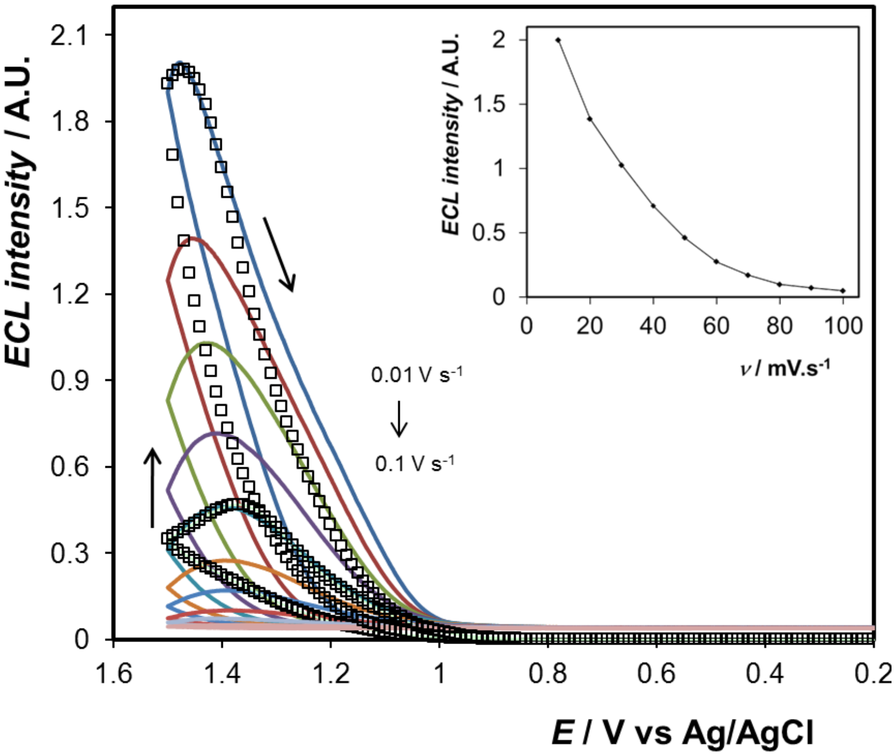

Figure 3.6: Conventional ECL generated at the 98% carbon v/v film electrode in 0.1 M PBS containing 100 μM $[Ru(bpy)_3]^{2+}$ and 5.0 mM TPA solution. From top to bottom at +1.4 V, the scan rates are 0.1, 0.09, 0.08, 0.07, 0.06, 0.05, 0.04, 0.03, 0.02, and 0.01 V s^{-1}. The potential was linearly scanned from 0.2 to 1.5 V as indicated by the arrows. The open squares are best fit response to the model described by equations 1−3, where standard heterogeneous electron transfer rates, k^o, for oxidation of $[Ru(bpy)_3]^{2+}$ and TPA are 5×10^{-4} cm s^{-1} and 1×10^{-6} cm s^{-1}, respectively, and the rate of reaction of $[Ru(bpy)_3]^{3+}$ and the TPA radical is 1×10^{5} M^{-1} s^{-1}. The inset shows the dependence of the maximum ECL intensity on the scan rate. Voltage of the photomultiplier tube was biased at -850V.

3.2.3 Conductivity

The possibility of controlling the electrical characteristics of polymers by systematically varying the loading of particles is important for a range of applications ranging from molecular electronic devices to sensors.[183,194] When microparticles of conductivity σ_n are blended with a polymer having a conductivity σ_p to a loading, φ, the conductivity of the resulting composite, σ, typically increases dramatically.[195] Specifically, when the percolation threshold, φ_c, is reached a pseudo-infinite conductive cluster is formed and the composite may become highly conducting. As the particle loading increases from φ_c to the limiting value F, the conductivity of the nafion-carbon particle composite increases by several orders of magnitude, from the value σ_c at the percolation threshold to the maximal value σ_m.[196] Below the percolation threshold, the conductivity does not change appreciably with increasing loading and the conductivity of the composite is similar to the polymer conductivity, σ_p, or slightly higher. To a first order approximation, the dependence of the conductivity on the carbon particle loading can be described by Equation 3.5:

$$\sigma = \sigma_p + (\sigma_m - \sigma_c)[(\varphi - \varphi_c)/(F - \varphi_c)]^t \qquad \textbf{[3.5]}$$

where t is the critical exponent and is typically between 1.6 and 1.9 depending on the dimensionality of the system.

Figure 3.7 (○ axis to right) illustrates the dependence of the composite electrical conductivity on the volume fraction of the carbon particles. The solid curve represents the best fit of Equation 3.5 to the experimental data. It should be noted that it is not possible to generate a best fit curve representative of the experimental electrical conductivity results at low carbon loadings. This is because below the percolation limit the conductivity of the composite is given by the conductivity of the matrix and that is why the straight line can be observed at low loadings. The conductivity increases sharply when the volume percentage is 71 ± 8% suggesting that this is the percolation threshold and that above this loading an electrically connected network of particles exists. This result, taken with the SEM images shown in Figure 3.3 indicates that for loadings less than this percolation threshold, the carbon particles exist as localised aggregates that are not interconnected from one side of the film to the other. Significant electrical conductivity is only observed for the highest loading, giving a high percolation threshold. The conductivity critical exponent is supposed to depend solely on the dimensionality of the network and to be independent of the composition of the matrix. For 2D arrays, an exponent of approximately 1.3 is expected but for 3D systems that value expected is higher, approximately 2.0.[197] The value of the critical exponent, t, observed in this work is significantly higher, 3.8. Large t values have been reported previously[198,199] and assumed to be associated with contributions from tunnelling conductivity or complicated conduction pathways through the composite. In the present case, it most likely arises because of specific interactions between the nafion and the surface of the carbon particles. Specifically, the formation of extended, closely packed agglomerates that can interact with many nearby neighbours can give long range conductivity and narrow the critical regime giving rise to mean-field behaviour where an exponent of 3 is expected.[200]

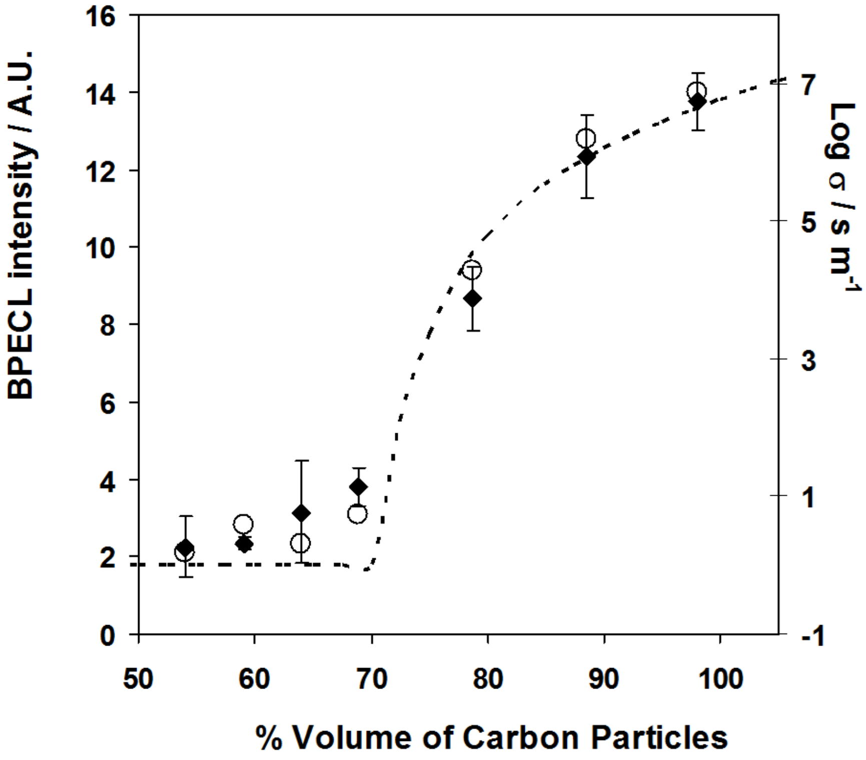

Figure 3.7: Dependence of the bipolar ECL intensity (⧫ axis to left) and the film conductivity (○ axis to right) on the % carbon v/v in carbon/nafion composite films. The bipolar ECL was generated using 5.0 mM $[Ru(bpy)_3]^{2+}$ and 25.0 mM TPA dissolved in ultrapure water (no deliberately added electrolyte), at a fixed theoretical applied electric field of 18 V cm^{-1}. The error bars represent the standard deviation (n = 3 for each point).

3.2.4 BPE/ECL

Figure 3.1 illustrates an open BPE configuration used to study the effect of inter-particle separation on the intensity of the electrochemiluminescence generated. The potential between the gold feeder electrodes was varied from 0 to 15 V giving a maximum theoretical electric field (V_0) of approximately 20 V cm^{-1} across the 0.5 cm wide carbon BP_{elec}. However, even in the absence of deliberately added electrolyte, a fraction of the total potential difference drops exponentially close to the surface of the feeder electrodes. For the current system, even when a fully electronically conducting electrode is used as the bipolar electrode, an external voltage difference of a minimum of 7 V was needed to drive electrochemiluminescence from the $[Ru(bpy)_3]^{2+}$/TPA system at the anodic end and simultaneous reduction of oxygen at the cathodic end.[116] Figure 3.8 shows the relation between the driving voltage and the ECL intensity. Here, the value obtained with a concentration of 0 mM TPA was defined as background. The ECL intensity increased with an increase in the driving voltage from 7 to 9 V. The ECL intensity reached plateau when the driving voltage was 11 V. However, when the driving voltage was higher than 11 V, ECL signals decreased. It has been reported that a high driving voltage can initiate background reactions, such as the oxidation of water on the anode of a BP_{elec}, and subsequently leads to the formation of oxygen that both chemically and physically interferes with ECL emission.[201] Thus, a driving voltage of 10 V was selected to carry out light emitting experiments.

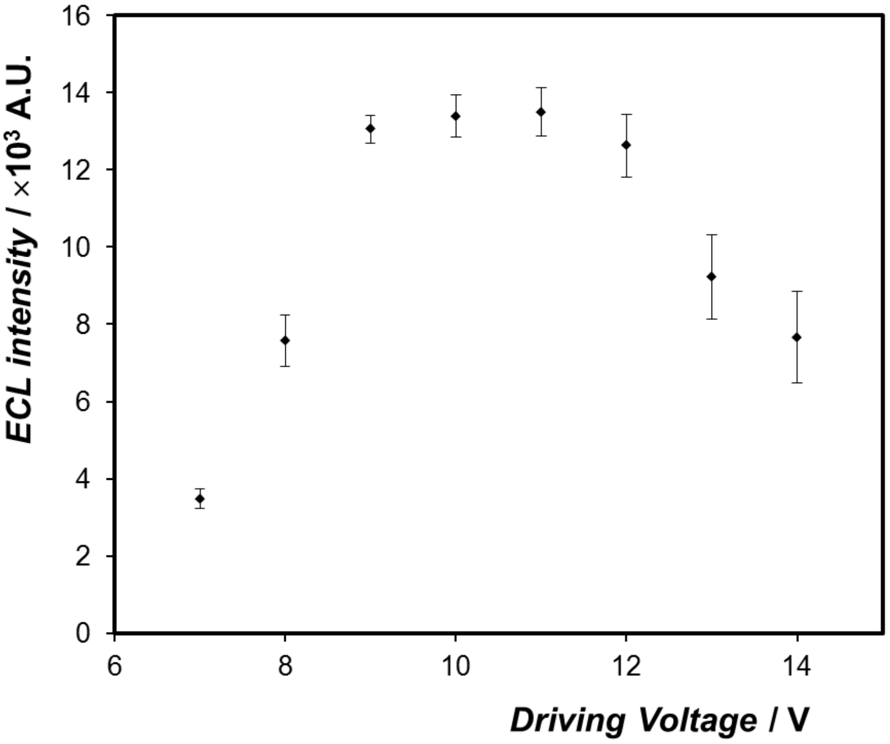

Figure 3.8: Calibration curve for variation of the ECL intensity as a function of the electric field applied between two feeder electrodes for the 98% carbon v/v film electrode, the driving voltage (E_{tot}) ranged from 7 to 14 V. The error bars represent the standard deviation (n = 3 for each point).

Figure 3.7 (♦ axis to left) shows the dependence of the overall ECL intensity on the loading of carbon particles, while Figure 3.9 shows images of the spatial distribution of the ECL response. For low volume fractions of carbon particles (<60%) the bipolar ECL intensity is low because the particles are predominantly isolated from one another, i.e., there are relatively few interconnections that span the entire film so as to allow $[Ru(bpy)_3]^{2+}$ and TPA to be oxidized at one side and oxygen reduced at the other. At the low particle loadings, ECL is only generated in those regions where the particles aggregate to give a conducting structure that is large enough to generate a potential difference that can drive both coupled reactions. As the volume fraction increases, more interconnections exist and the particulate electrode begins to act as a monolithic conductor. The total light intensity for all loadings is reproducible because the overall quantity of carbon particles for each loading was kept constant.

Significantly, Figure 3.7 (♦ axis to left) indicates that the ECL intensity shows a similar dependence on the carbon particle loading as the conductivity (Figure 3.7 (○ axis to right)). Theoretically the light emitting region for a 0.5 cm wide fully conducting BP_{elec} should be ~2.5 mm. Here, the width of the light emitting region is ~1.75 mm and it is statistically indistinguishable for loadings >60% and <90% but is approximately 30% wider for the 98% carbon film (Figure 3.9). At the highest loading, the response is indistinguishable from that observed at a conventional monolithic glassy carbon electrode. Since the electric field strength is kept constant for all experiments, this increase in the emitting area most likely arises from a reduced ohmic drop across the width of the electrode at a high loading. At lower loadings <60% the width as well as the intensity of the light emitting region changes and this is because the carbon film is not fully conducting.

These results suggest that bipolar electrodes can be constructed using particles as building blocks and that the ECL intensity can be controlled through the average inter-particle separation.[202]

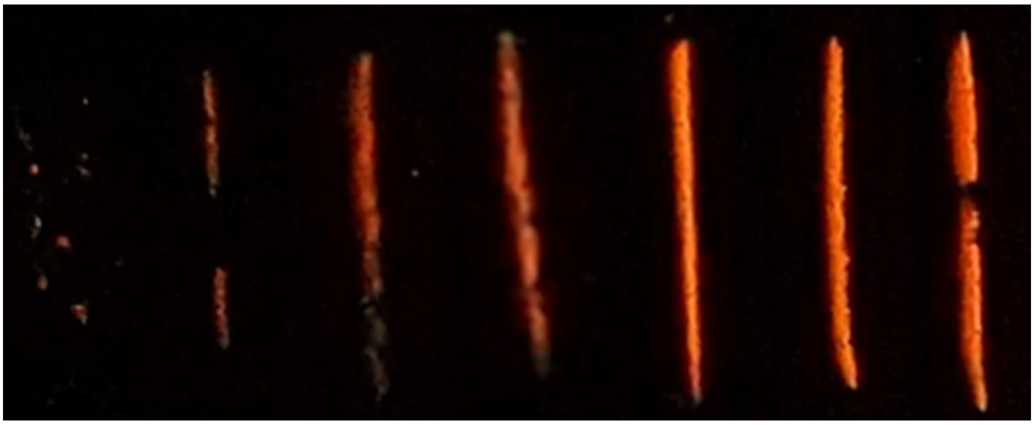

Figure 3.9: Images of the spatial distribution of the bipolar ECL as a function of the carbon loading of the film. From left to right, the loadings are 54, 59, 64, 69, 78, 88, and 98%, respectively. The total applied potential, E_{tot}, was set to 10 V.

3.2.5 Carbon Film Modification

To further demonstrate the use of carbon films as electrodes in electrochemical processes, their electrochemical properties by surface modification was investigated. Electropolymerization of PANI was performed on the 59, 64, 69, 78 and 88% v/v carbon film electrodes. The cyclic voltammograms seen in Figure 3.10A represents the last cycle (30th cycle) of the electropolymerization process for each carbon film electrode. It is evident from Figure 3.10A that no visible peak characteristic of PANI is present at the 59% carbon film electrode (low particle loading). As the % carbon v/v in carbon/nafion composite films increased, an increase in growth of PANI was observed. For this reason, the highest particle loading film of 98% v/v was considered.

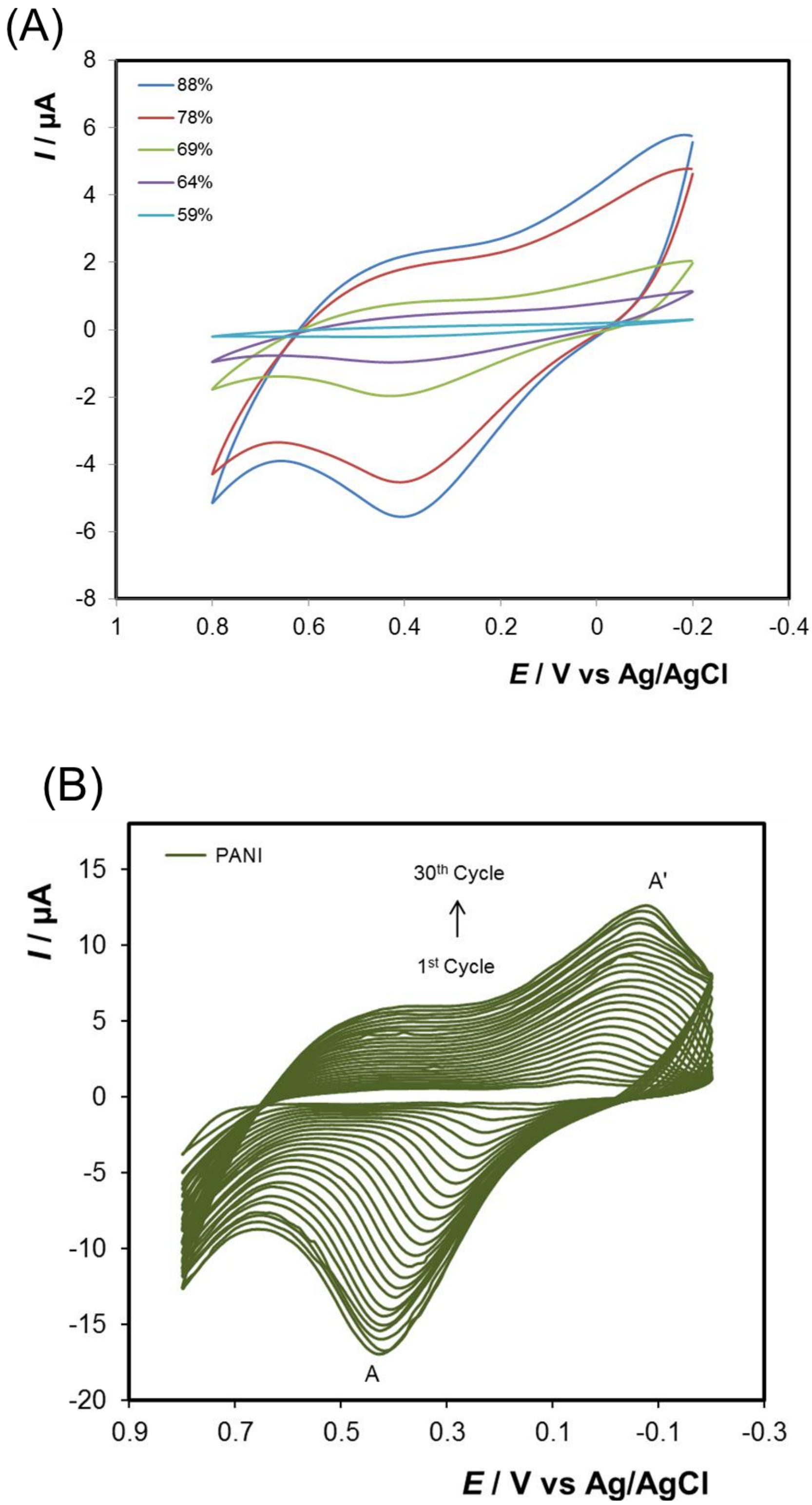

Figure 3.10: Electrodeposition of PANI at (A) 59, 64, 69, 78, 88% carbon films, and (B) 98% carbon film electrode. The potential was scanned between -0.2 and +0.8 V, at 0.02 V s^{-1}.

Figure 3.10B shows electrodeposition of PANI at the 98% v/v carbon film electrode. Here, a gradual current increase with successive polymerization cycles is noticeable and a pair of redox peaks can be observed. Furthermore, there is a slight shift in peak potentials with successive scanning. After the electrodeposition process, the PANI modified carbon electrode was rinsed and cycled between -0.2 and +0.8 V in fresh H_2SO_4 electrolyte solution. Figure 3.11 shows the resulting voltammogram overlaid with the voltammogram of unmodified carbon electrode obtained under the same scanning conditions. From these voltammograms, it is evident that only one redox couple for PANI is present at cathodic peak potential, $E_{p,c}$ (denoted by A’), of ≈ 0.08 V (due to the leucoemeraldine) and anodic peak potential $E_{p,a}$ (denoted by A), of ≈ +0.45 V (due to emeraldine state- the most conductive form of PANI).[203] The peak potentials observed for the PANI voltammogram are similar to those previously reported in H_2SO_4,[204,205] suggesting that PANI was successfully electrodeposited on the carbon film electrode. However, the conversion of emeraldine to pernigraniline salt at about $E_{p,a}$ of ≈ +0.75 V, cannot be clearly identified.

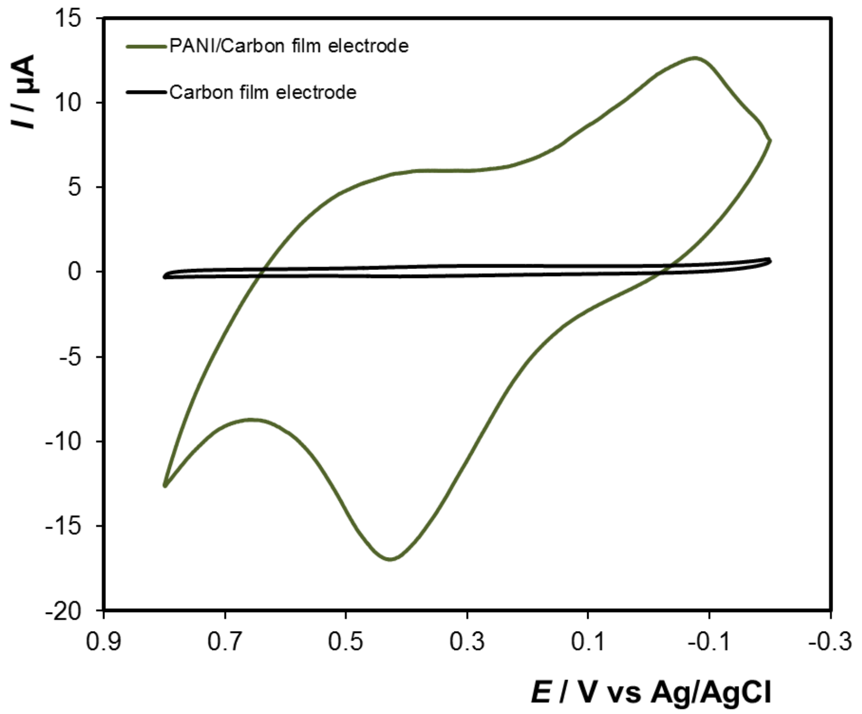

Figure 3.11: Cyclic voltammograms of unmodified carbon film electrode (black line) and PANI/carbon film electrode (green line) cycled between -0.2 to +0.8 V, in 0.1 M H_2SO_4, at a scan rate of 0.1 V s^{-1}.

An understanding of the electrochemistry and corresponding mechanism of film formation of PANI is difficult because of the complicated reaction kinetics involved in the electro-oxidation of aniline. For this reason, the structural characteristics of the PANI modified carbon electrode were investigated by Raman. Figure 3.12A shows the Raman spectrum of the PANI exhibiting bands at 1162, 1338, 1507 and 1597 cm^{-1} which corresponds to C-H bending of the quinoid ring, $C\text{-}N^{+\bullet}$ stretching of the bipolaron structure, N-H bending of the bipolaronic structure and C-C stretching of the benzenoid ring, respectively.[206] Other bands observed at 412 and 530 cm^{-1} are out of plane deformations of the ring,[207] while 833

cm^{-1} are due to the benzene ring deformations. The Raman spectrum of PANI at different % v/v carbon film electrodes was also recorded (Figure 3.12B). Interestingly, the 59% carbon film electrode appears to have PANI present on its surface even though during electrochemical characterisation PANI peaks were not visible at the 59% carbon film electrode. Table 3.1 illustrates comparative Raman assignments of the carbon film electrode and the PANI modified carbon film electrode.

Table 3.1: Raman vibrational modes of Carbon and PANI spectra.

Sample	Raman band (cm^{-1})	Assignment
Carbon	~1340 ~1585	Graphitic vibration Sp^2 hybridisation and structural defects
PANI	~412 ~530 ~833 ~1162 ~1338 ~1507 ~1597	Out of plane ring deformation Out of plane ring deformation Benzene ring deformation C-H bending C- N stretching N-H bending C-C stretching

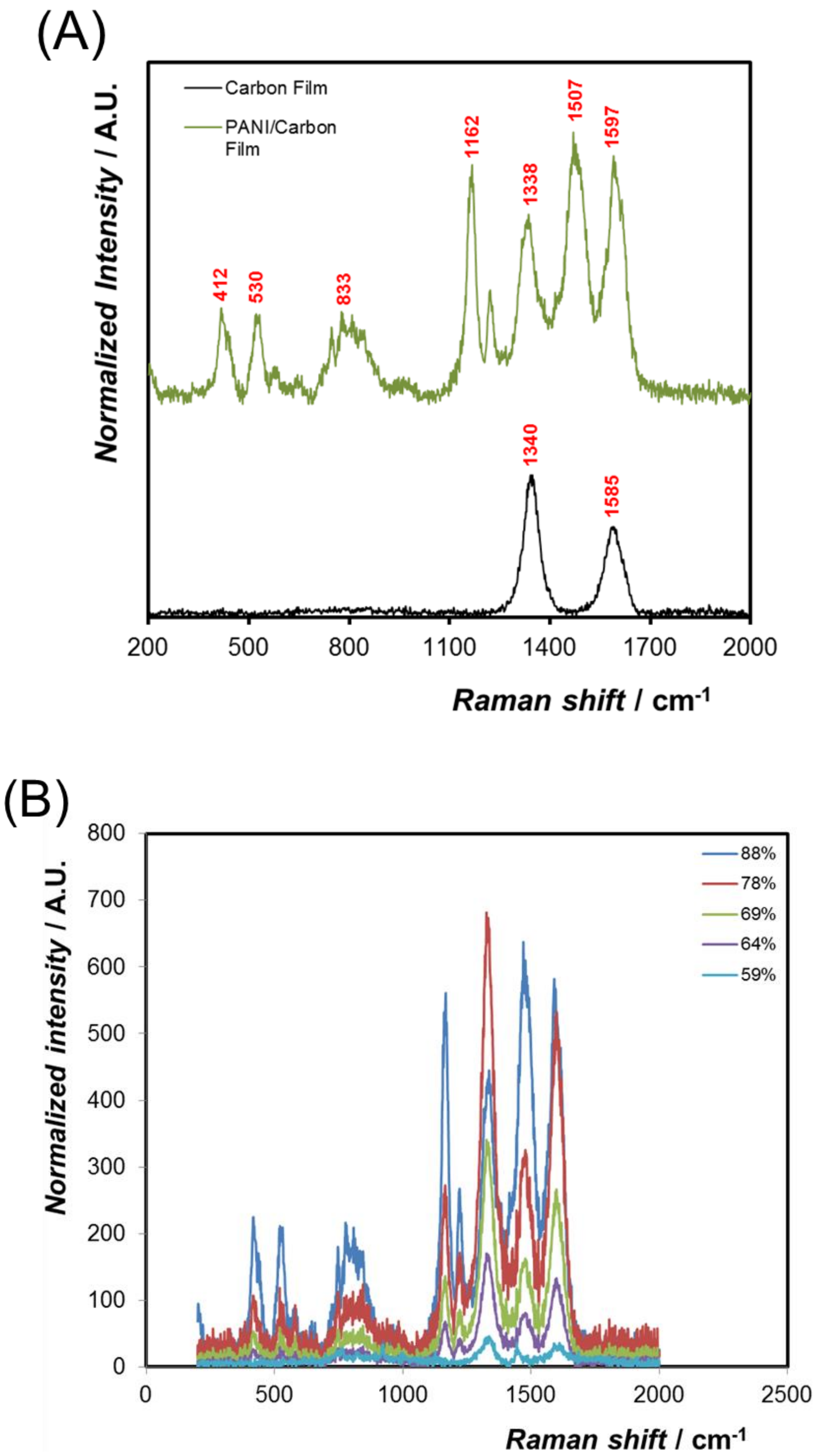

Figure 3.12: Shows (A) Raman spectrum of carbon film electrode (black line) and PANI modified carbon film electrode (green line), and (B) PANI

Raman band characteristics at the 59, 64, 69, 78 and 88% carbon films. The samples were excited at 633 nm.

Moreover, scanning electron microscopy was carried out to help draw a conclusion about the growth of PANI. Figure 3.13 illustrates SEM micrographs of the 98% carbon film electrode with PANI deposits spread across the surface. It seems that little polymerization occurs at the 98% carbon film electrode surface. It is assumed that during the polymerization of PANI, aniline monomers are adsorbed on the surface of the carbon particles via π–π conjugation and chemical bonding effects,[208] The PANI appears to be aggregates formed randomly and non-uniformly on a small number of active sites (in this case on a few carbon particles). It's said that experimental conditions such as the electropolymerisation method, electrode material, electrolyte composition, and the pH of the electrolyte, all have a strong influence on the nature of the polymerisation process, morphology, and the growth rate of PANI.[209]

The SEM results are in agreement with the electrochemical and structural characterisation data of PANI. The ability to modify the fabricated particulate electrodes opens up the possibility to be utilised in a wide range of applications such as rechargeable power sources, electrochemical capacitors and sensors.[209] The utilisation of PANI based carbon electrodes demonstrates high conductivity coupled with excellent flexibility. However, the utilisation of such systems in electrochemical setups is highly dependent on the PANI morphology.[210] Agglomerate morphologies of PANI (as seen in Figure 3.13) usually lead to the inefficient utilisation of PANI. For this reason, further work is necessary to obtain controlled progressive nucleation of PANI. BPE would be an interesting choice for electropolymerization of PANI in a controlled manner.

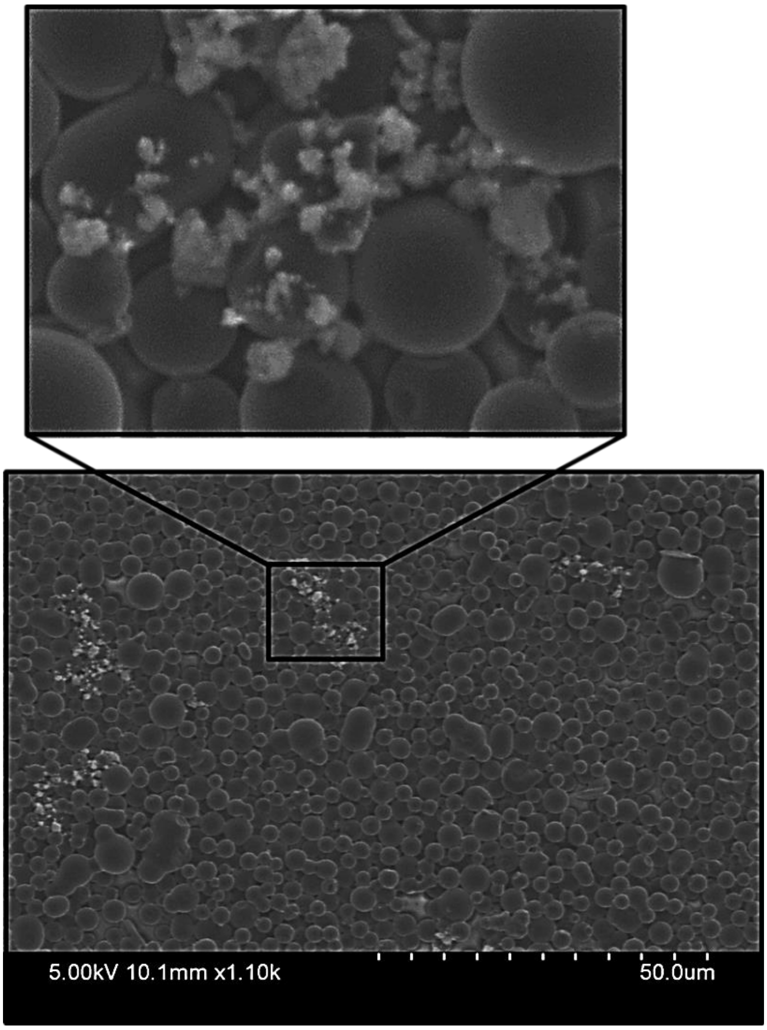

Figure 3.13: SEM micrograph of carbon film electrode covered with PANI formed by electropolymerization of aniline, at 50 µm scale view with a zoomed in micrograph of PANI deposits.

3.3 CONCLUSION

Here, carbon thin films were successfully fabricated by a simple and cheap custom-built spin coater. Surface characterisation was carried out using Raman and SEM. The results revealed that the carbon particles retained its spherical shape and that the carbon film consists of a single microparticle layer. The electrochemical properties of the nafion-carbon composites, including heterogeneous electron transfer rates, were probed using cyclic voltammetry, and its electrochemical performance was compared to that of a conventional glassy carbon electrode. The results revealed that the potential windows for the two electrodes are indistinguishable. Surface modification of the carbon film electrodes was possible by electropolymerization of aniline. In addition, the electrical characteristics (conductivity) of the carbon-nafion composite were controlled by varying the carbon particle loading. Conventional and bipolar electrochemiluminescence were generated at the polymer-carbon particle composite. The intensity of bipolar electrochemiluminescence correlates with the conductivity of the film and increases significantly from $<6 \times 10^3$ S m^{-1} to $2.0 \pm 0.1 x 10^7$ S m^{-1}, once the percolation limit of 71 ± 8 is reached.

These results are important because it gives insights into how particles can be used as “building blocks” for the construction, or self-assembly, of miniaturised electrodes. The combination of the percolation phenomenon and bipolar electrochemistry opens up new possibilities with respect to developing wireless micro-electromechanical systems and flexible sensing strategies at particulate level.

4 Chapter 4:

Electron Transfer and ECL Properties of 3D Titanium Electrodes

4.1 INTRODUCTION

Three-dimensional (3D) electrodes offer significant advantages in areas such as highly sensitive electrochemical analysis, electronic devices[211] and energy storage devices.[212] In particular, 3D electrodes can be highly beneficial for understanding the electrochemical properties of biological systems where the organisation of components in 3D directly affects their function and transport properties.[213–215] Moreover, 3D electrodes can have enhanced properties due to unique combinations of radial transport to the electrode tips while linear diffusion dominates transport to the side walls. By taking advantage of their hierarchical structures in the vertical dimension higher Faradaic currents may be observed.[216] Furthermore, generator-collector type experiments may be possible in 3D due to the short diffusion distance.[217] 3D architectures can be conveniently fabricated *via* 3D-printing or additive manufacturing (AM).[218,219]

In this study, the electrochemical and electrochemiluminescence properties of a 3D-printed titanium alloy structure (supplied by Prof. Gordon G. Wallace group, Intelligent Polymer Research Institute, ARC Centre of Excellence for Electromaterials Science, UOW) were investigated. Selective laser melting (SLM) [220,221] technique was used to produce the 3D-printed architectures. The SML additive manufacture approach uses a high power laser to incrementally melt and fuse thin layers of metal powder to create a custom electrode according to a pre-designed CAD file. Here, microscopy, EDX and cyclic voltammetry have been used to characterise the 3D-printed electrodes, especially the surface roughness and the impact of the electrode geometry and composition on the voltammetric response is assessed. The ability to electrodeposit gold onto the 3D-printed electrodes without significant "shadowing" by adjacent 3D-printed electrode pillars was also demonstrated. This approach is attractive since a "scaffold" can be 3D-printed and then modified to optimise the properties for particular applications. Significantly, ECL allows the diffusion fields to be imaged and reveals that radial mass transport to the tips of the individual pillars generates the brightest emission. The combination of high resolution 3D-printing followed by electrodeposition of a different metal opens up the possibility of creating structures with interesting properties, e.g., plasmonically enhanced ECL, where both the electrode structure and composition influence the voltammetric response.

4.2 RESULTS AND DISCUSSION

4.2.1 Structural Characterisation

4.2.1.1 SEM

The properties of the 3D-printed electrode depend on its macroscopic properties, e.g., the post thickness and separation, as well as the surface composition and topography, e.g., the surface roughness. Therefore, SEM was used to image the 3D-printed electrodes produced. Figure 4.1 displays cross-sectional SEM images, obtained from secondary electrons, of the 3D titanium (Ti) electrode array. Here, the average length and diameter was found to be 0.3 cm and 0.03 cm, respectively. Also, breakage of some pillars is visible (Figure 4.1). Breakage of these pillars occurred during the mounting of the 3D structure onto the SEM stub.

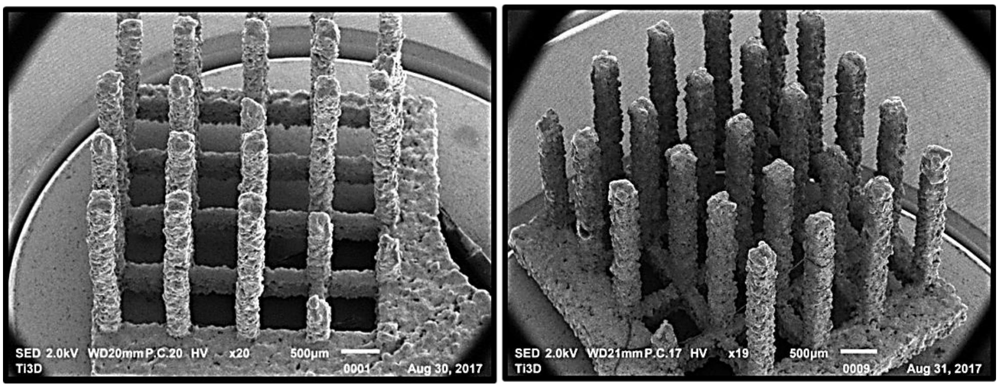

Figure 4.1: Shows cross-sectional SE-SEM images of the 3D-printed titanium electrode array fabricated by a simple additive manufacturing technique.

Figure 4.2A shows FE-SEM micrographs of one of the pillars of the 3D Ti electrode array. This figure reveals that the SLM fabrication process produces a rough surface consisting of fused titanium grains. The roughness extends from the nano to 100 µm length scales. In SEM micrographs obtained from backscattered electrons, heavier elements (higher average atomic number) produce brighter images because more primary electrons are scattered back out of the sample.[167] Thus, they can provide useful insights into compositional differences within a sample.[222] Figure 4.3A shows backscattered SEM images of the Ti 3D electrodes consisting of dominant brighter regions (most likely Ti) and darker regions perhaps suggesting other materials, such as oxides or binders for the laser based deposition, may be present.

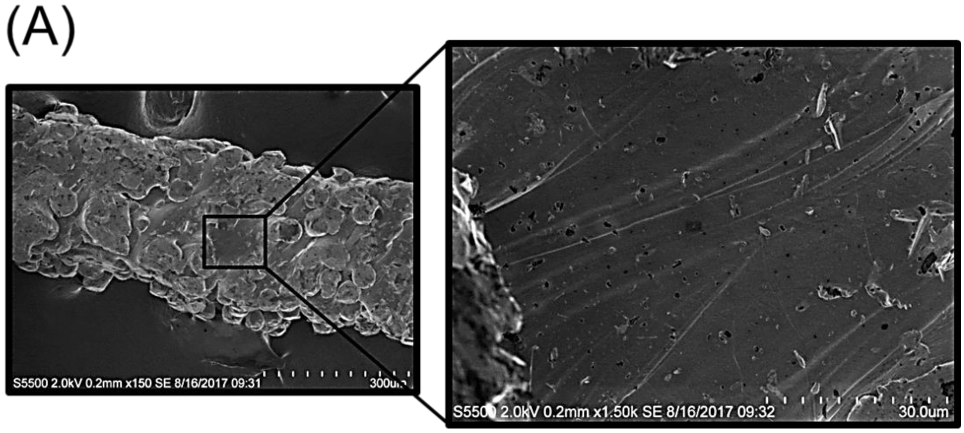

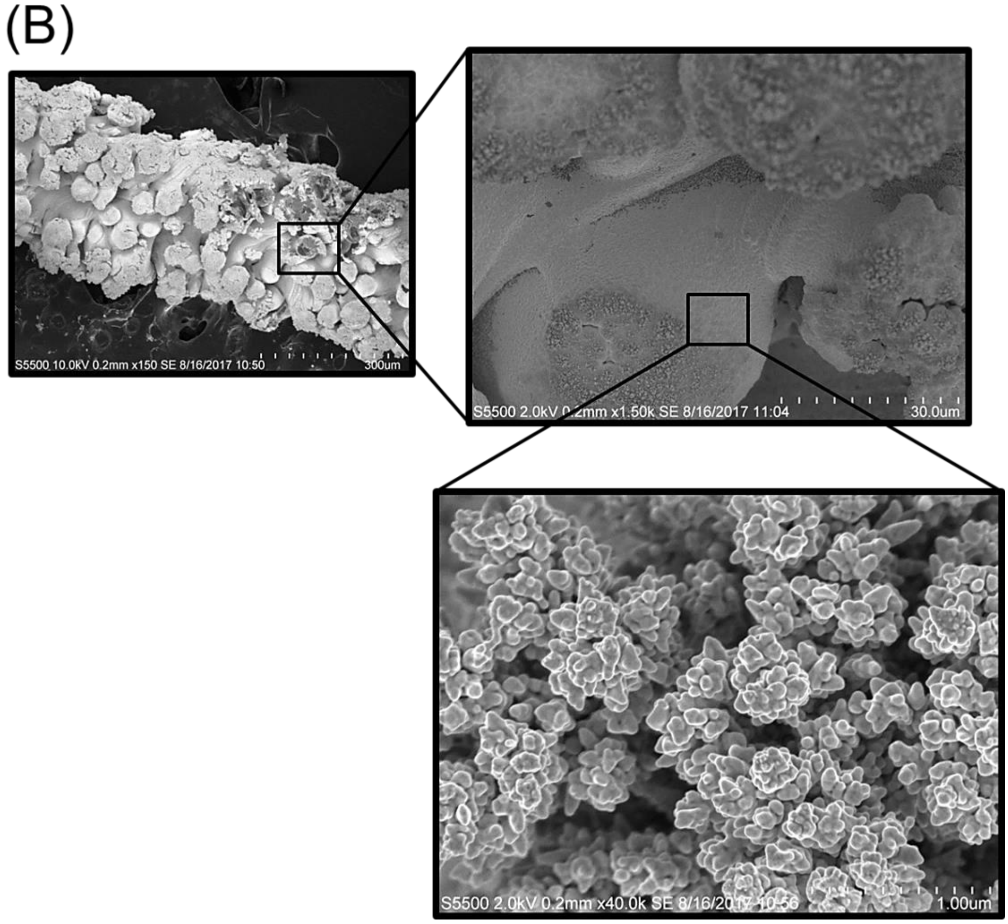

Figure 4.2: Secondary electrons FE-SEM micrographs showing (A) 3D Ti and (B) 3D Au-coated Ti electrodes, at low and high magnifications, using accelerating voltages that range from 2-10 kV, respectively.

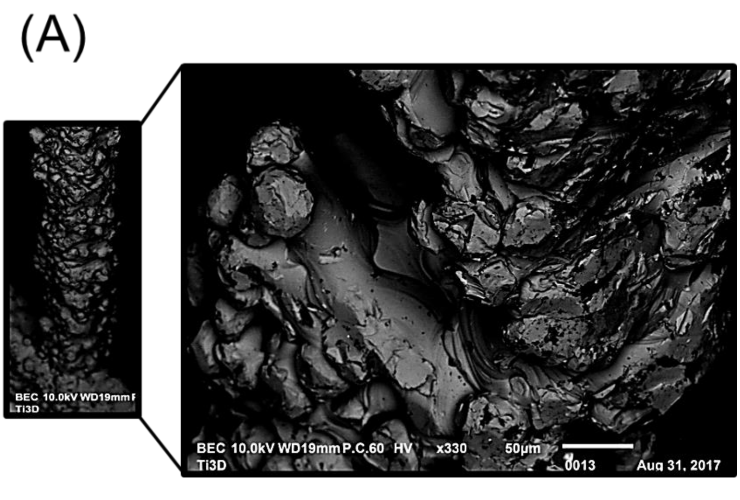

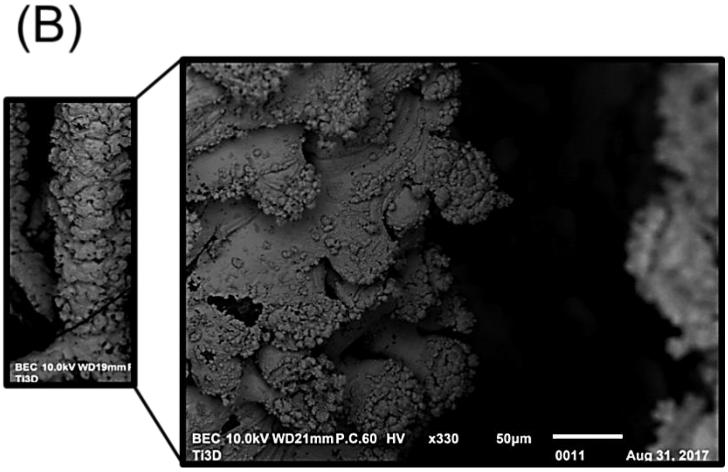

Figure 4.3: Backscattered SEM images showing topography/surface roughness and the compositional differences (material contrast) between the (A) 3D Ti and (B) 3D Au-coated Ti electrodes, at low and high magnifications, using a 10 kV accelerating voltage. Heavier Au atoms (B) scatter more electrons back towards the detector than the lighter Ti atoms (A) and therefore appear brighter in contrast in SEM image.

4.2.1.2 EDX Analysis

EDX was used to probe the elemental composition of the electrodes.[223] Figure 4.4A shows that the EDX spectrum is dominated by peaks associated with Ti, but carbon peaks are also present due to adventitious impurities. Aluminium and vanadium are also observed and are components of the powder used to create the 3D-printed electrodes.

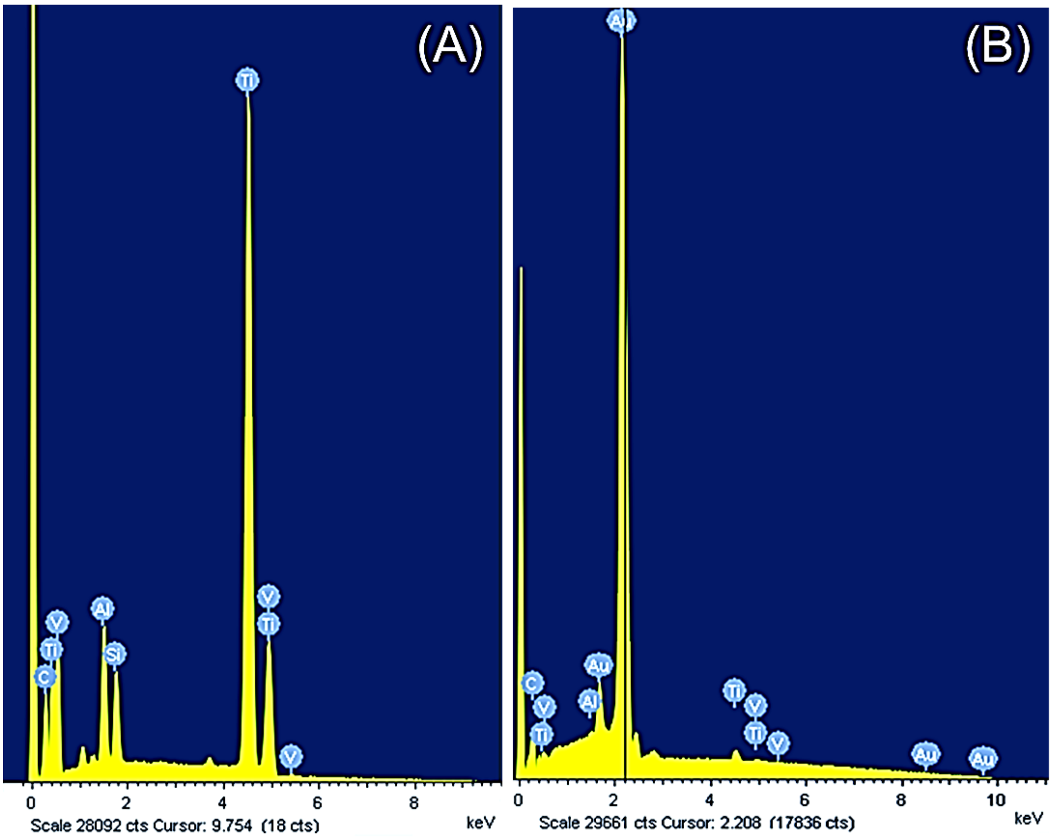

Figure 4.4: FE-SEM coupled EDX spectrum showing the elemental composition of the 3D Ti electrode (A) and 3D Au-coated Ti electrode (B), respectively. Signal Intensity of the Au modified 3D Ti electrode suggests packed Au distribution.

4.2.2 Electrochemical Performance

4.2.2.1 Voltammetry

Electrochemistry can provide deep insights into the composition of the 3D-printed structures as well as their interfacial properties and suitability for use as electrodes. Thus, cyclic voltammetry was used to determine the available potential window and to gain an insight into the electrochemically active area of the 3D Ti electrodes and hence their surface roughness. While recognising that Ti is generally stable at negative potentials,[224] the background electrochemical properties of the 3D-printed electrodes across a wide potential range was investigated.

Figure 4.5A shows the results obtained for a voltammetric scan from +0.2 V to +1.5 V in 0.1 M H_2SO_4, at 0.1 V s^{-1}. Significantly, no redox peaks are observed and the background currents are low for potentials less than approximately +1.2V. Figure 4.5B shows the response obtained between +0.5 V to -0.5 V in 0.1 M H_2SO_4, at 0.1 V s^{-1}. The background current increases only for potentials more negative than approximately -0.4 V due to water reduction.

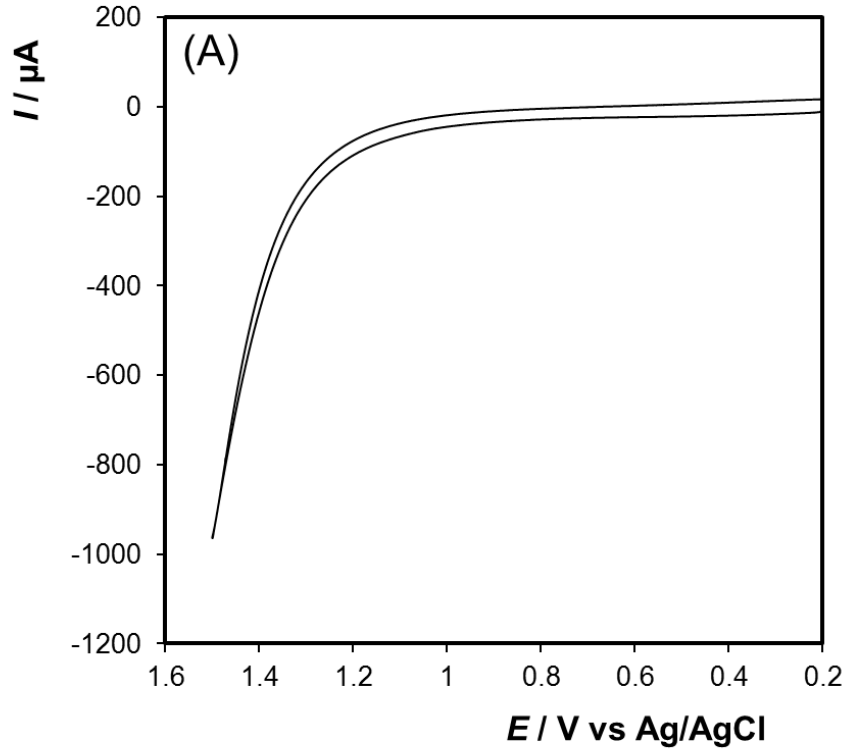

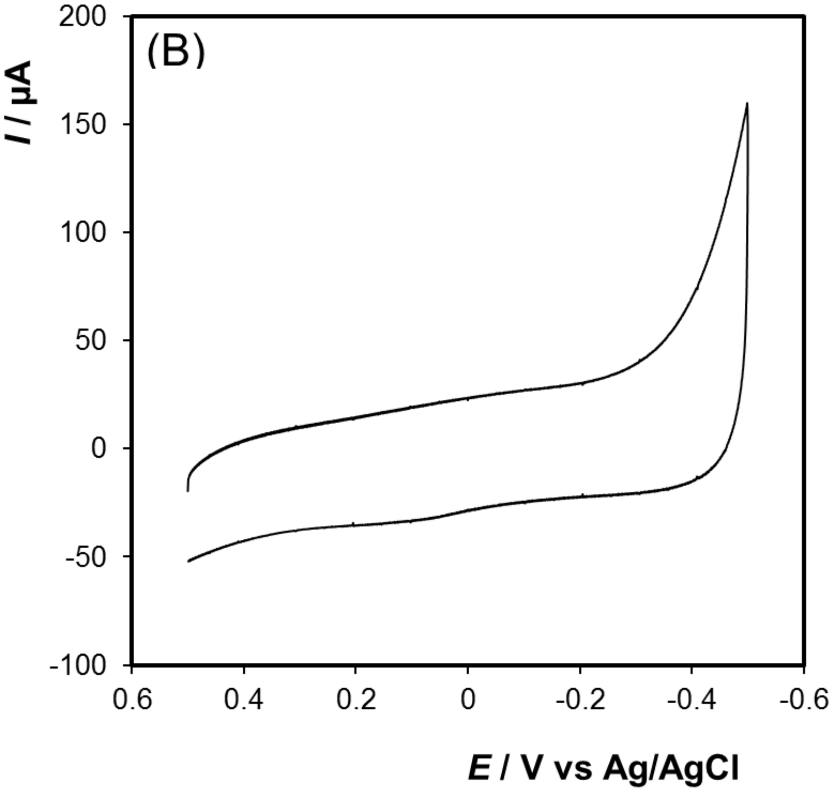

Figure 4.5: Voltammograms of the 3D Ti electrode acquired in different potential windows (positive and negative ranges), in an aqueous solution containing 0.1 M H_2SO_4 as supporting electrolyte, at a scan rate of 0.1 V s^{-1}.

Having established the useful potential window for the 3D Ti electrode, its electrochemical behaviour was investigated using ferri/ferrocyanide.[225,226] Figure 4.6A shows a voltammogram for the 3D Ti electrode in a 1 mM ferrocyanide solution containing 0.1 M H_2SO_4 as supporting electrolyte, at different scan rates, ranging from 0.01 V s^{-1} to 0.1 V s^{-1}, while Figure 4.6B shows peak current dependence on the square root of scan rates. Figure 4.6A shows that a Faradaic response is observed at approximately +0.5 V. It is evident that the current magnitude of the anodic peak at +0.5V increases linearly with increase of scan rate. The $I_{p,a}$ is found to be proportional to the square root of scan rate (Figure 4.6B) indicating that the ferri/ferrocyanide oxidation at the 3D Ti electrode is a diffusion-controlled reaction. Under semi-infinite linear diffusion control, well defined peaks are expected and the response should be similar to that observed at a conventional millimetre dimensioned electrode. In contrast, if electron transfer at the tips of the 3D electrode redox dominates, the response would be controlled by radial diffusion and sigmoidal shaped peaks would be observed. Figure 4.6A shows sigmoidal type responses in which well-defined peaks are not observed. This result may suggest that at these scan rates Faradaic reactions at the small tips of the electrodes dominate the response since at this timescale the thickness of the depletion layer (≈0.05 mm) is significantly smaller than the separation between adjacent pillars (≈0.8 mm) and the depletion zones do not overlap. However, it is also possible that there is a passivating coating on the electrode, most likely an oxide layer on the surface.[227,228]. An oxide layer would decrease the active surface or present a barrier to heterogeneous electron transfer both of which would decrease the peak current and cause a non-ideal voltammetric response to be observed. It should be noted that the oxide was not electrochemically induced and that Ti oxide films (mono-oxide, bi-oxide, tri-oxide) form spontaneously and rapidly on the surface of pure Ti.[229] For Ti alloys, thicker oxide layers can form and can reach 10-20 µm.[230]

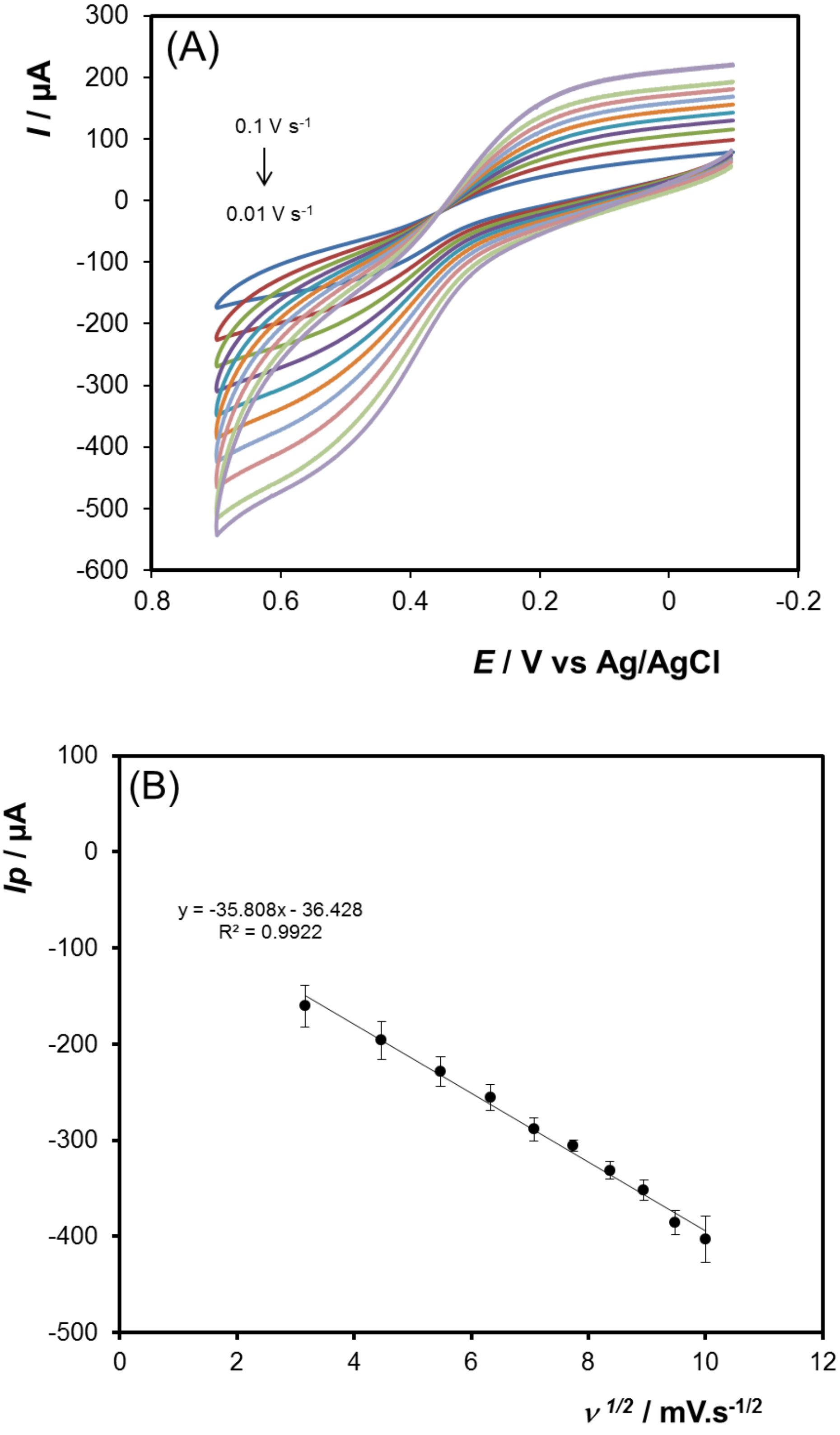

Figure 4.6: CV of 3D Ti electrode (A) and corresponding peak current dependence of the square root of scan rate (B) in 1 mM ferrocyanide in 0.1 M H_2SO_4 as supporting electrolyte. From smallest to largest peak

currents, the scan rates are in the range from 0.01 to 0.1 V s^{-1}. The error bars represent the standard deviation (n = 3 for each point).

4.2.2.1.1 Electrodeposited Gold Coating

One strategy to understanding the relative importance of the 3D geometry and the rate of heterogeneous electron transfer in dictating the response observed is to electrodeposit gold onto the electrode array. The gold surface will be oxide free leading to a higher rate of electron transfer thus allowing diffusional transport effects to be more clearly observed. Moreover, depositing gold extends the potential window available particularly in the negative potential region. Here, a current-time curve was established to get insight into the initial stage of nucleation and growth of gold onto the 3D-printed electrode. Figure 4.7 shows a detailed plot of current versus time of the electrodeposition process of gold.

At the beginning of the electrodeposition process the current decreases (i). This initial drop in current can be attributed to rapid nucleation and growth. After the decrease in current a sudden increase in current (ii) is visible. At this stage the surface of the electrode becomes saturated, thus the rate of nucleation and growth decreases which results in the decrease of current gradually (iii) until it finally reaches a steady state (iv). This trend has been previously observed in the electrochemical deposition of metals and has been discussed in terms of three contributions: adsorption, 2D nucleation and growth, 3D nucleation with diffusion-controlled growth.[231] However, the data presented in Figure 4.7 are insufficient to reach a conclusion as to which of these dominates the response.

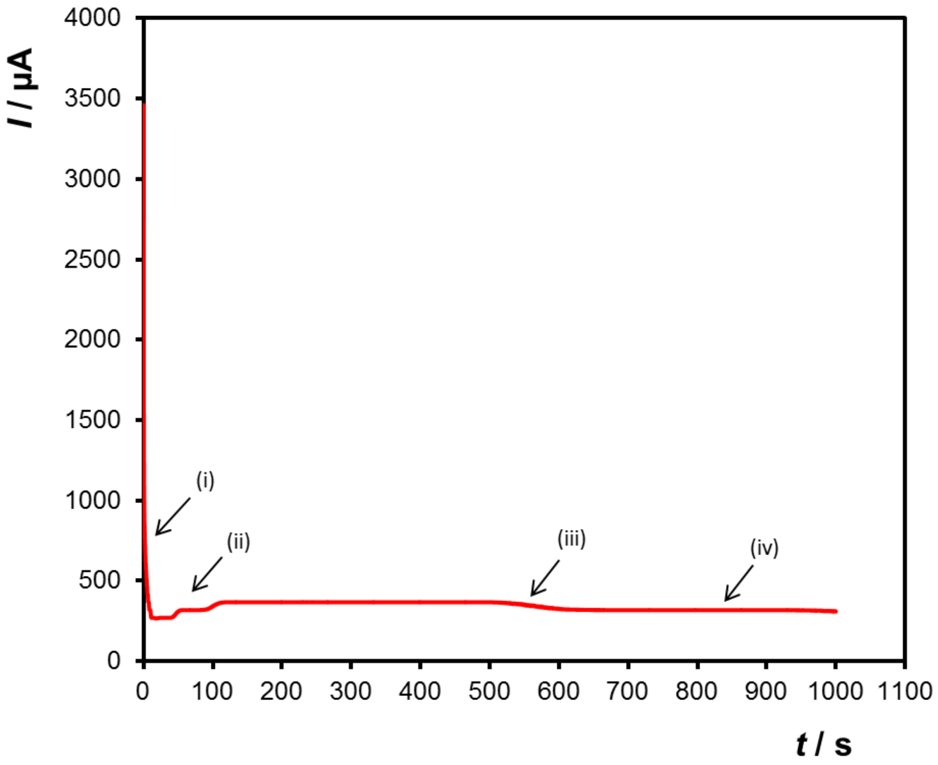

Figure 4.7: Potentiostatic current-time curves for the electrodeposition of gold at -0.9 V for 1000 sec in an aqueous gold plating bath containing gold sulphite.

The FE-SEM illustrated in Figure 4.2B shows that following gold deposition the topography seems similar to that observed for the Ti electrode. Under identical conditions, Figure 4.3B reveals that the brightness of the backscattered image following gold electrodeposition is higher than that observed for the 3D titanium array which is consistent with successful deposition of Au. Moreover, EDX spectra taken across the array surface following gold deposition, Figure 4.4B, are dominated by gold indicating that a gold layer is formed over the array.

One advantage of gold is that an oxide monolayer can be formed electrochemically by cycling in dilute acid and subsequently removed. The charge passed during reduction of the gold oxide provides the surface area and an estimate of the roughness. Figure 4.8 shows the voltammetric response obtained when the gold coated array is cycled from +0.2 V to +1.5 V in 0.1 M H_2SO_4, at 0.1 V s^{-1}. The onset of gold oxide formation occurs at approximately +1.08 V. Three distinct peaks can be observed at around a (~1.15 V), b (~1.2 V) and c (~1.35 V) which most likely reflect oxide formation on Au(100), Au(110) and Au(111) faces, respectively.[232,233] The potential range, scan rate and number of scans have been restricted so as to prevent bulk oxidation, i.e., the objective is to form a gold oxide monolayer only. The gold oxide monolayer is reduced at approximately +0.8 V. The charge associated with the reduction of gold oxide is approximately 390 µC cm^{-2} and so by integrating the area under the gold oxide reduction peak in the background corrected cyclic voltammogram it is possible to measure the microscopic surface area of the 3D Au-coated Ti electrode.[234] For the gold coated array, the charge passed, 9.16×10^{-3} C, corresponds to a microscopic area of 23.5 cm^2. The geometric area of the array is 1.32 cm^2, which, when taken in conjunction with the microscopic area, gives a surface roughness of 17.8. This large value is consistent with the FE-SEM data and indicates that the laser fusion 3D deposition method produces electrodes that have a large surface area which would be useful in energy and chemical sensing applications.

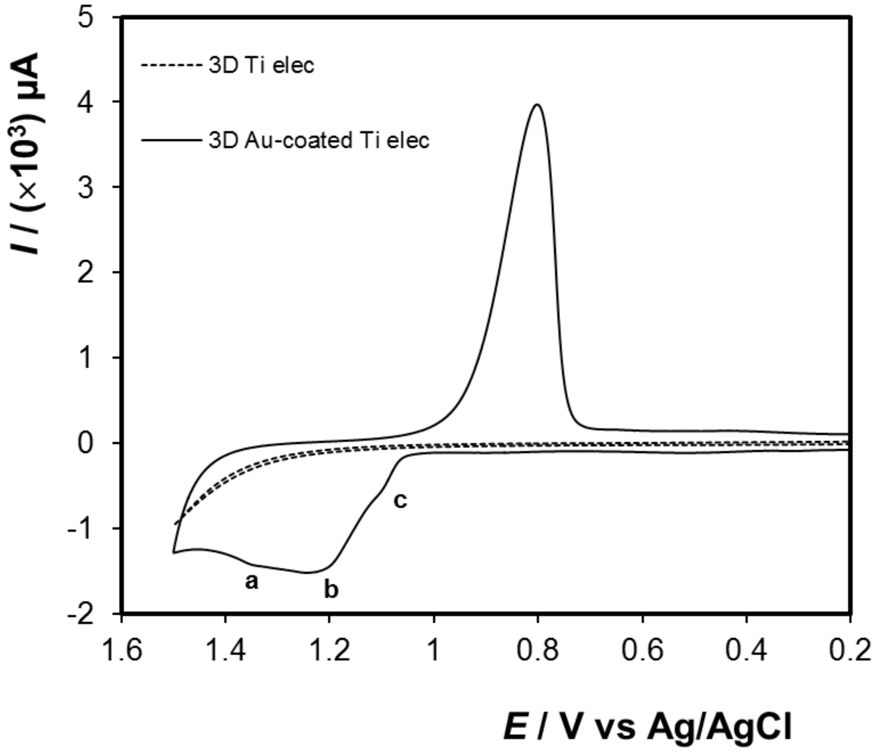

Figure 4.8: Voltammograms of 3D Ti (dashed line) and 3D Au-coated Ti (solid line) electrodes in an aqueous solution containing 0.1 M H_2SO_4 as supporting electrolyte, at a scan rate of 0.1 V s^{-1}.

Figure 4.9A shows scan rate dependent voltammograms obtained for 1 mM ferrocyanide dissolved in 0.1 M H_2SO_4 at the gold coated arrays. Despite the negligible difference in geometry of the parent titanium and gold coated electrodes (gold coating is thin which does not significantly increase the thickness of the wires), the response is strikingly different at the gold coated electrodes. The peak currents obtained from the voltammogram in Figure 4.9A vary linearly with the square root of scan rate (Figure 4.9B). Specifically, well defined peaks are observed, however the cathodic peak potentials shift to more negative values with increasing scan rate. The peak-to-peak separation, ΔE_p, at low scan rates are <80 mV and the ratio of oxidation to reduction peak currents is one. While larger than the 57 mV expected for an ideal reversible reaction under semi-infinite linear control, the ΔE_p value is consistent with a quasi-reversible process. The open circles show the best fit to the 0.01 V s^{-1} experimental data assuming semi-infinite linear diffusion control where there is only one freely adjustable parameter, the standard heterogeneous electron transfer rate constant, k^o. Significantly, a satisfactory fit is obtained where k^o is $8x10^{-3}$ s^{-1}. The fact that the response at the gold coated array is consistent with semi-infinite linear diffusion control at the scan rates investigated suggests that the sigmoidal response observed at the titanium arrays arises due to a small k^o. It is perhaps important to note that the depletion layer thickness will be of the order of $5x10^{-3}$ cm, i.e., larger than the length scale of a significant fraction of the surface roughness meaning that the geometric area dominates the response. In contrast, when the 0.1 V s^{-1} is simulated using a k^o of $8x10^{-3}$ s^{-1}, the peak potentials are satisfactorily predicted but to match the peak currents, the theoretical response must be multiplied by a factor of 1.5. This result suggests that at the higher scan rate where the depletion layer is thinner, surface roughness influences the voltammogram observed.

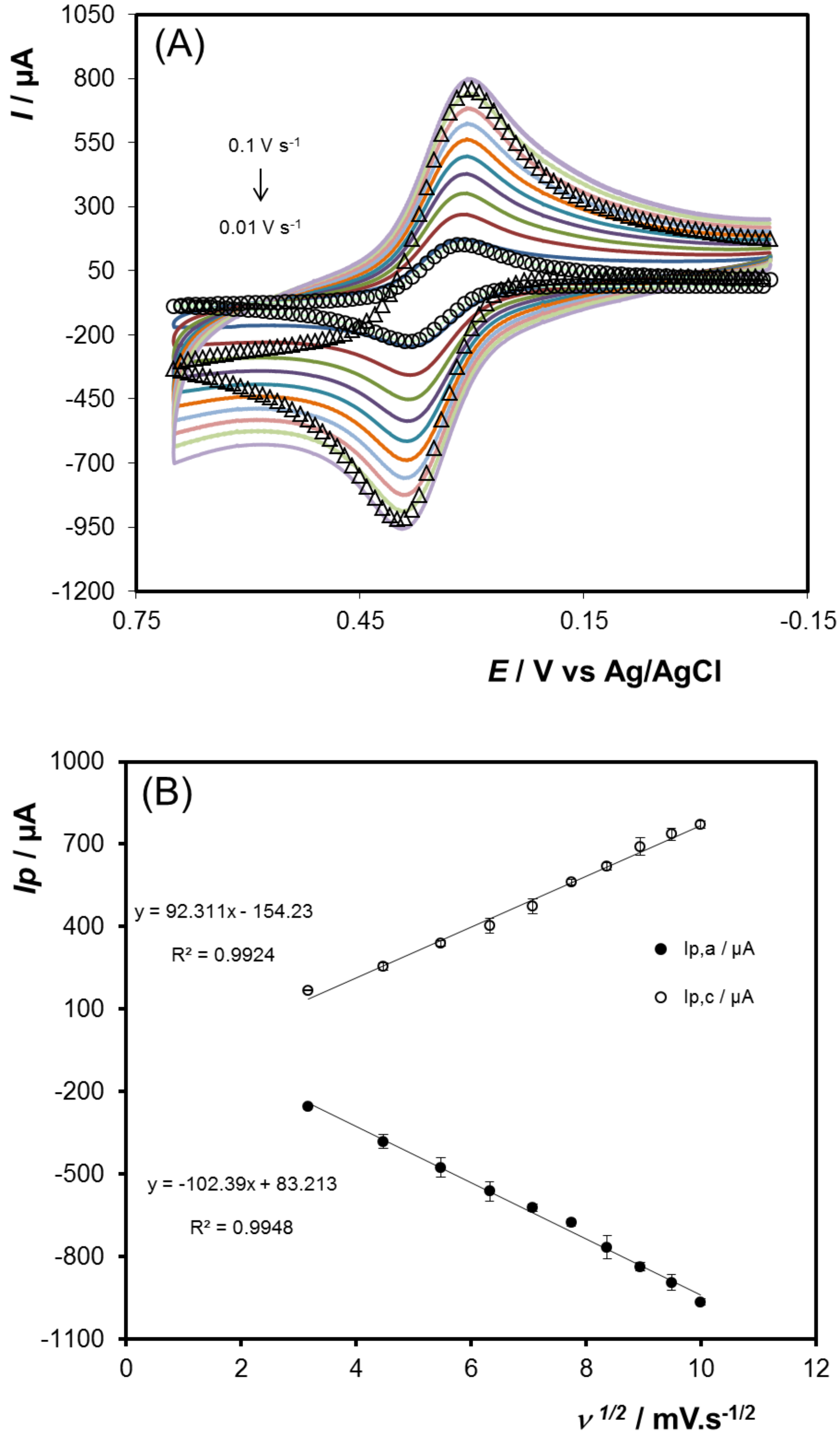

Figure 4.9: Scan rate dependence voltammogram of Au-coated 3D Ti electrode (A) and corresponding peak current dependence of the square root of scan rate (B) in 1 mM ferrocyanide in 0.1 M H_2SO_4 as supporting

electrolyte. The voltammogram is plotted incrementally at 0.01 V s^{-1} intervals, for lower scan rates of 0.01 V s^{-1} to higher scan rates of 0.1 V s^{-1}. The open circles (○) in (A), represent the best fit under semi-infinite linear diffusion control where the standard rate of heterogeneous electron transfer, k^o, is $8x10^{-3}$ s^{-1}, while the open triangles (∆) represent the predicted response at 0.1 V s^{-1} but where the currents have been multiplied by a factor of 1.5. The error bars represent the standard deviation (n = 3 for each point).

4.2.2.2 Impedance

Electrochemical impedance spectroscopy (EIS) is an effective method to study the surface modification characteristics of electrodes.[235] The EIS behaviour is a reflection of electrical and electrochemical properties of the electrode materials and electrolyte solution, as well as the microscopic morphology of the interface.[236] For this reason, EIS was employed to provide a full description of the charge transfer kinetics occurring at the 3D Ti electrode and the gold modified 3D Ti electrode. The results obtained for the impedance measurements of these electrodes were depicted by Nyquist and Bode plots.

Figure 4.10 shows an overlay of the Nyquist plots of the 3D-printed Ti electrode before and after the Au deposition process. The EIS measurements were performed in 0.1 M $LiClO_4$ solution containing 1 mM $Fe(CN)_6^{3-}/Fe(CN)_6^{4-}$, at open circuit potential, at ac amplitude of 25 mV and the frequency range was from 1 MHz to 1 Hz. It is evident that the

Nyquist plots consist of a semicircle part and a linear part. The semicircle portion corresponds to the electron-transfer- limited process, and the linear portion represents the diffusion-limited process.[237] The formal potential of $[Fe(CN)_6]^{3-/4-}$ couple under these conditions is +0.23 V. The direct current potential (E_{DC}) has been set to 0.21 V. Therefore in the equivalent circuit there will be these four elements namely; (1) electron-transfer resistance (R_{CT}) at the 3D-printed electrode surface is equal to the semicircle diameter, and it can be used to describe the interface properties of the 3D electrodes; (2) the Warburg impedance (Z_w) resulting from the diffusion of ions from the bulk $[Fe(CN)_6]^{3-/4-}$ electrolyte to the 3D electrode interface; (3) electrolyte resistance (R_s) between 3D-printed electrode and reference electrode; and (4) the interfacial double layer capacitance (C_{dl}) between the 3D electrode and $[Fe(CN)_6]^{3-/4-}$ electrolyte solution, relating to the surface condition of the electrode. The obtained Nyquist plots for the 3D Ti and 3D Au-coated Ti electrodes are almost in a semi-circular appearance. Deviations of perfect circular shape are often referred to the frequency dispersion of interfacial impedance and might be attributed to the inhomogeneity of the 3D electrode surface arising from either surface roughness or oxide formation.

Bode plots of impedance modulus and phase angle versus log frequency is shown in Figure 4.11A and B, respectively. For both the bare 3D Ti electrode and 3D Au-coated Ti electrode a single slope can be observed in the high and low frequency range, respectively. The bare 3D Ti electrode and 3D Au-coated Ti electrode show no differences in the impedance after a frequency of 1000 Hz, however, at lower frequencies the impedance of the 3D Au-coated Ti electrode is less compared to the bare 3D Ti electrode (Figure 4.11A). This may be due to the presence of a Au layer on the Ti surface. Furthermore, the evaluation of the phase angle versus log frequency data reveals the 3D Au-coated Ti electrode has a phase angle of approximately 15° and the bare 3D Ti electrode has a phase angle of approximately 70°.

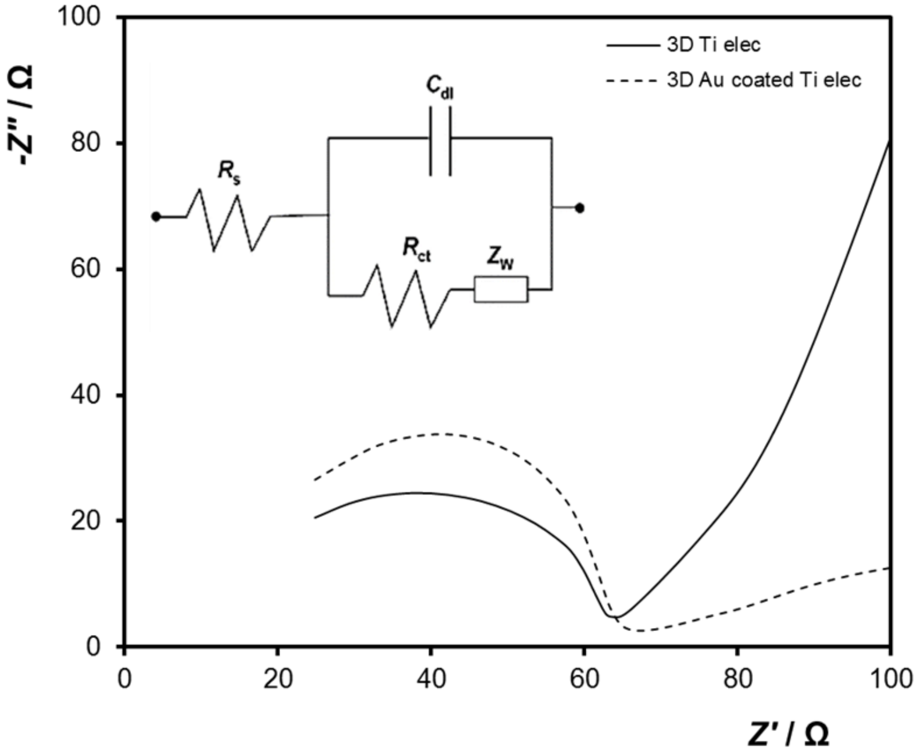

Figure 4.10: Nyquist plots of bare 3D Ti electrode and 3D Au-coated Ti electrode recorded in 0.1 M $LiClO_4$ solution containing 1 mM $Fe(CN)_6^{3-}$ /$Fe(CN)_6^{4-}$. The frequency range is from 1 MHz to 1 Hz with a signal amplitude of 25 mV. The inset is the equivalent circuit model.

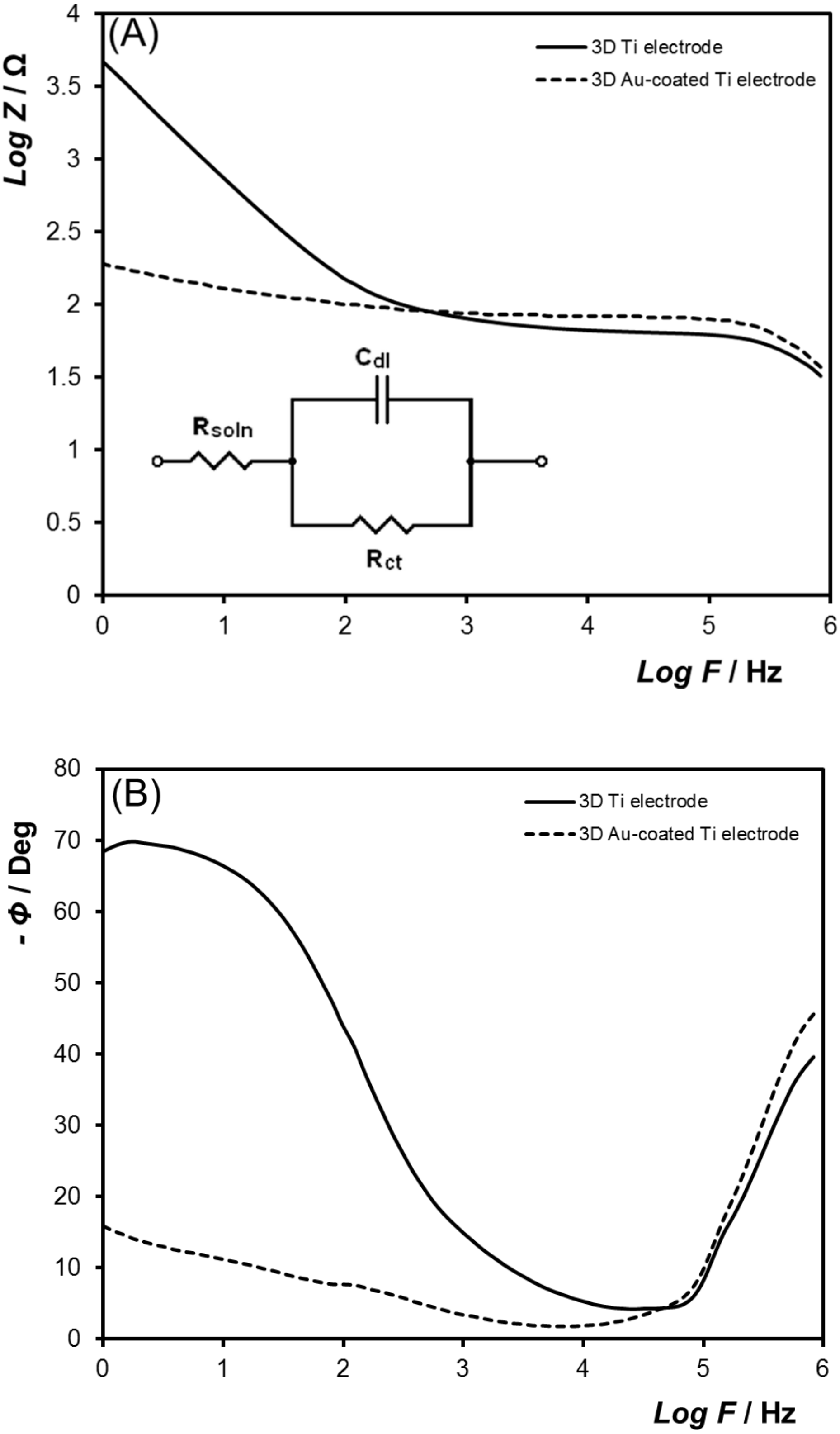

Figure 4.11: Bode plots of logarithm of complex impedance (A) and phase angle (B) vs logarithm of frequency for the bare 3D Ti electrode and 3D

Au-coated Ti electrode in 0.1 M $LiClO_4$ solution containing equimolar mixture of $K_4Fe(CN)_6$ and $K_3Fe(CN)_6$.

4.2.2.3 ECL Analysis

3D electrodes open up the possibility of generating electrochemiluminescence throughout a 3D volume rather than at a 2D planar surface and, depending on the geometry of the 3D electrode, it may be possible to selectively enhance the brightness of the emission in particular regions. Here, the ECL properties of the bare 3D Ti- and Au-coated 3D Ti electrodes were investigated using $[Ru(bpy)_3]^{2+}$ and tripropylamine (TPA) as the co-reactant. Figure 4.12 shows voltammograms of the bare 3D Ti- and 3D Au-coated Ti electrodes in 0.1 M chloride-free PBS (pH 7.4) containing 50 µM $[Ru(bpy)_3]^{2+}$. This figure shows that no redox peaks are observed for $[Ru(bpy)_3]^{2+}$ at the bare 3D Ti electrode (*solid line*). At the gold coated electrode, it can be difficult to obtain well-defined peaks for the ruthenium complex due to overlap with gold oxide peaks. The formal potential of the $Ru^{2+/3+}$ couple is 1.1±0.1 V and the gold coated array shows broad oxidation and reduction peaks at approximately +1.3 V and +0.4 V, respectively.

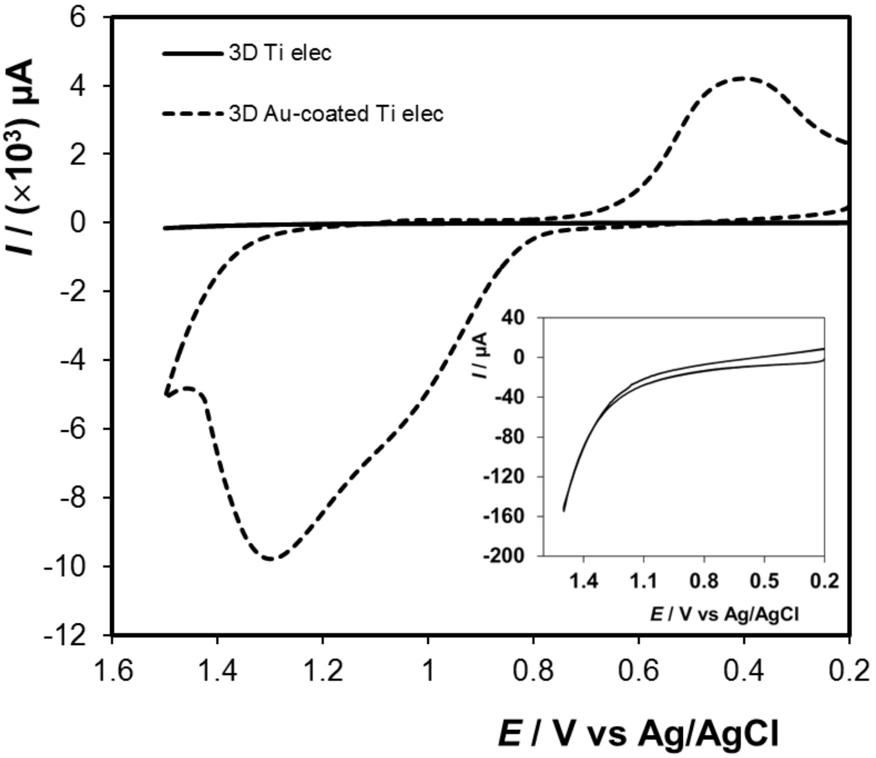

Figure 4.12: Voltammograms of 3D Ti (solid line) and 3D Au-coated Ti (dashed line) electrodes in 0.1 M chloride-free PBS (pH 7.4) solution containing 50 µM $[Ru(bpy)_3]^{2+}$, at a scan rate of 0.1 V s^{-1}. The inset shows a magnified view of the CV of the 3D Ti electrode.

To investigate the possible ECL mechanism of $[Ru(bpy)_3]^{2+}$/TPA system at the fabricated 3D electrodes, the ECL and its corresponding CV curves were measured. Figure 4.13A and B, and Figure 4.14A and B show the ECL and its corresponding CV behaviour, respectively, of the bare 3D Ti electrode and 3D Au-coated Ti electrode, in 0.1 M chloride-free PBS (pH 7.4) solution, containing 50.0 µM $[Ru(bpy)_3]^{2+}$ and 5.0 mM TPA. Significantly, both electrode arrays produce significant ECL and the ECL intensities increase with increasing scan rate in the range 0.01 V s^{-1} to 0.1 V s^{-1} (inset). Since ECL can only be generated from the Ru^{3+} species, these results indicate that while a well-defined Faradaic response is not observed in voltammetry of the 3D Ti electrode (Figure 4.14A), some oxidation of Ru^{2+} occurs at its surface.

The onset potential of the ECL signal of $[Ru(bpy)_3]^{2+}$ was observed at ~ +1.1 V for both the bare 3D Ti- (Figure 4.13A) and 3D Au-coated Ti (Figure 4.13B) electrodes which is consistent with ECL being generated by reaction of Ru^{3+} with the TPA radical. Despite the more ideal voltammetric response of the gold coated array (Figure 4.14B), the dependence of the ECL intensity on the scan rate is quite complex. This complexity reflects the fact that the ECL intensity observed depends on both the rate of heterogeneous electron transfer and the geometry of the array. For example, fast heterogeneous electron transfer could cause depletion of the reagents *within* the array. If diffusion into the array is slow, then a peak will be observed in the ECL intensity such as those observed in Figure 4.13B. In simpler terms, the Ru^{3+} produced by direct oxidation of Ru^{2+} at the electrode surface has not been consumed by the time the potential was switched to a value lower than that for Ru^{3+}. Thus, the second ECL peak observed in the reverse scan is believed to be controlled by reaction kinetics. Moreover, TPA might also contribute to this response due to the fact that it is in vast excess compared to Ru^{2+}. Here, the second ECL peak in the reverse scan is observed in the potential region where oxidation of TPA occurs.

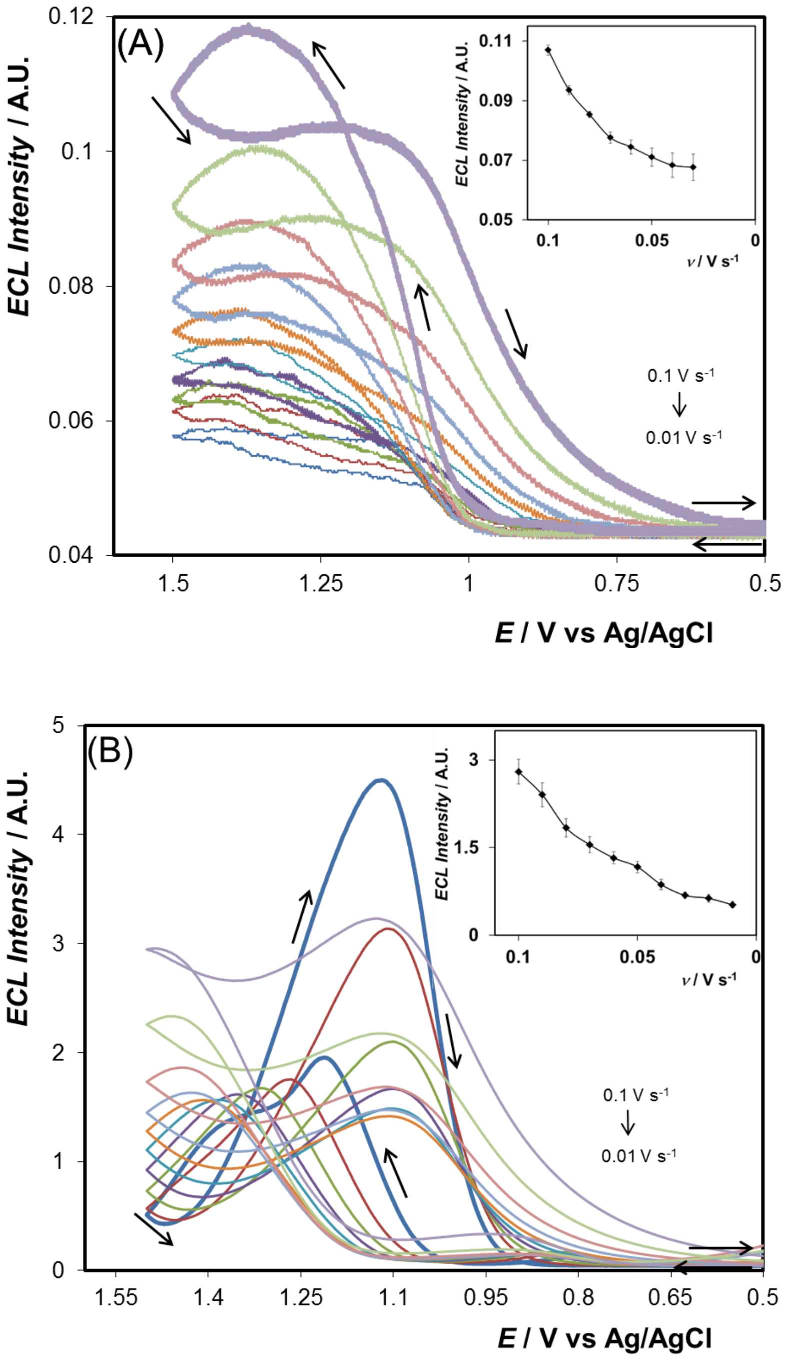

Figure 4.13: ECL generated at a 3D Ti electrode (A) and a 3D Au-coated Ti electrode (B) in 0.1 M chloride-free PBS (pH 7.4) solution containing 50.0 µM $[Ru(bpy)_3]^{2+}$ and 5.0 mM TPA, at scan rates ranging from 0.01 V s^{-1} to 0.1 V s^{-1}. The potential was linearly scanned from 0.5 to 1.5 V as indicated by the arrows. The insets show the dependence of the maximum ECL intensity on the scan rate for each electrode.

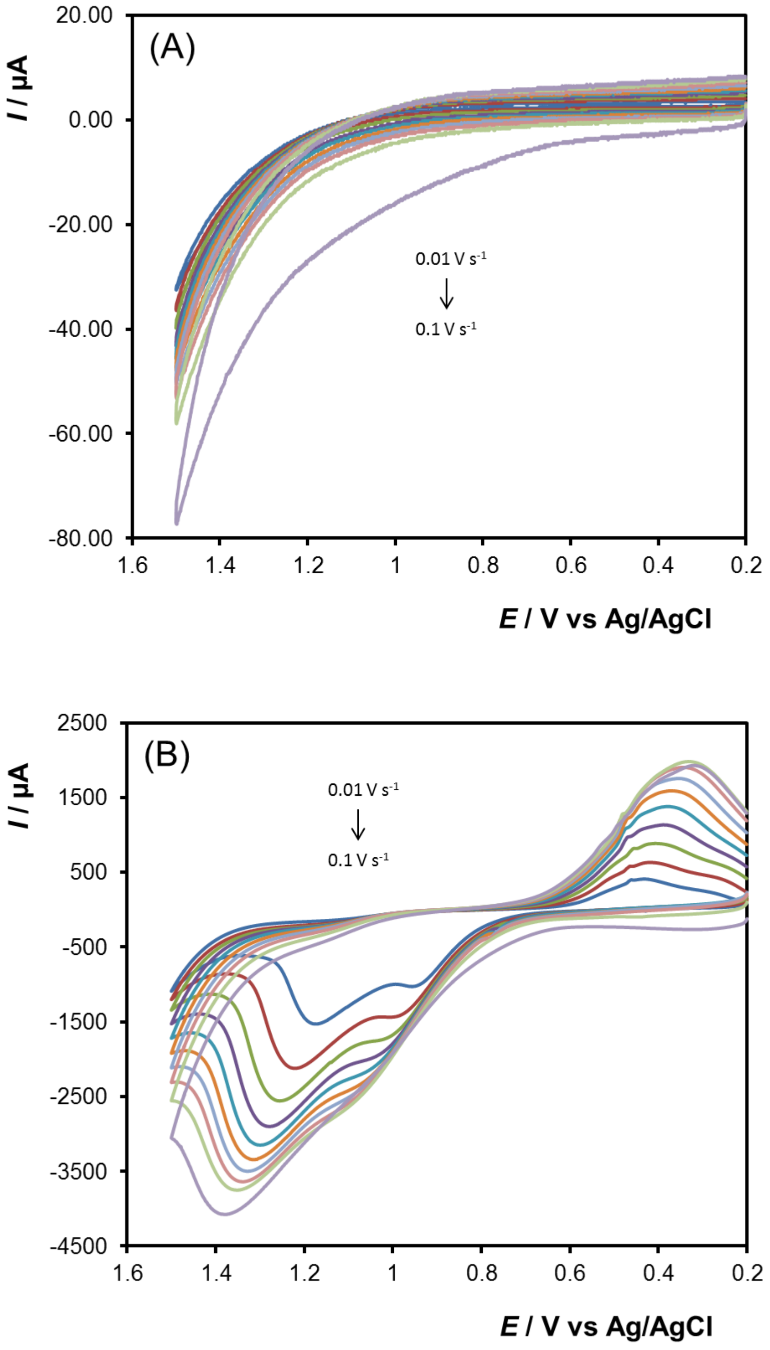

Figure 4.14: Corresponding voltammograms of the ECL-voltage curves for 3D Ti electrode (A) and 3D Au-coated Ti electrode (B) in 0.1 M chloride-free PBS (pH 7.4) solution containing 50.0 μM $[Ru(bpy)_3]^{2+}$ and 5.0 mM TPA, at scan rates ranging from 0.01 V s^{-1} to 0.1 V s^{-1}.

4.2.3 BPE/ECL

In the frame of designing the 3D Ti electrodes, the initial proof-of-concept was to use these 3D arrays as bipolar electrodes (BP_{elec}) and investigate electric field focusing within the array structure for possible enhancement of ECL output. However, one shortcoming of the 3D structure was its inability to generate simultaneous oxidation and reduction reactions at its surface. For this reason, surface modification of the electrode was done and its electrochemical properties investigated. From the electrochemical and morphological data it was concluded that the 3D-printed electrode exhibited improved electrochemical activity once it was modified with gold. The 3D Au-coated BP_{elec} was immersed in a solution of 5.0 mM $[Ru(bpy)_3]^{2+}$ and 25.0 mM TPA between two gold feeder electrodes in a bipolar cell, and the potential difference between the two electrodes varied from 0 V to 17 V. Figure 4.15 shows images of the 3D BP_{elec} with (A) and without (B) background light. BPE experiments were conducted in the dark so that the onset of BPE/ECL (wireless light emission from surface of the 3D array) could be recorded by a CCD camera as illustrated in Figure 4.16.

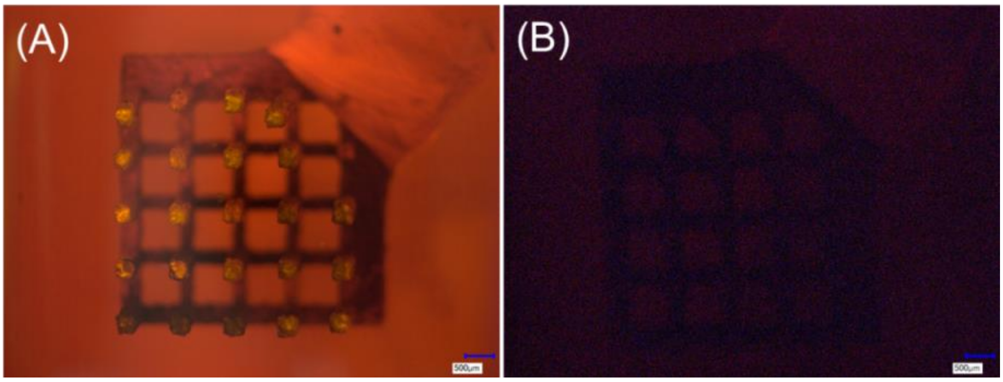

Figure 4.15: Photographs of the 3D BP_{elec} with (A) and without (B) background light.

As the potential increased from 0 V to 9 V no apparent BPE/ECL occurred, however, at ~3 V light was observed at the anodic feeder electrode and at ~5 V the light switched “OFF”. The anodic feeder electrode exhibited light due to a fraction of total potential loss at the feeder/solution interface. Once the potential reached ~10 V the base and the first row of five pillars of the 3D BP_{elec} switched “ON” (Figure 4.16). Here, oxidation of the $[Ru(bpy)_3]^{2+}$/TPA system occurred at the anodic pole and simultaneous reduction of oxygen at the cathodic pole of the 3D BP_{elec}.[238] The potential was kept constant for a few seconds and then increased to 11 V where light was seen growing along the base and pillars (Figure 4.16). At about 12 V the light appeared to be more enhanced at the tips of the pillars. This might be attributed to radial diffusion.

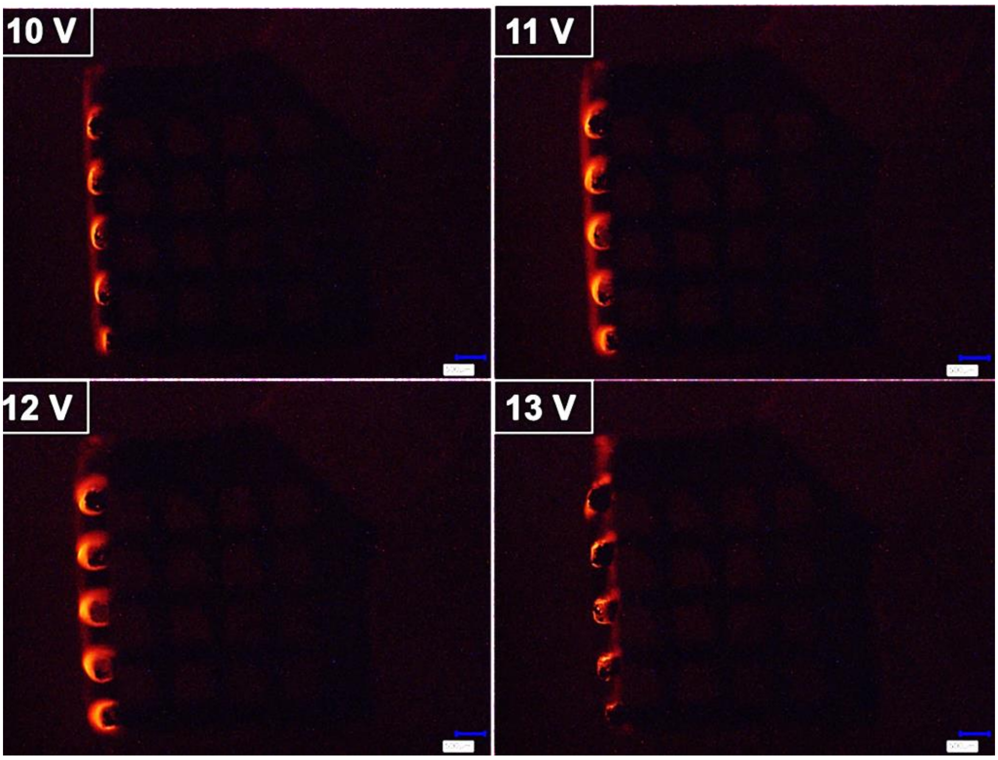

As the potential increased from 13 V to 15 V, the light at the pillars switched “OFF”. Strikingly, this is in sharp contrast with what was expected as the potential increase from 10 V to 17 V. It should be noted that when the potential reached 18 V the 3D BP_{elec} switched “OFF” completely. This can be attributed to the reduction of H_2O in the form of bubbles at the cathodic pole of the 3D BP_{elec} as shown in Figure 4.17A.[119] In addition, black deposits were observed at the cathodic pole of the BP_{elec} (Figure 4.17B (ii)) and the cathodic feeder electrode (Figure 4.17B (i)).

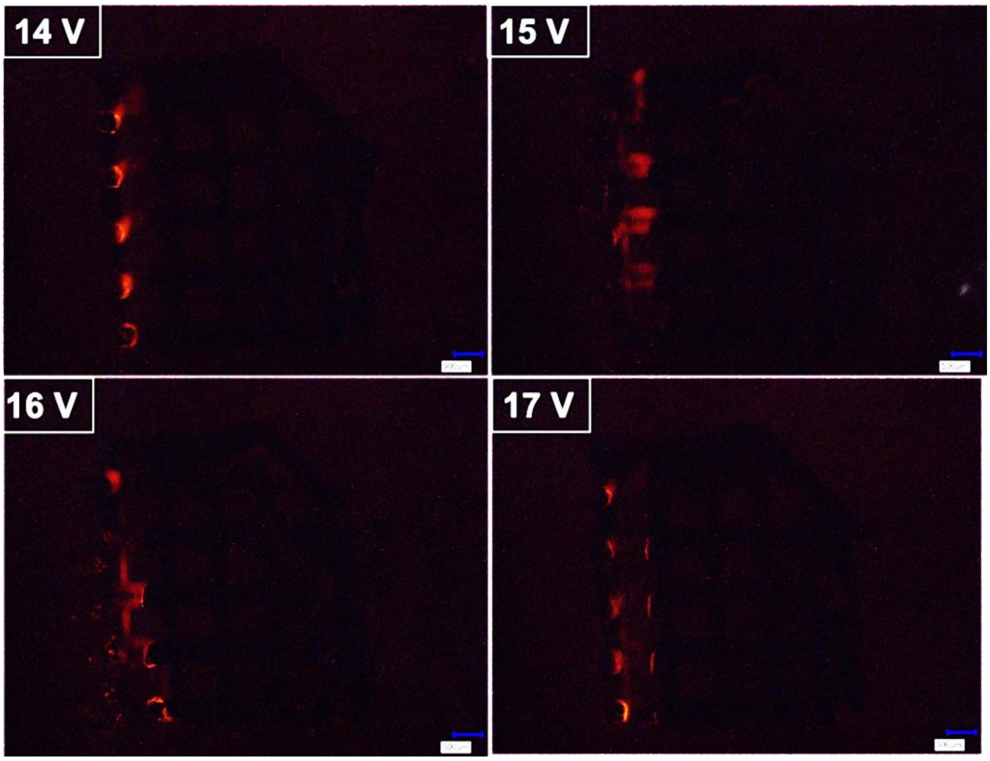

Figure 4.16: Photographs of ECL emitted on the anodic pole of the 3D BP_{elec} array in the presence of 5.0 mM $[Ru(bpy)_3]^{2+}$ and 25.0 mM TPA. The potential between the gold feeder electrodes was varied from 10 V to 17 V giving a maximum electric field (V_0) of approximately 30 V cm^{-1} on the 0.5 cm wide 3D BP_{elec}.

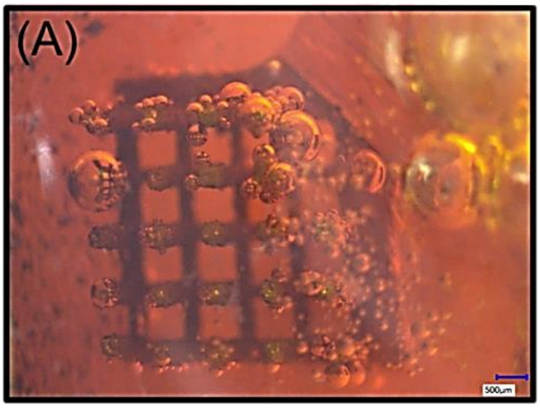

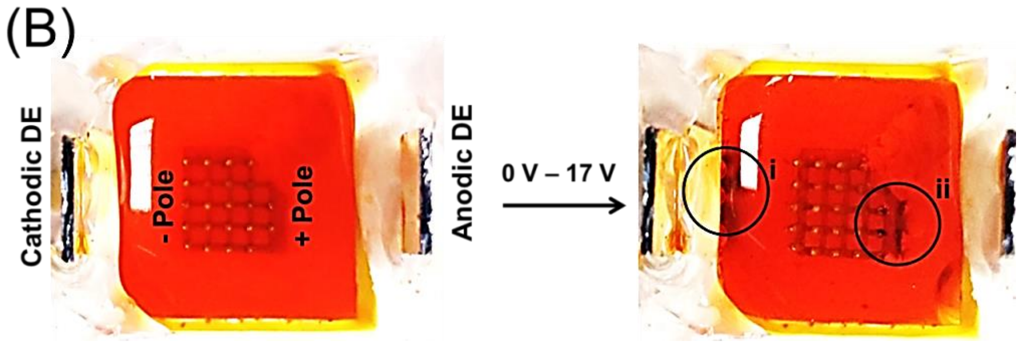

Figure 4.17: Photographs of (A) background reactions (in the form of bubble formation), and (B) black deposits occurring at the cathodic pole of the 3D BP_{elec} (ii) and cathodic feeder electrode (i).

Clearly, this is a very simple demonstration of a proof-of-concept approach; however, the results obtained are important in the sense that it gives an understanding of the BPE/ECL phenomenon at 3D electrodes. The findings also reveal the need to properly adjust some parameters like the electrode design and perhaps adding a sacrificial agent to optimise the amount of light emitted by the 3D system. One of the main points of this experiment is to show that BPE/ECL cannot only be confined to 2D systems but BPE/ECL can be generated at 3D architectures. These results allow envisioning 3D configurations for the design of high performance ECL sensors (whether it be electronic or medical) in the near future.

4.3 CONCLUSION

This work describes the fabrication and electrochemical properties of a 3D-printed titanium electrode array. The 3D titanium array comprises twenty five round pillars and has a geometric area of 1.32 cm^2. SEM analysis revealed that the surface roughness extends from the nano to 100 μm length scales. While voltammetry revealed that the native titanium 3D array demonstrates poor electrochemical response. Here, the 3D titanium array was functionalised with a thin gold layer to alter the electrode surface composition and therefore tune its catalytic properties which significantly enhances the rate of heterogeneous electron transfer. Both the native titanium and gold coated 3D arrays generate conventional and bipolar electrochemiluminescence in ruthenium tris-bipyridyl solutions that contain tripropyl amine as a co-reactant. At the gold coated 3D titanium array the dependence of conventional ECL intensity is more complex since heterogeneous electron transfer is rapid and the response is strongly influenced by the geometry of the array.

The ability to optimise the electrochemical properties of the 3D array by electrodeposition and use it in bipolar electrochemistry experiments opens up exciting new possibilities by enabling the creation of devices with a much wider range of functionalities.

5 Chapter 5:

Sandwich-Type ECL Sensing Platform for Ultrasensitive Detection of Cardiac Troponin I, A Biomarker for Cardiovascular Disease

5.1 INTRODUCTION

According to the World Health Organization (WHO), cardiovascular disease (CVD) is one of the major reasons for death in humans worldwide with acute myocardial infarction (AMI) being the leading cause.[239] Myocardial infarction (MI) describes the process of myocardial cell death due to an inadequate blood supply to the heart.[240] Despite the use of existing classical clinical methods like the electrocardiogram (ECG), patient survival rates are still quite low. This can be attributed to the poor diagnostic capabilities of the ECG. Some patients suffering from CVD show normal or no diagnostic electrocardiograms even after experiencing characteristic chest pain associated with the CVD.[241,242] Thus, in the year 2000, a joint committee of the European Society of Cardiology and the American College of Cardiology (ESC/ACC) issued new criteria that acknowledged that elevations in biomarkers were fundamental to the diagnosis of AMI. [243,244] An ideal biomarker for AMI should be in high concentration in cardiac tissue, absent in non-cardiac tissue, released rapidly in a linear fashion following myocardial cell death, and present in the blood long enough to be easily detectable by a relatively inexpensive and widely available method. There have been a few biomarkers capable of detecting AMI such as, lactate dehydrogenase isoenzymes, creatine kinase isoenzyme MB (CK-MB), myoglobin (MYO) and cardiac troponins.[245–248] Among these cardiac markers, cardiac troponin I (cTnI), is regarded as a reliable biomarker for AMI diagnosis because of its superior cardiac specificity and selectivity.[249]

To date, the quantitative detection of cTnI mainly relies on immunoassay-based protocols such as enzyme-linked immunosorbent assay (ELISA), immunochromatographic tests, radio-immunoassays and fluorescence immunoassays.[250–253] Despite the extensive development of these methods they still suffer from drawbacks such as poor sensitivity, expensive and sophisticated instruments and long diagnostic times which make them not suitable as point-of-care assays. Therefore, the development of fast, sensitive and low cost detection strategies are of the utmost importance when dealing with ultra-low level concentrations of cTnI during early stages of disease progress. Bio-sensing has received much attention because of their high sensitivity, rapidness, cheapness and simple design. A biosensor is a device that integrates biomolecules with a suitable transducer to convert biochemical signals into quantifiable electronic signals. When coupled to a powerful electrochemical readout method like, electrochemiluminescence (ECL), these devices can integrate outstanding selectivity from biological recognition and the high sensitivity of ECL signalling to produce sensing strategies for ultrasensitive detection and/or quantification of cTnI.

Several ECL methods have been developed for the determination of cTnI. Li and co-workers designed ECL immunosensor for the detection of human cTnI by using luminol.[254] While Dong and co-workers developed a peptide-integrating $Ru(bpy)_3^{2+}$ -functionalised gold nanoparticle based ECL immunosensor.[255] ECL has also been integrated in commercially available high-throughput automatic analysis systems for utilisation in clinical settings, such as AxSYM System (Abbott), Elecsys 2010 (Roche), and Access (Beckman Coulter).[256] However, challenges remain in improving the sensitivity of clinical immunoassays to meet the increasing demand for early disease diagnosis.

Thus, this thesis focused on the development of a simple, fast and sensitive sandwich-type ECL immunosensor for cTnI detection by using synthesised $[Ru(bpy)_2(picCOOH)]^{2+}$ dye-antibody conjugate as an ECL readout signal. Here, the sensing device was achieved by modifying the surface of transduction substrates (ITO PET, ITO glass, Au wafer, Au-Au wafer and Au disc electrode) with the primary antibody through a 16-carbon length self-assembled monolayer. The sensor was exposed to different concentrations of the target analyte, troponin I, and finally incubated with the secondary antibody-dye conjugate. Furthermore, the utility of bipolar electrochemistry (BPE) for wireless detection of target analyte was investigated. The proposed sandwich immunosensor showed excellent analytical performance using both conventional ECL and BPE/ECL and achieved signal readout at very low troponin I levels.

5.2 RESULTS AND DISCUSSION

5.2.1 Characterisation of Electrochemiluminescent Emitter

5.2.1.1 UV-vis

Figure 5.1 shows the ultraviolet-visible absorbance spectrum for the $[Ru(bpy)_2(picCOOH)]^{2+}$complex synthesised. Because the complex will be utilised in aqueous based applications, its electronic absorption properties were studied in 0.10 M chloride-free PBS (pH 7.4). Three absorption peaks at 285, 330 and 458 nm can be observed. The absorption at 458 nm is the smallest exciton wavelength and can be attributed to a ruthenium metal dπ to carboxyl ligand π* (metal-to-ligand charge transfer (MLCT)) transition.[257,258] The strong absorbance band at approximately 285 nm may be assigned to π-π* transitions within the bpy ligands, whereas the shoulder at approximately 330 nm is attributed to the π-π* transitions of the [pic-COOH] ligands containing the two ionisable protons on the imidazole ring. The benzimidazole spacer (Chapter 2, Figure 2.5) has little effect on the absorbance spectra of the complex as the energies and absorbance profile of these transitions are almost identical to that of $[Ru(bpy)_3]^{2+}$, a standard electrochemiluminescent emitter.[175]

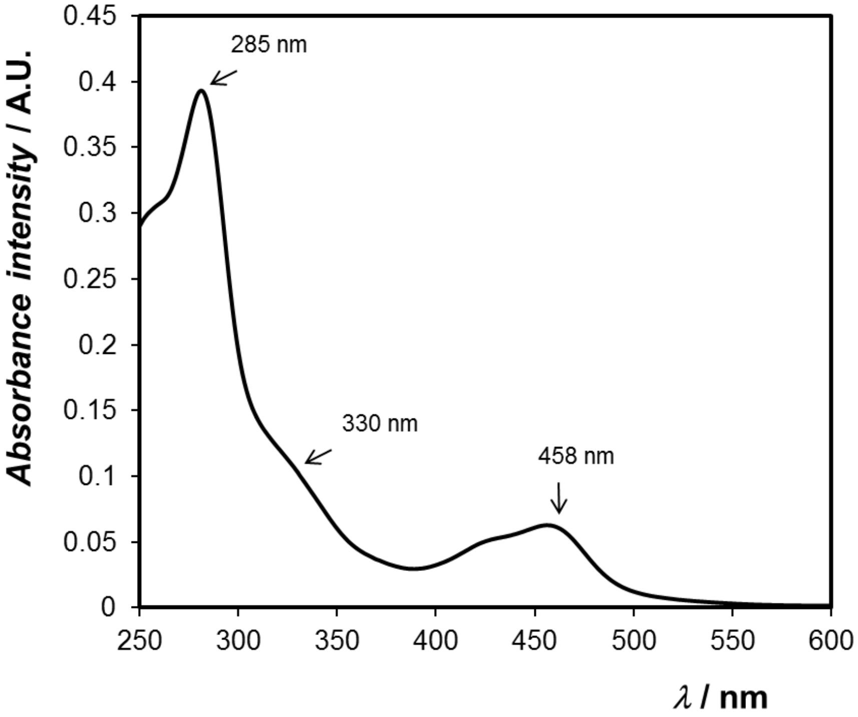

Figure 5.1: Absorbance spectra of 20 µM $[Ru(bpy)_2(picCOOH)]^{2+}$ in 0.10 M chloride-free PBS (pH 7.4).

5.2.1.2 Emission

The emission spectrum of the $[Ru(bpy)_2(picCOOH)]^{2+}$ complex in 0.10 M chloride-free PBS solution are illustrated in Figure 5.2. A maximum emission at 608 nm is visible and occurs by exciting the complex at approximately 400 nm. The emission is the mirror image of the absorbance because it occurs subsequent after excitation. This can be attributable to the vibrational spacing in the ground electronic singlet state (S_0) that is often similar to the first excited singlet state (S_1). The luminescence lifetime of the $[Ru(bpy)_2(picCOOH)]^{2+}$ complex were evaluated in deaerated PBS solution and was found to be 811 ± 4 ns. It is known that Ru (II) polypyridyl complexes exhibits an enhanced lifetime in aqueous and in protic solvents compared with non-protic organic media.[175] The longer lifetimes in aqueous media may be explained by stabilisation of the emissive ^{3}MLCT of the carboxyl complex as a result of H-bonding between the solvent and complex. This demonstrates the importance of H-bonding in controlling the properties of the complex.[175,259] Furthermore, these optical properties are of importance when dealing with electrogenerated chemiluminescence emitters like ruthenium (II) polypyridyl complexes since it gives an understating about the potential redox behaviour and the electrochemically generated excited states of the species under study.

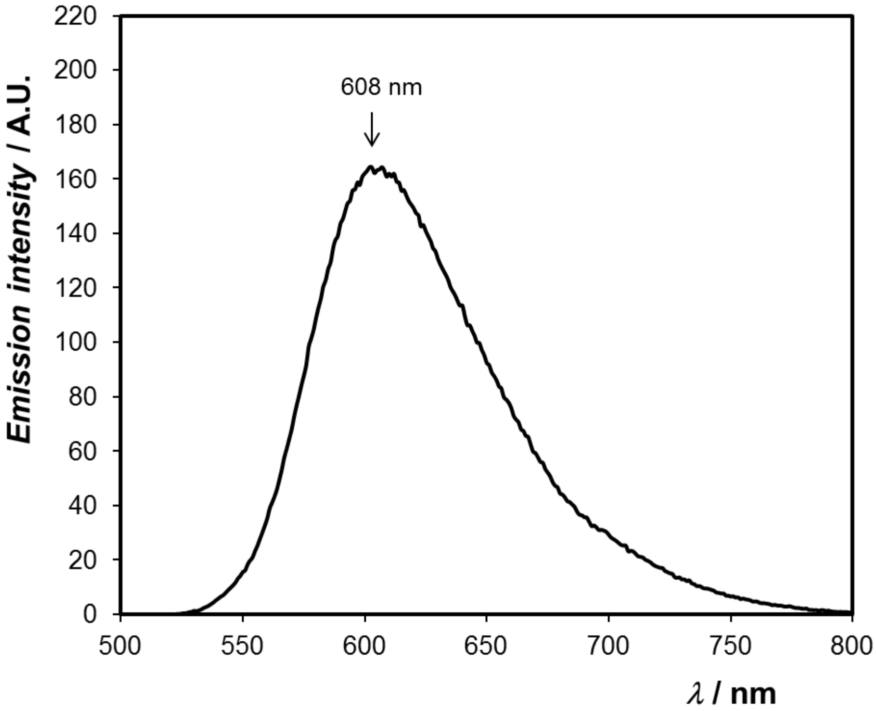

Figure 5.2: Emission profile of 20 µM $[Ru(bpy)_2(picCOOH)]^{2+}$in 0.10 M chloride-free PBS (pH 7.4). Emission spectra were collected with a slit width of 5 nm.

5.2.1.3 Raman analysis

Figure 5.3 illustrates the Raman spectra for the $[Ru(bpy)_2(picCOOH)]^{2+}$ complex acquired using a 458 nm laser in the range 200−1700 cm^{-1}. The Raman spectra mainly in the region of 2000 to 500 cm^{-1} are useful for the identification of ruthenium coordination compounds and provide further information on ligand and anion coordination as well as the structure of the complexes studied.[260] Following excitation of $[Ru(bpy)_2(picCOOH)]^{2+}$ at 458 nm the bipyridyl vibrational modes can be observed at 666, 1026, 1196, 1273, 1318, 1488, 1561 and 1606 cm^{-1} and can be attributed to pyridyl in-plane twisting, ring breathing, CCH (in-plane bending), C-C (inter-ring bending), C=N stretching, C=N stretching, C=C stretching and C=C stretching, respectively.[261] Additional Raman bands observed at 340, 1427 and 1457 cm^{-1} can be attributed to Metal-Ligand stretching (ruthenium-nitrogen stretch) and post-resonance, respectively.[262,263] The 458 nm laser line is coincident with the main visible MLCT absorption of the $[Ru(bpy)_2(picCOOH)]^{2+}$complex (as shown in the UV-vis absorbance profiles (Figure 5.1)) and under these resonance conditions the vibrational modes associated only with the chromophores are enhanced.[175]

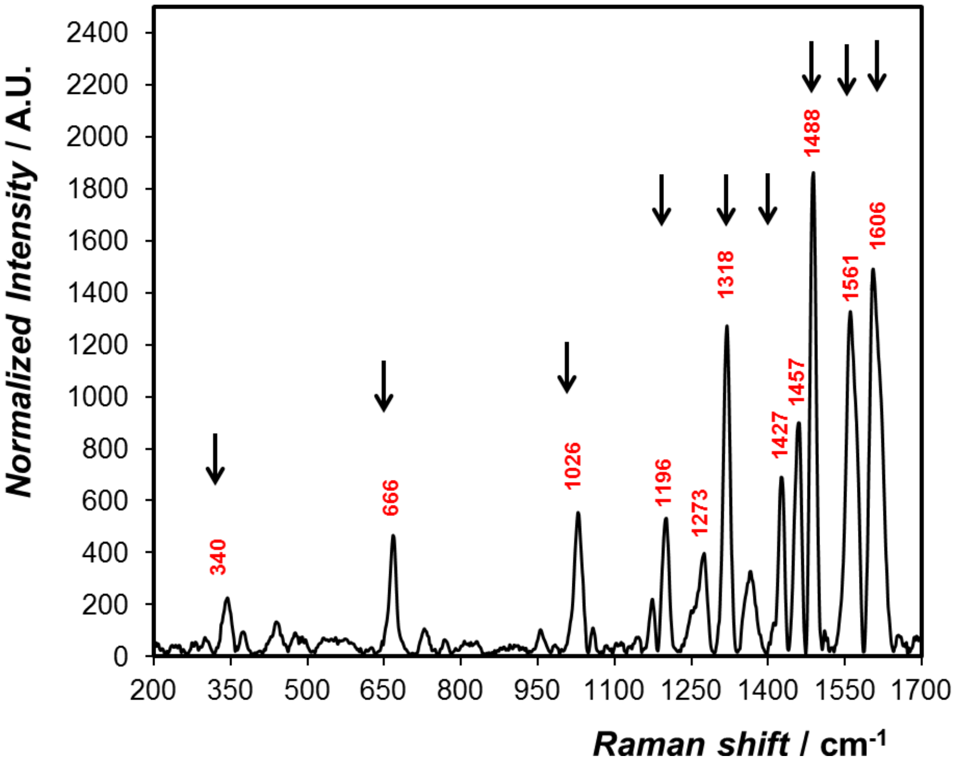

Figure 5.3: Raman spectra of $[Ru(bpy)_2(picCOOH)]^{2+}$. Solid state analysis of the samples was conducted using the 458 nm excitation laser line. The spectrum was gathered with 5 acquisitions and an exposure time of 3 seconds with a laser power of 2 mW. The arrows visible on the spectrum indicate signature bipyridyl vibrational modes.

5.2.1.4 ECL

Figure 5.4A and B shows CV curves and corresponding ECL response of 50 µM $[Ru(bpy)_2(picCOOH)]^{2+}$ complex recorded in the presence of 1mM TPA in 0.1 M PBS at a gold electrode and ITO electrode, respectively. It is important to note, that unlike traditional PBS the PBS used in this thesis is chloride free and the formation of the gold oxide is not associated with chloride. From Figure 5.4A for the CV profiles, it is evident that in the presence of TPA the anodic peak of gold appears to be small. This might be attributed to the catalytic oxidation of TPA at the electrode surface.[264] Furthermore, the anodic peak currents for the $Ru^{2+/}Ru^{3+}$ couple exist at approximately 1.1 V.[265] From Figure 5.4A it is evident that at scan rates of 0.01 V s^{-1} (slow) and 0.05 V s^{-1} (intermediate) the ECL signals appeared to be quite low in comparison to the ECL signal observed for the fast scan rate (0.1 V s^{-1}). This is because at the fast scan rate gold oxides might not have yet formed and thus direct oxidation of TPA might be favoured at the surface of the gold electrode. Another explanation might be that at 0.1 V s^{-1} both the Ru^{2+} and TPA was in high concentrations. When the scan rate was changed to a slower scan, in this case, 0.01 V s^{-1} (the time for the species to be consumed has been increased) the electrogenerated species in solution becomes depleted and thus a decrease in ECL intensity is observed. Similarly, Figure 5.4B illustrates an increase in ECL signal for a scan rate of 0.1 V s^{-1}. The ECL onset and maximum intensity potential at this scan rate is approximately +0.9 V and +1.4 V, respectively. TPA oxidation at the ITO electrode surface results in the production of a short lived radical cation, $TPA^{+\bullet}$, which is a highly reducing intermediate.[266] The Ru^{2+} centres are oxidized to Ru^{3+} at the electrode which are then chemically reduced by the $TPA^{\bullet}$ to an electronically excited state, $Ru^{2+}*$, resulting in an enhanced oxidation current (Figure 5.4B). The obtained results suggests that the $[Ru(bpy)_2(picCOOH)]^{2+}$ complex demonstrates good electrochemical and photophysical behaviour, and thus can be employed as an ECL emitter in the proposed ECL immunosensor.

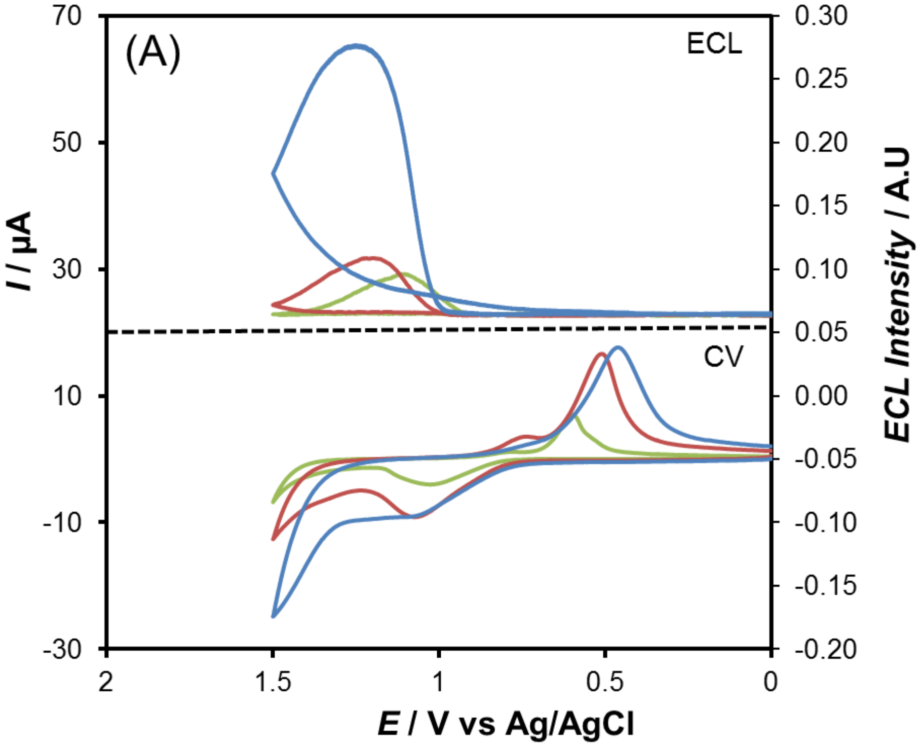

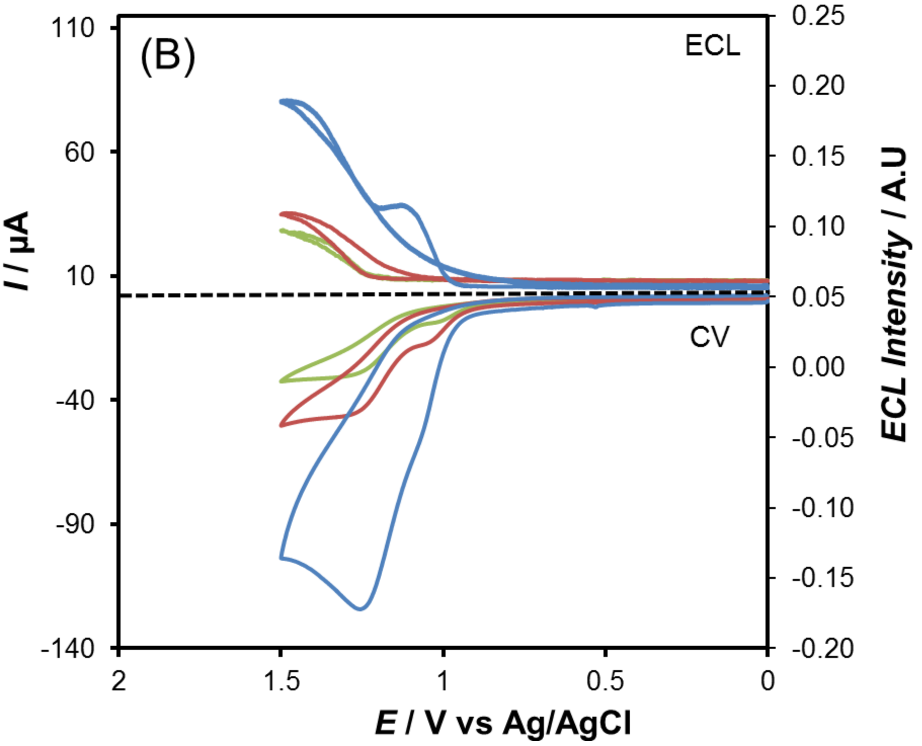

Figure 5.4: ECL response and corresponding cyclic voltammograms of 50 μM [Ru(bpy)$_2$(picCOOH)]$^{2+}$ in 0.10 M chloride-free PBS containing 1 mM TPA, at a gold disc electrode with an area of 0.0314 cm^2 (A) and ITO

electrode with an area of 1.25 cm^2 (B), respectively, at scan rates 0.01, 0.05 and 0.1 V s^{-1}. The scan was linearly swept from +0.2 V to +1.5 V.

5.2.2 Characterisation of the Antibody-dye Conjugate

5.2.2.1 Absorbance

It should be noted that biological reactions naturally occur in aqueous environments, thus it was important to use aqueous media throughout the antibody-dye conjugation and the sensor application process. However, the $[Ru(bpy)_2(picCOOH)]^{2+}$ complex is not soluble in aqueous media, thus it had to be dissolved in 0.1% final concentration (v/v) of DMSO which is an acceptable limit for biological materials.[267,268] Thus, its presence did not interfere with the antibody functioning.

The antibody-dye conjugate was synthesised according to the procedure described in the Chapter 2, Section 2.3.3.3. Figure 5.5 shows UV-vis spectra of a commercially available secondary monoclonal antibody (Mab), known as 19C7; $[Ru(bpy)_2(picCOOH)]^{2+}$ dye and the $[Ru(bpy)_2(picCOOH)]^{2+}$ labelled 19C7 secondary Mab conjugate in 10 mM chloride-free Dulbecco's phosphate buffered saline (DPBS, pH 7.4, 0.1 M). From Figure 5.5 distinct bands of the antibody-dye conjugate (green line) can be observed at approximately 280 nm and 457 nm which corresponds to the characteristic peaks of the 19C7 secondary Mab due to amino acids (blue line) and the ruthenium due to MLCT transitions (red line), respectively. This indicates that $[Ru(bpy)_2(picCOOH)]^{2+}$ has been successfully labelled to the secondary Mab. Furthermore, the degree of dye labelling was determined by using Equations 5.1, 5.2 and 5.3 as seen below.

Known parameters (obtained from UV-vis spectrum in Figure 5.5):

(ε) - protein molar extinction coefficient.

(A_{max}) - Absorbance (A) measured at the wavelength maximum (λ_{max}).

(A_{280nm}) - Correction factor (CF); adjusts for the amount of absorbance at 280 nm caused by the dye.

$[Ru(bpy)_2(picCOOH)]^{2+}$ dye

Ru dye (ε) = 13033 M^{-1} cm^{-1}

Ru dye (A_{max}) = 0.061

Ru dye (A_{280nm}) = 0.392

- Since Ru absorbs at 280 a correction factor is required

$$\therefore CF = \frac{Dye\ A_{280\ nm}}{Dye\ A_{\lambda max}} = \frac{0.392}{0.061} = 6.426 \qquad \textbf{[5.1]}$$

19C7 Secondary Mab

19C7 Mab (Molecular weight) = 160 000 g mol^{-1}

19C7 Mab (ε) = 208 000 M^{-1} cm^{-1}

19C7 Mab (A_{280nm}) = 0.137

Ru dye- antibody conjugate

Ru dye-antibody (A_{max}) = 0.023

Ru dye-antibody (A_{280nm}) = 0.235

$$19C7\ Mab\ conc\ (M) = \frac{Conjugate(A_{280\ nm}) - Conjugate(A_{max}) \times CF}{\varepsilon_{19C7\ Mab}} \quad \textbf{[5.2]}$$

$$\frac{0.087}{208\,000\ M^{-1}cm^{-1}} = 4.192 \times 10^{-7} mol\ L^{-1}$$

$$Moles\ Ru\ dye\ per\ mole\ 19C7\ Mab = \frac{Conjugate\ (A_{max})}{\varepsilon_{Dye} \times 19C7\ Mab_{concentration}} \quad \textbf{[5.3]}$$

$$\frac{0.023}{13033\ M^{-1}cm^{-1} \times 4.192 \times 10^{-7} mol\ L^{-1}}$$

$$= 4.21\ moles\ Ru\ dye\ per\ mole\ of\ 19C7\ Mab$$

Thus, an average of 4 dye labels is present on each antibody. This is a desirable ratio since over-labelling can cause quenching of dye or loss of biological activity of the antibody, and in contrast, too few dye labels will yield a less intense weak ECL signal.[269,270]

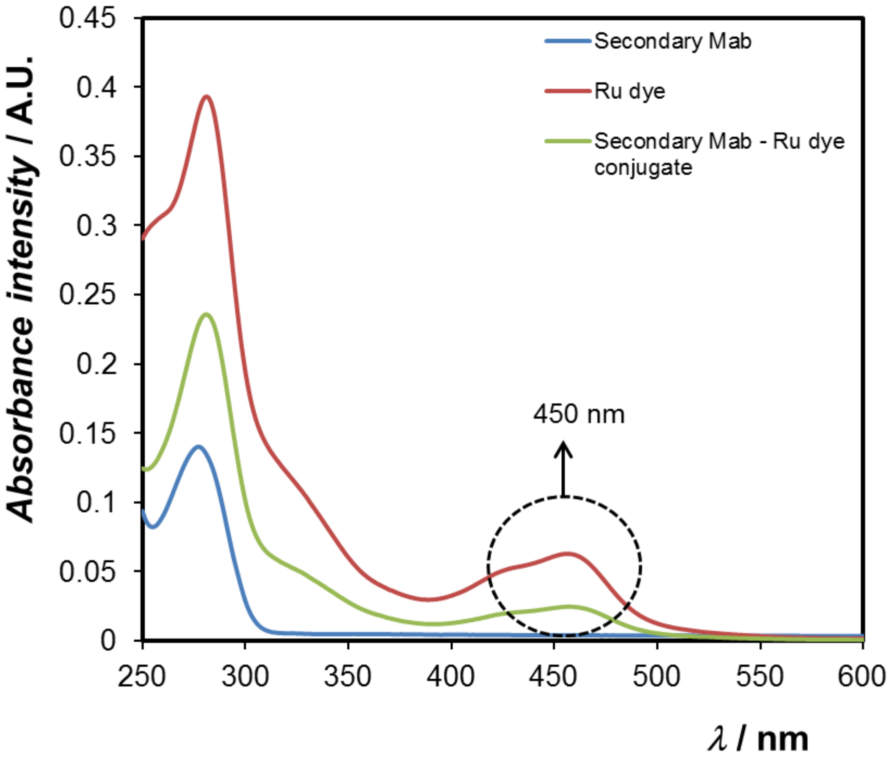

Figure 5.5: UV–vis absorption spectra of 19C7 secondary Mab (blue line), $[Ru(bpy)_2(picCOOH)]^{2+}$ dye (red line) and $[Ru(bpy)_2(picCOOH)]^{2+}$ labelled 19C7 secondary Mab (green line) in 10 mM chloride-free DPBS (pH 7.4).

After the successful conjugation process, the concentration of the secondary Mab labelled dye in the deposition solution was optimised based on the ECL intensity in the overall assy. Figure 5.6 shows fluorescence spectra of the 19C7 Mab-Ru dye conjugate. Upon analysing the conjugate by a fluorescence plate reader, a maximum emission at 608 nm could be seen. This is attributed to the presence of the $[Ru(bpy)_2(picCOOH)]^{2+}$ dye when excited into the MLCT absorbance band at 457 nm. Here, an increase in the concentration of the secondary Mab labelled dye results in an increase in the intensity, as would expect. A concentration of 100 µg mL^{-1} of the secondary Mab labelled dye was chosen because the response at this concentration was the highest and also to ensure that every troponin I (cTnI) target is labelled with the secondary Mab labelled dye. By using optical excitation, nanomolar concentrations of the secondary labelled antibody can be detected.

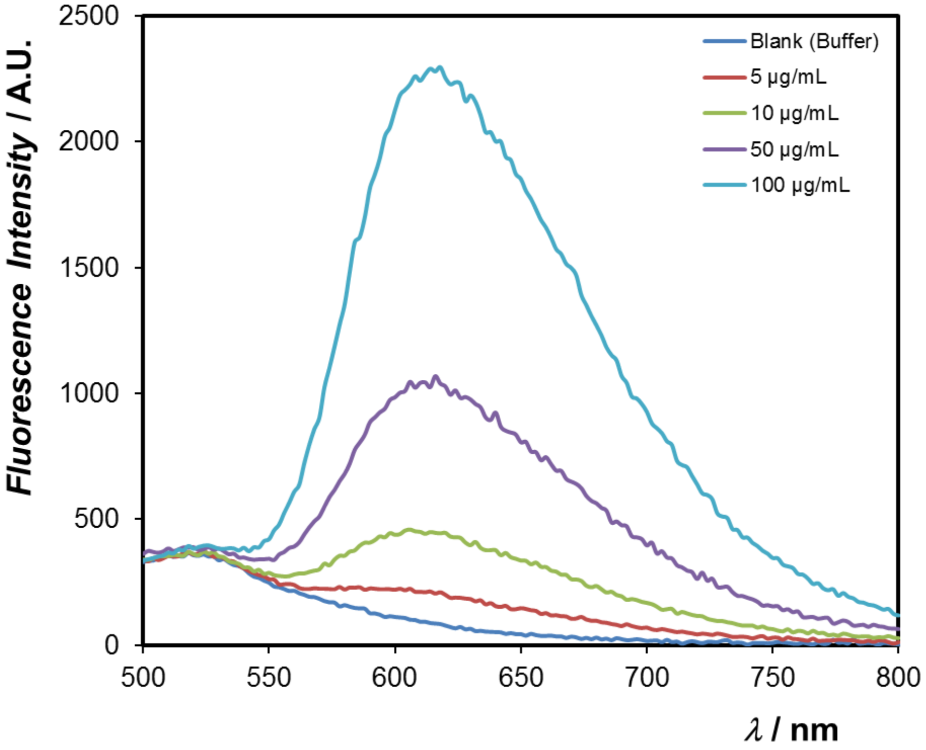

Figure 5.6: Illustrates fluorescence spectra of different concentrations of the secondary Mab labelled dye incubated with fixed concentrations of anti-cTnI primary Mab (100 µg mL^{-1}) and cTnI target (1 µg mL^{-1}) in a black 96 well-plate for 1 hour, at 37°C. The analysis was done on a Safire 2 plate reader (Tecan).

5.2.3 Characterisation of Sandwich Immunosensor

5.2.3.1 ECL Response with and without cTnI

Here, the electrochemical response of the synthesised $[Ru(bpy)_2(picCOOH)]^{2+}$ labelled secondary Mab in the absence and presence of target analyte, cTnI, was investigated, by using ECL as signal readout. Figure 5.7 shows the ECL response of the Ru dye-antibody conjugate reacted with different modified surfaces (A) primary monoclonal antibody (Mab)/16-mercaptohexadecanoic acid (16-MHDA)/gold (Au), (B) bovine serum albumin (BSA)/primary Mab/16-MHDA/Au and (C) cTnI/BSA/primary Mab/16-MHDA/Au. From Figure 5.7 no ECL signal was observed for secondary Mab-Ru/primary Mab/16-MHDA/Au (blue line). This is a positive result in the sense that it provide evidence that no cross-reactivity between the primary and the secondary antibody occurred. It should be noted that the most common reason for the discrepancy between immunoassay measurements is the difference in the epitope specificities of the antibodies.[271] In this case the primary and secondary antibodies have different epitope binding sites which are specific to certain regions along the cTnI molecule, thus no cross-reactivity should occur. For the secondary Mab-Ru/BSA/primary Mab/16-MHDA modified Au surface (green line) the ECL intensity increased greatly even in the absence of the cTnI antigen. This result suggests that BSA promotes non-specific adsorption due to the presence of mouse IgG.[272,273] Mouse IgG can bind to the sticky sites on the anti-cTnI mouse primary Mab and the anti-cTnI mouse labelled secondary Mab due to it being from the same host species. Thus, the ECL signal observed in the presence of BSA should be considered as background. Furthermore, in the presence of 0.1 pg mL^{-1} cTnI (red line) a higher ECL signal can be observed than for the secondary Mab-Ru/BSA/primary Mab/16-MHDA/Au surface. This indicates that both the primary and secondary antibodies are selective to cTnI antigen. The obtained data demonstrates that the Ru dye-antibody conjugate results in the generation of a high ECL signal. It is expected that an increase in cTnI analyte concentration will yield an increase in the ECL intensity in the presence of the Ru dye-antibody conjugate.

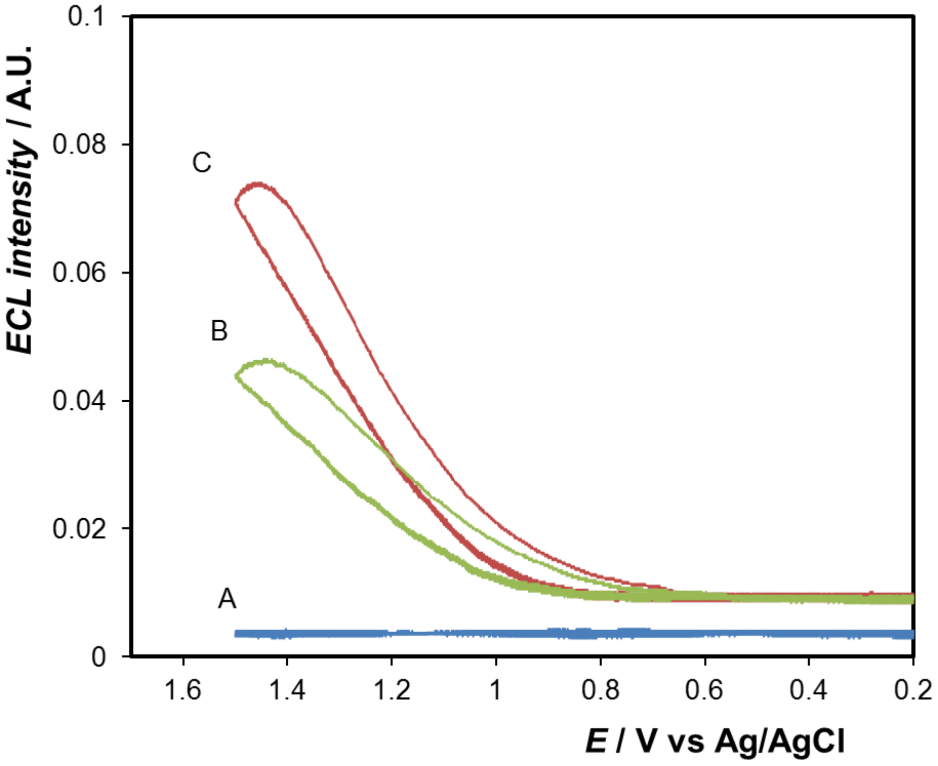

Figure 5.7: ECL intensity vs potential profiles for different modified electrodes (A) secondary Mab-Ru/primary Mab/16-MHDA/Au, (B) secondary Mab-Ru/BSA/primary Mab/16-MHDA/Au and (C) secondary Mab-Ru/cTnI/BSA/primary Mab/16-MHDA/Au. Measurement solutions:

0.10 M chloride-free DPBS (pH 7.4) containing 50 mM TPA, scan rate, 0.05 V s^{-1}. Voltage of the photomultiplier tube was biased at -850V.

5.2.4 Effect of Electrode Material on ECL Response

In order to obtain maximum ECL readout, experimental parameters that directly affect the sensitivity of the immunoassay were optimised; in particular, the supporting substrate for immunoassay fabrication. Additionally, the working concentrations of the primary and secondary antibodies were chosen to be 100 µg mL^{-1}. While the binding time for the primary Mab, secondary Mab and the cTnI antigen was 60 minutes, respectively. Figure 5.8 shows the fabrication of the immunoassay on different supporting substrates such as, indium tin oxide coated polyethylene terephthalate plastic (ITO PET)/glass, gold (Au) coated silica wafer, Au-Au coated silica wafer and Au disc electrodes. The same sensor fabrication protocol was used for the various substrates and a more detailed description on the protocol can be found in Chapter 2, Section 2.3.3.5. However, in the case of ITO surface chemistries, 16-phosphonohexadecanoic acid was used to form hydroxyl groups with the oxides of the ITO for antibody attachement.[274] Also, the ITO electrode and Au silica wafers have larger surface areas compared to the Au disc electrode. For this reason, the amount of moles of antibody in the working solutions was considered. The coverage (whether low or high) of the primary antibody on the electrode surface will influence the amount of target analyte and hence the amount of antibody-dye conjugate that will bind. From Figure 5.8 it can be seen that the ITO glass (red line) gave a higher ECL signal output compared to the ITO PET (dark blue line) electrode. While the Au-Au coated silica electrode appeared to have a higher maximum ECL signal compared to the Au coated silica electrode. Adsorption and electrode hydrophobicity might influence the performance of these electrodes. Figure 5.8 further revealed that the conventional Au disc electrode (pink line) demonstrates the highest ECL intensity due to its pure bulk nature and for this reason has been chosen as the underlying substrate for future immunoassay fabrication.

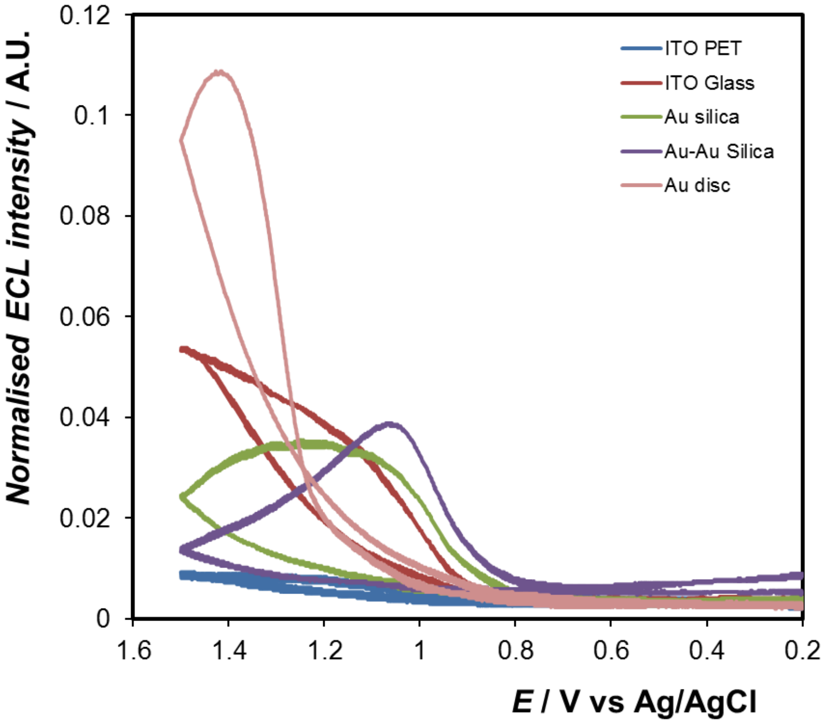

Figure 5.8: ECL intensity versus potential profiles for different electrode substrates. 100 µg mL^{-1} secondary Mab-Ru / 0.1 pg mL^{-1} cTnI/ 1% BSA/ 100 µg mL^{-1} primary Mab/16-MHDA modified ITO PET, ITO glass, Au coated silica, Au-Au coated silica and Au disc electrodes in 0.10 M

chloride-free DPBS (pH 7.4) containing 50 mM TPA, at 0.05 V s^{-1}. Voltage of the photomultiplier tube was biased at -850V.

5.2.5 Application of Sandwich Immunosensor

5.2.5.1 Conventional ECL

In order to evaluate the performance of the fabricated sandwich immunosensor, different concentrations of cTnI were measured by using electrochemiluminescence as signal readout. Figure 5.9 showed that the ECL intensity increased with increasing concentration of cTnI in the range 0.001 pg mL^{-1} to 0.50 pg mL^{-1}. Figure 5.10 illustrates the corresponding calibration curve of the ECL intensity profiles of the immunosensor for different concentrations of cTnI. The curve showed a linear relationship, meaning the ECL intensity was linearly dependent on the concentration of the cTnI antigen with a correlation coefficient (R^2) of 0.99. The sensitivity of 2.4 pg mL^{-1} was derived from the slope of the calibration curve and the limit of detection (LOD) was calculated to be 0.03 pg mL^{-1}. Furthermore, the assay precision of the ECL immunosensor was also evaluated using three different electrodes fabricated independently. The proposed immunosensor exhibited a very high sensitivity towards cTnI making this sensor a feasible method for detection because the levels of cTnI in serum samples are between 5 and 50 ng mL^{-1} when cardiac events occur.[275] Additionally, a comparative study between the proposed immunosensor with previous reported sensors has been done and it was tabulated in Table 5.1.[256,276–279] It can be seen that the proposed immunosensor exhibited excellent analytical response to cTnI compared with other reported immunoassays.

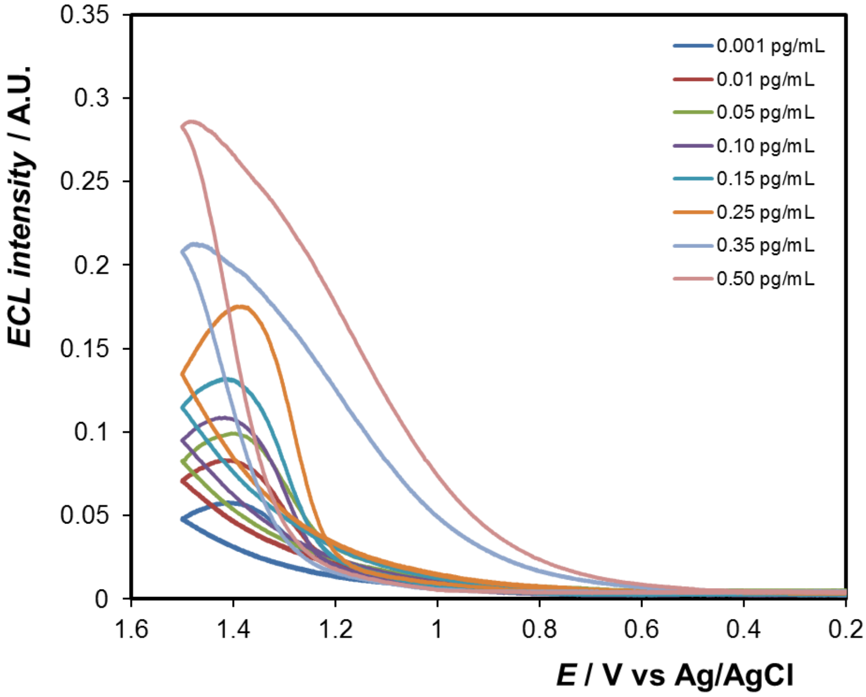

Figure 5.9: ECL intensity profiles of the immunosensor in the presence of different concentrations of cTnI based on sandwich-type format in 0.10 M DPBS (pH 7.4) containing 50 mM TPA, at 0.05 V s^{-1}. The concentrations of cTnI range from 0.001 pg mL^{-1}, 0.01 pg mL^{-1}, 0.05 pg mL^{-1}, 0.10 pg mL^{-1}, 0.15 pg mL^{-1}, 0.25 pg mL^{-1}, 0.35 pg mL^{-1} and 0.50 pg mL^{-1}. Binding time was 60 minutes. The supporting substrate is a 2 mm diameter Au disc electrode with an area of 0.0314 cm^2. Voltage of the photomultiplier tube was biased at -850V.

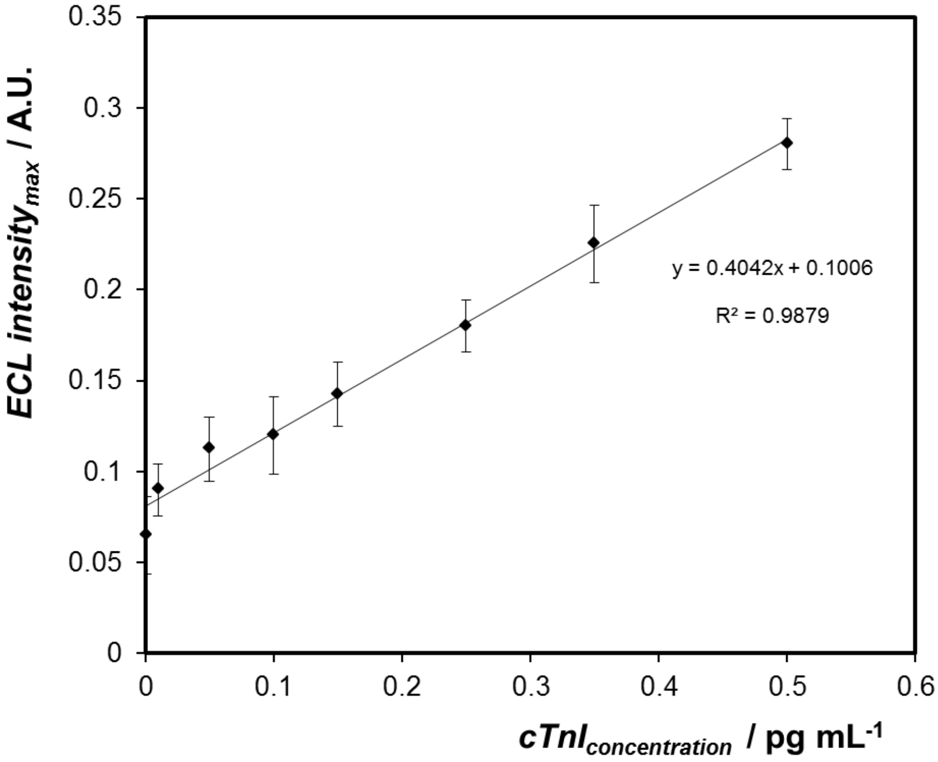

Figure 5.10: Corresponding calibration curve of the ECL intensity profiles of the immunosensor for different concentrations of cTnI. The error bars represent the standard deviation (n = 3 for each point).

Table 5.1: Comparison of various cTnI detection strategies with the proposed ECL sandwich immunoassay

Method of analysis	**LOD/ pg mL^{-1}**	**References**
ELISA	27	Cho et al.[276]
ECL immunoassay	2	Shen et al.[256]
ECL immunoassay	0.083	Zhou et al.[277]
Electrochemical immunoassay	500	Guo et al.[278]
Optomagnetic biosensor	30	Dittmer et al.[279]
ECL immunoassay	**0.03**	**Present work**

5.2.6 Bipolar Electrochemical Studies

5.2.6.1 Independently Addressable Microband Gold Electrodes

As discussed previously one of the key considerations of this thesis is to integrate ECL in miniaturised wireless sensors for possible use in bioanalytical applications. With this in mind, having successfully fabricated and applied an ECL immunosensor for troponin detection by conventional means, a wireless ECL detection setup of the same system was investigated. Here, an independently addressable microband electrode (IAME) was employed as the miniaturised device. IAME fall under the category of microelectrodes and offer advantages over conventional larger electrodes like, high signal-to-background ratio, steady-state current on a short time scale, and low ohmic *iR* drop.[280] Owing to this behaviour, IAME can be used as point-of-care (POC) in biological systems that deal with low quantities of analyte. Furthermore, IAMEs can give an understanding about the fundamentals of transport, kinetics, and double-layer structure at their surfaces.[281] Detection at individual microelectrodes offers very small responses.[282] However, to overcome this issue, two or more of the microband array members can be employed to act as a generator and collector/redox cycling system, and thus allow for a larger response. In this thesis the IAME was employed as a three and/or four electrode system for possible wireless sensor development.

5.2.6.1.1 Voltammetry

The first step was to evaluate the electrochemical response of the IAME by using CV. The IAME employed here, consists of four gold microbands that are 2 mm long and 10 µm wide with an inter-electrode distance of 10 µm (Figure 5.11A). Three of the four bands were employed as a reference electrode (RE), counter electrode (CE) and working electrode (WE), respectively. Figure 5.11B illustrates voltammograms of IAME in the absence (i) and presence (ii) of 50 µM $[Ru(bpy)_3]^{2+}$ in 0.1 M PBS (pH 7.4), at a scan rate of 0.1 V s^{-1}. It is important to note, that unlike traditional PBS the PBS used here and throughout is chloride free and the formation of the gold oxide is not associated with chlorides. It is evident from Figure 5.11B that no oxidation or reduction peaks for the $[Ru(bpy)_3]^{2+}$ at the IAME was observed (ii), however, the current seems smaller. This is an unexpected result and it's unclear how addition of an electroactive species can decrease the faradaic current.

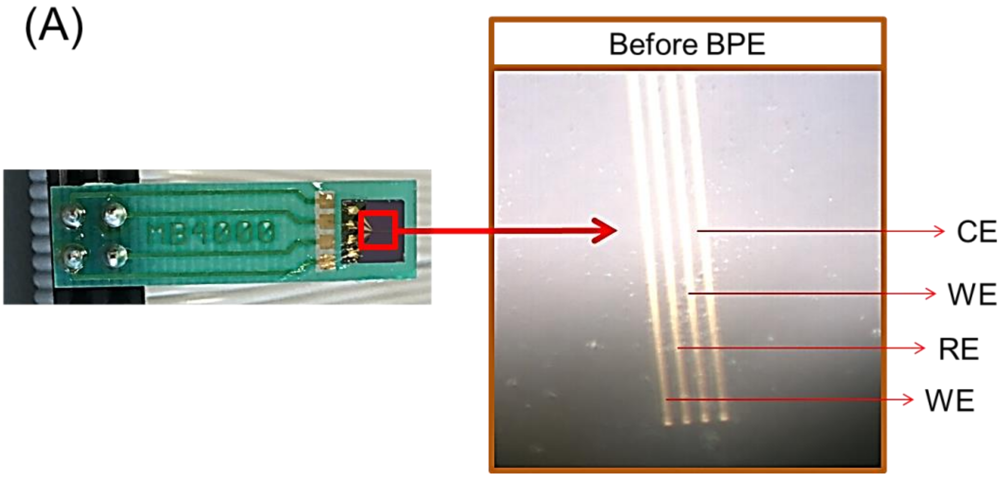

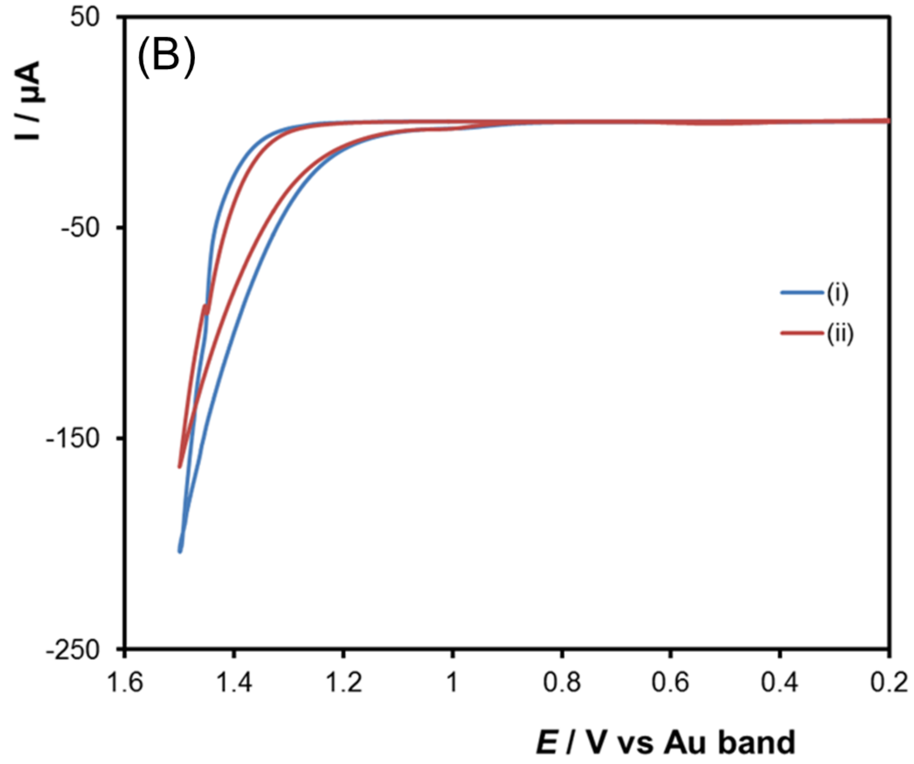

Figure 5.11: Displays (A) design of the independently addressable microband electrode consisting of four gold microbands that are 2 mm long and 10 µm wide with inter-band spacing of 10 µm, and (B) voltammetry of IAME in the absence (i) and presence (ii) of 50 µM $[Ru(bpy)_3]^{2+}$ in 0.1 M chloride-free PBS (pH 7.4), at a scan rate of 0.1 V s^{-1}.

5.2.6.1.2 ECL

Figure 5.12 illustrates the ECL and corresponding CV response of the IAME in 0.1 M chloride-free PBS (pH 7.4) containing 50 µM $[Ru(bpy)_3]^{2+}$ and 1 mM TPA, at a scan rate of 0.1 V s^{-1}. Here, all four gold microbands were employed, where two of the four were used as WEs and one as RE and another as the CE. One of the working electrodes was used as the generator while the second one was used as the collector. This setup was preferred because need two microbands to double the light intensity.[283]

In the generator-collector ECL experiment the generator potential was scanned from 0 V to 1.5 V to oxidise $[Ru(bpy)_3]^{2+}$. While the potential at the collector was kept constant at approximately 0.85 V, this is the potential at which TPA oxidation occurs.[91] This type of set up allows for the simultaneous production of radical cations $[Ru(bpy)_3]^{2+}$ and TPA, respectively, and since the radicals are continuously produced they are readily available to react with each other. The radical species formed at the generator and collector microband diffuse together and react to form $[Ru(bpy)_3]^{2+*}$. From Figure 5.12 it is evident that the onset of ECL started at approximately 0.75 V which is about 100 mV to 350 mV less positive than the peak potential for TPA oxidation and $[Ru(bpy)_3]^{2+}$ oxidation versus Ag/AgCl, respectively. However, the ECL wave reached a maximum at approximately 1.3 V.

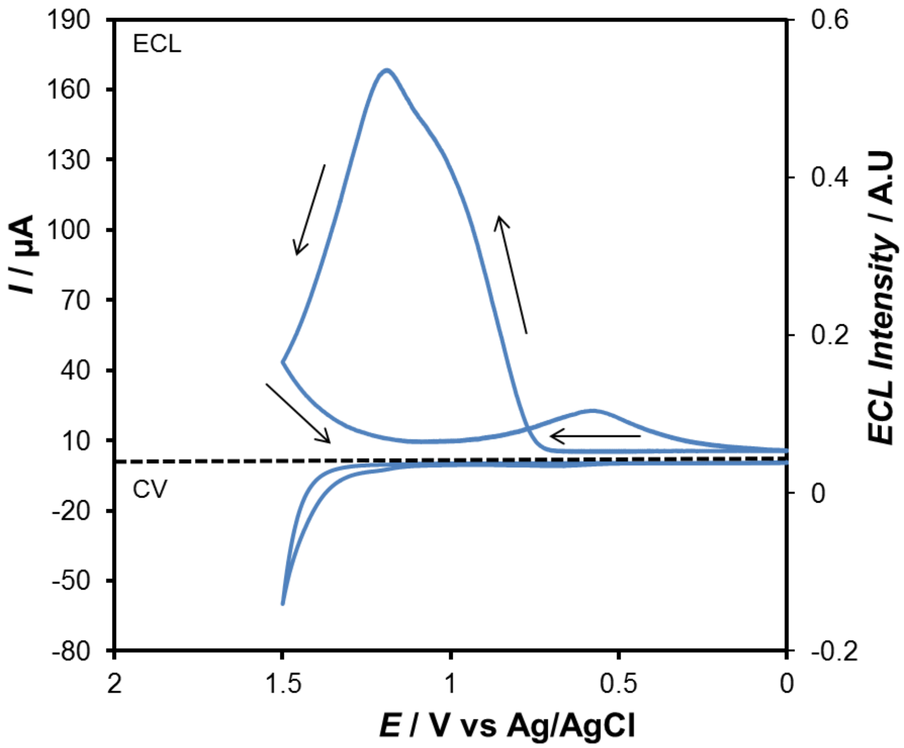

Figure 5.12: ECL response and corresponding cyclic voltammogram of 50 µM $[Ru(bpy)_3]^{2+}$ in 0.10 M chloride-free PBS containing 1 mM TPA, at an IAME. The scan rate is 0.1 V s^{-1} and the arrows show the direction of the scan. Voltage of the photomultiplier tube was biased at -850V.

Having studied the IAME's electrochemical performance, further analysis by bipolar electrochemistry was done. In the bipolar electrochemical setup two of the four microbands were used as bipolar electrodes (BP_{elecs}) while the second pair was used as feeder electrodes. The working solution consisted of 5mM $[Ru(bpy)_3]^{2+}$ and 25 mM TPA in a very low concentration of DPBS. High molar concentrations of the ECL emitter and coreactant were used so that visual detection by a CCD camera could be realised. A drop of the reactant solution mixture was placed on the microbands and the voltage was varied from 0 V to 5 V. As soon as the potential reached 3

V, bubbles started to form. This can be attributed to water reduction.[119] No light was observed at the anodic poles of the BP_{elecs}, and once the bubbles subsided, gold seemed to have been stripped from the silicon underlying base support (Figure 5.13). This result suggests that this IAME is not suitable for use in the fabrication of a wireless immunoassay system. Thus, a new bipolar cell design was developed and investigated.

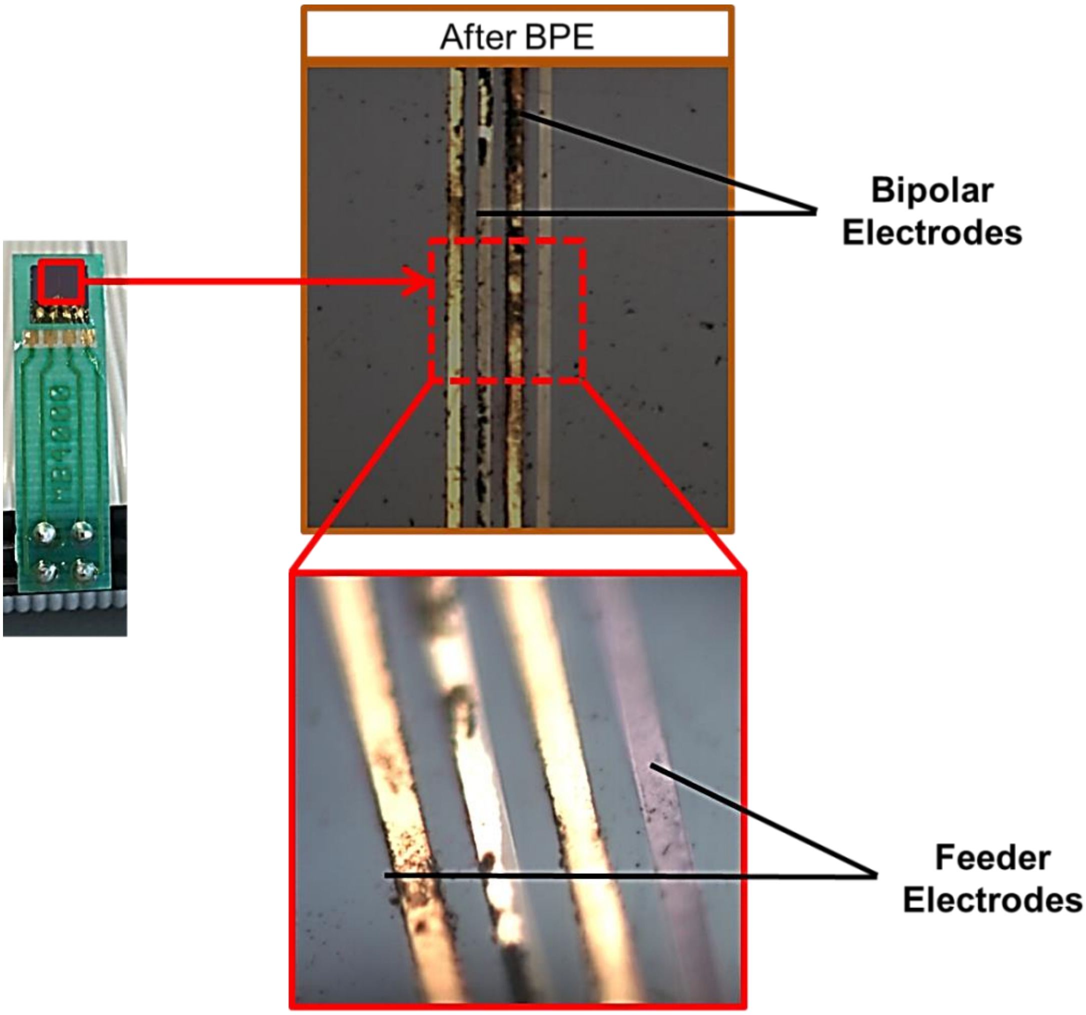

Figure 5.13: Shows photographs of peeled gold on the IAME after applying a voltage to drive bipolar electrochemical reactions.

5.2.6.2 Teflon cell

The attempt to drive bipolar electrochemical reactions at the IAME surface was unsuccessful due to the system and not due to solution chemistries. For this reason, a new bipolar cell was developed. However, one drawback of this design is that it is bigger in size (ideal design for POC should be miniaturised) with one solution compartment (in other words an “open” bipolar cell configuration). This new design was employed to (1) confirm if wireless detection of troponin was possible and (2) determine if ECL output could be enhanced. The bipolar cell can be seen in Figure 5.14 and its design was discussed in detail in Chapter 2 under Section 2.3.3.6.1.

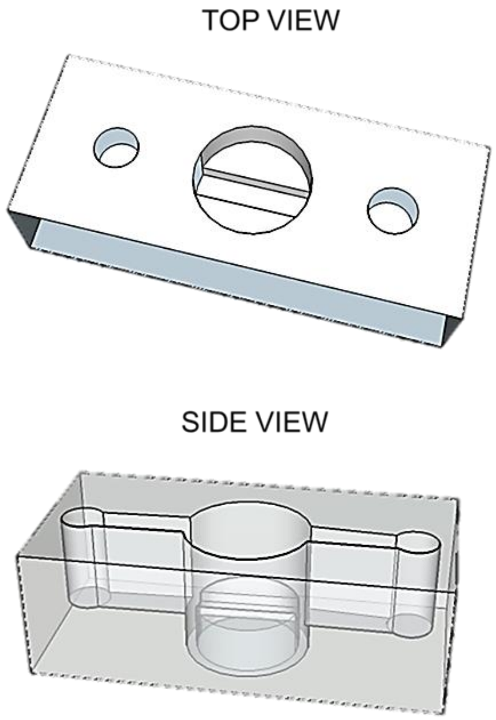

Figure 5.14: Top and side view images of the Teflon bipolar cell. The channel of the cell is 3.6 cm long and can fit a 2.5 cm bipolar electrode.

ITO was used as the BP_{elec} due to its superior transparency which can help to facilitate ECL signal collection by the PMT.[9] Here, the sandwich immunoassay was formed on the anodic pole of the ITO BP_{elec} ex-situ. The modified BP_{elec} was immersed in 50 mM TPA/DPBS solution between two tin feeder electrodes located on opposite ends of the Teflon bipolar cell. Generally, when an external potential between two feeder electrodes are applied, a potential difference occurs across the bipolar electrode, and thus results in redox reactions to occur at the BP_{elec}, that is, oxidation of $[Ru(bpy)_3]^{2+}$/TPA at the anodic pole and simultaneous reduction of oxygen at the cathodic pole.[99]

Figure 5.15 shows the ECL intensity versus time curves for different total potentials applied. This study was conducted to determine the onset potential of wireless cTnI detection. All ECL signals were generated at the same BP_{elec}. The potential difference, ΔE_{elec}, across the 2.5 cm ITO BP_{elec} was calculated to be 4.8 V for an applied total potential of 7 V. This potential difference exceeds the difference between the formal potentials of the redox processes, that is, 0.03 V; thus, simultaneous redox reactions could occur.[88] From Figure 5.15 it is evident that the onset potential for driving bipolar reactions at the BP_{elec} was at 7 V. Here, 1 pg mL^{-1} of cTnI was detected.

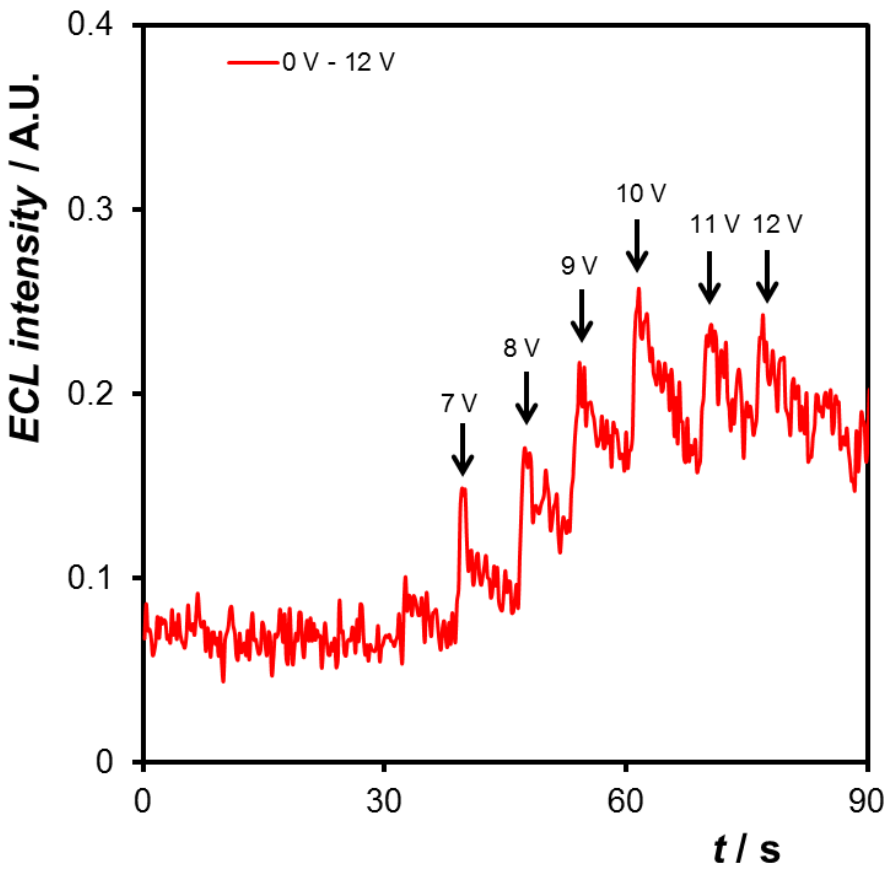

Figure 5.15: Wireless ECL response of the sandwich immunoassay as a function of onset potential responsible for driving redox reactions at the BP$_{elec}$. Voltage of the photomultiplier tube was biased at -850V with an increased sensitivity to reduce signal-to-noise ratio.

In order to improve the performance of the wireless detection system, important parameters like the driving voltage were optimised. Here, 1 pg mL^{-1} of cTnI was detected and the measurements were conducted by using three sets of six different BP$_{elecs}$ fabricated independently. Figure 5.16 shows ECL intensity increased with the driving voltage from 7 V to 10 V. When the driving voltage was below 7 V, no ECL signal was observed. When the driving voltage reached 11 V, the ECL signal became weak and plateaued at about 12 V. Thus, for future bipolar electrochemical experiments a driving voltage of 10 V was preferred because it gave the highest ECL readout.

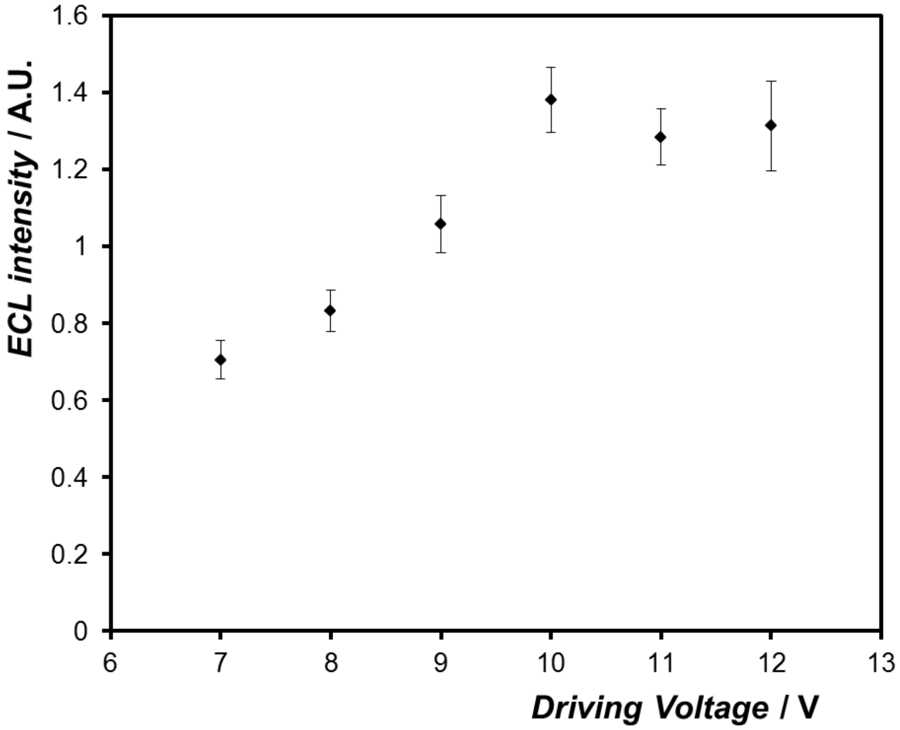

Figure 5.16: BPE/ECL intensity profiles of 1 pg mL^{-1} cTnI as a function of the applied total potential (E_{tot}), ranging from 7 V to 12 V. The error bars represent the standard deviation (n = 3 for each point).

To demonstrate the potential application of the wireless sensing platform, two concentrations of cTnI were detected under the optimised conditions. Figure 5.18 shows that the BP_{elec} displayed an increase in ECL signal from 0.1 pg mL^{-1} to 1 pg mL^{-1} concentrations of cTnI. Here, $[Ru(bpy)_2(picCOOH)]^{2+}$ and TPA were oxidised at the ITO BP_{elec} anode.

The produced TPA$^{\bullet}$ radical species reduced the Ru(bpy)$_2$(picCOOH)]$^{3+}$ to form Ru(bpy)$_2$(picCOOH)]$^{2+*}$ and thus light could be observed.[12]

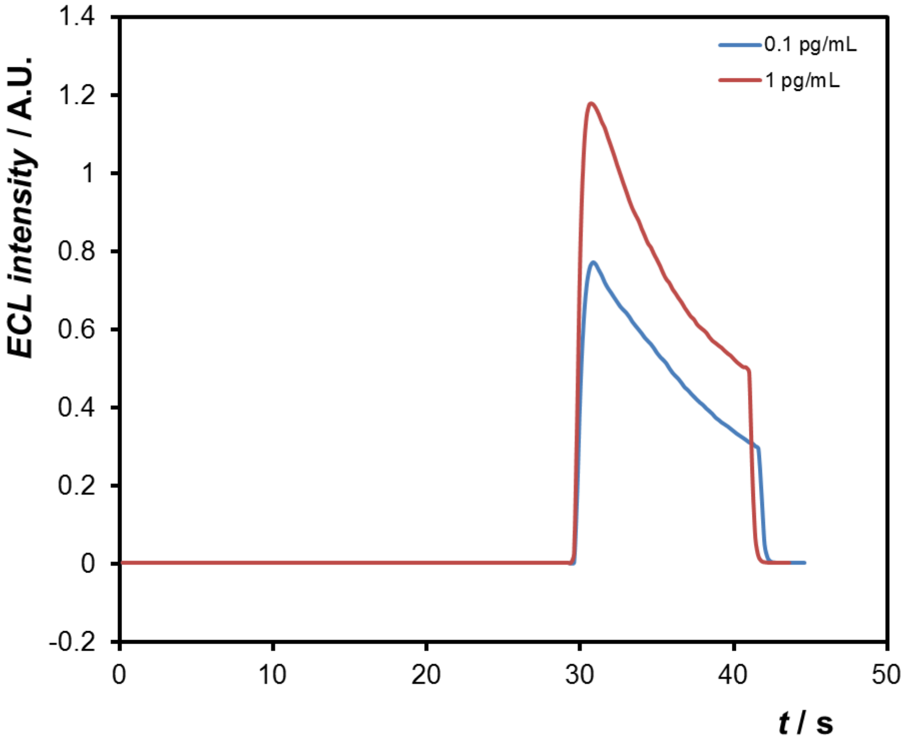

Figure 5.17: ECL response of the wireless sandwich immunoassay incubated with 0.1 pg mL^{-1} and 1 pg mL^{-1} concentrations of cTnI, respectively. The detection was carried out in DPBS solution containing 50 mM TPA, at E_{tot} = 10 V. The voltage of the photomultiplier tube was biased at -850V and the sensitivity was increased to 1×10^7 to reduce signal-to-noise ratio.

In BPE, an oxidation reaction is accompanied by a reduction reaction at the cathode of the BP$_{elec}$. While typically, this cathodic reaction involves reduction of oxygen in the system, here, even when the system was deoxygenated the ECL intensity didn't decrease suggesting that oxygen was not reduced at the cathodic pole of the ITO BP_{elec}. However, experimental observation after running the bipolar experiments suggests that SnO_2 has been reduced to Sn (Figure 5.18).[284] The reduction of ITO is a result of its lower (more negative) reduction potential (-0.94 V vs Ag/AgCl). Furthermore, the reduction of SnO_2 on the cathodic side competed with the reduction of oxygen (about 1.23 V vs Ag/AgCl) and resulted in $[Ru(bpy)_2(picCOOH)]^{2+}$ to be oxidised at a lower external potential, that is, 6 V. In other words, it's quite likely that the SnO_2 was a sacrificial reductant on the cathode side of the ITO BP_{elec}. It is known that anodic reactions could be accelerated by substances which can be reduced more easily on the cathodic pole than that of dissolved oxygen.[119,285] A summary of the redox reactions occurring at the two poles of the ITO BP_{elec} can be seen below, that is:

Anodic pole:

$$[\mathrm{Ru(bpy)_2(picCOOH)}]^{2+} - e^- \rightarrow [\mathrm{Ru(bpy)_2(picCOOH)}]^{3+} \qquad \textbf{[5.4]}$$

$$\mathrm{TPA} - e^- \rightarrow \mathrm{TPA}^{\bullet +} \rightarrow \mathrm{TPA}^{\bullet} + H^+ \qquad \textbf{[5.5]}$$

$$[\mathrm{Ru(bpy)_2(picCOOH)}]^{3+} + \mathrm{TPA}^{\bullet} \rightarrow [\mathrm{Ru(bpy)_2(picCOOH)}]^{2+*} \qquad \textbf{[5.6]}$$

Cathodic pole:

$$O_2 + 4e^- + 4H^+ \rightarrow 2H_2O \qquad \textbf{[5.7]}$$

$$SnO_2 + 4e^- + 4H^+ \rightarrow Sn + 2H_2O \qquad \textbf{[5.8]}$$

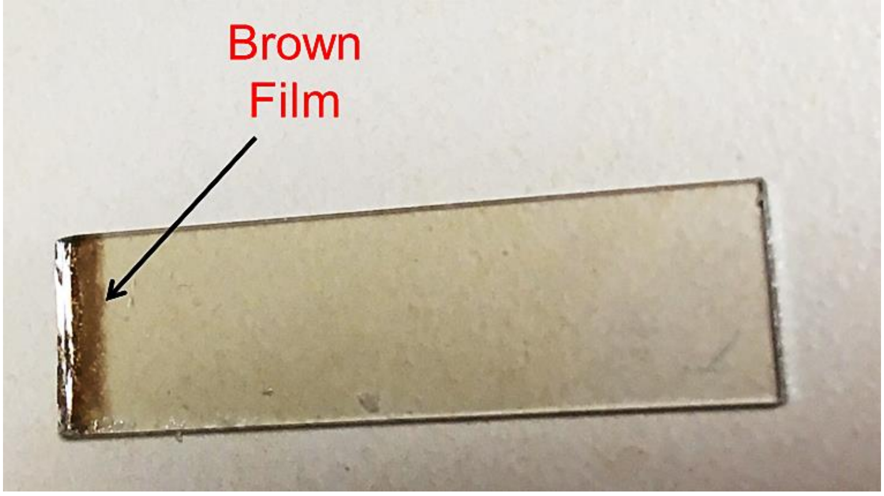

Figure 5.18: Reduction of SnO_2 to Sn at the cathodic pole of the 2.5 cm ITO BP_{elec}.

Moreover, to gain a better understanding of signal production by the BPE approach, comparison studies with a traditional three-electrode system using ITO as working electrode was carried out. The study was conducted under the same experimental conditions, that is, 0.1 pg mL^{-1} and 1 pg mL^{-1} concentrations of cTnI was detected in 0.10 M DPBS (pH 7.4) containing 50 mM TPA. Figure 5.19 illustrates ECL intensity profiles for cTnI detection and it can be seen that the maximum peak value of the ECL emission for 0.1 pg mL^{-1} and 1 pg mL^{-1} of cTnI was ~0.06 and ~0.10, respectively, with an onset potential of 0.8 V (vs Ag/AgCl). Compared with the BPE detection approach, it is evident that in both instances there is only a two-fold increase in signal for a 10-fold increase in concentration from 0.1 pg mL^{-1} to 1 pg mL^{-1}. This might be attributed to the inter-secondary quenching of the labelled secondary Mab.

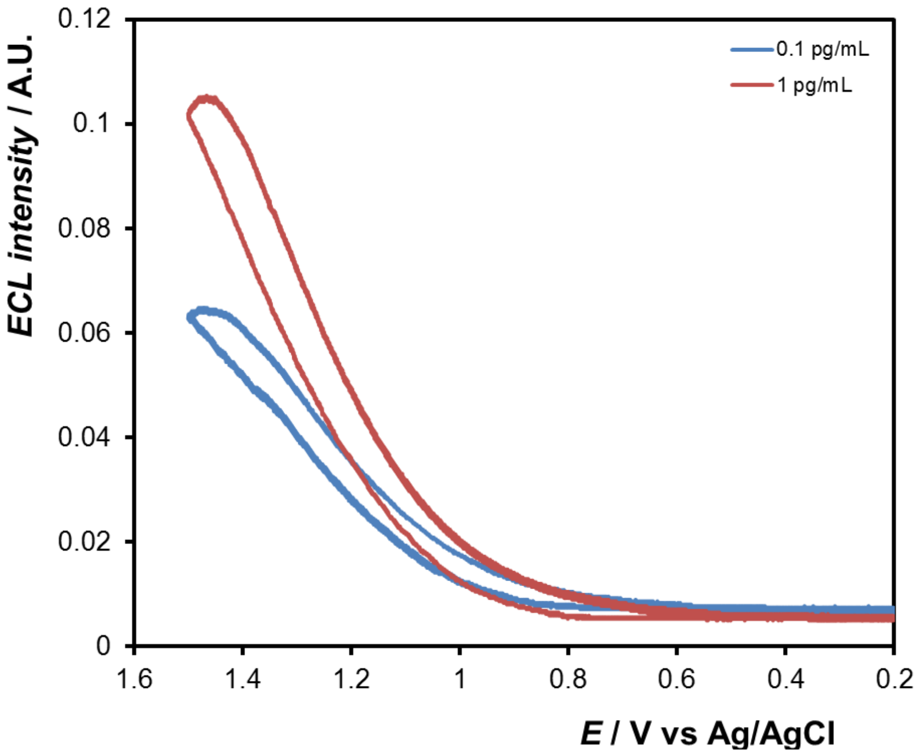

Figure 5.19: Conventional ECL intensity profiles for 0.1 pg mL^{-1} and 1 pg mL^{-1} cTnI, respectively, in 0.10 M DPBS containing 50 mM TPA. Voltage of the photomultiplier tube was biased at -850V.

5.3 CONLUSION

This study demonstrated the successful fabrication and application of a sandwich immunosensor for troponin I detection. Here, ECL was employed as detection strategy and the detection principle of the immunosensor was based on the direct detection of the ECL emitter, $[Ru(bpy)_2(picCOOH)]^{2+}$, that is directly linked to the antigen–antibody immunoreactions. The response of the immunosensor was investigated in the absence and presence of the troponin I analyte and the results revealed that both the primary and labelled secondary antibodies are selective to troponin I antigen. Furthermore, the immunosensor response using different transduction platforms (ITO PET, ITO glass, Au coated silica, Au-Au coated silica and Au disc electrodes) were investigated and the results revealed that the conventional Au disc electrode demonstrates the highest ECL intensity due to its pure bulk nature and for this reason has been chosen as the underlying substrate for the sandwich immunoassay fabrication. Compared with other well-established ECL immunoassays for troponin I detection, the proposed sandwich immunosensor exhibited excellent analytical performance with high sensitivity (2.4 pg mL^{-1}) towards troponin I and an extremely low detection limit of 0.03 pg mL^{-1} (SD, n=3). Furthermore, successful wireless detection of troponin I was achieved here for the first time. Both conventional and bipolar electrochemical detection strategies show great promise and could be easily extended to other biomarkers in the field of clinical applications.

REFERENCES

(1) Ye, S.; Li, H.; Cao, W. Electrogenerated Chemiluminescence Detection of Adenosine Based on Triplex DNA Biosensor. *Biosens. Bioelectron.* **2011**, *26* (5), 2215–2220.

(2) Wei, H.; Wang, E. Electrochemiluminescence of Tris(2,2′-Bipyridyl)Ruthenium and Its Applications in Bioanalysis: A Review: ECL of Ru(Bpy)32+ and Its Applications in Bioanalysis. *Luminescence* **2011**, *26* (2), 77–85.

(3) Benoist, D. M.; Pan, S. Activation of a TiO $_2$ Electrode Using Gold Particles for Efficient Electrogenerated Chemiluminescence from a Ruthenium Complex in Aqueous Solution. *J. Phys. Chem. C* **2010**, *114* (4), 1815–1821.

(4) Snizhko, D. V.; Zholudov, Y. T.; Bilash, O. M.; Kukoba, A. V.; Rozhitskii, M. M. Electrochemiluminescence at Nitrogen Doped Diamond-like Carbon Film Electrodes. *Russ. J. Electrochem.* **2014**, *50* (3), 260–266.

(5) Sentic, M.; Arbault, S.; Bouffier, L.; Manojlovic, D.; Kuhn, A.; Sojic, N. 3D Electrogenerated Chemiluminescence: From Surface-Confined Reactions to Bulk Emission. *Chem Sci* **2015**, *6* (8), 4433–4437.

(6) Arthur, T. S.; Bates, D. J.; Cirigliano, N.; Johnson, D. C.; Malati, P.; Mosby, J. M.; Perre, E.; Rawls, M. T.; Prieto, A. L.; Dunn, B. Three-Dimensional Electrodes and Battery Architectures. *MRS Bull.* **2011**, *36* (7), 523–531.

(7) Duval, J.; Kleijn, J. M.; van Leeuwen, H. P. Bipolar Electrode Behaviour of the Aluminium Surface in a Lateral Electric Field. *J. Electroanal. Chem.* **2001**, *505* (1–2), 1–11.

(8) Yin, X.-B.; Dong, S.; Wang, E. Analytical Applications of the Electrochemiluminescence of Tris (2,2′-Bipyridyl) Ruthenium and Its Derivatives. *TrAC Trends Anal. Chem.* **2004**, *23* (6), 432–441.

(9) Wu, M.-S.; Yuan, D.-J.; Xu, J.-J.; Chen, H.-Y. Sensitive Electrochemiluminescence Biosensor Based on Au-ITO Hybrid Bipolar Electrode Amplification System for Cell Surface Protein Detection. *Anal. Chem.* **2013**, *85* (24), 11960–11965.

(10) Blackburn, G. F.; Shah, H. P.; Kenten, J. H.; Leland, J.; Kamin, R. A.; Link, J.; Peterman, J.; Powell, M. J.; Shah, A.; Talley, D. B. Electrochemiluminescence Detection for Development of Immunoassays and DNA Probe Assays for Clinical Diagnostics. *Clin. Chem.* **1991**, *37* (9), 1534–1539.

(11) Parveen, S.; Aslam, M. S.; Hu, L.; Xu, G. *Electrogenerated Chemiluminescence: Protocols and Applications*; Springer Science & Business Media, 2013.

(12) Richter, M. M. Electrochemiluminescence (ECL). *Chem. Rev.* **2004**, *104* (6), 3003–3036.

(13) Huang, H.; Li, J.; Zhu, J.-J. Electrochemiluminescence Based on Quantum Dots and Their Analytical Application. *Anal Methods* **2011**, *3* (1), 33–42.

(14) Hu, L.; Xu, G. Applications and Trends in Electrochemiluminescence. *Chem. Soc. Rev.* **2010**, *39* (8), 3275.

(15) Knight, A. W. A Review of Recent Trends in Analytical Applications of Electrogenerated Chemiluminescence. *TrAC Trends Anal. Chem.* **1999**, *18* (1), 47–62.

(16) Hercules, D. M. Chemiluminescence Resulting from Electrochemically Generated Species. *Science* **1964**, *145* (3634), 808–809.

(17) Santhanam, K. S. V.; Bard, A. J. Chemiluminescence of Electrogenerated 9,10-Diphenylanthracene Anion Radical1. *J. Am. Chem. Soc.* **1965**, *87* (1), 139–140.

(18) Dufford, R. T.; Nightingale, D.; Gaddum, L. W. Luminescence of Grignard Compounds in Electric and Magnetic Fields, and Related Electrical Phenomena. *J. Am. Chem. Soc.* **1927**, *49* (8), 1858–1864.

(19) Harvey, N. Luminescence during Electrolysis. *J. Phys. Chem.* **1928**, *33* (10), 1456–1459.

(20) Faulkner, L. R.; Bard, A. J. Techniques of Electrogenerated Chemiluminescence. In *Electroanalytical Chemistry*; Wiley: New York, 1977; Vol. 10, pp 1–95.

(21) Park, S.-M.; Tryk, D. A. Excited State Intermediates Probed by Electrogenerated Chemiluminescence. *Rev. Chem. Intermed.* **1981**, *4* (1–4), 43–79.

(22) Faulkner, L. R. [40] Chemiluminescence from Electron-Transfer Processes; Enzymology, B.-M. in, Ed.; Bioluminescence and Chemiluminescence; Academic Press, 1978; Vol. 57, pp 494–526.

(23) Velasco, J. Electrogenerated Chemiluminescence. *Bull. Electrochem.* **1994**, *10* (1), 29–38.

(24) Rivera, V. R.; Gamez, F. J.; Keener, W. K.; White, J. A.; Poli, M. A. Rapid Detection of Clostridium Botulinum Toxins A, B, E, and F in Clinical Samples, Selected Food Matrices, and Buffer Using Paramagnetic Bead-Based Electrochemiluminescence Detection. *Anal. Biochem.* **2006**, *353* (2), 248–256.

(25) Luo, L.; Zhang, Z.; Chen, L.; Ma, L. Chemiluminescent Imaging Detection of Staphylococcal Enterotoxin C1 in Milk and Water Samples. *Food Chem.* **2006**, *97* (2), 355–360.

(26) Zhan, W.; Alvarez, J.; Crooks, R. M. A Two-Channel Microfluidic Sensor That Uses Anodic Electrogenerated Chemiluminescence as a Photonic Reporter of Cathodic Redox Reactions. *Anal. Chem.* **2003**, *75* (2), 313–318.

(27) Maus, R. G.; Wightman, R. M. Microscopic Imaging with Electrogenerated Chemiluminescence. *Anal. Chem.* **2001**, *73* (16), 3993–3998.

(28) Choi, J.-P.; Bard, A. J. Electrogenerated Chemiluminescence (ECL) 79. *Anal. Chim. Acta* **2005**, *541* (1–2), 143–150.

(29) Pyati, R.; Richter, M. M. ECL—Electrochemical Luminescence. *Annu. Rep. Sect. C Phys. Chem.* **2007**, *103* (0), 12–78.

(30) Beideman, F. E.; Hercules, D. M. Electrogenerated Chemiluminescence from 9,10-Diphenylanthracene Cations Reacting with Radical Anions. *J. Phys. Chem.* **1979**, *83* (17), 2203–2209.

(31) Bard, A. J.; Debad, J. D.; Leland, J. K.; Sigal, G. B.; Wilbur, J. L.; Wohlsatdter, J. N. Applications, Theory and Instrumentation. In

Chemiluminescence electrogenerated: Encyclopedia of Analytical Chemistry; Wiley: New York, 2000; Vol. 11, pp 9842–9849.

(32) Leland, J. K.; Powell, M. J. Electrogenerated Chemiluminescence: An Oxidative-Reduction Type ECL Reaction Sequence Using Tripropyl Amine. *J. Electrochem. Soc.* **1990**, *137* (10), 3127–3131.

(33) Kanoufi, F.; Zu, Y.; Bard, A. J. Homogeneous Oxidation of Trialkylamines by Metal Complexes and Its Impact on Electrogenerated Chemiluminescence in the Trialkylamine/$Ru(Bpy)_3^{2+}$ System. *J. Phys. Chem. B* **2001**, *105* (1).

(34) Mccord, P.; Bard, A. Electrogenerated Chemiluminescence .54. Electrogenerated Chemiluminescence of Ruthenium(Ii) 4,4'-Diphenyl-2,2'-Bipyridine and Ruthenium(Ii) 4,7-Diphenyl-1,10-Phenanthroline Systems in Aqueous and Acetonitrile Solutions. *J. Electroanal. Chem.* **1991**, *318* (1–2), 91–99.

(35) FAULKNER, L. R.; GLASS, R. S. 6 - Electrochemiluminescence A2 - Adam, Waldemar. In *Chemical and Biological Generation of Excited States*; Cilento, G., Ed.; Academic Press: San Diego, 1982; pp 191–227.

(36) Miao, W.; Choi, J.-P.; Bard, A. J. Electrogenerated Chemiluminescence 69: The Tris (2, 2'-Bipyridine) Ruthenium (II),(Ru (Bpy) 32+)/Tri-n-Propylamine (TPrA) System Revisited A New Route Involving TPrA+ Cation Radicals. *J. Am. Chem. Soc.* **2002**, *124* (48), 14478–14485.

(37) Wightman, R. M.; Forry, S. P.; Maus, R.; Badocco, D.; Pastore, P. Rate-Determining Step in the Electrogenerated Chemiluminescence

from Tertiary Amines with Tris(2,2‘-Bipyridyl)Ruthenium(II). *J. Phys. Chem. B* **2004**, *108* (50), 19119–19125.

(38) White, H. S.; Bard, A. J. Electrogenerated Chemiluminescence. 41. Electrogenerated Chemiluminescence and Chemiluminescence of the Ru(2,21 - Bpy)32+-S2O82- System in Acetonitrile-Water Solutions. *J. Am. Chem. Soc.* **1982**, *104* (25), 6891–6895.

(39) Ege, D.; Becker, W. G.; Bard, A. J. Electrogenerated Chemiluminescent Determination of Tris(2,2’-Bipyridine)Ruthenium Ion (Ru(Bpy)32+) at Low Levels. *Anal. Chem.* **1984**, *56* (13), 2413–2417.

(40) Tsafack, V. C.; Marquette, C. A.; Pizzolato, F.; J. Blum, L. Chemiluminescent Choline Biosensor Using Histidine-Modified Peroxidase Immobilised on Metal-Chelate Substituted Beads and Choline Oxidase Immobilised on Anion-Exchanger Beads Co-Entrapped in a Photocrosslinkable Polymer. *Biosens. Bioelectron.* **2000**, *15* (3–4), 125–133.

(41) Rongen, H. A.; Hoetelmans, R. M.; Bult, A.; van Bennekom, W. P. Chemiluminescence and Immunoassays. *J. Pharm. Biomed. Anal.* **1994**, *12* (4), 433–462.

(42) Juris, A.; Balzani, V.; Barigelletti, F.; Campagna, S.; Belser, P.; von Zelewsky, A. Ru(II) Polypyridine Complexes: Photophysics, Photochemistry, Eletrochemistry, and Chemiluminescence. *Coord. Chem. Rev.* **1988**, *84*, 85–277.

(43) Tokel, N. E.; Bard, A. J. Electrogenerated Chemiluminescence. IX. Electrochemistry and Emission from Systems Containing Tris(2,2’-

Bipyridine)Ruthenium(II) Dichloride. *J. Am. Chem. Soc.* **1972**, *94* (8), 2862–2863.

(44) Bard, A. J. *Electrogenerated Chemiluminescence*; CRC Press, 2004.

(45) Chang, M.-M.; Saji, T.; Bard, A. J. Electrogenerated Chemiluminescence. 30. Electrochemical Oxidation of Oxalate Ion in the Presence of Luminescers in Acetonitrile Solutions. *J. Am. Chem. Soc.* **1977**, *99* (16), 5399–5403.

(46) Zu, null; Bard, null. Electrogenerated Chemiluminescence. 66. The Role of Direct Coreactant Oxidation in the Ruthenium Tris(2,2')Bipyridyl/Tripropylamine System and the Effect of Halide Ions on the Emission Intensity. *Anal. Chem.* **2000**, *72* (14), 3223–3232.

(47) Skotty, D. R.; Lee, W.-Y.; Nieman, T. A. Determination of Dansyl Amino Acids and Oxalate by HPLC with Electrogenerated Chemiluminescence Detection Using Tris(2,2'-Bipyridyl)Ruthenium(II) in the Mobile Phase. *Anal. Chem.* **1996**, *68* (9), 1530–1535.

(48) Zorzi, M.; Pastore, P.; Magno, F. A Single Calibration Graph for the Direct Determination of Ascorbic and Dehydroascorbic Acids by Electrogenerated Luminescence Based on Ru(Bpy)32+ in Aqueous Solution. *Anal. Chem.* **2000**, *72* (20), 4934–4939.

(49) Shi; Liu; Li; Xu. Electrochemiluminescent Detection Based on Solid-Phase Extraction at Tris(2,2'-Bipyridyl)Ruthenium(II)-Modified Ceramic Carbon Electrode. *Anal. Chem.* **2006**, *78* (20), 7330–7334.

(50) Xu, G.; Dong, S. Electrochemiluminescent Detection of Chlorpromazine by Selective Preconcentration at a Lauric Acid-Modified Carbon Paste Electrode Using Tris(2,2’-Bipyridine)Ruthenium(II). *Anal. Chem.* **2000**, *72* (21), 5308–5312.

(51) Bard, A. J.; Faulkner, L. R. *Electrochemical Methods: Fundamentals and Applications*, 2nd ed.; Wiley: New York, 2001.

(52) Wasalathanthri, D. P.; Malla, S.; Bist, I.; Tang, C. K.; Faria, R. C.; Rusling, J. F. High-Throughput Metabolic Genotoxicity Screening with a Fluidic Microwell Chip and Electrochemiluminescence. *Lab. Chip* **2013**, *13* (23), 4554–4562.

(53) Lee, W.-Y. Tris (2,2′-Bipyridyl)Ruthenium(II) Electrogenerated Chemiluminescence in Analytical Science. *Microchim. Acta* **1997**, *127* (1–2), 19–39.

(54) Browne, W. R.; O’Boyle, N. M.; McGarvey, J. J.; Vos, J. G. Elucidating Excited State Electronic Structure and Intercomponent Interactions in Multicomponent and Supramolecular Systems. *Chem. Soc. Rev.* **2005**, *34* (8), 641.

(55) Walworth, J.; Brewer, K. J.; Richter, M. M. Enhanced Electrochemiluminescence from Os(Phen)2(Dppene)2+ (Phen=1,10-Phenanthroline and Dppene=bis(Diphenylphosphino)Ethene) in the Presence of Triton X-100 (Polyethylene Glycol Tert-Octylphenyl Ether). *Anal. Chim. Acta* **2004**, *503* (2), 241–245.

(56) Bruce, D.; Richter, M. M.; Brewer, K. J. Electrochemiluminescence from Os(Phen) $_2$ (Dppene) $^{2+}$ (Phen = 1,10-Phenanthroline and

Dppene = Bis(Diphenylphosphino)Ethene). *Anal. Chem.* **2002**, *74* (13), 3157–3159.

(57) Bolletta, F.; Rossi, A.; Balzani, V. Chemiluminescence on Oxidation of Tris(2,2′-Bipyridine)Chromium(II): Chemical Generation of a Metal Centered Excited State. *Inorganica Chim. Acta* **1981**, *53*, L23–L24.

(58) Kumaresan, D.; Shankar, K.; Vaidya, S.; Schmehl, R. H. Photochemistry and Photophysics of Coordination Compounds: Osmium. In *Photochemistry and Photophysics of Coordination Compounds II*; Balzani, V., Campagna, S., Eds.; Topics in Current Chemistry; Springer Berlin Heidelberg, 2007; pp 101–142.

(59) Abruña, H. D. Electrogenerated Chemiluminescence of Bipyridine and Phenanthroline Complexes of Osmium. *J. Electroanal. Chem. Interfacial Electrochem.* **1984**, *175* (1), 321–326.

(60) Abruña, H. D. Electrochemiluminescence of Osmium Complexes Spectral, Electrochemical, and Mechanistic Studies. *J. Electrochem. Soc.* **1985**, *132* (4), 842–849.

(61) Kapturkiewicz, A.; Angulo, G. Extremely Efficient Electrochemiluminescence Systems Based on Tris (2-Phenylpyridine) Iridium (III). *Dalton Trans.* **2003**, No. 20, 3907–3913.

(62) Kapturkiewicz, A.; Nowacki, J.; Borowicz, P. Electrochemiluminescence Studies of the Cyclometalated Iridium(III) L2Ir(Acetyl Acetonate) Complexes. *Electrochimica Acta* **2005**, *50* (16–17), 3395–3400.

(63) Zanarini, S.; Rampazzo, E.; Bonacchi, S.; Juris, R.; Marcaccio, M.; Montalti, M.; Paolucci, F.; Prodi, L. Iridium Doped Silica−PEG

Nanoparticles: Enabling Electrochemiluminescence of Neutral Complexes in Aqueous Media. *J. Am. Chem. Soc.* **2009**, *131* (40), 14208–14209.

(64) Bandini, M.; Bianchi, M.; Valenti, G.; Piccinelli, F.; Paolucci, F.; Monari, M.; Umani-Ronchi, A.; Marcaccio, M. Electrochemiluminescent Functionalizable Cyclometalated Thiophene-Based Iridium(III) Complexes. *Inorg. Chem.* **2010**, *49* (4), 1439–1448.

(65) Bruce, D.; Richter, M. M. Green Electrochemiluminescence from Ortho-Metalated Tris(2-Phenylpyridine)Iridium(III). *Anal. Chem.* **2002**, *74* (6), 1340–1342.

(66) Shin, I.-S.; Kim, J. I.; Kwon, T.-H.; Hong, J.-I.; Lee, J.-K.; Kim, H. Efficient Electrogenerated Chemiluminescence from Bis-Cyclometalated Iridium(III) Complexes with Substituted 2-Phenylquinoline Ligands. *J. Phys. Chem. C* **2007**, *111* (5), 2280–2286.

(67) Yan, Z.; Xu, Z.; Yu, J.; Liu, G. Enhanced Electrochemiluminescence Performance of Ru(Bpy)32+/CuO/TiO2 Nanotube Array Sensor for Detection of Amines. *Electroanalysis* **2014**, *26* (9), 2017–2022.

(68) Lyons, C. H.; Abbas, E. D.; Lee, J.-K.; Rubner, M. F. Solid-State Light-Emitting Devices Based on the Trischelated Ruthenium(II) Complex. 1. Thin Film Blends with Poly(Ethylene Oxide). *J. Am. Chem. Soc.* **1998**, *120* (46), 12100–12107.

(69) Sun, X.; Du, Y.; Zhang, L.; Dong, S.; Wang, E. Luminescent Supramolecular Microstructures Containing Ru(Bpy)32+: Solution-

Based Self-Assembly Preparation and Solid-State Electrochemiluminescence Detection Application. *Anal. Chem.* **2007**, *79* (6), 2588–2592.

(70) Guo, Z.; Shen, Y.; Wang, M.; Zhao, F.; Dong, S. Electrochemistry and Electrogenerated Chemiluminescence of SiO2 Nanoparticles/Tris(2,2‘-Bipyridyl)Ruthenium(II) Multilayer Films on Indium Tin Oxide Electrodes. *Anal. Chem.* **2004**, *76* (1), 184–191.

(71) Gao, W.; Xia, X.-H.; Xu, J.-J.; Chen, H.-Y. Three-Dimensionally Ordered Macroporous Gold Structure as an Efficient Matrix for Solid-State Electrochemiluminescence of Ru(Bpy)32+/TPA System with High Sensitivity. *J. Phys. Chem. C* **2007**, *111* (33), 12213–12219.

(72) Premkumar, J.; Khoo, S. B. Immobilization of Ruthenium(II)Bipyridyl Complex at Highly Oxidized Glassy Carbon Electrodes. *Electrochem. Commun.* **2004**, *6* (10), 984–989.

(73) Dennany, L.; O’Reilly, E. J.; Keyes, T. E.; Forster, R. J. Electrochemiluminescent Monolayers on Metal Oxide Electrodes: Detection of Amino Acids. *Electrochem. Commun.* **2006**, *8* (10), 1588–1594.

(74) Ding, S.-N.; Xu, J.-J.; Zhang, W.-J.; Chen, H.-Y. Tris(2,2′-Bipyridyl)Ruthenium(II)–Zirconia–Nafion Composite Modified Electrode Applied as Solid-State Electrochemiluminescence Detector on Electrophoretic Microchip for Detection of Pharmaceuticals of Tramadol, Lidocaine and Ofloxacin. *Talanta* **2006**, *70* (3), 572–577.

(75) Zhang, L.; Dong, S. Electrogenerated Chemiluminescence Sensing Platform Using Doped Silica Nanoparticles and Carbon Nanotubes. *Electrochem. Commun.* **2006**, *8* (10), 1687–1691.

(76) Miao, W.; Bard, A. J. Electrogenerated Chemiluminescence. 72. Determination of Immobilized DNA and C-Reactive Protein on Au(111) Electrodes Using Tris(2,2‘-Bipyridyl)Ruthenium(II) Labels. *Anal. Chem.* **2003**, *75* (21), 5825–5834.

(77) Fang, L.; Lü, Z.; Wei, H.; Wang, E. A Electrochemiluminescence Aptasensor for Detection of Thrombin Incorporating the Capture Aptamer Labeled with Gold Nanoparticles Immobilized onto the Thio-Silanized ITO Electrode. *Anal. Chim. Acta* **2008**, *628* (1), 80–86.

(78) Liu, X.; Niu, W.; Li, H.; Han, S.; Hu, L.; Xu, G. Glucose Biosensor Based on Gold Nanoparticle-Catalyzed Luminol Electrochemiluminescence on a Three-Dimensional Sol–Gel Network. *Electrochem. Commun.* **2008**, *10* (9), 1250–1253.

(79) Shan, Y.; Xu, J.-J.; Chen, H.-Y. Distance-Dependent Quenching and Enhancing of Electrochemiluminescence from a CdS:Mn Nanocrystal Film by Au Nanoparticles for Highly Sensitive Detection of DNA. *Chem. Commun.* **2009**, No. 8, 905–907.

(80) Sardesai, N.; Pan, S.; Rusling, J. Electrochemiluminescent Immunosensor for Detection of Protein Cancer Biomarkers Using Carbon Nanotube Forests and [Ru-(Bpy)3]2+-Doped Silica Nanoparticles. *Chem. Commun.* **2009**, No. 33, 4968–4970.

(81) Liu, Z.; Qi, W.; Xu, G. Recent Advances in Electrochemiluminescence. *Chem. Soc. Rev.* **2015**, *44* (10), 3117–3142.

(82) Fiaccabrino, G. C.; de Rooij, N. F.; Koudelka-Hep, M. On-Chip Generation and Detection of Electrochemiluminescence. *Anal. Chim. Acta* **1998**, *359* (3), 263–267.

(83) Ge, L.; Yan, J.; Song, X.; Yan, M.; Ge, S.; Yu, J. Three-Dimensional Paper-Based Electrochemiluminescence Immunodevice for Multiplexed Measurement of Biomarkers and Point-of-Care Testing. *Biomaterials* **2012**, *33* (4), 1024–1031.

(84) Miao, W. Electrogenerated Chemiluminescence and Its Biorelated Applications. *Chem. Rev.* **2008**, *108* (7), 2506–2553.

(85) Mavré, F.; Anand, R. K.; Laws, D. R.; Chow, K.-F.; Chang, B.-Y.; Crooks, J. A.; Crooks, R. M. Bipolar Electrodes: A Useful Tool for Concentration, Separation, and Detection of Analytes in Microelectrochemical Systems. *Anal. Chem.* **2010**, *82* (21), 8766–8774.

(86) Loget, G.; Kuhn, A. Shaping and Exploring the Micro- and Nanoworld Using Bipolar Electrochemistry. *Anal. Bioanal. Chem.* **2011**, *400* (6), 1691–1704.

(87) Crooks, R. M. Principles of Bipolar Electrochemistry. *ChemElectroChem* **2016**, *3* (3), 357–359.

(88) Loget, G.; Zigah, D.; Bouffier, L.; Sojic, N.; Kuhn, A. Bipolar Electrochemistry: From Materials Science to Motion and Beyond. *Acc. Chem. Res.* **2013**, *46* (11), 2513–2523.

(89) Arora, A.; Eijkel, J. C. T.; Morf, W. E.; Manz, A. A Wireless Electrochemiluminescence Detector Applied to Direct and Indirect Detection for Electrophoresis on a Microfabricated Glass Device. *Anal. Chem.* **2001**, *73* (14), 3282–3288.

(90) Loget, G.; Kuhn, A. Bipolar Electrochemistry in the Nanosciences. In *Electrochemistry*; 2012; pp 71–103.

(91) Mavré, F.; Chow, K.-F.; Sheridan, E.; Chang, B.-Y.; Crooks, J. A.; Crooks, R. M. A Theoretical and Experimental Framework for Understanding Electrogenerated Chemiluminescence (ECL) Emission at Bipolar Electrodes. *Anal. Chem.* **2009**, *81* (15), 6218–6225.

(92) Loget, G.; Roche, J.; Kuhn, A. True Bulk Synthesis of Janus Objects by Bipolar Electrochemistry. *Adv. Mater.* **2012**, *24* (37), 5111–5116.

(93) Dhopeshwarkar, R.; Hlushkou, D.; Nguyen, M.; Tallarek, U.; Crooks, R. M. Electrokinetics in Microfluidic Channels Containing a Floating Electrode. *J. Am. Chem. Soc.* **2008**, *130* (32), 10480–10481.

(94) Warakulwit, C.; Nguyen, T.; Majimel, J.; Delville, M.-H.; Lapeyre, V.; Garrigue, P.; Ravaine, V.; Limtrakul, J.; Kuhn, A. Dissymmetric Carbon Nanotubes by Bipolar Electrochemistry. *Nano Lett.* **2008**, *8* (2), 500–504.

(95) Ulrich, C.; Andersson, O.; Nyholm, L.; Björefors, F. Potential and Current Density Distributions at Electrodes Intended for Bipolar Patterning. *Anal. Chem.* **2009**, *81* (1), 453–459.

(96) Ramakrishnan, S.; Shannon, C. Display of Solid-State Materials Using Bipolar Electrochemistry. *Langmuir* **2010**, *26* (7), 4602–4606.

(97) Duval, J. F. L.; Huijs, G. K.; Threels, W. F.; Lyklema, J.; van Leeuwen, H. P. Faradaic Depolarization in the Electrokinetics of the Metal–Electrolyte Solution Interface. *J. Colloid Interface Sci.* **2003**, *260* (1), 95–106.

(98) Duval, J. F. L.; Buffle, J.; van Leeuwen, H. P. Quasi-Reversible Faradaic Depolarization Processes in the Electrokinetics of the Metal/Solution Interface. *J. Phys. Chem. B* **2006**, *110* (12), 6081–6094.

(99) Wu, M.-S.; Liu, Z.; Shi, H.-W.; Chen, H.-Y.; Xu, J.-J. Visual Electrochemiluminescence Detection of Cancer Biomarkers on a Closed Bipolar Electrode Array Chip. *Anal. Chem.* **2015**, *87* (1), 530–537.

(100) Guerrette, J. P.; Oja, S. M.; Zhang, B. Coupled Electrochemical Reactions at Bipolar Microelectrodes and Nanoelectrodes. *Anal. Chem.* **2012**, *84* (3), 1609–1616.

(101) Cox, J. T.; Guerrette, J. P.; Zhang, B. Steady-State Voltammetry of a Microelectrode in a Closed Bipolar Cell. *Anal. Chem.* **2012**, *84* (20), 8797–8804.

(102) Wang, T.; Fan, S.; Erdmann, R.; Shannon, C. Detection of Ferrocenemethanol and Molecular Oxygen Based on Electrogenerated Chemiluminescence Quenching at a Bipolar Electrode. *Langmuir* **2013**, *29* (51), 16040–16044.

(103) Feng, Q.-M.; Pan, J.-B.; Zhang, H.-R.; Xu, J.-J.; Chen, H.-Y. Disposable Paper-Based Bipolar Electrode for Sensitive

Electrochemiluminescence Detection of a Cancer Biomarker. *Chem. Commun.* **2014**, *50* (75), 10949.

(104) Koizumi, Y.; Shida, N.; Tomita, I.; Inagi, S. Bifunctional Modification of Conductive Particles by Iterative Bipolar Electrodeposition of Metals. *Chem. Lett.* **2014**, *43* (8), 1245–1247.

(105) Fleischmann, M.; Ghoroghchian, J.; Rolison, D.; Pons, S. Electrochemical Behavior of Dispersions of Spherical Ultramicroelectrodes. *J. Phys. Chem.* **1986**, *90* (23), 6392–6400.

(106) Ellis, K. G.; Jansson, R. E. W. Further Studies on the Epoxidation of Propylene in a Bipolar Trickle Bed. *J. Appl. Electrochem.* **1981**, *11* (4), 531–535.

(107) Manji, A.; Oloman, C. W. Electrosynthesis of Propylene Oxide in a Bipolar Trickle-Bed Reactor. *J. Appl. Electrochem.* **1987**, *17* (3), 532–544.

(108) Lee, J. K.; Shemilt, L. W.; Chun, H. S. Studies of Bipolarity in Fluidized Bed Electrodes. *J. Appl. Electrochem.* **1989**, *19* (6), 877–881.

(109) Plimley, R. E.; Wright, A. R. A Bipolar Mechanism for Charge Transferin a Fluidised Bed Electrode. *Chem. Eng. Sci.* **1984**, *39* (3), 395–405.

(110) Smotkin, E.; Bard, A. J.; Campion, A.; Fox, M. A.; Mallouk, T.; Webber, S. E.; White, J. M. Bipolar Titanium Dioxide/Platinum Semiconductor Photoelectrodes and Multielectrode Arrays for Unassisted Photolytic Water Splitting. *J. Phys. Chem.* **1986**, *90* (19), 4604–4607.

(111) Cervera-March, S.; Smotkin, E. S.; Bard, A. J.; Campion, A.; Fox, M. A.; Mallouk, T.; Webber, S. E.; White, J. M. Modeling of Bipolar Semiconductor Photoelectrode Arrays for Electrolytic Processes. *J. Electrochem. Soc.* **1988**, *135* (3), 567–573.

(112) Ishiguro, Y.; Inagi, S.; Fuchigami, T. Gradient Doping of Conducting Polymer Films by Means of Bipolar Electrochemistry. *Langmuir* **2011**, *27* (11), 7158–7162.

(113) Shida, N.; Ishiguro, Y.; Atobe, M.; Fuchigami, T.; Inagi, S. Electro-Click Modification of Conducting Polymer Surface Using Cu(I) Species Generated on a Bipolar Electrode in a Gradient Manner. *ACS Macro Lett.* **2012**, *1* (6), 656–659.

(114) Perdue, R. K.; Laws, D. R.; Hlushkou, D.; Tallarek, U.; Crooks, R. M. Bipolar Electrode Focusing: The Effect of Current and Electric Field on Concentration Enrichment. *Anal. Chem.* **2009**, *81* (24), 10149–10155.

(115) Laws, D. R.; Hlushkou, D.; Perdue, R. K.; Tallarek, U.; Crooks, R. M. Bipolar Electrode Focusing: Simultaneous Concentration Enrichment and Separation in a Microfluidic Channel Containing a Bipolar Electrode. *Anal. Chem.* **2009**, *81* (21), 8923–8929.

(116) Chow, K.-F.; Mavré, F.; Crooks, R. M. Wireless Electrochemical DNA Microarray Sensor. *J. Am. Chem. Soc.* **2008**, *130* (24), 7544–7545.

(117) Zhan, W.; Alvarez, J.; Crooks, R. M. Electrochemical Sensing in Microfluidic Systems Using Electrogenerated Chemiluminescence as

a Photonic Reporter of Redox Reactions. *J. Am. Chem. Soc.* **2002**, *124* (44), 13265–13270.

(118) Chow, K.-F.; Mavré, F.; Crooks, J. A.; Chang, B.-Y.; Crooks, R. M. A Large-Scale, Wireless Electrochemical Bipolar Electrode Microarray. *J. Am. Chem. Soc.* **2009**, *131* (24), 8364–8365.

(119) Chang, B.-Y.; Chow, K.-F.; Crooks, J. A.; Mavré, F.; Crooks, R. M. Two-Channel Microelectrochemical Bipolar Electrode Sensor Array. *The Analyst* **2012**, *137* (12), 2827.

(120) Xiao, Y.; Xu, L.; Qi, L.-W. Electrochemiluminescence Bipolar Electrode Array for the Multiplexed Detection of Glucose, Lactate and Choline Based on a Versatile Enzymatic Approach. *Talanta* **2017**, *165*, 577–583.

(121) Gao, W.; Muzyka, K.; Ma, X.; Lou, B.; Xu, G. A Single-Electrode Electrochemical System for Multiplex Electrochemiluminescence Analysis Based on a Resistance Induced Potential Difference. *Chem. Sci.* **2018**, *9* (16), 3911–3916.

(122) Fosdick, S. E.; Knust, K. N.; Scida, K.; Crooks, R. M. Bipolar Electrochemistry. *Angew. Chem. Int. Ed.* **2013**, *52* (40), 10438–10456.

(123) Zhang, X.; Bard, A. J. In-Trough Cyclic Voltammetric Studies of Langmuir-Blodgett Monolayers of a Surfactant Derivative of Tris(2,2’-Bipyridine)Ruthenium(2+) at an Indium-Tin Oxide Electrode. *J. Am. Chem. Soc.* **1989**, *111* (21), 8098–8105.

(124) Kissinger, P. T.; Heineman, W. R. Cyclic Voltammetry. *J Chem Educ* **1983**, *60* (9), 702.

(125) Mabbott, G. A. An Introduction to Cyclic Voltammetry. *J Chem Educ* **1983**, *60* (9), 697.

(126) Brownson, D. A. C.; Banks, C. E. Interpreting Electrochemistry. In *The Handbook of Graphene Electrochemistry*; Springer London: London, 2014; pp 23–77.

(127) Neghmouche, N. S.; Lanez, T. Calculation of Electrochemical Parameters Starting from the Polarization Curves of Ferrocene at Glassy Carbon Electrode. *Int. Lett. Chem. Phys. Astron.* **2013**, *Vol. 4*, 37–45.

(128) Birke, R. L.; Kim, M.-H.; Strassfeld, M. Diagnosis of Reversible, Quasi-Reversible, and Irreversible Electrode Processes with Differential Pulse Polarography. *Anal. Chem.* **1981**, *53* (6), 852–856.

(129) Ye, T.; He, Y.; Borguet, E. Adsorption and Electrochemical Activity: An In Situ Electrochemical Scanning Tunneling Microscopy Study of Electrode Reactions and Potential-Induced Adsorption of Porphyrins. *J. Phys. Chem. B* **2006**, *110* (12), 6141–6147.

(130) Wang, J.; John Wiley & Sons, I. *Analytical Electrochemistry (Second Edition)*; Wiley-VCH: S.l, 2000.

(131) He, P.; Crooks, R. M.; Faulkner, L. R. Adsorption and Electrode Reactions of Disulfonated Anthraquinones at Mercury Electrodes. *J. Phys. Chem.* **1990**, *94* (3), 1135–1141.

(132) Eckermann, A. L.; Feld, D. J.; Shaw, J. A.; Meade, T. J. Electrochemistry of Redox-Active Self-Assembled Monolayers. *Coord. Chem. Rev.* **2010**, *254* (15–16), 1769–1802.

(133) *Handbook of Electrochemistry*, 1st ed.; Zoski, C. G., Ed.; Elsevier: Amsterdam ; Boston, 2007.

(134) Zhao, F.; T. Slade, R. C.; R. Varcoe, J. Techniques for the Study and Development of Microbial Fuel Cells: An Electrochemical Perspective. *Chem. Soc. Rev.* **2009**, *38* (7), 1926–1939.

(135) Honeychurch, K. C. 13 - Printed Thick-Film Biosensors. In *Printed Films*; Prudenziati, M., Hormadaly, J., Eds.; Woodhead Publishing Series in Electronic and Optical Materials; Woodhead Publishing, 2012; pp 366–409.

(136) Guy, O. J.; Walker, K.-A. D. Chapter 4 - Graphene Functionalization for Biosensor Applications. In *Silicon Carbide Biotechnology (Second Edition)*; Saddow, S. E., Ed.; Elsevier, 2016; pp 85–141.

(137) Emery, S. B.; Hubbley, J. L.; Roy, D. Voltammetric and Amperometric Analyses of Electrochemical Nucleation: Electrodeposition of Copper on Nickel and Tantalum. *J. Electroanal. Chem.* **2004**, *568*, 121–133.

(138) Ratnakumar, B. V.; Smart, M. C.; Surampudi, S. Electrochemical Impedance Spectroscopy and Its Applications to Lithium Ion Cells. In *Seventeenth Annual Battery Conference on Applications and Advances. Proceedings of Conference (Cat. No.02TH8576)*; 2002; pp 273–277.

(139) Sacco, A. Electrochemical Impedance Spectroscopy: Fundamentals and Application in Dye-Sensitized Solar Cells. *Renew. Sustain. Energy Rev.* **2017**, *79*, 814–829.

(140) Park, S.-M.; Yoo, J.-S. Peer Reviewed: Electrochemical Impedance Spectroscopy for Better Electrochemical Measurements. *Anal. Chem.* **2003**, *75* (21), 455 A-461 A.

(141) Fernández-Sánchez, C.; McNeil, C. J.; Rawson, K. Electrochemical Impedance Spectroscopy Studies of Polymer Degradation: Application to Biosensor Development. *TrAC Trends Anal. Chem.* **2005**, *24* (1), 37–48.

(142) Randviir, E. P.; Banks, C. E. Electrochemical Impedance Spectroscopy: An Overview of Bioanalytical Applications. *Anal. Methods* **2013**, *5* (5), 1098–1115.

(143) Scully, J. R.; Silverman, D. C. *Electrochemical Impedance: Analysis and Interpretation*; ASTM International, 1993.

(144) Singh, Y. ELECTRICAL RESISTIVITY MEASUREMENTS: A REVIEW. *Int. J. Mod. Phys. Conf. Ser.* **2013**, *22*, 745–756.

(145) Li, J. C.; Wang, Y.; Ba, D. C. Characterization of Semiconductor Surface Conductivity by Using Microscopic Four-Point Probe Technique. *Phys. Procedia* **2012**, *32*, 347–355.

(146) Yagüe, J. L.; Guimerà, A.; Villa, R.; Agulló, N.; Borrós, S. A New Four-Point Probe Design to Measure Conductivity in Polymeric Thin Films. *Afinidad* **2013**, *70* (563).

(147) Li, M.-Y.; Yang, M.; Vargas, E.; Neff, K.; Vanli, A.; Liang, R. Analysis of Variance on Thickness and Electrical Conductivity Measurements of Carbon Nanotube Thin Films. *Meas. Sci. Technol.* **2016**, *27* (9), 095004.

(148) Viscarra Rossel, R. A.; Walvoort, D. J. J.; McBratney, A. B.; Janik, L. J.; Skjemstad, J. O. Visible, near Infrared, Mid Infrared or Combined Diffuse Reflectance Spectroscopy for Simultaneous Assessment of Various Soil Properties. *Geoderma* **2006**, *131* (1), 59–75.

(149) Ferree, M. A.; Shannon, R. D. Evaluation of a Second Derivative UV/Visible Spectroscopy Technique for Nitrate and Total Nitrogen Analysis of Wastewater Samples. *Water Res.* **2001**, *35* (1), 327–332.

(150) McCauley, J. D. (usda; Engel, B. A.; Scudder, C. E.; Morgan, M. T.; Elliott, P. W. Assessing the Spatial Variability of Organic Matter. *Am. Soc. Agric. Eng. Meet. USA* **1993**.

(151) Kamal, A. H.; El-Malla, S. F.; Hammad, S. F. A Review on UV Spectrophotometric Methods for Simultaneous Multicomponent Analysis. *Eur. J. Pharm. Med. Res.* **2016**, *3* (2), 348–360.

(152) Behera, S. UV-Visible Spectrophotometric Method Development and Validation of Assay of Paracetamol Tablet Formulation. *J. Anal. Bioanal. Tech.* **2012**, *03* (06).

(153) Mäntele, W.; Deniz, E. UV–VIS Absorption Spectroscopy: Lambert-Beer Reloaded. *Spectrochim. Acta. A. Mol. Biomol. Spectrosc.* **2017**, *173*, 965–968.

(154) Tissue, B. M. Ultraviolet and Visible Absorption Spectroscopy. In *Characterization of Materials*; John Wiley & Sons, Inc., 2002.

(155) Valeur, B.; Berberan-Santos, M. N. *Molecular Fluorescence: Principles and Applications*; John Wiley & Sons, 2012.

(156) Karoui, R.; Blecker, C. Fluorescence Spectroscopy Measurement for Quality Assessment of Food Systems—a Review. *Food Bioprocess Technol.* **2011**, *4* (3), 364–386.

(157) Sauer, M.; Hofkens, J.; Enderlein, J. *Handbook of Fluorescence Spectroscopy and Imaging: From Single Molecules to Ensembles*; Wiley-VCH: Weinheim, 2011.

(158) Lakowicz, J. R. *Principles of Fluorescence Spectroscopy*, 3rd ed.; Springer: New York, 2006.

(159) Ladokhin, A. S. Fluorescence Spectroscopy in Peptide and Protein Analysis. In *Encyclopedia of Analytical Chemistry*; Meyers, R. A., Ed.; John Wiley & Sons, Ltd: Chichester, UK, 2000.

(160) Guilbault, G. G. *Practical Fluorescence, Second Edition*; CRC Press, 1990.

(161) Bumbrah, G. S.; Sharma, R. M. Raman Spectroscopy – Basic Principle, Instrumentation and Selected Applications for the Characterization of Drugs of Abuse. *Egypt. J. Forensic Sci.* **2016**, *6* (3), 209–215.

(162) Das, R. S.; Agrawal, Y. K. Raman Spectroscopy: Recent Advancements, Techniques and Applications. *Vib. Spectrosc.* **2011**, *57* (2), 163–176.

(163) Neuville, D. R.; Ligny, D. de; Henderson, G. S. Advances in Raman Spectroscopy Applied to Earth and Material Sciences. *Rev. Mineral. Geochem.* **2014**, *78* (1), 509–541.

(164) Raman, C. V. A New Radiation. **1928**.

(165) Kudelski, A. Analytical Applications of Raman Spectroscopy. *Talanta* **2008**, *76* (1), 1–8.

(166) Efremov, E. V.; Ariese, F.; Gooijer, C. Achievements in Resonance Raman Spectroscopy: Review of a Technique with a Distinct Analytical Chemistry Potential. *Anal. Chim. Acta* **2008**, *606* (2), 119–134.

(167) Vernon-Parry, K. D. Scanning Electron Microscopy: An Introduction. *III-Vs Rev.* **2000**, *13* (4), 40–44.

(168) Bogner, A.; Jouneau, P.-H.; Thollet, G.; Basset, D.; Gauthier, C. A History of Scanning Electron Microscopy Developments: Towards “Wet-STEM” Imaging. *Micron* **2007**, *38* (4), 390–401.

(169) Joy, D. C. Scanning Electron Microscopy for Materials Characterization. *Curr. Opin. Solid State Mater. Sci.* **1997**, *2* (4), 465–468.

(170) Collett, B. M. Scanning Electron Microscopy: A Review and Report of Research in Wood Science. *Wood Fiber Sci.* **2007**, *2* (2), 113–133.

(171) Joy, D. C. Scanning Electron Microscopy: Second Best No More. *Nat. Mater.* **2009**, *8* (10), 776–777.

(172) Casuccio, G. S.; Lersch, T. L.; Schlaegle, S. F.; Martello, D. V. Characterization of Ambient Carbonaceous Particles Using Electron Microscopy Techniques. *Fuel Chem Div Prepr.* **2002**, *47* (2), 624–626.

(173) Sutton, M. A.; Li, N.; Joy, D. C.; Reynolds, A. P.; Li, X. Scanning Electron Microscopy for Quantitative Small and Large Deformation

Measurements Part I: SEM Imaging at Magnifications from 200 to 10,000. *Exp. Mech.* **2007**, *47* (6), 775–787.

(174) Zhu, Y.; Inada, H.; Nakamura, K.; Wall, J. Imaging Single Atoms Using Secondary Electrons with an Aberration-Corrected Electron Microscope. *Nat. Mater.* **2009**, *8* (10), 808–812.

(175) Pellegrin, Y.; Forster, R. J.; Keyes, T. E. PH Dependent Photophysics and Role of Medium on Photoinduced Electron Transfer between Ruthenium Polypyridyl Complex and Anthraquinone. *Inorganica Chim. Acta* **2009**, *362* (6), 1715–1722.

(176) Geddes, L. A. Who Introduced the Tetrapolar Method for Measuring Resistance and Impedance? *IEEE Eng. Med. Biol. Mag.* **1996**, *15* (5), 133–134.

(177) Zhao, C.; Wang, C.; Gorkin, R.; Beirne, S.; Shu, K.; Wallace, G. G. Three Dimensional (3D) Printed Electrodes for Interdigitated Supercapacitors. *Electrochem. Commun.* **2014**, *41*, 20–23.

(178) Kalaitzidou, K.; Fukushima, H.; Drzal, L. T. A Route for Polymer Nanocomposites with Engineered Electrical Conductivity and Percolation Threshold. *Materials* **2010**, *3* (2), 1089–1103.

(179) Yoshimoto, S.; Murata, Y.; Kubo, K.; Tomita, K.; Motoyoshi, K.; Kimura, T.; Okino, H.; Hobara, R.; Matsuda, I.; Honda, S.; et al. Four-Point Probe Resistance Measurements Using PtIr-Coated Carbon Nanotube Tips. *Nano Lett.* **2007**, *7* (4), 956–959.

(180) Sandu, I.; Florescu, L. G.; Fleaca, C.; Dragomirescu, A. Nanocarbon Film as a Percolation Network for Nanocarbon/Polymer Composites. *J. Reinf. Plast. Compos.* **2009**, *28* (19), 2397–2404.

(181) Sandler, J. K. W.; Kirk, J. E.; Kinloch, I. A.; Shaffer, M. S. P.; Windle, A. H. Ultra-Low Electrical Percolation Threshold in Carbon-Nanotube-Epoxy Composites. *Polymer* **2003**, *44* (19), 5893–5899.

(182) de Poulpiquet, A.; Diez-Buitrago, B.; Dumont Milutinovic, M.; Sentic, M.; Arbault, S.; Bouffier, L.; Kuhn, A.; Sojic, N. Dual Enzymatic Detection by Bulk Electrogenerated Chemiluminescence. *Anal. Chem.* **2016**, *88* (12), 6585–6592.

(183) Pan, Y.; Weng, G. J.; Meguid, S. A.; Bao, W. S.; Zhu, Z.-H.; Hamouda, A. M. S. Percolation Threshold and Electrical Conductivity of a Two-Phase Composite Containing Randomly Oriented Ellipsoidal Inclusions. *J. Appl. Phys.* **2011**, *110* (12), 123715.

(184) Ferrari, A. C.; Robertson, J. Interpretation of Raman Spectra of Disordered and Amorphous Carbon. *Phys. Rev. B* **2000**, *61* (20), 14095–14107.

(185) Patel, M.; Azanza Ricardo, C. L.; Scardi, P.; Aswath, P. B. Morphology, Structure and Chemistry of Extracted Diesel Soot—Part I: Transmission Electron Microscopy, Raman Spectroscopy, X-Ray Photoelectron Spectroscopy and Synchrotron X-Ray Diffraction Study. *Tribol. Int.* **2012**, *52*, 29–39.

(186) Antony, R. P.; Preethi, L. K.; Gupta, B.; Mathews, T.; Dash, S.; Tyagi, A. K. Efficient Electrocatalytic Performance of Thermally Exfoliated Reduced Graphene Oxide-Pt Hybrid. *Mater. Res. Bull.* **2015**, *70*, 60–67.

(187) Chu, P. K.; Li, L. Characterization of Amorphous and Nanocrystalline Carbon Films. *Mater. Chem. Phys.* **2006**, *96* (2–3), 253–277.

(188) Ungár, T.; Gubicza, J.; Tichy, G.; Pantea, C.; Zerda, T. W. Size and Shape of Crystallites and Internal Stresses in Carbon Blacks. *Compos. Part Appl. Sci. Manuf.* **2005**, *36* (4), 431–436.

(189) Donald, A. M. The Use of Environmental Scanning Electron Microscopy for Imaging Wet and Insulating Materials. *Nat. Mater.* **2003**, *2* (8), 511–516.

(190) Kim, J.; Song, X.; Kinoshita, K.; Madou, M.; White, R. Electrochemical Studies of Carbon Films from Pyrolyzed Photoresist. *J. Electrochem. Soc.* **1998**, *145* (7), 2314–2319.

(191) Zeng, A.; Liu, E.; Tan, S. N.; Zhang, S.; Gao, J. Cyclic Voltammetry Studies of Sputtered Nitrogen Doped Diamond-Like Carbon Film Electrodes. *Electroanalysis* **2002**, *14* (15–16), 1110–1115.

(192) Zittel, H. E.; Miller, F. J. A Glassy-Carbon Electrode for Voltammetry. *Anal. Chem.* **1965**, *37* (2), 200–203.

(193) Leyva-García, S.; Lozano-Castelló, D.; Morallón, E.; Cazorla-Amorós, D. Silica-Templated Ordered Mesoporous Carbon Thin Films as Electrodes for Micro-Capacitors. *J. Mater. Chem. A* **2016**, *4* (12), 4570–4579.

(194) Gong, S.; Lai, D. T. H.; Wang, Y.; Yap, L. W.; Si, K. J.; Shi, Q.; Jason, N. N.; Sridhar, T.; Uddin, H.; Cheng, W. Tattoolike Polyaniline Microparticle-Doped Gold Nanowire Patches as Highly Durable

Wearable Sensors. *ACS Appl. Mater. Interfaces* **2015**, *7* (35), 19700–19708.

(195) Mamunya, Y. P.; Davydenko, V. V.; Pissis, P.; Lebedev, E. V. Electrical and Thermal Conductivity of Polymers Filled with Metal Powders. *Eur. Polym. J.* **2002**, *38* (9), 1887–1897.

(196) Ramírez-García, S.; Alegret, S.; Céspedes, F.; Forster, R. J. Carbon Composite Microelectrodes: Charge Percolation and Electroanalytical Performance. *Anal. Chem.* **2004**, *76* (3), 503–512.

(197) Sahimi, M.; Hughes, B. D.; Scriven, L. E.; Davis, H. T. Critical Exponent of Percolation Conductivity by Finite-Size Scaling. *J. Phys. C Solid State Phys.* **1983**, *16* (16), L521.

(198) Oskouyi, A. B.; Sundararaj, U.; Mertiny, P. Tunneling Conductivity and Piezoresistivity of Composites Containing Randomly Dispersed Conductive Nano-Platelets. *Materials* **2014**, *7* (4), 2501–2521.

(199) Hicks, J.; Behnam, A.; Ural, A. A Computational Study of Tunneling-Percolation Electrical Transport in Graphene-Based Nanocomposites. *Appl. Phys. Lett.* **2009**, *95* (21), 213103.

(200) Heaney, M. B. Measurement and Interpretation of Nonuniversal Critical Exponents in Disordered Conductor-Insulator Composites. *Phys. Rev. B* **1995**, *52* (17), 12477–12480.

(201) Liu, R.; Zhang, C.; Liu, M. Open Bipolar Electrode-Electrochemiluminescence Imaging Sensing Using Paper-Based Microfluidics. *Sens. Actuators B Chem.* **2015**, *216*, 255–262.

(202) Rubin, Z.; Sunshine, S. A.; Heaney, M. B.; Bloom, I.; Balberg, I. Critical Behavior of the Electrical Transport Properties in a Tunneling-Percolation System. *Phys. Rev. B* **1999**, *59* (19), 12196.

(203) Silwana, B.; Horst, C. van der; Iwuoha, E.; Somerset, V. Inhibitive Determination of Metal Ions Using a Horseradish Peroxidase Amperometric Biosensor. **2013**.

(204) Ninh, D. H.; Thi Thao, T.; Duy Long, P.; Dinh, N. N. Characterization of Electrochromic Properties of Polyaniline Thin Films Electropolymerized in H2SO4 Solution. *Open J. Org. Polym. Mater.* **2016**, *06* (01), 30–37.

(205) Obaid, A. Y.; El-Mossalamy, E. H.; Al-Thabaiti, S. A.; El-Hallag, I. S.; Hermas, A. A.; Asiri, A. M. Electrodeposition and Characterization of Polyaniline on Stainless Steel Surface via Cyclic, Convolutive Voltammetry and SEM in Aqueous Acidic Solutions. *Int J Electrochem Sci* **2014**, *9*, 1003–1015.

(206) Wang, H.; Hao, Q.; Yang, X.; Lu, L.; Wang, X. A Nanostructured Graphene/Polyaniline Hybrid Material for Supercapacitors. *Nanoscale* **2010**, *2* (10), 2164–2170.

(207) Rohom, A. B.; Londhe, P. U.; Mahapatra, S. K.; Kulkarni, S. K.; Chaure, N. B. Electropolymerization of Polyaniline Thin Films. *High Perform. Polym.* **2014**, *26* (6), 641–646.

(208) Ma, J.; Tang, S.; Syed, J. A.; Meng, X. Asymmetric Hybrid Capacitors Based on Novel Bearded Carbon Fiber Cloth–Pinhole Polyaniline Electrodes with Excellent Energy Density. *RSC Adv.* **2016**, *6* (86), 82995–83002.

(209) Babaiee, M.; Pakshir, M.; Hashemi, B. Effects of Potentiodynamic Electropolymerization Parameters on Electrochemical Properties and Morphology of Fabricated PANI Nanofiber/Graphite Electrode. *Synth. Met.* **2015**, *199* (Supplement C), 110–120.

(210) Wang, H.; Lin, J.; Shen, Z. X. Polyaniline (PANi) Based Electrode Materials for Energy Storage and Conversion. *J. Sci. Adv. Mater. Devices* **2016**, *1* (3), 225–255.

(211) Wang, Q.; Yu, Y.; Yang, J.; Liu, J. Fast Fabrication of Flexible Functional Circuits Based on Liquid Metal Dual-Trans Printing. *Adv. Mater.* **2015**, *27* (44), 7109–7116.

(212) Ambrosi, A.; Pumera, M. 3D-Printing Technologies for Electrochemical Applications. *Chem. Soc. Rev.* **2016**, *45* (10), 2740–2755.

(213) Durmus, N. G.; Tasoglu, S.; Demirci, U. Bioprinting: Functional Droplet Networks. *Nat. Mater.* **2013**, *12* (6), 478–479.

(214) Xie, X.; Criddle, C.; Cui, Y. Design and Fabrication of Bioelectrodes for Microbial Bioelectrochemical Systems. *Energy Environ. Sci.* **2015**, *8* (12), 3418–3441.

(215) Heuschkel, M. O.; Fejtl, M.; Raggenbass, M.; Bertrand, D.; Renaud, P. A Three-Dimensional Multi-Electrode Array for Multi-Site Stimulation and Recording in Acute Brain Slices. *J. Neurosci. Methods* **2002**, *114* (2), 135–148.

(216) Minteer, S. D. Three-Dimensional Electrodes. In *Encyclopedia of Microfluidics and Nanofluidics*; Li, D., Ed.; Springer US: Boston, MA, 2013; pp 1–7.

(217) Chabi, S.; Peng, C.; Hu, D.; Zhu, Y. Ideal Three-Dimensional Electrode Structures for Electrochemical Energy Storage. *Adv. Mater.* **2014**, *26* (15), 2440–2445.

(218) Ambrosi, A.; Moo, J. G. S.; Pumera, M. Helical 3D-Printed Metal Electrodes as Custom-Shaped 3D Platform for Electrochemical Devices. *Adv. Funct. Mater.* **2016**, *26* (5), 698–703.

(219) Xu, Y.; Wu, X.; Guo, X.; Kong, B.; Zhang, M.; Qian, X.; Mi, S.; Sun, W. The Boom in 3D-Printed Sensor Technology. *Sensors* **2017**, *17* (6), 1166.

(220) Yap, C. Y.; Tan, H. K.; Du, Z.; Chua, C. K.; Dong, Z. Selective Laser Melting of Nickel Powder. *Rapid Prototyp. J.* **2017**, *23* (4), 750–757.

(221) Huang, X.; Chang, S.; Lee, W. S. V.; Ding, J.; Xue, J. M. Three-Dimensional Printed Cellular Stainless Steel as a High-Activity Catalytic Electrode for Oxygen Evolution. *J. Mater. Chem. A* **2017**, *5* (34), 18176–18182.

(222) Erlandsen, S.; Chen, Y.; Frethem, C.; Detry, J.; Wells, C. High-Resolution Backscatter Electron Imaging of Colloidal Gold in LVSEM. *J. Microsc.* **2003**, *211* (3), 212–218.

(223) Lee, Y. J.; Oh, C.; Park, J. Y.; Kim, Y. Fabrication and Characterization of Macroporous Gold Hybrid Sensing Electrodes With Electroplated Platinum Nanoparticles. *IEEE Trans. Nanotechnol.* **2011**, *10* (6), 1298–1305.

(224) Diniz, A. V.; Ferreira, N. G.; Corat, E. J.; Trava-Airoldi, V. J. Boron Doped Diamond Thin Films on Large Area Ti6Al4V Substrates for Electrochemical Application. *Mater. Res.* **2003**, *6* (1), 57–61.

(225) Kiryushov, V. N.; Skvortsova, L. I.; Aleksandrova, T. P. Electrochemical Behavior of the System Ferricyanide-Ferrocyanide at a Graphite-Epoxy Composite Electrode. *J. Anal. Chem.* **2011**, *66* (5), 510–514.

(226) Daum, P. H.; Enke, C. G. Electrochemical Kinetics of the Ferri-Ferrocyanide Couple on Platinum. *Anal. Chem.* **1969**, *41* (4), 653–656.

(227) Bewer, G.; Debrodt, H.; Herbst, H. Titanium for Electrochemical Processes. *JOM* **1982**, *34* (1), 37–41.

(228) Heakal, F. E.-T.; Awad, K. A. Electrochemical Corrosion and Passivation Behavior of Titanium and Its Ti–6Al–4V Alloy in Low and Highly Concentrated HBr Solutions. *Int J Electrochem Sci* **2011**, *6*, 6483.

(229) Li, J.; Wu, G.; Jiang, J.; Zhao, Y. Surface Characteristics and Bioactivity of Oxide Films with Haloid Ions Formed by Micro-Arc Oxidation on Titanium in Vitro. *Mater. Manuf. Process.* **2011**, *26* (2), 188–192.

(230) Vasilescu, V. G.; Sandu, I.; Nemtoi, G.; Sandu, A. V.; Popescu, V.; Vasilache, V.; Sandu, I. G.; Vasilescu, E. The Reactivity of Ti10Zr Alloy in Biological and Electrochemical Systems in the Presence of Chitosan. *RSC Adv.* **2017**, *7* (23), 13919–13927.

(231) Mendoza-Huizar, L. H.; Robles, J.; Palomar-Pardavé, M. Nucleation and Growth of Cobalt onto Different Substrates: Part II. The Upd-Opd Transition onto a Gold Electrode. *J. Electroanal. Chem.* **2003**, *545*, 39–45.

(232) Burke, L. D.; Nugent, P. F. The Electrochemistry of Gold: I the Redox Behaviour of the Metal in Aqueous Media. *Gold Bull.* **1997**, *30* (2), 43–53.

(233) Jeyabharathi, C.; Ahrens, P.; Hasse, U.; Scholz, F. Identification of Low-Index Crystal Planes of Polycrystalline Gold on the Basis of Electrochemical Oxide Layer Formation. *J. Solid State Electrochem.* **2016**, *20* (11), 3025–3031.

(234) Trasatti, S.; Petrii, O. A. Real Surface Area Measurements in Electrochemistry. *J. Electroanal. Chem.* **1992**, *327* (1), 353–376.

(235) Nalini, S.; Nandini, S.; Madhusudana Reddy, M. B.; Suresh, G. S.; Melo, J. S.; Neelagund, S. E.; NaveenKumar, H. N.; Shanmugam, S. A Novel Bioassay Based Gold Nanoribbon Biosensor to Aid the Preclinical Evaluation of Anticancer Properties. *RSC Adv.* **2016**, *6* (65), 60693–60703.

(236) Cui, X.; Martin, D. C. Fuzzy Gold Electrodes for Lowering Impedance and Improving Adhesion with Electrodeposited Conducting Polymer Films. *Sens. Actuators Phys.* **2003**, *103* (3), 384–394.

(237) Luo, X.-L.; Xu, J.-J.; Zhang, Q.; Yang, G.-J.; Chen, H.-Y. Electrochemically Deposited Chitosan Hydrogel for Horseradish

Peroxidase Immobilization through Gold Nanoparticles Self-Assembly. *Biosens. Bioelectron.* **2005**, *21* (1), 190–196.

(238) Chow, K.-F.; Mavré, F.; Crooks, J. A.; Chang, B.-Y.; Crooks, R. M. A Large-Scale, Wireless Electrochemical Bipolar Electrode Microarray. *J. Am. Chem. Soc.* **2009**, *131* (24), 8364–8365.

(239) Qureshi, A.; Gurbuz, Y.; Niazi, J. H. Biosensors for Cardiac Biomarkers Detection: A Review. *Sens. Actuators B Chem.* **2012**, *171–172*, 62–76.

(240) Daubert, M. A.; Jeremias, A. The Utility of Troponin Measurement to Detect Myocardial Infarction: Review of the Current Findings. *Vasc. Health Risk Manag.* **2010**, *6*, 691–699.

(241) Yusuf, S.; Pearson, M.; Sterry, H.; Parish, S.; Ramsdale, D.; Rossi, P.; Sleight, P. The Entry ECG in the Early Diagnosis and Prognostic Stratification of Patients with Suspected Acute Myocardial Infarction. *Eur. Heart J.* **1984**, *5* (9), 690–696.

(242) Stubbs, P.; Collinson, P. O. Point-of-Care Testing: A Cardiologist's View. *Clin. Chim. Acta Int. J. Clin. Chem.* **2001**, *311* (1), 57–61.

(243) Antman, E.; Bassand, J.-P.; Klein, W.; Ohman, M.; Lopez Sendon, J. L.; Rydén, L.; Simoons, M.; Tendera, M. Myocardial Infarction Redefined—a Consensus Document of The Joint European Society of Cardiology/American College of Cardiology Committee for the Redefinition of Myocardial Infarction: The Joint European Society of Cardiology/ American College of Cardiology Committee∗∗A List of Contributors to This ESC/ACC Consensus Document Is Provided in Appendix B. *J. Am. Coll. Cardiol.* **2000**, *36* (3), 959–969.

(244) Ferguson, J. L.; Beckett, G. J.; Stoddart, M.; Walker, S. W.; Fox, K. A. A. Myocardial Infarction Redefined: The New ACC/ESC Definition, Based on Cardiac Troponin, Increases the Apparent Incidence of Infarction. *Heart* **2002**, *88* (4), 343–347.

(245) Apple, F. S.; Jesse, R. L.; Newby, L. K.; Wu, A. H. B.; Christenson, R. H.; Cannon, C. P.; Francis, G.; Morrow, D. A.; Ravkilde, J.; Storrow, A. B.; et al. National Academy of Clinical Biochemistry and IFCC Committee for Standardization of Markers of Cardiac Damage Laboratory Medicine Practice Guidelines: Analytical Issues for Biochemical Markers of Acute Coronary Syndromes. *Clin. Chem.* **2007**, *53* (4), 547–551.

(246) Gibler, W. B.; Young, G. P.; Hedges, J. R.; Lewis, L. M.; Smith, M. S.; Carleton, S. C.; Aghababian, R. V.; Jorden, R. O.; Allison, E. J.; Otten, E. J. Acute Myocardial Infarction in Chest Pain Patients with Nondiagnostic ECGs: Serial CK-MB Sampling in the Emergency Department. The Emergency Medicine Cardiac Research Group. *Ann. Emerg. Med.* **1992**, *21* (5), 504–512.

(247) Kim, W.-J.; Kim, B. K.; Kim, A.; Huh, C.; Ah, C. S.; Kim, K.-H.; Hong, J.; Park, S. H.; Song, S.; Song, J.; et al. Response to Cardiac Markers in Human Serum Analyzed by Guided-Mode Resonance Biosensor. *Anal. Chem.* **2010**, *82* (23), 9686–9693.

(248) Hamm, C. W.; Goldmann, B. U.; Heeschen, C.; Kreymann, G.; Berger, J.; Meinertz, T. Emergency Room Triage of Patients with Acute Chest Pain by Means of Rapid Testing for Cardiac Troponin T or Troponin I. *N. Engl. J. Med.* **1997**, *337* (23), 1648–1653.

(249) Bodor, G. S.; Porter, S.; Landt, Y.; Ladenson, J. H. Development of Monoclonal Antibodies for an Assay of Cardiac Troponin-I and Preliminary Results in Suspected Cases of Myocardial Infarction. *Clin. Chem.* **1992**, *38* (11), 2203–2214.

(250) Cummins, B.; Cummins, P. Cardiac Specific Troponin-I Release in Canine Experimental Myocardial Infarction: Development of a Sensitive Enzyme-Linked Immunoassay. *J. Mol. Cell. Cardiol.* **1987**, *19* (10), 999–1010.

(251) Penttilä, K.; Koukkunen, H.; Kemppainen, A.; Halinen, M.; Rantanen, T.; Pyörälä, K.; Penttilä, I. Myoglobin, Creatine Kinase MB, Troponin T, and Troponin I - Rapid Bedside Assays in Patients with Acute Chest Pain. *Int. J. Clin. Lab. Res.* **1999**, *29* (2), 93–101.

(252) Apple, F. S.; Falahati, A.; Paulsen, P. R.; Miller, E. A.; Sharkey, S. W. Improved Detection of Minor Ischemic Myocardial Injury with Measurement of Serum Cardiac Troponin I. *Clin. Chem.* **1997**, *43* (11), 2047–2051.

(253) Kar, P.; Pandey, A.; Greer, J. J.; Shankar, K. Ultrahigh Sensitivity Assays for Human Cardiac Troponin I Using TiO2 Nanotube Arrays. *Lab. Chip* **2012**, *12* (4), 821–828.

(254) Li, F.; Yu, Y.; Cui, H.; Yang, D.; Bian, Z. Label-Free Electrochemiluminescence Immunosensor for Cardiac Troponin I Using Luminol Functionalized Gold Nanoparticles as a Sensing Platform. *Analyst* **2013**, *138* (6), 1844–1850.

(255) Dong, M.; Li, M.; Qi, H.; Li, Z.; Gao, Q.; Zhang, C. Electrogenerated Chemiluminescence Peptide-Based Biosensing Method for Cardiac

Troponin I Using Peptide-Integrating Ru(Bpy)<Subscript>3</Subscript> <Superscript>2+</Superscript>-Functionalized Gold Nanoparticles as Nanoprobe. *Gold Bull.* **2015**, *48* (1–2), 21–29.

(256) Shen, W.; Tian, D.; Cui, H.; Yang, D.; Bian, Z. Nanoparticle-Based Electrochemiluminescence Immunosensor with Enhanced Sensitivity for Cardiac Troponin I Using N-(Aminobutyl)-N-(Ethylisoluminol)-Functionalized Gold Nanoparticles as Labels. *Biosens. Bioelectron.* **2011**, *27* (1), 18–24.

(257) Kerr, E.; Doeven, E. H.; Barbante, G. J.; Hogan, C. F.; Hayne, D. J.; Donnelly, P. S.; Francis, P. S. New Perspectives on the Annihilation Electrogenerated Chemiluminescence of Mixed Metal Complexes in Solution. *Chem. Sci.* **2016**, *7* (8), 5271–5279.

(258) Barbante, G. J.; Hogan, C. F.; Wilson, D. J. D.; Lewcenko, N. A.; Pfeffer, F. M.; Barnett, N. W.; Francis, P. S. Simultaneous Control of Spectroscopic and Electrochemical Properties in Functionalised Electrochemiluminescent Tris(2,2′-Bipyridine)Ruthenium(II) Complexes. *Analyst* **2011**, *136* (7), 1329–1338.

(259) Hankache, J.; Hanss, D.; Wenger, O. S. Hydrogen-Bond Strengthening upon Photoinduced Electron Transfer in Ruthenium–Anthraquinone Dyads Interacting with Hexafluoroisopropanol or Water. *J. Phys. Chem. A* **2012**, *116* (13), 3347–3358.

(260) Jabłońska-Wawrzycka, A.; Rogala, P.; Michałkiewicz, S.; Hodorowicz, M.; Barszcz, B. Ruthenium Complexes in Different

Oxidation States: Synthesis, Crystal Structure, Spectra and Redox Properties. *Dalton Trans.* **2013**, *42* (17), 6092.

(261) Keyes, T. E.; Jayaweera, P. M.; McGarvey, J. J.; Vos, J. G. Electronic Properties of Hydroquinone-Containing Ruthenium Complexes Indifferent Oxidation States. *J. Chem. Soc. Dalton Trans.* **1997**, *0* (9), 1627–1632.

(262) Adam Webb, M.; Knorr, F. J.; McHale, J. L. Resonance Raman Spectrum of [Ru(Bipyridine)3]2+ in Water, Acetonitrile and Their Deuterated Derivatives: The Possible Role of Solvent in Excited-State Charge Localization. *J. Raman Spectrosc.* **2001**, *32* (6–7), 481–485.

(263) Poizat, O.; Sourisseau, C. Infrared, Raman and Resonance Raman Studies of the Ru(2,2'-Bipyridine)32+ Cation in Its Chloride Crystal and as an Intercalate in the Layered Manganese Phosphide Sulfide (MnPS3) Compound. *J. Phys. Chem.* **1984**, *88* (14), 3007–3014.

(264) Choi, H. N.; Lee, J.-Y.; Lyu, Y.-K.; Lee, W.-Y. Tris (2, 2′-Bipyridyl) Ruthenium (II) Electrogenerated Chemiluminescence Sensor Based on Carbon Nantube Dispersed in Sol–Gel-Derived Titania–Nafion Composite Films. *Anal. Chim. Acta* **2006**, *565* (1), 48–55.

(265) Ackermann, M. N.; Interrante, L. V. Ruthenium(II) Complexes of Modified 1,10-Phenanthrolines. 1. Synthesis and Properties of Complexes Containing Dipyridophenazines and a Dicyanomethylene-Substituted 1,10-Phenanthroline. *Inorg. Chem.* **1984**, *23* (24), 3904–3911.

(266) Venkatanarayanan, A.; Martin, A.; Molapo, K. M.; Iwuoha, E. I.; Keyes, T. E.; Forster, R. J. Tuning the Electrochemiluminescence Potential from Immobilised BODIPY by Co-Reactant Selection. *Electrochem. Commun.* **2013**, *Complete* (31), 116–119.

(267) Tamagnini, F.; Scullion, S.; Brown, J. T.; Randall, A. D. Low Concentrations of the Solvent Dimethyl Sulphoxide Alter Intrinsic Excitability Properties of Cortical and Hippocampal Pyramidal Cells. *PLOS ONE* **2014**, *9* (3), e92557.

(268) Voets, I. K.; Cruz, W. A.; Moitzi, C.; Lindner, P.; Arêas, E. P. G.; Schurtenberger, P. DMSO-Induced Denaturation of Hen Egg White Lysozyme. *J. Phys. Chem. B* **2010**, *114* (36), 11875–11883.

(269) Vira, S.; Mekhedov, E.; Humphrey, G.; Blank, P. S. Fluorescent Labeled Antibodies - Balancing Functionality and Degree of Labeling. *Anal. Biochem.* **2010**, *402* (2), 146–150.

(270) Toseland, C. P. Fluorescent Labeling and Modification of Proteins. *J. Chem. Biol.* **2013**, *6* (3), 85–95.

(271) Frank, S. A. *Specificity and Cross-Reactivity*; Princeton University Press, 2002.

(272) Xiao, Y.; Isaacs, S. N. Enzyme-Linked Immunosorbent Assay (ELISA) and Blocking with Bovine Serum Albumin (BSA) - Not All BSAs Are Alike. *J. Immunol. Methods* **2012**, *384* (1–2), 148–151.

(273) Terato, K.; Do, C. T.; Cutler, D.; Waritani, T.; Shionoya, H. Preventing Intense False Positive and Negative Reactions Attributed to the Principle of ELISA to Re-Investigate Antibody Studies in Autoimmune Diseases. *J. Immunol. Methods* **2014**, *407*, 15–25.

(274) Paniagua, S. A.; Giordano, A. J.; Smith, O. L.; Barlow, S.; Li, H.; Armstrong, N. R.; Pemberton, J. E.; Brédas, J.-L.; Ginger, D.; Marder, S. R. Phosphonic Acids for Interfacial Engineering of Transparent Conductive Oxides. *Chem. Rev.* **2016**, *116* (12), 7117–7158.

(275) Kontos, M. C.; Anderson, F. P.; Alimard, R.; Ornato, J. P.; Tatum, J. L.; Jesse, R. L. Ability of Troponin I to Predict Cardiac Events in Patients Admitted from the Emergency Department. *J. Am. Coll. Cardiol.* **2000**, *36* (6), 1818–1823.

(276) Cho, I.-H.; Paek, E.-H.; Kim, Y.-K.; Kim, J.-H.; Paek, S.-H. Chemiluminometric Enzyme-Linked Immunosorbent Assays (ELISA)-on-a-Chip Biosensor Based on Cross-Flow Chromatography. *Anal. Chim. Acta* **2009**, *632* (2), 247–255.

(277) Zhou, Y.; Zhuo, Y.; Liao, N.; Chai, Y.; Yuan, R. Ultrasensitive Electrochemiluminescent Detection of Cardiac Troponin I Based on a Self-Enhanced Ru(II) Complex. *Talanta* **2014**, *129*, 219–226.

(278) Guo, H.; He, N.; Ge, S.; Yang, D.; Zhang, J. MCM-41 Mesoporous Material Modified Carbon Paste Electrode for the Determination of Cardiac Troponin I by Anodic Stripping Voltammetry. *Talanta* **2005**, *68* (1), 61–66.

(279) Dittmer, W. U.; Evers, T. H.; Hardeman, W. M.; Huijnen, W.; Kamps, R.; de Kievit, P.; Neijzen, J. H. M.; Nieuwenhuis, J. H.; Sijbers, M. J. J.; Dekkers, D. W. C.; et al. Rapid, High Sensitivity, Point-of-Care Test for Cardiac Troponin Based on Optomagnetic Biosensor. *Clin. Chim. Acta* **2010**, *411* (11), 868–873.

(280) Lewis, P. M.; Sheridan, L. B.; Gawley, R. E.; Fritsch, I. Signal Amplification in a Microchannel from Redox Cycling with Varied Electroactive Configurations of an Individually Addressable Microband Electrode Array. *Anal. Chem.* **2010**, *82* (5), 1659–1668.

(281) Nagale, M. P.; Fritsch, I. Individually Addressable, Submicrometer Band Electrode Arrays. 2. Electrochemical Characterization. *Anal. Chem.* **1998**, *70* (14), 2908–2913.

(282) Skotheim, T. A.; Reynolds, J. *Conjugated Polymers: Processing and Applications*; CRC Press, 2006.

(283) Bartelt, J. E. Electrochemiluminescence at Band Array Electrodes. *J. Electrochem. Soc.* **1992**, *139* (1), 70.

(284) Zhang, H.-R.; Wang, Y.-Z.; Zhao, W.; Xu, J.-J.; Chen, H.-Y. Visual Color-Switch Electrochemiluminescence Biosensing of Cancer Cell Based on Multichannel Bipolar Electrode Chip. *Anal. Chem.* **2016**, *88* (5), 2884–2890.

(285) Shi, H.-W.; Wu, M.-S.; Du, Y.; Xu, J.-J.; Chen, H.-Y. Electrochemiluminescence Aptasensor Based on Bipolar Electrode for Detection of Adenosine in Cancer Cells. *Biosens. Bioelectron.* **2014**, *55*, 459–463.

6 Chapter 6:

Conclusions and Future Directions

6.1 General Discussions and Summary of Conclusions

This chapter gives a brief overview of the main objectives achieved and outlines future directions for optimising ECL systems for specific applications. The primary focus of this thesis was to improve the performance of ECL based sensors by tuning and/or remodelling the signal transduction approach.

Firstly, the thesis focused on the fabrication of thin film composites. This was achieved by suspending carbon micro-particles in nafion/ethanol solution and depositing it on non-conducting substrates. Given the challenges of producing thin films while retaining favourable electrochemical and physical properties, a simple custom built spin coater was used to fabricate the films. The thin films were characterised by Raman to obtain structural information as well as the degree of graphitisation. The data obtained are important because it can give insight into the film thickness. SEM was employed to study the topography of the thin films and it was revealed that the particles retained its spherical structure with some charging phenomenon on films with low particle loadings. These findings suggest that the conductivity of the films depends on the amount of particles distributed on the underlying substrates. Four-point conductivity measurements were done and the data revealed that films with low particle loadings exhibited very low conductivity ($<6 \times 10^3$ S m^{-1}), but once the volume percentage of particles increased, the conductivity of the films increased, and a maximum conductivity of $2.0 \pm 0.1 \times 10^7$ S m^{-1} was achieved. Furthermore, the electrochemical properties of the films were investigated, and due to its impressive analytical performance, generation of ECL at its surface was possible. Additionally, bipolar ECL were generated and the results revealed that bipolar ECL can be generated with films that contain >65% (by volume) carbon particles using $[Ru(bpy)_3]^{2+}$ as the luminophore and tripropylamine as the coreactant, at an electric field of 14 V cm^{-1}, leading to a maximum of V drop across the 0.5 cm electrode. Based on the film's good electrochemical performance and ability to generate wireless ECL, it can be used as building blocks for more complex sensing designs, that is, portable and flexible electronics, and sensors.

Secondly, the thesis reported a three-dimensional (3D)-printed electrode array for possible use in sensing and screening applications. This design is a more scaled-up version of the previously described thin film electrodes. Here, the topography of the 3D array was studied by SEM. From the SEM results it was evident that the array consisted of 25 vertical pillars with a surface roughness that ranged from nano to approximately 100 µm in length scales. The elemental composition of the 3D array was confirmed by EDX, and the results revealed that the most dominant material was titanium. Moreover, the 3D array's electrochemical behaviour, including their electrochemically active area, was probed by cyclic voltammetry. The results revealed a non-ideal voltammetric response due to a passivating layer on the electrode surface. For this reason, the 3D array was modified with a gold layer. The analytical performance of both the gold modified- and bare- 3D electrodes were investigated. The results revealed that the gold coated 3D array exhibited superior analytical performance compared to the bare 3D array. However, significant ECL was generated at the bare 3D electrode array with increase in intensity due to the increase in scan rate. Significantly, at the gold coated 3D electrodes, the dependence of the ECL intensity was more complex since heterogeneous electron transfer was rapid and the response was strongly influenced by the geometry of the 3D electrode. Bipolar electrochemistry using ECL as signal readout was also demonstrated at the 3D arrays. Here, detection of wireless ECL generation was achieved by a CCD camera and the obtained images provided some interesting insights into the light distribution across the 3D array. These wireless data can be modelled to extract underlying charge transport kinetics of the bipolar electrochemical system. The combination of 3D-printing with bipolar electrochemistry can provide 3D structures of different sizes, shapes and chemical nature to be employed as sensor technologies, especially as multiplexed miniaturised biological devices.

Finally, the thesis focused on sensor development for diagnostic applications. Here, an ECL immunoassay was fabricated and its response performance was studied by conventional and bipolar ECL. But first, the efficacy of any given immunoassay depends on two major factors, that is, the efficiency of antigen-antibody complex formation and the ability to detect these complexes. In this thesis, a few approaches were adopted to meet these goals. That is, the thesis made use of a customised monoclonal antibody (Mab) that was specifically designed for binding to a certain region on the cardiac troponin-I (cTnI) antigen. This was done to improve the specificity of the proposed assay developed for cTnI detection. It should be noted that the utilisation of two or more antibodies improves assay sensitivity. For this reason, a commercially available secondary Mab was used in the development of the immunoassay. The assay detection method was based on electrochemiluminescence. Here, ruthenium(II)(bis-2,2-bipyridyl)-2(4-carboxylphenyl)imidazo[4,5-f][1,10]phenanthroline ($[Ru(bpy)_2(picCOOH)]^{2+}$) was employed as the ECL emitter. The ECL label was directly linked to the secondary Mab using standard solution chemistries. The immunoreactivity and/or solubility of the secondary Mab was unaffected after attachment to the $[Ru(bpy)_2(picCOOH)]^{2+}$ ECL label. Normally, the majority of ECL detection systems make use of solution phase reactions, where the ECL emitter is suspended in solution rather than attached to the sensing platform. In this instance, ECL signals can be lost due to the diffusion of the ECL emitter away from the electrode surface and/or due to depletion of the ECL reagents. Thus, by immobilising the ECL emitter on the electrode surface, such as in the case of the sandwich ECL immunoassay, where the $[Ru(bpy)_2(picCOOH)]^{2+}$ becomes immobilised on the sensing platform via the secondary Mab, an increase in signal output could be achieved. Furthermore, the secondary Mab was directed against a different epitope on the cTnI molecule; thus, no cross-reactivity occurred between the primary and secondary antibodies. This was confirmed by the absence of ECL light when the primary and secondary antibodies were incubated without the target analyte. Additionally, it was established that the sensor’s performance depends on its underlying supporting substrate, that is, the signal transduction platform. For this reason, the immunoassay was constructed on different supporting substrates such as, ITO PET/Glass, Au coated silica, Au-Au coated silica and an Au disc electrode. The Au disc electrode exhibited the highest ECL signals for the antigen-antibody reaction, thus it was employed as the sensing substrate for cTnI detection. The fabricated immunosensor exhibited a very high sensitivity (2.4 pg mL^{-1}) towards cTnI with an extremely low detection limit of 0.03 pg mL^{-1} (standard deviation, n=3). Furthermore, this immunoassay was extended to a bipolar electrochemical system so that wireless detection of cTnI could be realised. The data revealed that the wireless detection of cTnI resulted in about 10-fold ECL enhancement compared to the detection of cTnI by conventional means. The possibility of increasing the sensitivity of a sensing system by the wireless approach opens up new opportunities and directions toward the ultimate goal of developing lab-on-chip devices for clinical applications.

6.2 Future Directions

It is evident from the results discussed above that the factors affecting ECL generation are electrochemical in nature. For this reason, the transduction platforms discussed previously, warrants further investigation and optimisation to fully utilise their sensing capabilities.

The carbon based thin films presented in this thesis; represent an important class of sensing materials, especially due to its impressive conductivity and chemical stability it can be employed in a variety of technological applications. However, to fully utilise these films a few factors needs to be considered during the fabrication of these films, that is, surface roughness, substrate adhesion and mechanical stability. These are important factors, especially if the thin films need to be integrated into flexible and stretchable electronics.

The previously mentioned performance metrics of the 3D-printed electrodes revealed that their use would be beneficial in screening applications. This is because wireless ECL generation at the 3D electrode array was achieved by controlling the electric field across its surface using only a single DC power supply. However, it was observed that due to a flaw in the 3D array design (extra handle for electrical connection) wireless ECL generation was not fully extended to all the pillars in the array. For this reason, it is recommended to remove the handle (Figure 6.1) so that electroneutrality could be maintained across the 3D array (anodic and cathodic currents should be equal based on the active area of the bipolar electrode), and thus ECL light could be observed for each row of five pillars until x_0 (the point where the net faradaic current is zero) is reached. The combination of bipolar electrochemistry with this 3D array design can allow for screening of multiple analytes on a single sensing device. In addition focus can also be placed on the interlocking design of the 3D electrode array (Figure 6.2). This feature of the 3D electrodes can allow production of smart 3D systems for micro- and/or nano- based experiments, in particular, energy storage devices and implantable or injectable sensing devices for drug release experiments.

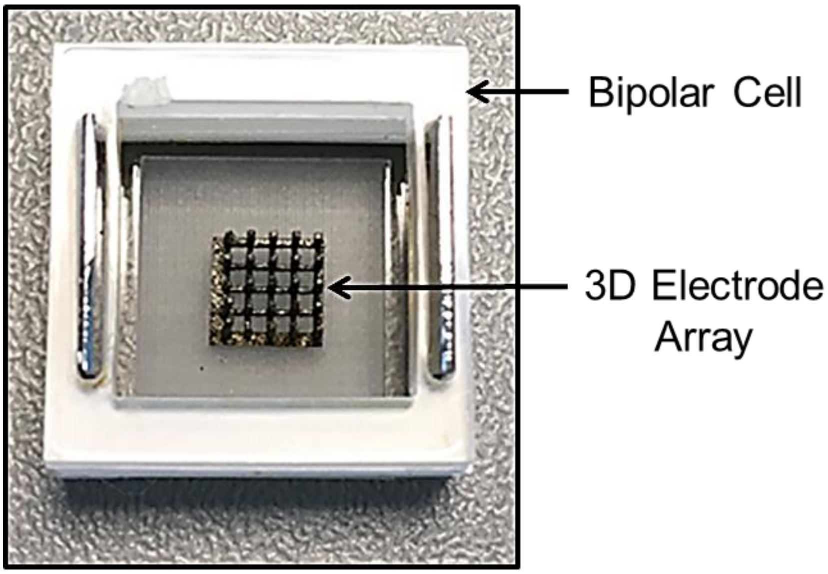

Figure 6.1: 3D-printed electrode array without a handle.

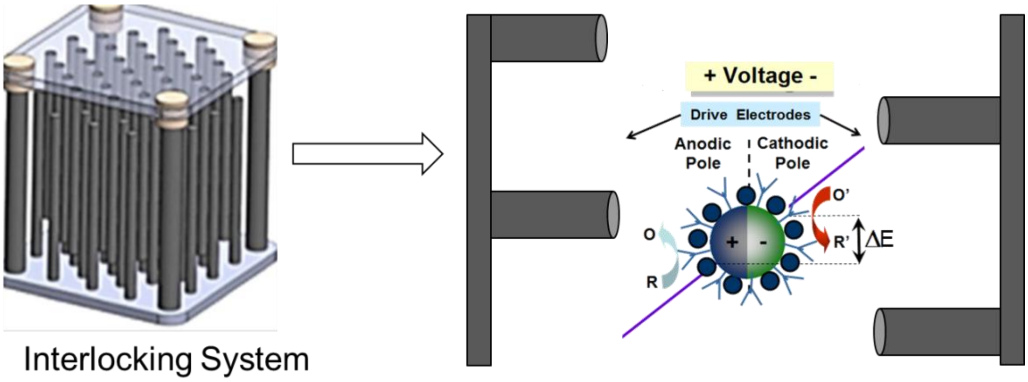

Figure 6.2: Illustrates a drug-containing particle embedded between the 3D-printed interlocking system.

Furthermore, with regard to the immunoassay results, the findings suggest that the sensitivity and specificity of the assay not only depends on the type of antibody but also the design and detection method. Thus, the sensitivity of the ECL based immunosensor can be further enhanced, by either tuning properties of existing ECL sensing platforms or by looking for new and emerging luminophore alternatives that can favour ECL generation. Here, bipolar electrochemistry was employed and the results revealed an increase in sensitivity for wireless detection of troponin. The Teflon bipolar cell used in this study can be further exploited by making some simple alterations to its design. For instance, the system can be adjusted to a closed bipolar configuration. This will allow the sensing and reporting reagents to be separated into different compartments (Figure 6.3). This type of design will be beneficial if the presence of the reporting reagents might chemically interfere with the target analyte in solution. Because the Teflon bipolar cell has a build-in microscope attachment (Chapter 2, Section 2.3.3.6, Figure 2.5) it can also be employed as a multiplexed sensing system. Meaning more than one bipolar electrode can be analysed without the use of a multichannel electrochemical workstation. Here, signal collection will be accomplished using the CCD camera of the microscope to achieve visual detection.

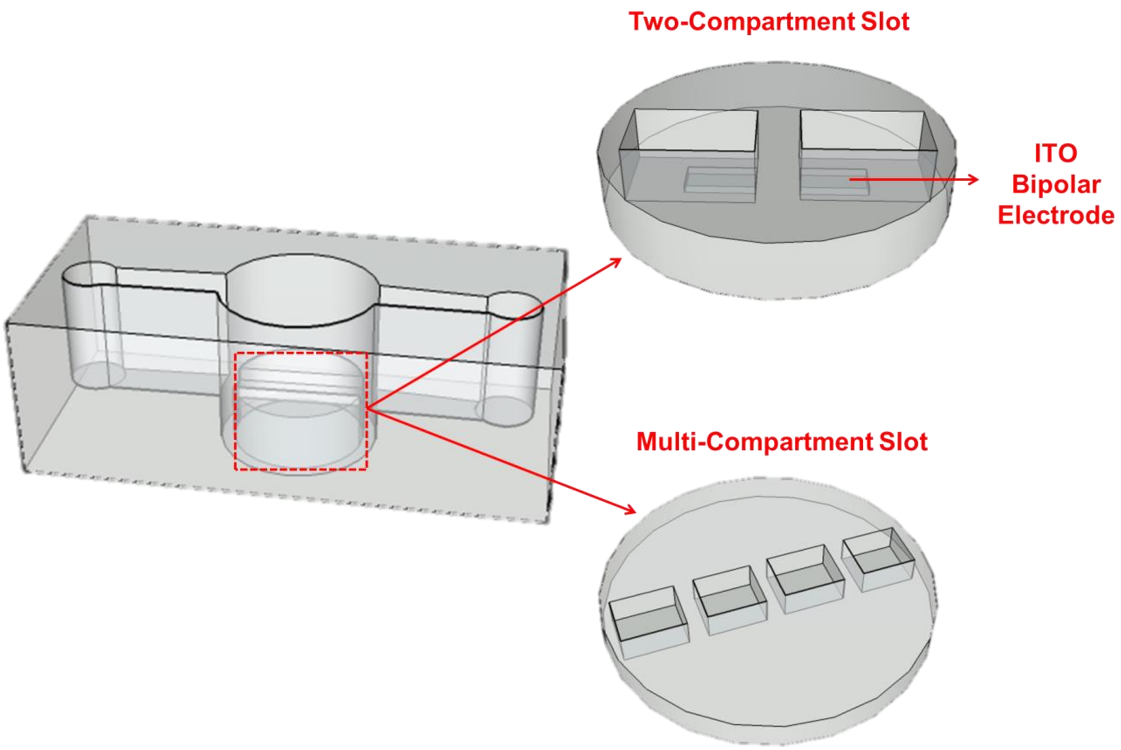

Figure 6.3: Different bipolar electrode slot designs for the Teflon bipolar cell.

The different concepts investigated in this thesis demonstrate the versatility of the ECL bipolar approach, especially in screening and sensing applications. The coupling of ECL and BPE is undoubtedly a successful combination and applications using this combination will progressively mature in the near future with improvements in analytical performances, especially in miniaturised setups such as in lab-on-chip devices.